Accepted for publication in the Astrophysical Journal
Preprint typeset using LaTeX style AASTeX6 v. 1.0

A COMPREHENSIVE SEARCH FOR STELLAR BOWSHOCK NEBULAE IN THE MILKY WAY: A CATALOG OF 709 MID-INFRARED SELECTED CANDIDATES

Henry A. Kobulnicky[1], William T. Chick[1], Danielle P. Schurhammer[1], Julian E. Andrews[1,2], Matthew S. Povich[2], Stephan A. Munari[1], Grace M. Olivier[1,3], Rebecca L. Sorber[1,4], Heather N. Wernke[1,5], Daniel A. Dale[1], and Don M. Dixon[2]

[1]Dept. of Physics & Astronomy, University of Wyoming, Laramie, WY 82070, USA
[2]Department of Physics & Astronomy, California State Polytechnic University, 3801 West Temple Avenue, Pomona, CA 91768, USA
[3]Department of Astronomy, Case Western Reserve University, Cleveland, OH 44106, USA
[4]Front Range Community College, 3645 W. 112th Avenue, Westminster, CO 80031, USA
[5]Department of Physical Sciences, Embry-Riddle Aeronautical University, Daytona Beach, FL 32114, USA

ABSTRACT

We identify 709 arc-shaped mid-infrared nebula in 24 μm *Spitzer Space Telescope* or 22 μm *Wide Field Infrared Explorer* surveys of the Galactic Plane as probable dusty interstellar bowshocks powered by early-type stars. About 20% are visible at 8 μm or shorter mid-infrared wavelengths as well. The vast majority (660) have no previous identification in the literature. These extended infrared sources are strongly concentrated near Galactic mid-Plane with an angular scale height of $\sim$0.6°. All host a symmetrically placed star implicated as the source of a stellar wind sweeping up interstellar material. These are candidate "runaway" stars potentially having high velocities in the reference frame of the local medium. Among the 286 objects with measured proper motions, we find an unambiguous excess having velocity vectors aligned with the infrared morphology — kinematic evidence that many of these are "runaway" stars with large peculiar motions responsible for the bowshock signature. We discuss a population of "in-situ" bowshocks ($\sim$103 objects) that face giant H II regions where the relative motions between the star and ISM may be caused by bulk outflows from an overpressured bubble. We also identify $\sim$58 objects that face 8 μm bright-rimmed clouds and apparently constitute a sub-class of in-situ bowshocks where the stellar wind interacts with a photo-evaporative flow from an eroding molecular cloud interface (i.e., "PEF bowshocks"). Orientations of the arcuate nebulae exhibit a correlation over small angular scales, indicating that external influences such as H II regions are responsible for producing some bowshock nebulae. However, the vast majority of this sample appear to be isolated (499 objects) from obvious external influences.

Keywords: Stars: massive — Interstellar medium (ISM), nebulae — surveys (ISM:) HII regions (Stars:) early-type — Stars: kinematics and dynamics —

1. INTRODUCTION

Stellar bowshock nebulae are arcuate structures created by the interaction between stellar winds and the surrounding interstellar medium (ISM) where the relative velocity between the two is supersonic (van Buren et al. 1990; Mac Low et al. 1990). A shock front forms at the interface of the high speed stellar wind and the ambient interstellar medium. The swept up interstellar dust and gas ahead of the high-velocity star forms an arc-like feature preceding the peculiar motion of the star. This material is most clearly visible in the mid-infrared and sometimes in optical emission lines such as Hα and O III (Brown et al. 2005; Meyer et al. 2014, 2016). Most bowshock nebulae are observed around high-velocity massive stars, but they have also been identified preceding high-velocity pulsars (Wang et al. 2013), red supergiants (Noriega-Crespo et al. 1997), and associated with proplyds in the Orion Nebula (Bally et al. 1998). Wilkin (1996) derived an exact analytic solution for this interaction by balancing the ISM pressure and ram pressure of the stellar winds. Based on this model, Comerón & Kaper (1998); Meyer et al. (2014, 2016) used computer simulations to demonstrate that stable bowshocks can be formed for a variety of interaction scenarios over a range of relative velocities, ISM densities, and stellar wind momentum fluxes.

A significant proportion (10±25%) of early-type stars reside outside of stellar clusters Gies & Bolton (1986). Because of their short main-sequence lifetimes these stars, known as runaway stars, must be moving at high peculiar velocities,

typically >30 km s^{-1} (Gies & Bolton 1986). Stone (1991) found that O and B type stars (OB stars) comprise 50% of all runaway stars, and these OB runaways are dominated by O type stars (12:1). Two general scenarios that generate runaway stars have been proposed: close dynamical interactions of either single stars (Poveda et al. 1967) or binary-binary interactions (Spitzer & Mathieu 1980), and ejection from close binary systems when the more evolved member undergoes a core-collapse supernova (CCSN; Zwicky 1957; Blaauw 1961).

Poveda et al. (1967) analytically simulated the dynamical interactions of small clusters of 5–6 50 M$_\odot$ stars and found that 2–17% of these stars were ejected from the cluster with velocities in excess of 35 km s^{-1}. Kroupa et al. (2001) concluded that dynamical few-body ejections of OB stars likely occur in the first $\lesssim$1 Myr of the cluster's history before the radiation of the OB stars expels the mass-dominant gas component of the cluster, causing the cluster to expand. Leonard (1991) simulated binary-binary gravitational interactions and found a maximum ejection velocity of 700 km s^{-1} for 60 M$_\odot$ stars and 1400 km s^{-1} for 1–4 M$_\odot$ stars. Though the initial multiplicity fraction of OB stars is unknown, studies have shown that the fraction is likely higher than 60% in stellar clusters, meaning that at least 75–90% of massive stars are in a multiple system and have the potential to participate in few-body interactions (García & Mermilliod 2001; Sana et al. 2012; Kiminki & Kobulnicky 2012; Kobulnicky et al. 2014).

Zwicky (1957) first proposed that stars that form in close binary systems could be ejected when one of the components explodes as a supernova. Liu et al. (2015) hydrodynamically simulated the effects of asymmetric CCSN in close binary systems and determined that the less-evolved companion could survive with minimal disruption and be ejected at runaway velocities. Fryer et al. (1998) used Monte Carlo simulations to determine the necessary impulse to account for the observed velocity distribution of pulsars and found by extension that the necessary forces could accelerate the surviving OB companions to velocities up to 100 km s^{-1}. Tauris (2015) expanded upon this work with new simulations and found that early-type B stars (10 M$_\odot$) could be accelerated up to ∼320 km s^{-1} under ideal conditions with increasing maximum velocities for lower mass stars (up to ∼1050 km s^{-1} for a 0.90 M$_\odot$ star).

It is likely that both few-body interactions and supernovae in binary systems combine to generate the observed population of runaway stars. Using Hipparcos proper motions Hoogerwerf et al. (2000) traced the motions of two known runaway stars, AE Aur and μ Col (O9.5V and O9.5B/B0, moving in opposite directions at 100 km s^{-1}) to a common origin ∼2.5 million years ago near the location of the binary pair ι Ori. They proposed that the two runaways may have been ejected in a binary-binary interaction. Gvaramadze et al. (2013) identified two O-type runaways that may have been ejected from the star cluster NGC 3603 in a single star-binary interaction when the single star captured one binary member and ejected the other with both systems being accelerated to high peculiar velocities relative to the cluster. The new binary system later merged into the single 'blue straggler' star observed. Hoogerwerf et al. (2000) used Hipparcos proper motions to trace ζ Oph and the pulsar J1932+1059 back to the same region of the Upper Scorpius star forming region ∼1 Myr ago, which could indicate that the two were once members of a common binary prior to the supernova creating the pulsar. Hoogerwerf et al. (2001) identified eight additional binary-binary and 16 binary-supernova ejection candidates by extrapolating their proper motions. A fraction of the ejected stars in the Liu et al. (2015) simulations accreted material from the CCSN, and these simulations predict that atmospheric chemical enrichments may be observable in the runaway stars if mixing is inefficient. Several runaway stars (Blaauw 1993; Gvaramadze 2009) have been observed with significant α-element enrichment, consistent with this prediction.

Hybrids of these ejection scenarios may also be possible. Pflamm-Altenburg & Kroupa (2010) suggested that a two-step scenario involving a dynamically ejected binary pair could accelerate a single runaway star following a CCSN. Because of the two kicks accelerating the star in this scenario, the star's observed proper motion vector may not point back to a cluster. de Wit et al. (2005) examined a sample of known runaway stars and found that 4±2% do not have proper motions that can be extrapolated back to a known cluster or association.

Hypervelocity stars (HVSs) are a special class of runaway stars with extremely high space velocities, typically defined as being greater than 400 km s^{-1} (Kenyon et al. 2008). Hills (1988, 1991) first predicted hypervelocity stars when modelling the close interaction of binary star systems with a supermassive black hole (SMBH), which produced stars with velocities in excess of 1000 km s^{-1}. Yu & Tremaine (2003) proposed two additional mechanisms: gravitational interaction between a pair of single stars with a extreme mass ratio or stellar acceleration by a binary SMBH system. However, they predicted that the HVS generation rate by single star interactions is likely low enough to be undetectable due to the extremely small impact parameter required. Brown et al. (2005) reported the discovery of the first HVS in the Galactic Halo, SDSS J090745.0+024507, a main sequence B star (Fuentes et al. 2006) which remains the fastest observed HVS with a Heliocentric radial velocity of 831.1±5.7 km s^{-1} (Brown et al. 2014). Brown et al. (2014) assembled the most complete catalog of HVSs with 24 confirmed objects and several additional candidates. Several simulations (Brown et al. 2005; Meyer et al. 2014, 2016) have demonstrated that it is unlikely that HVSs can support visible bowshock nebulae due to their high velocities inhibiting the accumulation of material in the leading shock.

Two general classes of bowshock nebulae are generally recognized: those supported by runaway stars, and "in-situ" bowshocks supported by a star overrun by an outflow of hot gas from a star-forming or H II region. Gull & Sofia (1979) used optical emission line imaging to catalog the first bowshock nebulae which appeared as "distorted interstellar bubbles". These nebulae were observed around the prototypical runaway ζ Oph and around the star LL Ori situated in an outflow from θ^1 Ori in the Orion Nebula. Povich et al. (2008) cataloged six arcuate nebulae around the star-forming regions M 17 and RCW 49 and identified these in-situ shocks as a distinct class. The associated physics of these in-situ shocks are similar to runaway bowshocks when considered within the rest frame of the stellar source.

Using 60 μm images from the Infrared Astronomical Satellite (*IRAS*) (Neugebauer et al. 1984) van Buren & McCray (1988) compiled the first catalog of bowshock nebulae. A more complete sample gathered from *IRAS* images found a total of 58 bowshock nebula candidates around 188 runaway OB stars (van Buren et al. 1995). Subsequent re-analysis of *IRAS* all-sky images concluded only 19 of the 58 candidate were bowshock nebulae with 2 additional questionable candidates (Noriega-Crespo et al. 1997). The increased angular resolution of infrared surveys conducted by the Spitzer Space Telescope (*SST*) and Wide-Field Infrared Survey Explorer (*WISE*) (Wright et al. 2010), enabled the identification of small collections of bowshock nebulae in both the LMC (Gvaramadze et al. 2010) and SMC (Gvaramadze et al. 2011a), generated by stars ejected from the star-forming regions NGC 6611 (Gvaramadze & Bomans 2008), Cygnus OB2 (Kobulnicky et al. 2010), NGC 6357 (Gvaramadze et al. 2011c), NGC 3603 (Gvaramadze et al. 2013), and Carina Nebula (Sexton et al. 2015), and powered by high-mass X-ray binaries (Gvaramadze et al. 2011b), pulsars (Wang et al. 2013), red (Noriega-Crespo et al. 1997; Cox et al. 2012; Gvaramadze et al. 2014a) and blue (Gvaramadze et al. 2014b) supergiants, and the A-type star δ Vel (Gáspár et al. 2008). Peri et al. (2012, 2015) conducted the most extensive search to date for bowshock nebulae and runaway stars by examining *WISE* archival images in the vicinity of several hundred runaway star candidates identified by Tetzlaff et al. (2010). The most recent release of their E-BOSS (Extensive Bow Shock Survey) catalog (Peri et al. 2015) contains a compilation of 73 bowshock nebulae candidates found in their visual search and those previously identified in the literature. Based on their work, it appears that 5–10% of runaway stars support bowshock nebulae, though some earlier studies have suggested higher rates of ∼15% (van Buren et al. 1995) or as high as ∼30% (van Buren & McCray 1988).

The present paper is the first in a series presenting and analyzing a new catalog of candidate bowshock nebulae. Our group has taken the opposite approach of the E-BOSS survey (Peri et al. 2012, 2015) by conducting a comprehensive visual inspection of existing space-based infrared surveys to identify candidate bowshock nebulae and runaway stars along the Galactic mid-Plane. In this paper, we report the identification of 708 candidate bowshock nebulae, 659 of which have not been previously identified in the literature. This catalog constitutes the largest collection of bowshock nebula candidates by an order of magnitude. In Chick et al. (2016), we present the results of spectroscopic follow-up of nearly 100 targets, that >95% of these infrared-selected stellar sources are, in fact, early-type massive stars, and that infrared nebular morphology alone is enough to select massive stars with confidence. In Section 2, we discuss the selection process and space-based infrared datasets used for identifying candidate nebulae. Section 3 presents the archival infrared images of our candidates and discusses the demographics of our sample including the sky distribution, proper motions, and their surrounding environments. We summarize our results in Section 4.

2. BOWSHOCK CANDIDATE IDENTIFICATION

2.1. *Infrared Survey Data and Strategy Employed*

Our team conducted a visual examination of mid-infrared images from *Spitzer Space Telescope* (*SST*; Werner et al. 2004) and the Wide-field Infrared Survey Explorer (WISE; Wright et al. 2010) to locate bowshock nebula candidates. The *Spitzer Space Telescope* data included several wide-area surveys conducted using the Infrared Array Camera (IRAC; Fazio et al. 2004) in its 3.6, 4.5, 5.8, and 8.0 μm bandpasses along with 24 μm data from the Multiband Imaging Photometer for Spitzer (MIPS; Rieke et al. 2004). The *Spitzer Space Telescope* beam size at these bands is 1.66, 1.72, 1.88, 1.98 and 6″ FWHM, respectively[1]. Survey data included images obtained as part of the Galactic Legacy MidPlane Survey Extraordinaire I and II (GLIMPSE, GLIMPSE II; Benjamin et al. 2003) and MIPSGAL (Carey et al. 2009) programs, the the *Spitzer* Legacy Survey of the Cygnus-X Complex (Hora et al. 2007), and the *Spitzer* Mapping of the Outer Galaxy (SMOG; Carey et al. 2008). Together these *SST* surveys cover slightly more than 304 square degrees of the Galactic Plane — a large continuous strip at $-65° < \ell < 65°$, $|b| \lesssim 1°$ (GLIMPSE and MIPSGAL), a 24 square degree regions near $\ell = 79°$ (Cyg-X), and a $2° \times 10°$ strip centered on ℓ=105° (SMOG). Our search used the large mosaics at each waveband constructed by the GLIMPSE team that are available at the Spitzer

[1] http://irsa.ipac.caltech.edu/data/SPITZER/docs/irac/iracinstrumenthandbook, http://irsa.ipac.caltech.edu/data/SPITZER/docs/mips/mipsinstrumenthandbook

Science Center. The *WISE* data include images at the 3.4, 4.6, 12, and 22 μm bandpasses which have beamsizes of 6.1″, 6.4″, 6.5″, and 12.0″ FWHM, respectively. Our search of the *WISE* all-sky survey images (about 460 square degrees of the Outer Galaxy) used 1° mosaics in regions along the Galactic Plane not covered by Spitzer and the Centre de Données astronomiques de Strasbourg's Aladin[2] interface which allows a viewer to rapidly browse large regions of the sky. Given the concentration of bowshock nebulae very near the Galactic Plane (Section 3.2), our search of the *WISE* data concentrated on regions $|b| < 2°$, but we also performed a cursory search using the Aladin (Bonnarel et al. 2000) Lite interface up to $|b| < 10°$. Only a few objects were discovered beyond $b = \pm 1°$.

We searched the *SST* mosaics for 1) arc-shaped or lima-bean-shaped nebulae at 24 μm and/or 8.0 μm that had 2) a high degree of symmetry with 3) at least one prominent star located near the axis of symmetry visible at 4.5 μm. For the majority of candidates, there is a single bright star located along the axis of symmetry; it constitutes the obvious early-type stellar candidate, even though there is no spectral information available for the vast majority of candidates. In some cases there are multiple candidate stars within the arc, and in a few cases there are no prominent stellar candidates, especially in the inner Galaxy where the stellar density is high and even early type stars may appear faint because they are located at large distances.

Our initial visual search team interpreted these three criteria liberally. The Galactic Plane exhibits very complex structures at 8.0 and 24 μm that vary greatly in surface brightness over small angular scales, producing a large number of initial candidates that do not meet one of more of the three search criteria. The final decision regarding which objects met all three criteria was ultimately made by the senior author (HAK). Relaxing these criteria would substantially increase the candidate list by at least a factor of two. The search process involved examining color representations of the 4.5, 8.0, and 24 μm images displayed with a square-root color stretch. Owing to the high dynamic range of the mosaics, it was necessary to use a variable maximum and minimum intensity levels to achieve the needed contrast, depending on the surface brightness in each region. Often in regions of large dynamic range several different scalings were used. This was necessary to find nebulae superimposed on regions with high background levels (e.g., within H II regions). No quantitative thresholds were used in the search process; indeed, the rms noise levels are not well defined, varying significantly on small spatial scales where regions of very high and very low surface brightness appear adjacent to one another. The maximum angular size of a detectable candidate is limited by the size of the survey mosaics at about 2 degrees; in practice, there are no candidates larger than 8.6′. The angular resolution of the *SST*/*WISE* surveys, described above, sets the lower limit on the angular size of detectable candidates.

Two or more team members searched each region of the Plane. In comparing candidate lists identified by each searcher we concluded that there was at least a 50–75% overlap between the candidate lists. Each searcher identified candidates not found by the others. We estimate that use of additional searchers could increase the current candidate list, most of this gain coming in areas of the Plane dominated by high-surface brightness H II regions. A search such as this can never be deemed "complete" given the inherent subjectivity of what constitutes "arc-shaped" or "symmetric", especially in regions having large changes in surface brightness over small angular scales where genuine bowshock nebulae may be confused with unrelated foreground or background emission.

All *SST* objects were discovered initially in the 24 μm bandpasses where emission is either thermal in nature or from (semi-)stochastic heating of small dust grains. Only a minority of the bowshock candidates exhibit morphologically similar counterparts in the 8.0 μm band, which predominantly includes a broad solid-state emission feature from polycyclic aromatic hydrocarbons (PAHs). However, the 8.0 μm band may also include a contribution from very hot dust near the sublimation temperature.

Our search of the WISE images concentrated on the 22 μm (W4) band for nebula identification and the 4.6 μm (W2) band for identification of a stellar source. We find that nearly all candidates identified in the W4 band also had counterparts in the 12 μm (W3) band, which may include both PAH and hot dust emission. Owing to the superior angular resolution of *SST* compared to WISE – 6.0″ at 24 μm versus 12.0″ FWHM at 22 μm – we gave preference to the *SST* data (where available) and did not search the overlapping *WISE* images.

Because the *WISE* beamsize is twice that of the *SST* at the longest wavelengths, objects that would appear arcuate in *SST* imaging might appear circular in *WISE* and, therefore, be rejected from the catalog. This leads to a kind of systematic decrease in the completeness (at fixed angular sizes of 6–12″) for the regions surveyed only with *WISE*. Similarly, we find a large number of small circular 24 μm nebulae near the angular resolution limit of *SST* that might appear arcuate if viewed under higher angular resolution.

Additionally, bowshock candidates listed in the literature were examined and retained if they met our mor-

[2] http://aladin.u-strasbg.fr/

phological selection criteria described above. Our survey of the literature included the compilations of Peri et al. (2015, Pe15), Sexton et al. (2015, S15), Peri et al. (2012, Pe12), Gvaramadze et al. (2011c, G11), Kobulnicky et al. (2010, K10), Gvaramadze & Bomans (2008, G08), Povich et al. (2008, P08), Comerón & Pasquali (2007, CP07), Noriega-Crespo et al. (1997, N97), and van Buren & McCray (1988). The final collection tabulated here does not include many of the candidates listed in these works, primarily because they fail to meet one of more of the morphological criteria.

2.2. *Search Results*

Table 1 lists parameters for the probable central stars of the 709 candidate bowshock nebula. The first twenty rows appear in the printed Journal to give guidance as to the table format and content. The entire table is available in digital format in the electronic edition. Column 1 is a sequential identification number unique to this work, column 2 is a generic name in Galactic coordinates, while columns 3 and 4 list the J2000 right ascension and declination for the putative central star. Column 5 gives the publication where the candidate is first identified as a bowshock candidate. A "T" indicates "this work", and other abbreviations refer to published works, as referenced fully in the table footnotes. Of the 709 tabulated objects, 660 are identified herein as bowshock candidates for the first time. Column 6 lists another common alias for the central stellar source, if one exists in the literature, such as an HD (Henry Draper Catalog) designation. Fully 581 of the 709 stellar sources have no alternate designation in the literature, indicating that the vast majority of the objects are faint and highly reddened. Column 7 is a single character designating whether the nebular object has an *SST* IRAC 8.0 counterpart with a similar morphology (Y), has no detection above background levels at this waveband (N), or has no data from IRAC (-).[3] We find that 130 of the 626 objects having IRAC data show a nebula at 8.0 μm, indicating a probable PAH contribution. Column 8 contains a single alphanumeric code, "C", in cases where the probable central stellar source is uncertain owing to faintness or to the presence of multiple stars of similar magnitude near the nebular axis; 115 objects fall into this category. In such cases we adopt the brightest point source nearest the axis of symmetry as the most probable star, but we urge caution with regard to the certainty of this identification. Columns 9 and 10 list the distance R_0 (in arcsec) from the putative central star to the apsis of the candidate bowshock and the position angle (in degrees from N toward E) of this vector in equatorial coordinates. These values were measured by eye and carry typical uncertainties of $1\farcs5$ and 5°, respectively. Columns 11 and 12 list the 2MASS H-band and IRAC 4.5/WISE 4.6 μm magnitudes of the central star, obtained from the 2MASS (Skrutskie et al. 2006) and GLIMPSE/WISE catalogs, respectively. In just a handful of cases (19), no H-band source is measured, implying an extremely red, highly extinguished object. Column 13 lists an estimate of the K-band extinction to each source, inferred using the H−4.5 color and the Rayleigh-Jean Color Excess formulation of Majewski et al. (2011).

The final column of Table 1 provides additional descriptors that characterize the local environment of each stellar candidate. Column 14 contains an alphanumeric code that describes the immediate environment of each candidate as either isolated (I; 499 instances), directly facing a large H II region within about 10 arcminutes (FH; 103 instances), facing a bright-rimmed cloud prominent at 8.0 μm within several arcminutes (FB; 58 instances), or situated within a giant H II region (H; 49 instances). In some cases two designations could apply, for example, a candidate that lies within an H II region that also faces a bright-rimmed cloud. In such cases FB is given preference over H. Objects designated FH may be instances of the "in-situ" bowshocks (Povich et al. 2008). These descriptors are qualitative judgments of the candidates' immediate environments intended to elucidate possible physical origins for what we regard as potentially different classes of bowshock nebulae. Given the unknown distances of each object and complex sightlines in the Galactic Plane, physical connections between bowshock candidates and other objects nearby on the sky are necessarily uncertain. Section 3.5 will discuss example objects in each of these five categories in more detail.

3. PROPERTIES OF THE BOWSHOCK CANDIDATES

3.1. *Infrared Images*

Figure 1 shows a collage of three-color representations for six objects from Table 1 that may be regarded as prototypical bowshock nebulae. The angular scale of each panel differs to accommodate the size of each object. Each panel displays a highly resolved, unmistakable arc-shaped nebulae and a bright central star with a substantial proper motion consistent with the nebular bowshock orientation. These six objects are ζ Oph (G006.2812+23.5877; upper left), AE Aur (G172.0813−02.2592; upper right), HD136003 (G322.6802+00.9060; center left), HD150898 (G329.9790−08.4736;

[3] Essentially all of the objects detected in the WISE 22 μm band also have counterparts in the WISE 12 μm band. Therefore, we do not tabulate detections for the WISE bandpasses.

center right), HD155755 (G348.7967+00.1455; lower left), HD143275 (G350.0969+22.4904; lower right), as "prototypical" examples of bowshock nebulae drawn from the literature. We use a color scale that depicts the *SST* 24 μm or *WISE* 22 μm image in red, the *SST* 8.0 or *WISE* 12 μm image in green, and the *SST* 3.6 or *WISE* 3.6 μm image in blue. A white arrow depicts the proper motion vector magnitude and direction. Images of G322.6802+00.9060 and G348.7967+00.1455 use IRAC data so the nebula is dominated by 24 μm emission (red) and appears red, while the other four use *WISE* data, and the combination of 22 μm (red) and 12 μm (green) emission results in a yellowish appearance.

Figure 1 reveals that only a minority of the objects display the ideal ("theoretical") bowshock morphology — e.g., see Figure 1 of Wilkin (1996) or Figure 9 of Meyer et al. (2016) or Figure 3 of Acreman et al. (2016) for a variety of viewing inclination angles). The ζ Oph nebula (upper left) appears flocculent and significantly asymmetric, perhaps because it is highly resolved as the nearest of the bowshocks at a distance of only 140 pc, based on its Hipparcos parallax (Perryman et al. 1997). Most of the nebulae are, to some degree, asymmetric. In some cases, the star appears slightly displaced from the axis of symmetry. Wilkin (2000) discusses such a displacement as the natural result of either a density gradient in the ambient medium transverse to the star's motion or a stellar wind that is anisotropic.

A digital Appendix contains images of all 709 candidate objects from Table 1 in Figures A.1 through A.118 using the same color scheme as Figure 1. These figures depict an angular field of view of 2 arcmin square in most cases to facilitate easy angular size comparison, but for some objects a window of $4'$ or $8'$ is necessary to include the entire nebula or pertinent features in the immediate environment. For a few objects observed by the *SST* IRAC but not at MIPS 24 μm, we use the *WISE* 22 μm image instead. In a just a few instances, the images are constructed using the IRAC 8.0/4.5/3.6 μm images. In some panels a white arrow depicts the proper motion vector magnitude and direction, if proper motion data are available and the measured proper motion is larger than the uncertainties. The vast majority of the 709 candidate bowshock nebulae have small angular sizes and are, consequently, less resolved than the prototypical examples; nevertheless, they share the overall shape, colors, and morphological symmetry of the prototypes.

3.2. *Candidate Bowshock Distribution*

Figure 2 plots the positions of the candidate bowshock nebulae on the Galactic Plane for the 663 objects that lie in the inner two Galactic quadrants at longitudes $-90° < \ell < 90°$. Colors denote the extiction values estimated from the H$-$4.5 μm color excess: cyan–A_V<2; green–2 <A_V< 5; red–5 <A_V< 10; magenta–A_V> 10; white–no data. The points appear superimposed on a three-color representation of the Galactic Plane with the Infrared Astronomical Satellite (*IRAS*) maps at 25/60/100 μm in blue/green/red, respectively. The distribution of objects is non-uniform, even allowing for the fact that they were selected from surveys covering only a portion of the Plane, principally within one degree of b=0° and within 60° of Galactic Center. For example, there is an overdensity of objects in the vicinity spiral arm tangencies near ℓ=25–30° where the path length through spiral arms is long. The Cygnus-X region near ℓ=79° also exhibits an abundance of objects, probably the result of having multiple nearby (1.2–1.5 kpc) regions of massive star formation. The Carina star forming region near ℓ=287° also exhibits a large number of candidates. A close examination of Figure 2 further reveals that objects having similar extinctions cluster together on the sky, a probable signature of clusterings of massive stars at similar distances and reddennings.

Figure 3 is a histogram of the Galactic latitudes for the 561 candidates that lie within the footprint of the GLIMPSE and MIPSGAL surveys where coverage is complete: $-60° < \ell < 60°$,$-1° < b < 1°$. The histogram is strongly peaked near b=0°, indicating that very few objects meeting our selection criteria are likely to be found at larger latitudes. The angular scale height for these objects is approximately 0.6° from mid-Plane, identical to the scale height for interstellar bubbles and H II regions (Churchwell et al. 2006).

3.3. *Bowshock Orientations*

Figure 4 displays the positions of bowshocks candidates at $0° < \ell < 60°$ (*upper panel*) and $300° < \ell < 360°$ (*lower panel*). Symbol color and the background three-color IRAS image is the same as in Figure 2. Vector directions indicate the orientation of the bowshock nebulae as determined by the IR morphology. This figure further illustrates that objects with similar extinctions often cluster together on the sky. Furthermore, there are also clusters of objects that have similar orientations. One notable example of this is at the base of the giant gas pillar in M 16 near ℓ=16.8°, b=0.6° where four objects all point toward the source of radiation that has sculpted the pillar.

Figure 5 depicts four candidate bowshock nebulae (G016.8118+00.6679, G016.8760+00.6456, G016.8930+00.6800, and G016.9278+00.6323) in the same field, all pointing in the same direction as the pillars. The central stars of the bowshocks are HD 168183 (O9.5III+B4V), BD$-$13 4936 (B0e), BD$-$13 4934 (B1Vp), and BD$-$13 4937 (B1.5V),

respectively, all early-type stars. BD−13 4937 has a measured proper motion directly *away* from the source of radiation in this young star forming region. These are excellent candidates for "in-situ" bowshocks (Povich et al. 2008) formed by the interaction between the star's own wind and an outflow from the M 16 H II region. In regions like this one, bowshocks exhibit a similar orientation not because they share a common space velocity but because a common source of external momentum flux impinges upon them. There are many other possible "in-situ" bowshocks in our sample, and these are flagged by FH in Table 1.

In order to test the hypothesis that bowshock orientations in this field and others may be correlated on small angular scales, we computed the difference in position angle between each pair of the N=709 nebulae (N×(N−1)/2 unique pairings) and then plotted the mean ΔPA versus angular separation in 8′ bins in Figure 6. For comparison to the null hypothesis (that the position angles are uncorrelated) we randomly shuffled the position angles among the objects 1000 times and computed the mean ΔPA and dispersion in each bin. Figure 6 plots the data (blue points) and the results of the random Monte Carlo iterations, where the heavy black line depicts the mean difference in position angle. The thin solid and dashed lines depict the 1σ and 2σ deviations about the mean. At small angular separations <20′ the two blue points lie near the 2σ envelope, while at larger angular separations the points scatter about the mean expected in the case of random orientations. This demonstrates that bowshock positions angles are correlated on small angular scales, as would be expected if some are produced by large-scale external influences such as outflows from nearby H II regions.

We also investigated whether the bowshock nebulae display preferred orientations in the Galactic coordinate system. Figure 7 displays a histogram of the morphological position angles, in Galactic coordinates, for all 709 objects. Error bars designate Poisson uncertainties for each bin. While the overall distribution is generally consistent with random, there is a small excess of objects at 90° and 270° orientations, parallel to the Plane.

3.4. *Bowshock Sizes*

Figure 8 shows a histogram of the base 10 logarithm of the standoff distance, $\log R_0$, in arcseconds, describing the separation of the central star from the apsis of the arc-shaped nebula. The peak of the distribution in the range 5–12″ indicates that the vast majority of the objects are compact, sufficiently small that the angular resolution of *Spitzer Space Telescope* is required to discern the arc-like shape of the nebula. The distribution declines smoothly from 12″ to about 50″, beyond which a small number of very large arcs with sizes up to 500″ populate the distribution more or less uniformly. On the smaller end of the distribution the number of objects drops steeply from sizes of 5″ to the resolution limit if the IRAC instrument at about 2″.

Figure 9 plots the angular size of the objects, R_0, versus extinction toward the star, A_V, as inferred from the $H-4.5$ μm color excess, assuming a standard extinction law with $A_V = 9\times A_K$. A weak correlation is evident, with the largest nebulae being the least extinguished and the smallest nebulae having preferentially larger extinctions. If extinction of the starlight were a proxy for distance, we might expect that the most extinguished objects would also have the smallest angular sizes, but no strong trends are evident.

3.5. *Bowshock Environments*

Figure 10 depicts the fraction of the bowshock candidate sample that lies in apparently isolated environments (I; 70.4%), facing H II regions (FH; 14.5%), facing bright-rimmed clouds (FB; 8.2%), and located within H II regions (H; 6.9%). Many objects designated as FB also lie within H II regions, so FB may entail H; FB and H together make up 15.3% of the sample. Isolated objects (499) make up more than two-thirds of the sample. However, this designation does not necessarily mean that the object is physically isolated from other potential astrophysical influences. In the complex regions near the Galactic Plane, most candidates are seen in projection near dark clouds, star forming regions, and other prominent features. Rather, the isolated designation simply means that the object does not obviously appear to lie within or to directly face a visible H II region, star or bright-rimmed cloud. As such, these are the best candidates for being genuine runaway stars with space velocities sufficient to sweep up ambient material into an infrared-emitting bowshock nebula.

About 14.6% (103 objects) of the sample exhibits a bowshock orientation that faces a prominent H II region within ≃10′. In such close proximity, outflows from a hot ionized bubble could plausibly interact with the wind of the OB star, producing an "in-situ" type bowshock even if the star does not have a high space velocity. The association of a bowshock nebulae with a particular H II region is necessarily speculative, but the relative orientation occurs frequently enough in our sample that the physical nature of this class of objects is highly suggestive.

Eight percent (58 objects) of the sample faces a bright-rimmed cloud within several arcminutes. Bright-rimmed features represent the photo-excited surfaces of molecular clouds emitting strongly in the 8.0 μm bandpass by virtue

of the solid state features of PAHs. They occur commonly at the peripheries of H II regions where massive stars create cavities or bubbles in the surrounding gas, e.g, the collection of interstellar bubbles cataloged by Churchwell et al. (2006). Figure 11 shows six objects that face bright-rimmed clouds, with the color scheme as in Figure 1. Frequently, this class of objects is located *within* an H II region. Physically, this class of objects may arise when an OB star's wind interacts with a photo-ablated flow from the molecular cloud boundary produced by the UV photons from the same star. The phenomenon may be similar to the stationary shocks visible as ionized arcs at the interface between the wind from θ^1 Ori C and the proplyds in the Orion Nebula (Bally et al. 1998; García-Arredondo et al. 2001). Figure 3 of García-Arredondo et al. (2001) conveniently illustrates the location of one object, proplyd 180-331, that hosts an arc facing the ionization front in the OMC1 molecular cloud rather than the facing the star θ^1 Ori C. Given that the phenomena operating in our subsample of IR-selected bowshock may be similar, we term this subclass of of in-situ bowshock nebulae "photo-evaporative flow" (PEF) bowshocks. However, in Orion, the arcs are very thin features visible primarily in $H\alpha$ and O III, whereas our sample is prominent in the mid-IR dust continuum and the ionization structure is not presently known. One prediction following from this interpretation is that the PEF bowshock candidates, designated here as FB, do not have high space velocities relative to their local environment.

The remaining 7.0% (49 objects) appear to lie within H II regions or interstellar bubbles, as outlined by either bright-rimmed clouds or by pillars of photo-excited gas. While they do not obviously face a bright-rimmed cloud at the periphery of the H II region, they may be produced where a stellar wind interacts with a high-velocity flow of material, including champagne flows. Even so, these objects may overlap with the FB subsample which are frequently found within H II regions.

3.6. *Proper Motions*

Following the analysis of van Buren et al. (1995), we collected proper motion measurements for the stellar counterparts to each bowshock nebula. In this analysis we use proper motion data from the Hipparcos (Perryman et al. 1997), UCAC4 (Zacharias et al. 2013), and the USNO B2 (Monet et al. 2003) catalogs, in order of preference. Of the 709 candidates, only 40% (286) have proper motion data of any kind, and of these only 139 have sufficiently small uncertainties that the proper motion position angles are known to better than 45°. Nevertheless, we computed the measured the angle between the nominal orientation angle of the putative bowshock nebula (column 10 of Table 1) and the proper motion vector. Figure 12 displays a histogram of this distribution in 45° bins between −180° and 180°. Error bars depict the uncertainties, taken to be the square root of the number of objects in each bin. A clear excess in the two bins on either side of zero indicates a preference for proper motions to coincide with the expected direction inferred from the infrared morphology. This suggests that at least 25% of the objects are good candidates for being runaway stars with high space velocities in the direction of apsis of the infrared arc. However, the fraction of sources in this plot having relative position angles exceeding |90°| is large compared to the sample studied by van Buren et al. (1995). Because our sample was selected on the basis of IR morphology rather than on the basis of stars known to have high proper motion (e.g., van Buren et al. 1995; Peri et al. 2015), it is not surprising that our sample displays a broader distribution of relative position angles. The broad distribution of relative position angles may indicate that factors other than a star's peculiar motion could produce relative velocities between a star and the surrounding interstellar material that generate a bowshock nebula. Section 3.5 above discusses physical scenarios that could explain these objects.

4. CONCLUSIONS

We have compiled the largest collection to date of candidate stellar bowshock nebulae selected on the basis of mid-IR morphology at 24 or 22 μm from *Spitzer Space Telescope* and *WISE* sky surveys of the Galactic Plane. The vast majority — 660 of the 709 objects — are identified here for the first time. A minority of objects (∼19%) appear at 8 μm or shorter wavelengths as well, indicating a population of very small hot dust grains within the swept-up nebula, or possibly a PAH contribution. While the infrared images alone do not demonstrate that the tabulated objects are necessarily shocks, the preponderance of ancillary evidence, including proper motions and spectral classifications of the host stars, strongly suggests that this is the best interpretation for the majority of objects. On further investigation, some of the objects may turn out to be other phenomena, such as asymmetric dust shells around evolved stars.

The distribution of these objects on the sky is tightly confined to the Galactic mid-Plane, consistent with their production by massive stars which have strong stellar winds. Proper motions of the central stars, where known, indicate a clear excess of objects having velocity vectors aligned with the symmetry axis of the infrared nebula. This is consistent with their production by a population of massive runaway stars. While the majority of the candidate bowshock nebulae and their central stars lie in relatively isolated environments, a substantial subset (∼20%) either face

giant H II regions or face bright-rimmed clouds. These may, respectively, constitute two classes of "in-situ" bowshocks where either an external flow overruns the star or "photoevaporative flow" bowshocks where a stellar wind interacts with material evaporating from a nearby molecular cloud skin. The correlation of bowshock orientations on angular scales of $\lesssim 10'$ provides evidence that local environmental phenomena, such as outflows from star forming regions, produce the relative motions between a nearby massive star and the ISM that generate the bowshock nebulae.

Table 1 and the Appendix of 709 stellar bowshock candidates may be used to further investigate the origins of runaway stars, phenomena associated with large-scale outflows of gas from star forming regions, and the physics of massive star winds. Additional scrutiny of existing infrared surveys could be expected to find a few additional bowshock candidates, especially at higher Galactic latitudes not covered by our search. However, we expect the yield to be small as the areal density of bowshocks within the *Spitzer Space Telescope* Plane surveys drops rapidly with latitude. In a forthcoming series of papers we will present an analysis of the characteristics of this comprehensive bowshocks sample, including their spectral types, binarity, distances, spectral energy distributions, and local environments.

Our team is grateful to support from the National Science Foundation through grant AST-1412845, AST-1411851, and REU grant AST-1063146, as well as NASA through grant NNX14AR35A. We thank our anonymous reviewer for comments that helped clarify aspects of this manuscript.

REFERENCES

Acreman, D. M., Stevens, I. R., & Harries, T. J. 2016, MNRAS, 456, 136

Bally, J., Sutherland, R. S., Devine, D., & Johnstone, D. 1998, AJ, 116, 293

Benjamin, R., et al. 2003, PASP 115, 953

Blaauw, A. 1961, Bulletin of the Astronomical Institutes of the Netherlands, 15, 265

Blaauw, A. 1993, in Massive Stars: Their Lives in the Interstellar Medium, eds. J. P. Cassinelli, & E. B. Churchwell, ASP Conf. Ser., 35, 207

Bonnarel, F., Fernique, P., Bienaymé, O., et al. 2000, A&AS, 143, 33

Brown, W. R., Geller, M. J., Kenyon, S. J., Kurtz, M. J. 2005, ApJ, 622, L33

Brown, W. R., Geller, M. J., Kenyon, S. J. 2014, ApJ, 787, 89

Carey, S. J., Noriega-Crespo, A., Mizuno, D. R., et al. 2009, PASP, 121, 76

Chick, W. T., Kobulnicky, H. A., Schurhammer, D., et al. 2016

Churchwell, E., Povich, M. S., Allen, D., et al. 2006, ApJ, 649, 759

Carey, S., etal. 2008, Spitzer Proposal ID #50398

Comerón, F., & Kaper, L. 1998, A&A, 338, 273

Comerón, F., & Pasquali, A. 2007, A&A, 467, L23

Cox, N. L. J.,Kerschbaum, F., van Marle, A. J., Decin, L., et al. 2012, A&A, 537, 35

de Wit W. J., Testi, L., Palla, F., Zinnecker, H. 2005, A&A, 437, 247

Fazio, G. G., Hora, J. L., Allen, L. E., et al. 2004, ApJS, 154, 10

Fryer, C., Burrows, A., Benz, W. 1998, ApJ, 496, 333

Fuentes, C. I., Stanek, K. Z. Gaudi, B. S., et al. 2006, ApJ, 636, L37

García, B., & Mermilliod, J. C. 2001, A&A, 368, 122

García-Arredondo, F., Henney, W. J., & Arthur, S. J. 2001, ApJ, 561, 830

Gáspár, A., Su, K. Y. L., Rieke, G. H., et al. 2008, ApJ, 672, 974

Gies, D. R. & Bolton, C. T. 1986, ApJS, 419, 61

Gull, T. R. & Sofia, S. 1979, ApJ, 230, 782

Gvaramadze, V. V., & Bomans, D. J. 2008, A&A, 490, 1071

Gvaramadze, V. V. 2009, MNRAS, 395, L85

Gvaramadze, V. V., Kroupa, P., & Pflamm-Altenburg, J. 2010, A&A, 519, 33

Gvaramadze, V. V., Pflamm-Altenburg, J., & Kroupa, P. 2011a, A&A, 525, 17

Gvaramadze, V. V., Röser, S., Scholz, R.-D., Schilbach, E. 2011b, A&A, 529, 14

Gvaramadze, V. V., Kniazev, A. Y., Kroupa, P., Oh, S. 2011c, A&A, 535, A29

Gvaramadze, V. V., Kniazev, A. Y., Chené A.-N., Schnurr, O. 2013, MNRAS, 430, L20

Gvaramadze, V. V., Menten, K. M., Kniazev, A. Y., et al. 2014a, MNRAS, 437, 843

Gvaramadze, V. V., Miroshnichenko, A. S., Castro, N., Langer, N., Zharikov, S. V. 2014b, MNRAS, 437, 2761

Hills, J. G. 1988, Nature, 331, 687

Hills, J. G. 1991, AJ, 102, 704

Hoogerwerf, R., de Bruijne, H. J., & de Zeeuw, P. T. 2000, ApJ, 544, L133

Hoogerwerf, R., de Bruijne, H. J., & de Zeeuw, P. T. 2001, A&A, 365, 49

Hora, J., et al. 2007, Spitzer Proposal ID #40184

Kenyon S. J., Bromley, B. C., Geller, M. J., Brown, W. R. 2008, ApJ, 680, 312

Kiminki, D. C., & Kobulnicky, H. A. 2012, ApJ, 751, 4

Kobulnicky, H. A, Gilbert, I. J., & Kiminki, D. C. 2010, ApJ, 710, 549

Kobulnicky, H. A., Kiminki, D. C., Lundquist, M. J., et al. 2014, ApJS, 213, 34

Kroupa, P., Aarseth, S., & Hurley, J. 2001, MNRAS, 321, 699

Leonard, P.J.T. 1991, AJ, 101, 562

Liu, Z.-W., Tauris T. M., Rpke, F. K., et al. 2015, A&A, 584, 11

Mac Low, M.-M., Klein, R. I., McKee, C. F., Stone, J., Norman, M. L. 1991, ApJ, 369, 395

Majewski, S. R., Zasowski, G., & Nidever, D. L. 2011, ApJ, 739, 25

Meyer, D. M.-A., Mackey, J., Langer, N., et al. 2014, MNRAS, 444, 2754

Meyer, D. M.-A., van Marle, A.-J., Kuiper, R., Kley, W. 2016, MNRAS, 459, 1146

Monet, D. G., Levine, S. E., Canzian, B., et al. 2003, AJ, 125, 984

Neugebauer, G., Habing, H. J., van Duinen, R., et al. 1984, ApJ, 278, L1

Noriega-Crespo, A., van Buren, D., & Dgani, R. 1997, AJ, 113, 780

Peri, C. S., Benaglia, P., Brookes, D. P., Stevens, I. R., & Isequilla, N. L. 2012, A&A, 538, A108

Peri, C. S., Benaglia, P., & Isequilla, N. L. 2015, A&A, 578, A45
Perryman, M. A. C., Lindegren, L., Kovalevsky, J., et al. 1997, A&A, 323,
Pflamm-Altenburg, J. & Kroupa P. 2010, 404, 1564
Pittard, J. M. 2009, MNRAS, 396, 1743
Pittard, J. M., & Dougherty, S. M. 2006, MNRAS, 372, 801
Poveda, A., Ruiz, J., & Allen, C. 1967, Bol. Obs. Tonantzintla y Tacubaya, 4, 86
Povich, M. S., Benjamin, R. A., Whitney, B. A., et al. 2008, ApJ, 689, 242-248
Rieke, G. H., Young, E. T., Engelbracht, C. W., et al. 2004, ApJS, 154, 25
Sana, H., de Mink, S. E., de Koter, A., et al. 2012, Science, 337, 444
Sexton, R. O., Povich, M. S., Smith, N., et al. 2015, MNRAS, 446, 1047
Skrutskie, M. F., Cutri, R. M., Stiening, R., et al. 2006, AJ, 131, 1163
Spitzer, L. Jr., & Mathieu, R. D. 1980, ApJ, 241, 618
Stevens, I. R., Blondin, J. M., & Pollock, A. M. T. 1992, ApJ, 386, 265
Stone, R. C. 1991, AJ, 102, 333
Tauris, T. M. 2015, MNRAS, 448, L6
Tetzlaff, N., Neuhauser, R., & Hohle, M. M. 2010, MNRAS, 410, 190
Usov, V. V. 1992, ApJ, 389, 635
van Buren, D., & McCray, R. 1988, ApJL, 329, L93
van Buren, D., Mac Low, M.-M.; Wood, D. O. S.; Churchwell, E. 1990, ApJ, 353, 570
van Buren, D. & Mac Low, M.-M. 1992, ApJ, 394, 534
van Buren, D., Noriega-Crespo, A., & Dgani, R. 1995, AJ, 110, 2914
Wang, Z., Kaplan, D. L., Slane, P., Morrell, N., Kaspi, V. M. 2013, ApJ, 769, 122
Werner, M. W., Roellig, T. L., Low, F. J., et al. 2004, ApJS, 154, 1
Wilkin, F. P. 1996, ApJL, 459, L31
Wilkin, F. P. 2000, ApJ, 532, 400
Wright, E. L., Eisenhardt, P. R. M., Mainzer, A. K., et al. 2010, AJ, 140, 1868-1881
Yu, Q. & Tremaine, S. 2003, 599, 1129
Zacharias, N., Finch, C. T., Girard, T. M., et al. 2013, AJ, 145, 44
Zwicky, F. 1957, *MorphologicalAstronomy* (Berlin: Springer), p. 258

Table 1. Central Stars of Bowshock Nebula Candidates

Num	Name	R.A. (2000.0)	Decl. (2000.0)	Ref.	Alias	8.0?	Flag	R_0 (arcsec)	P.A. (deg)	H (mag)	I2/W2 (mag)	A_K (mag)	Env.
1	G000.1169−00.5703	17:48:07.70	−29:07:55.5	T		Y	C	26.4	27	8.97	8.72	0.22	I
2	G000.3100−01.0495	17:50:27.59	−29:12:46.8	T		N	C	6.8	145	10.57	10.31	0.23	I
3	G001.0563−00.1499	17:48:41.78	−28:06:37.8	T		Y		6.2	200	11.14	9.8	1.22	H
4	G001.2588−00.0780	17:48:53.40	−27:53:59.7	T		N	C	10.2	215	12.28	11.22	0.96	FH
5	G003.5118−00.0470	17:53:56.10	−25:56:50.3	T		N		8.6	135	10.69	9.69	0.91	I
6	G003.7391+00.1425	17:53:43.26	−25:39:19.2	T		N		3.9	20	11.48	9.41	1.89	I
7	G003.8417−01.0440	17:58:30.64	−26:09:49.1	T		Y		12.6	25	10.22	9.87	0.31	FB
8	G004.3087+00.2222	17:54:41.61	−25:07:25.6	T		N		10.1	260	13.94	12.1	1.68	I
9	G004.7315−00.3875	17:57:57.62	−25:03:53.6	T		N	C	10.1	125	13.3	11.77	1.39	I
10	G004.8449−00.9309	18:00:17.51	−25:14:14.7	T	HD314937	N		3.1	140	9.36	9.31	0.03	I
11	G005.5941+00.7335	17:55:36.25	−23:45:21.8	T		N		7.6	350	9.78	9.22	0.50	I
12	G005.6985−00.6350	18:01:06.15	−24:21:34.4	T		N		20.8	180	11.56	9.11	2.24	I
13	G006.2812+23.5877	16:37:09.54	−10:34:01.5	V88[a]	Zeta Oph	-		29	30	2.59	-99	-99	I
14	G006.2977−00.2012	18:00:40.59	−23:36:50.7	T		N	C	24	210	13.07	12.16	0.82	H
15	G006.3600−00.1846	18:00:44.92	−23:33:06.3	T		N		5.5	110	9.32	9.11	0.18	I
16	G006.8933+00.0743	18:00:55.27	−22:57:36.9	T		N	C	29	65	8.73	8.36	0.33	I
17	G007.5265−00.2652	18:03:33.49	−22:34:38.3	T		N		4.1	350	9.06	8.11	0.86	I
18	G008.3690+00.0239	18:04:15.53	−21:42:05.3	T		N	C	27	50	9.07	8.3	0.69	I
19	G009.0177+00.1410	18:05:11.21	−21:04:43.3	T		N		9.1	290	8.85	8.41	0.39	I
20	G009.6852−00.2025	18:07:51.86	−20:39:48.8	T		N		8.3	335	10.92	9.69	1.12	I

[a] (van Buren & McCray 1988)

NOTE—The first 20 bowshock nebulae candidates. The complete list of 709 candidates is available as a machine readable table in the electronic version of the Journal. (1) Numeration of this work, 2(Generic name in Galactic coordinates, (3) Right ascension, (4) Declination, (5) First reported discovery reference; T denotes This Work, (6) Alternate name for star, (7) Flag indicating whether source is detected at 8 μm, (8) C denotes that there are multiple candidates for the central star, (9) Angular distance between the star and nebular apex in arcsec, (10) Position angle of nebula in degrees, (11) H-band magnitude, (12) IRAC 4.5 μm or WISE 4.6 μm magnitude, (13) Estimated extinction, (14) Code indicating the local environment, as described in Section 2.2

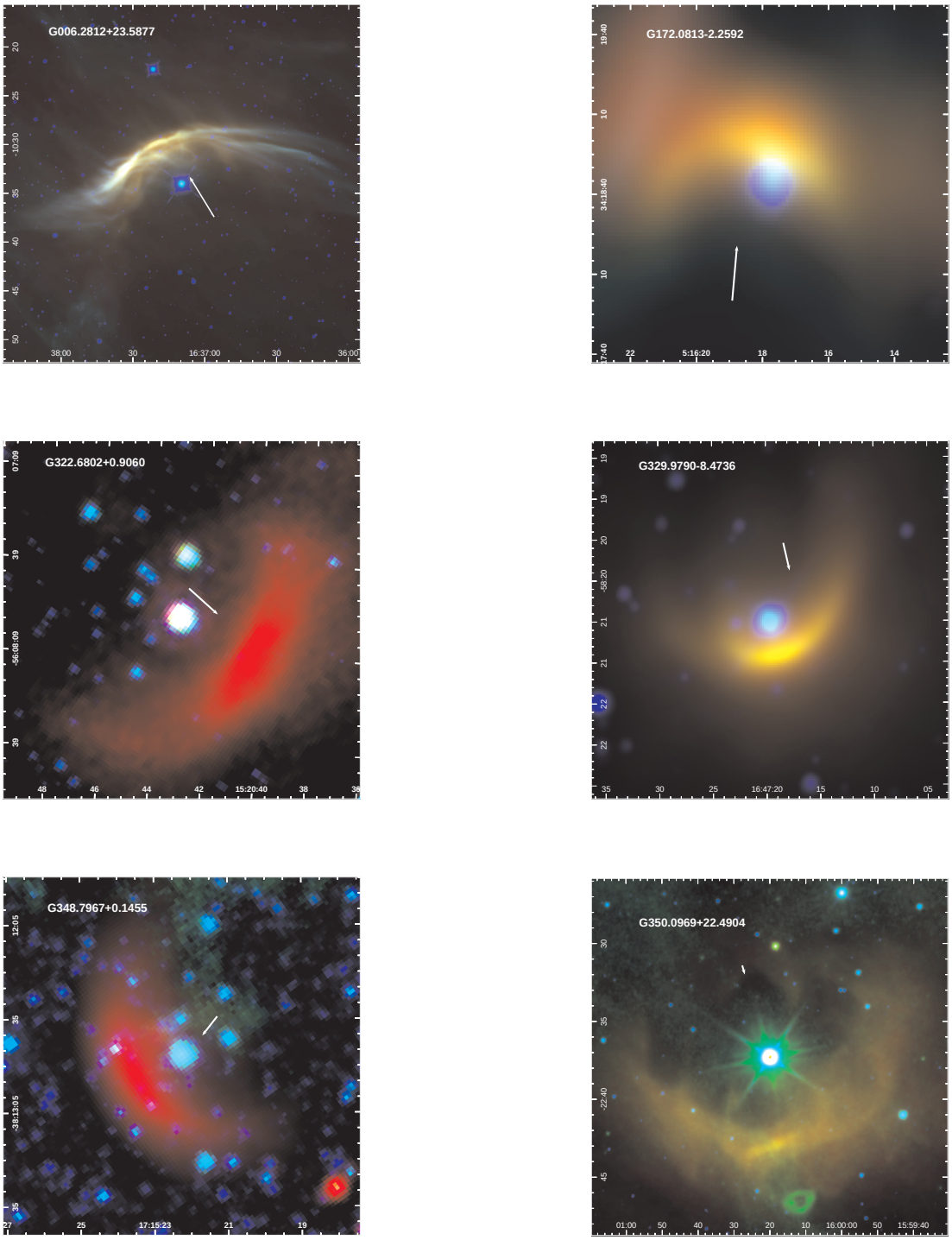

Figure 1. Six prototype bowshock nebulae, with the colors representing either the 24 μm *Spitzer Space Telescope* or 22 μm *WISE* band in red, either the 8 μm *Spitzer Space Telescope* or 12 μm *WISE* image in green, and the 4.5 μm *Spitzer Space Telescope*/*WISE* image in blue. These six objects are ζ Oph (G006.2812+23.5877; upper left), AE Aur (G172.0813−02.2592; upper right), HD136003 (G322.6802+00.9060; center left), HD150898 (G329.9790−08.4736; center right), HD155755 (G348.7967+00.1455; lower left), HD143275 (G350.0969+22.4904; lower right). Arrows in some panels indicate the direction of proper motion, if known.

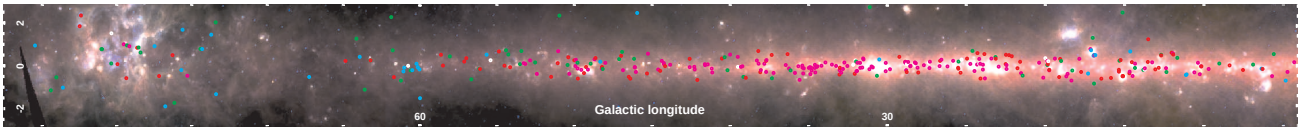

(a)

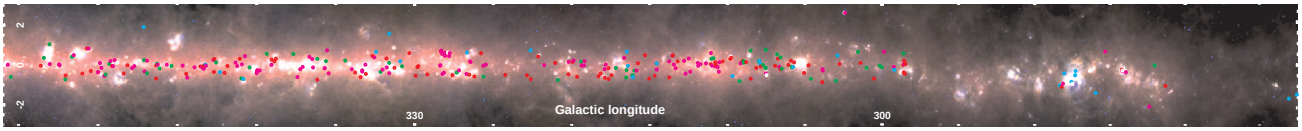

(b)

Figure 2. Candidate bowshock nebula in the inner two Galactic quadrants overlaid on a color representation of the *IRAS* 25/60/100 μm maps in blue/green/red. Colors denote the extiction values estimated from the $H-4.5$ μm color excess: cyan–$A_{\rm V}<2$; green–$2<A_{\rm V}<5$; red–$5<A_{\rm V}<10$; magenta–$A_{\rm V}>10$; white–no data.

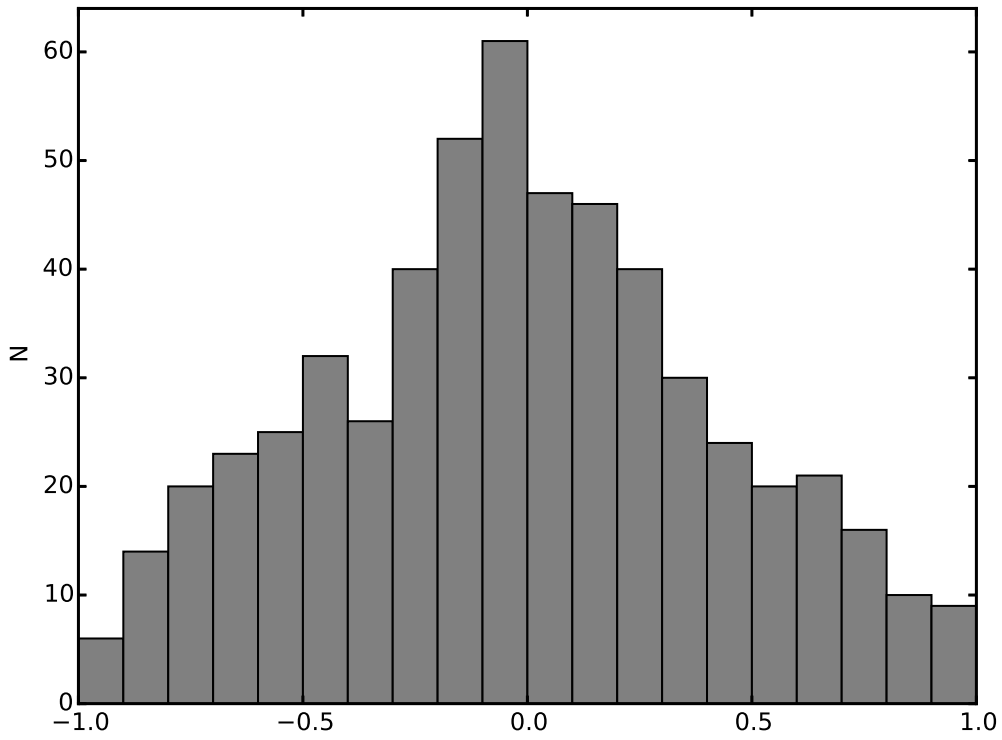

Figure 3. Histogram of Galactic latitudes for bowshock candidates within the footprint of the GLIMPSE and MIPSGAL surveys: $-60^\circ < \ell < 60^\circ$,$-1^\circ < b < 1^\circ$.

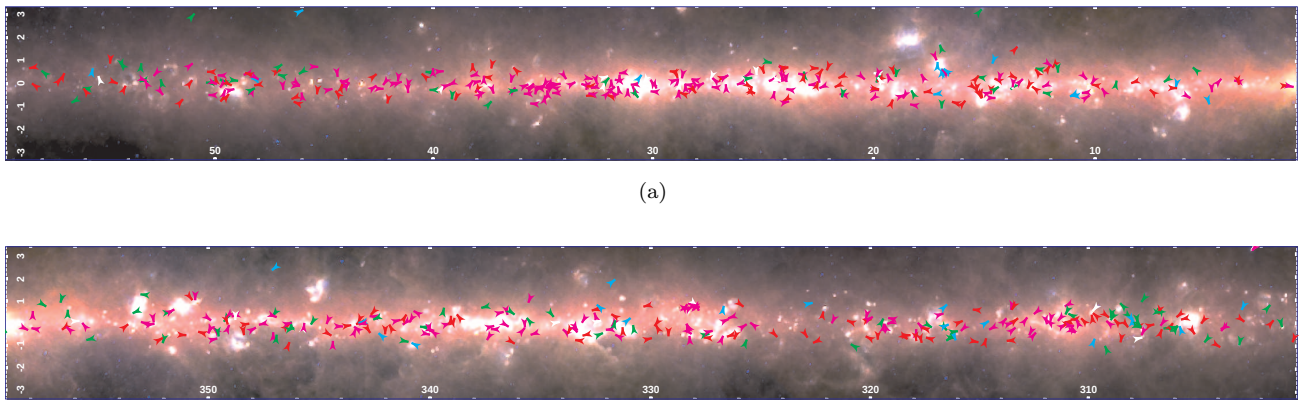

(a)

(b)

Figure 4. Locations of bowshock candidates drawn as arrows to indicate the morphological orientation of the nebula. Colors designate interstellar extinction values, as in Figure 2. The upper panel shows a portion of the Plane at $0^\circ < \ell < 60^\circ$ while the lower panel shows the $300^\circ < \ell < 360^\circ$ region.

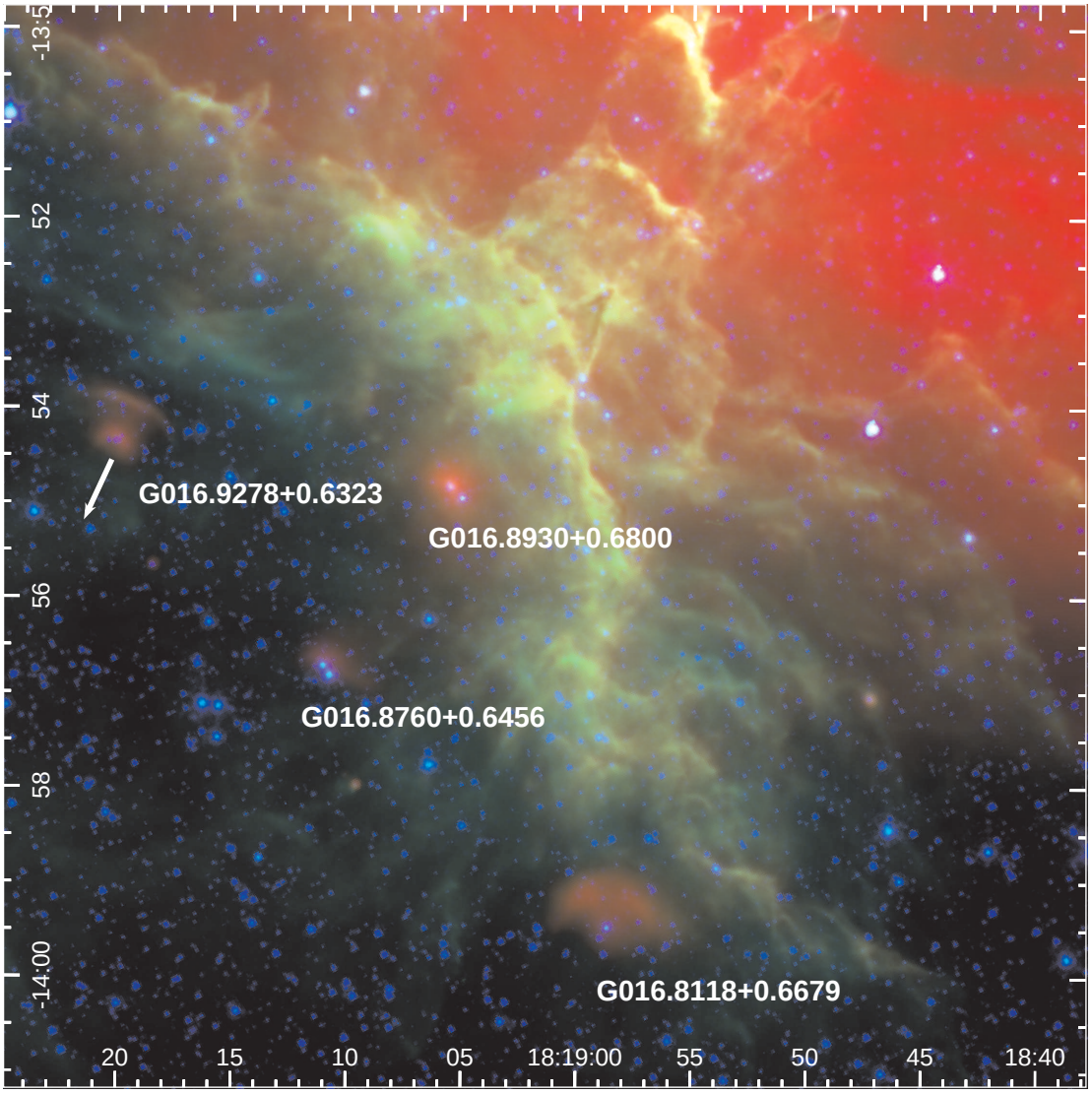

Figure 5. Three color depiction of four candidate bowshock nebulae exhibiting a similar orientation at the base of the giant pillar in M 16. Red/green/blue represent the *Spitzer Space Telescope* 4.5, 8.0, and 24 μm band images. The arrow indicates the proper motion of the one star having measured values.

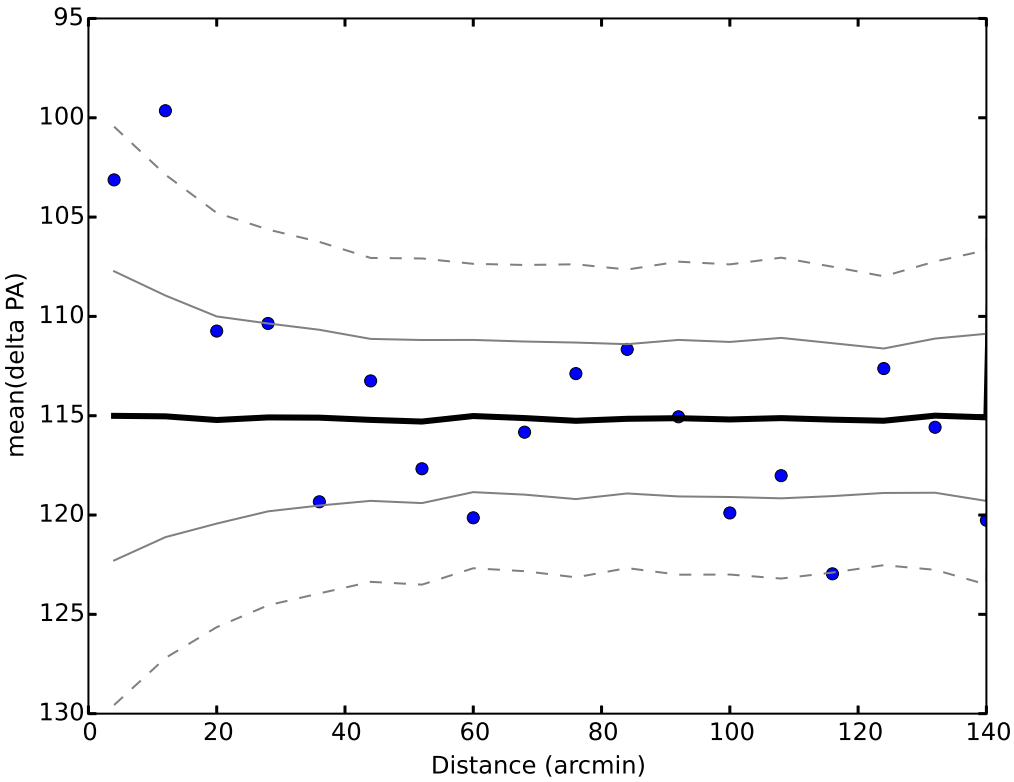

Figure 6. Mean deviation in bowshock position angle from nearest neighbors as a function of angular separation in arcminutes. Points show the data while the heavy black line shows the mean of 1000 random iterations simulating the null hypothesis that the position angles are uncorrelated. The gray and dashed lines illustrate the 1σ and 2σ deviations from the mean.

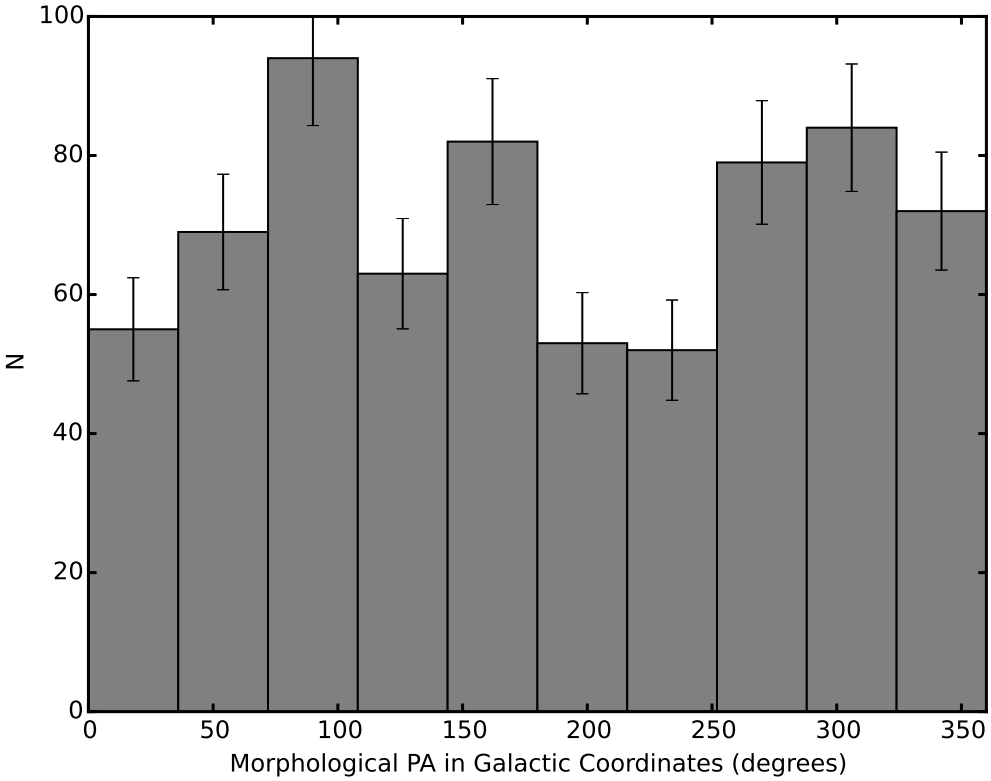

Figure 7. Histogram of orientations for candidate bowshock nebulae in Galactic coordinates. Error bars indicate the Poisson uncertainties in each bin.

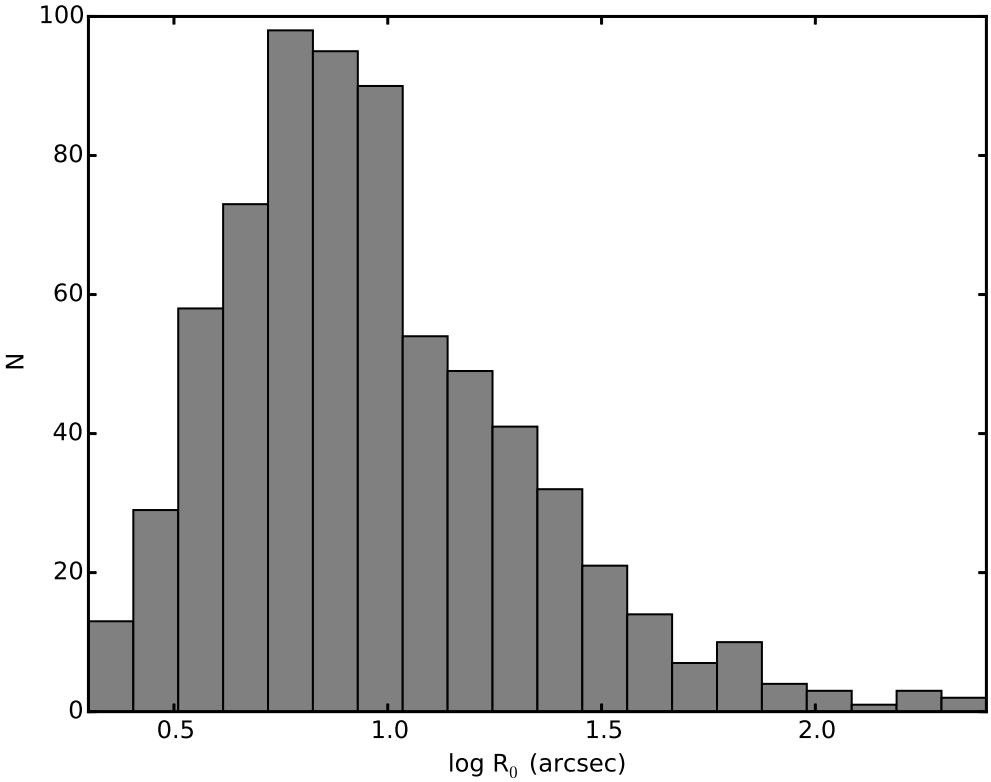

Figure 8. Histogram of bowshock sizes, as indicated by the standoff distance, R_0, in arcseconds between the central star and apsis of the nebular arc.

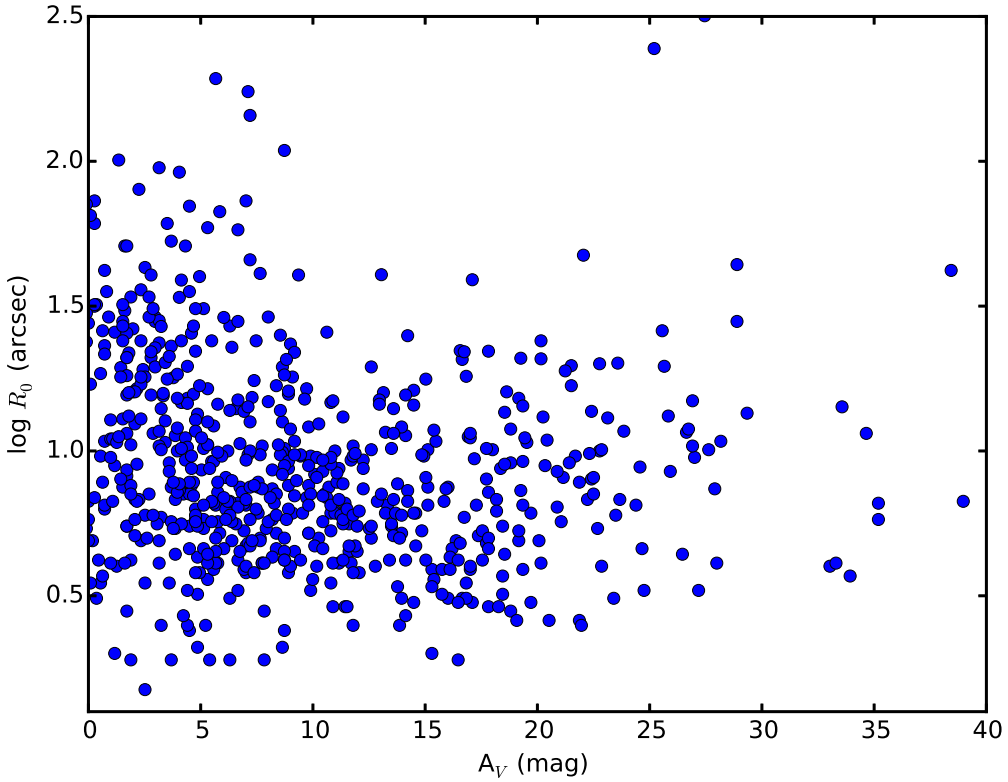

Figure 9. Base 10 log of bowshock size versus inferred extinction, $A_{\rm V}$.

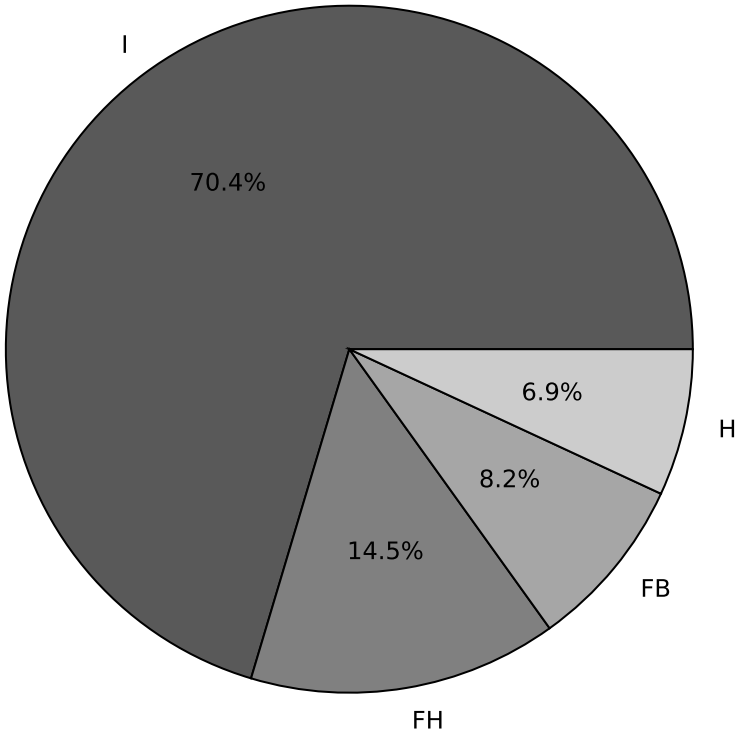

Figure 10. Fraction of candidates located in apparently isolated environments (I), facing H II regions (FH), facing bright-rimmed clouds (FB), and located within H II regions (H). FB frequently entails H.

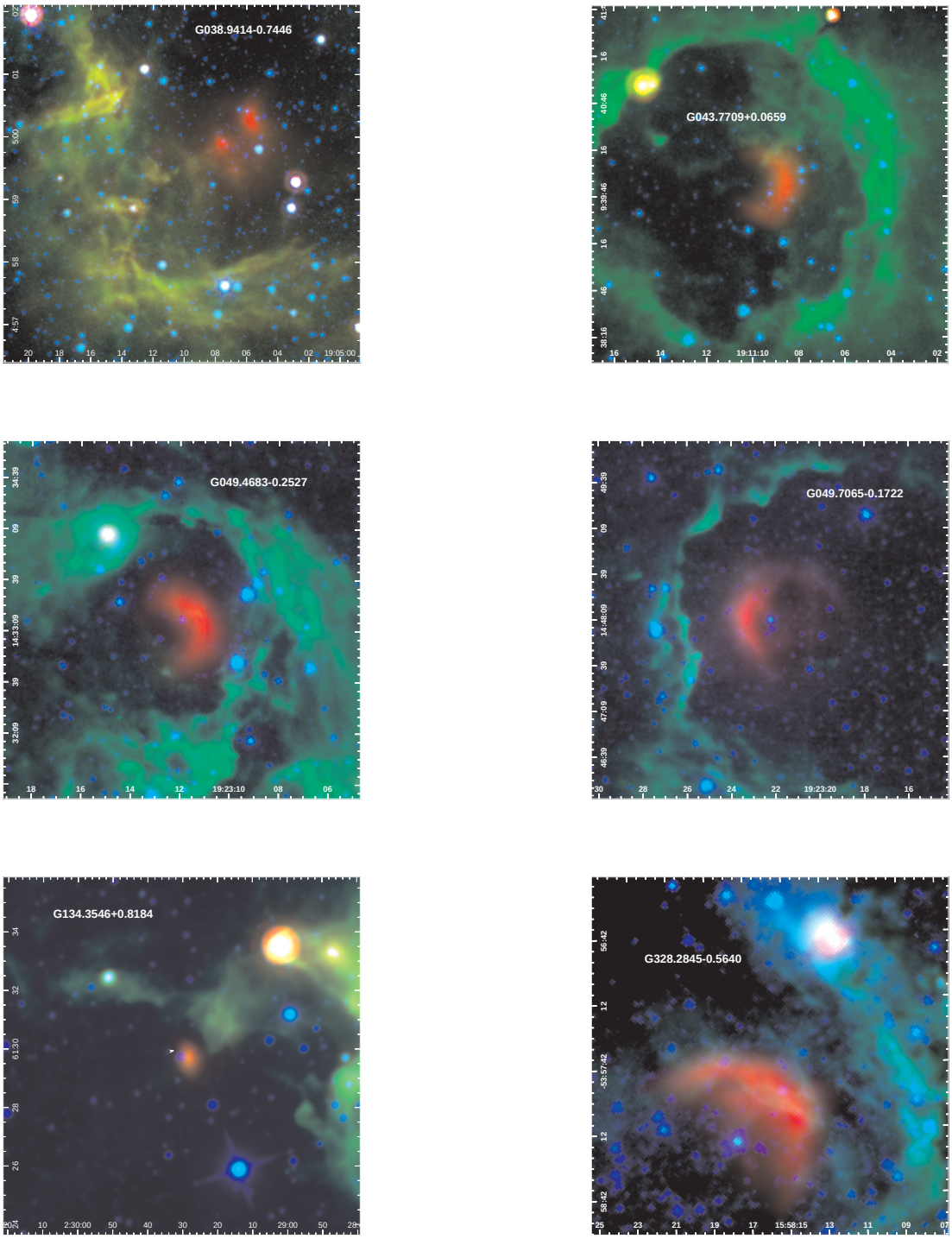

Figure 11. Examples of six candidate bowshock nebulae that face an 8 μm bright-rimmed cloud where the shock may be cause by the stellar wind interacting with a photoevaporative flow from the molecular cloud interface. These may be considered a subclass of in-situ bowshocks. The color scheme follows Figure 1.

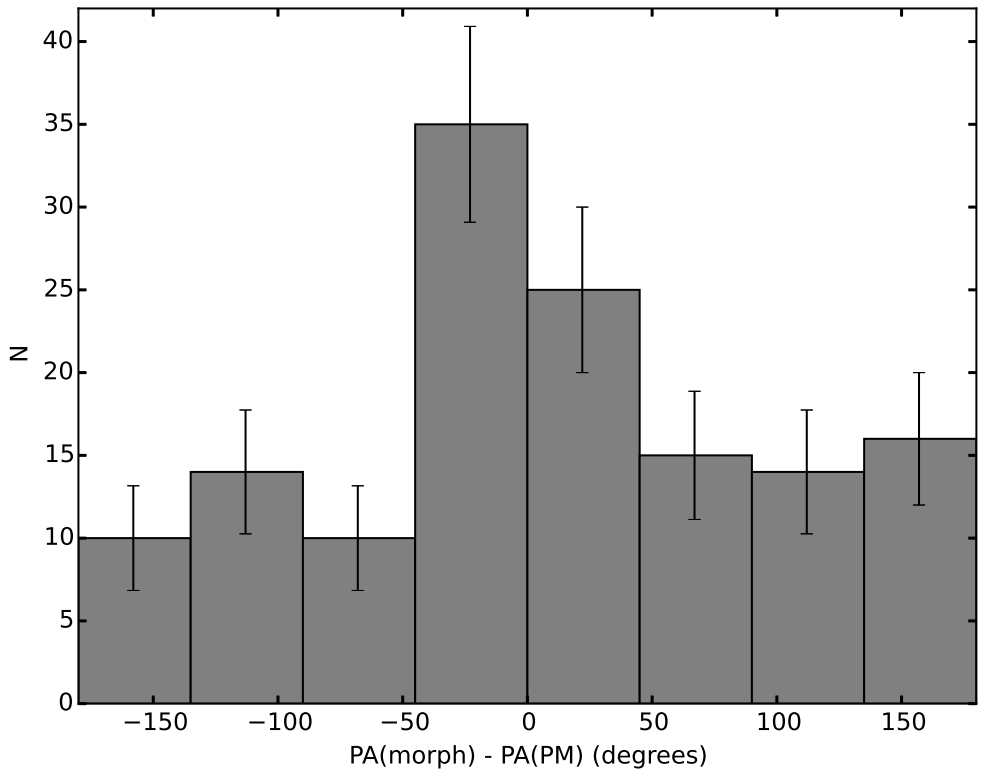

Figure 12. Difference between the mid-IR morphological axis and proper motion vector of the central star for 139 candidate bowshocks having proper motion position angles with uncertainties less than 45°. The statistically significant excess near zero degrees constitutes evidence that some fraction of these objects are runaway stars having high space velocities in a direction indicated by the IR morphology.

APPENDIX

A. ATLAS OF IMAGES

This electronic-only appendix contains an atlas of three-color images for each of the 709 bowshock nebula candidates. For the majority of the candidates that have *Spitzer Space Telescope* data, the color scheme is 24/8.0/4.5 μm in red/green/blue. For objects outside the coverage of the *Spitzer Space Telescope* surveys, we use the *WISE* 22/12/4.6 bands in red/green/blue. In a few cases where the *Spitzer Space Telescope* 24 μm data are not available, we substitute the *WISE* 22 μm data. Images are $2'$ square unless a larger field of view is required to show the entire nebulae or pertinent surrounding features. White arrows on some images depict the direction and magnitude of central star's proper motion, where known.

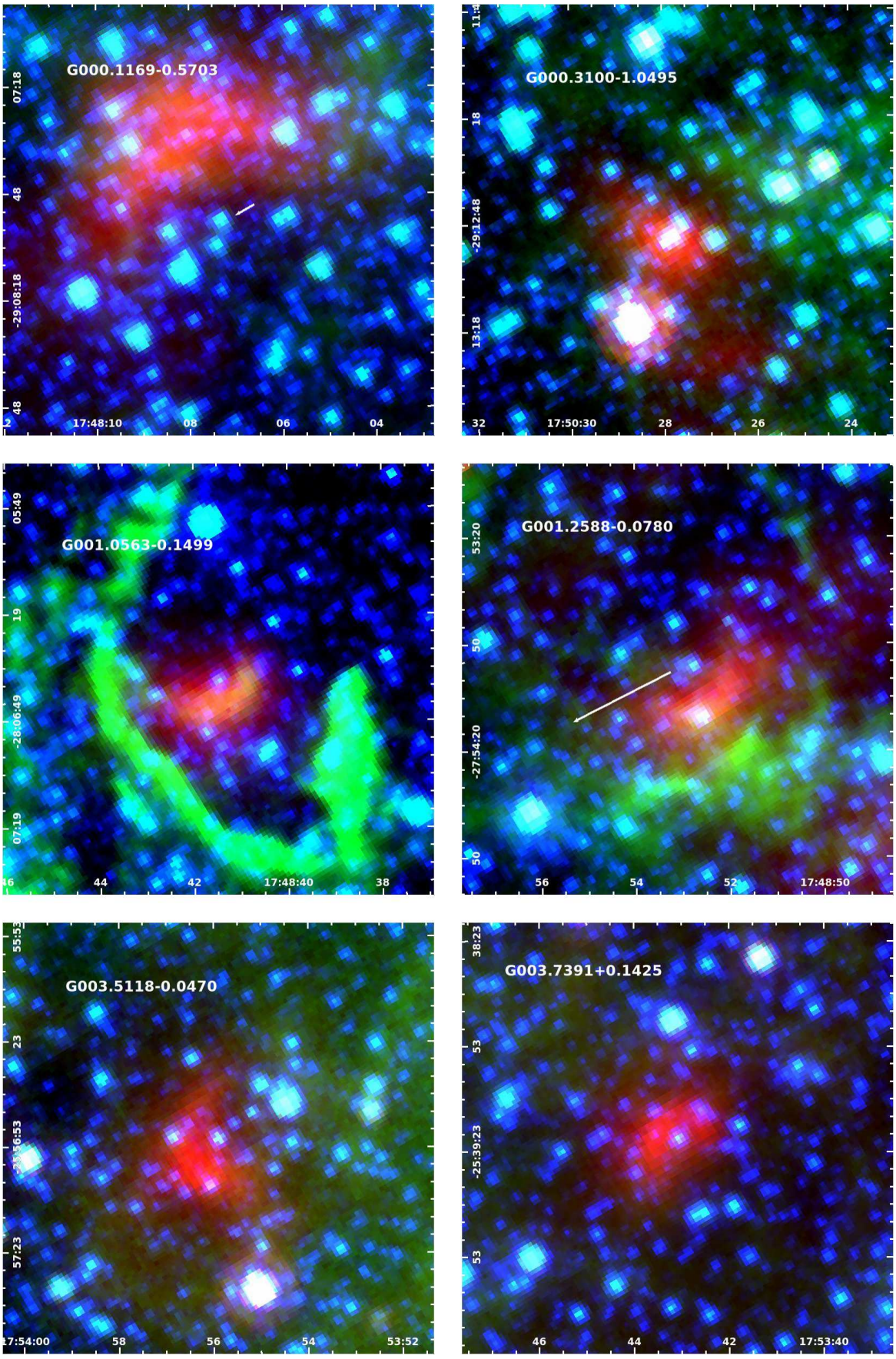
G000.1169-0.5703
G000.3100-1.0495
G001.0563-0.1499
G001.2588-0.0780
G003.5118-0.0470
G003.7391+0.1425

Figure A1.

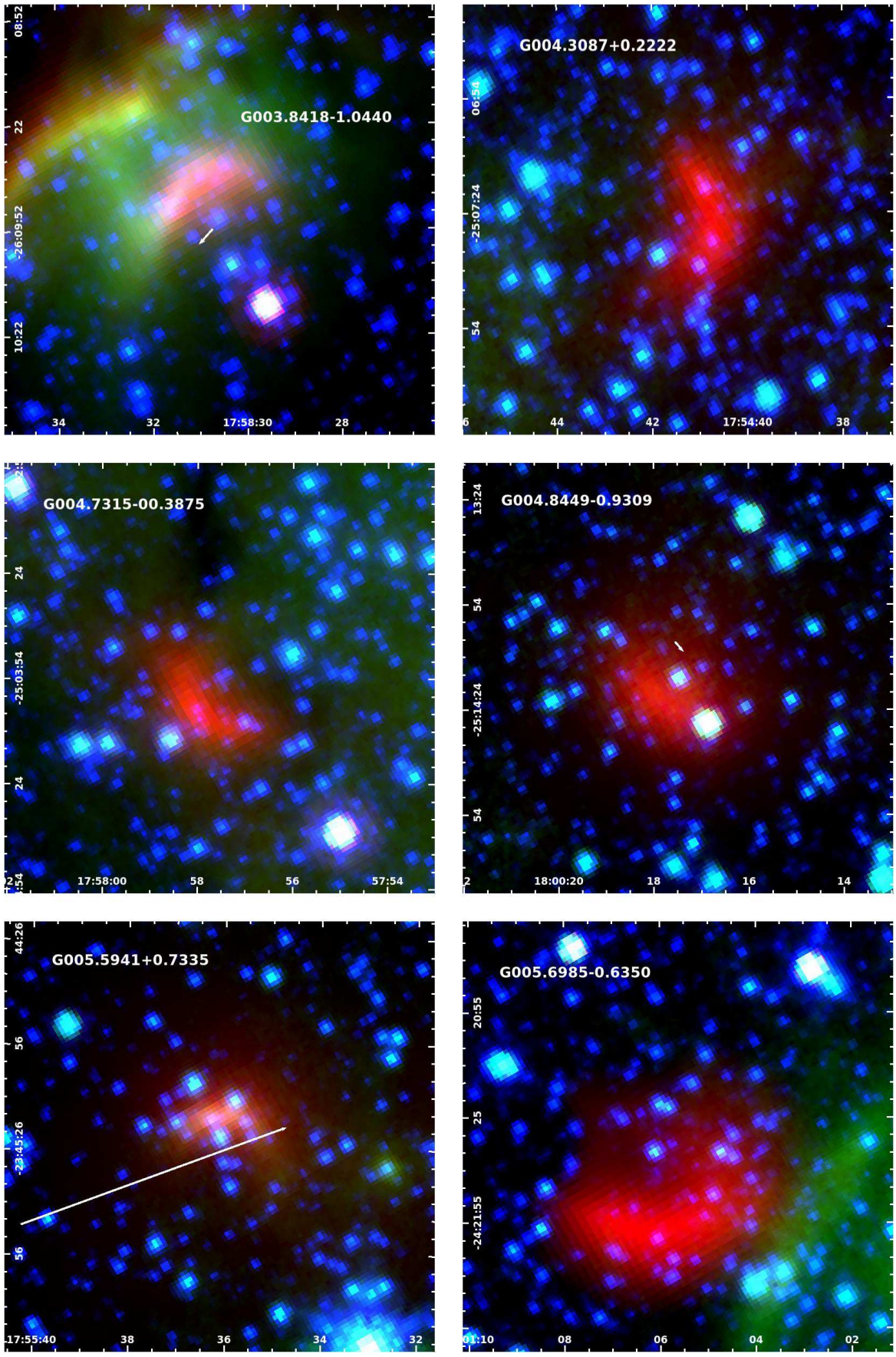
G003.8418-1.0440
G004.3087+0.2222
G004.7315-00.3875
G004.8449-0.9309
G005.5941+0.7335
G005.6985-0.6350

Figure A2.

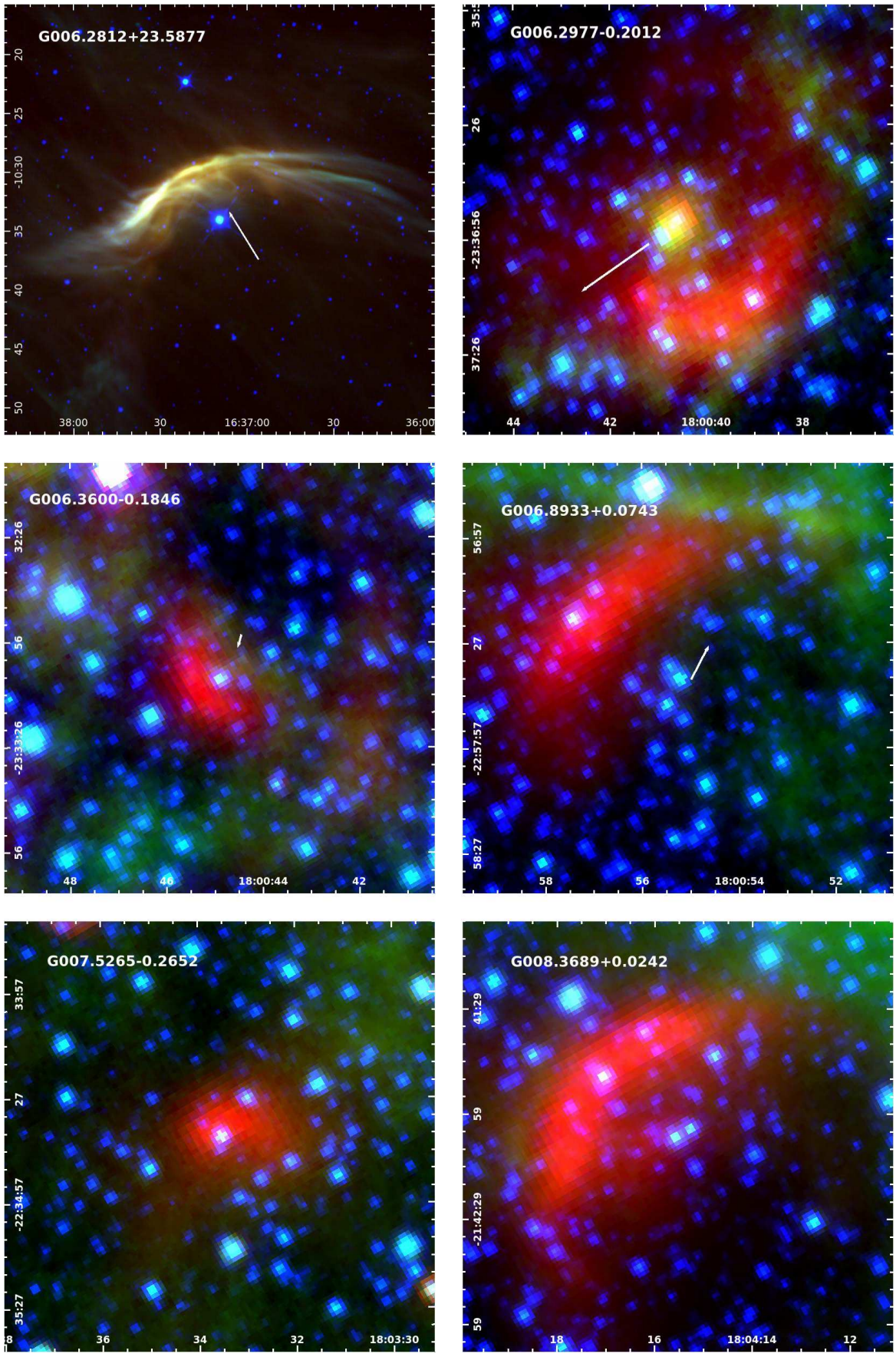
G006.2812+23.5877
G006.2977-0.2012
G006.3600-0.1846
G006.8933+0.0743
G007.5265-0.2652
G008.3689+0.0242

Figure A3.

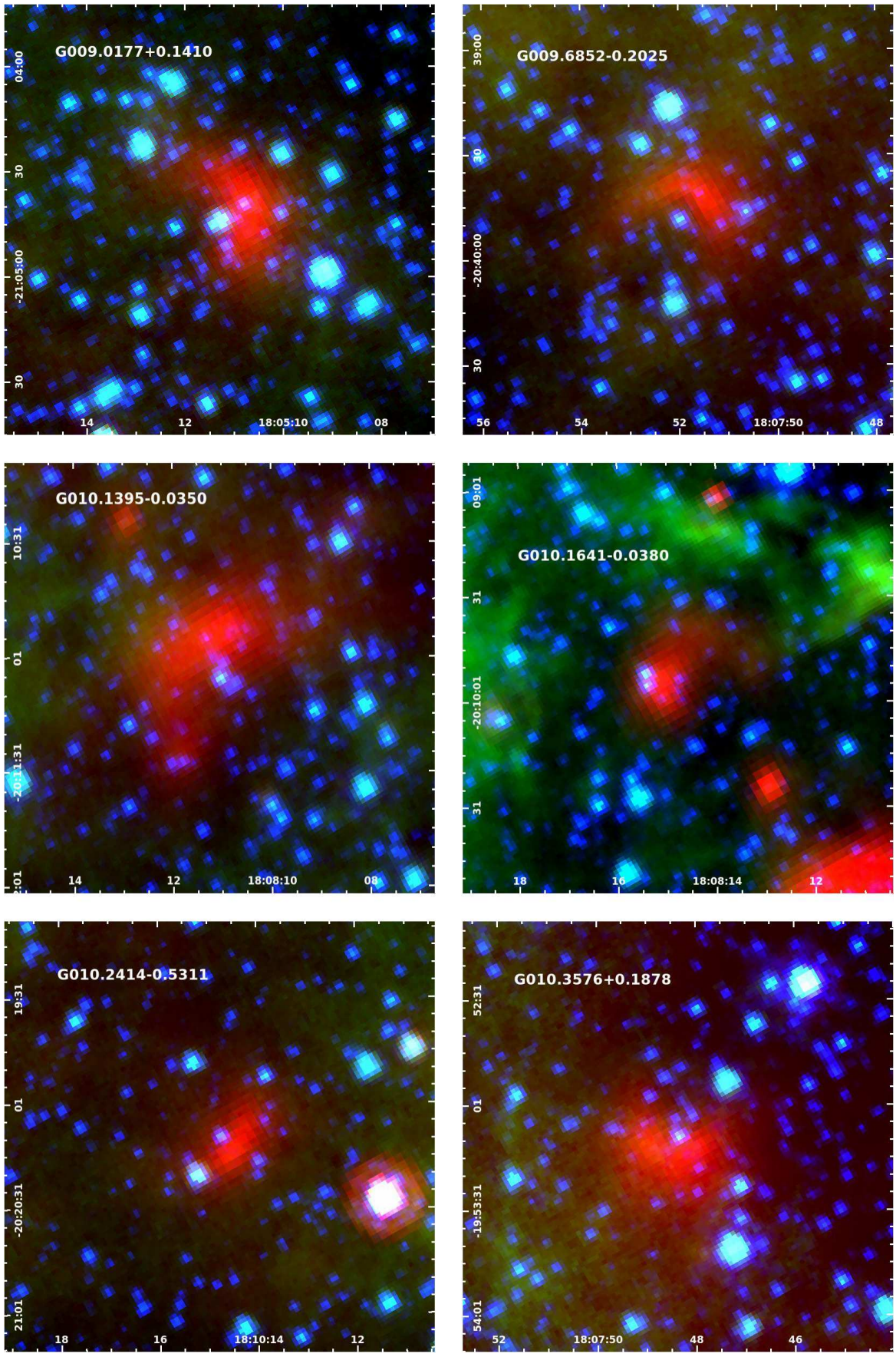
G009.0177+0.1410
04:00
30
-21:05:00
30
14
12
18:05:10
08
G009.6852-0.2025
39:00
30
-20:40:00
30
56
54
52
18:07:50
48
G010.1395-0.0350
10:31
01
-20:11:31
:01
14
12
18:08:10
08
G010.1641-0.0380
09:01
31
-20:10:01
31
18
16
18:08:14
12
G010.2414-0.5311
19:31
01
-20:20:31
21:01
18
16
18:10:14
12
G010.3576+0.1878
52:31
01
-19:53:31
54:01
52
18:07:50
48
46

Figure A4.

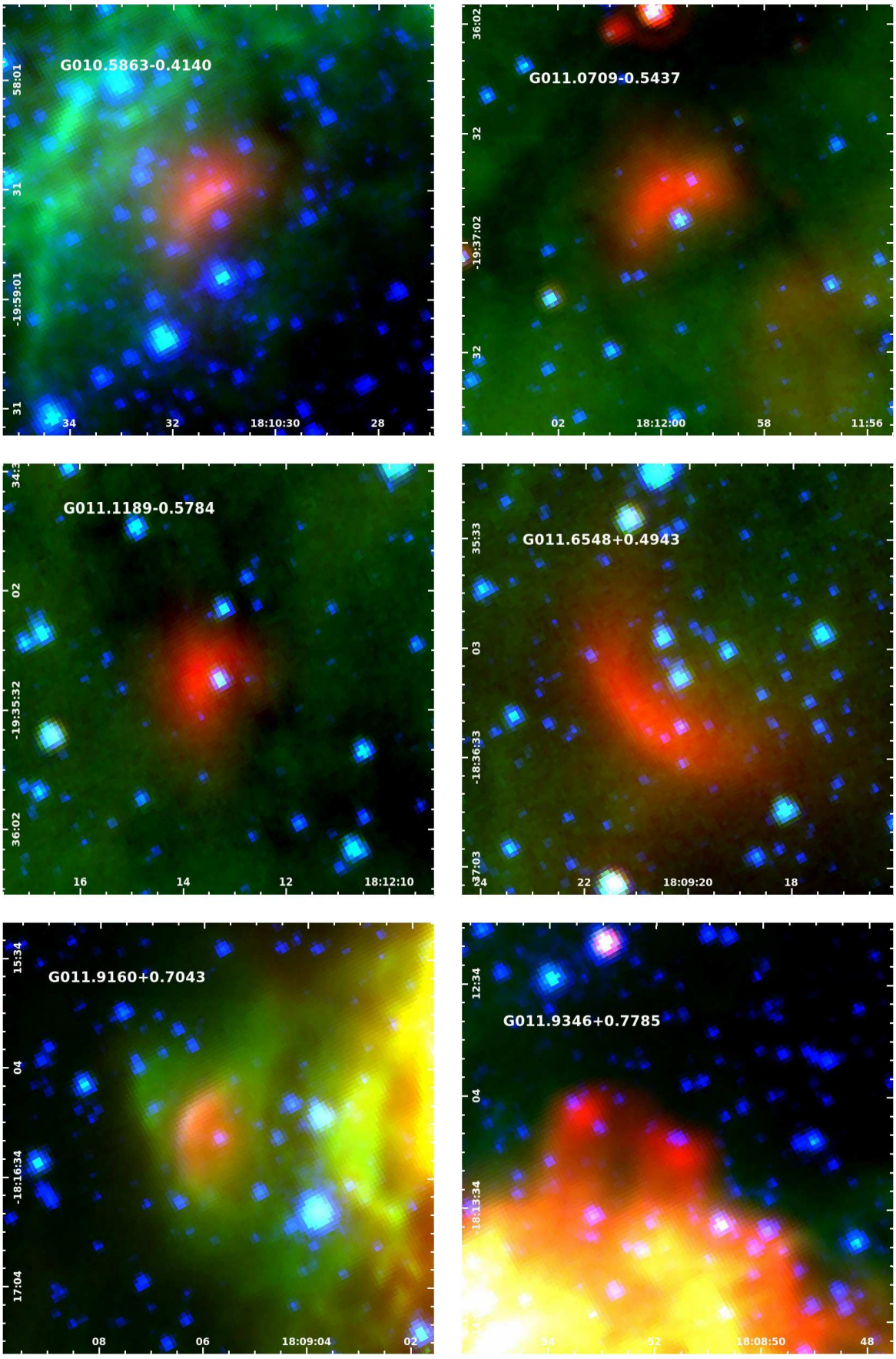
G010.5863-0.4140
58:01
31
-19:59:01
31
34
32
18:10:30
28
G011.0709-0.5437
36:02
32
-19:37:02
32
02
18:12:00
58
11:56
G011.1189-0.5784
34:5
02
-19:35:32
36:02
16
14
12
18:12:10
G011.6548+0.4943
35:33
03
-18:36:33
37:03
24
22
18:09:20
18
G011.9160+0.7043
15:34
04
-18:16:34
17:04
08
06
18:09:04
02
G011.9346+0.7785
12:34
04
-18:13:34
34
32
18:08:50
48

Figure A5.

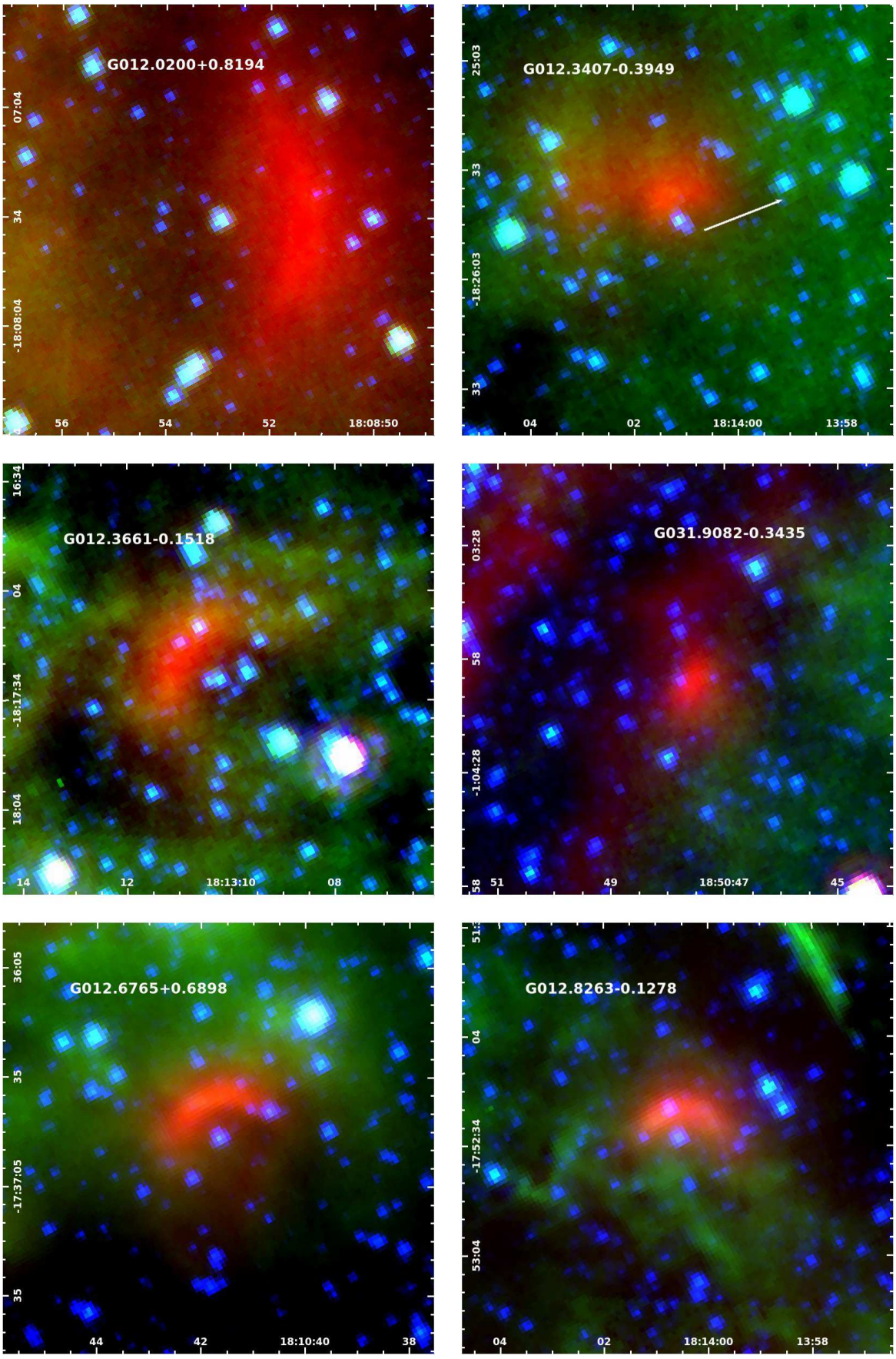
G012.0200+0.8194
07:04
34
-18:08:04
56
54
52
18:08:50
G012.3407-0.3949
25:03
33
-18:26:03
33
04
02
18:14:00
13:58
G012.3661-0.1518
16:34
04
-18:17:34
18:04
14
12
18:13:10
08
G031.9082-0.3435
03:28
58
-1:04:28
58
51
49
18:50:47
45
G012.6765+0.6898
36:05
35
-17:37:05
35
44
42
18:10:40
38
G012.8263-0.1278
04
-17:52:34
53:04
04
02
18:14:00
13:58

Figure A6.

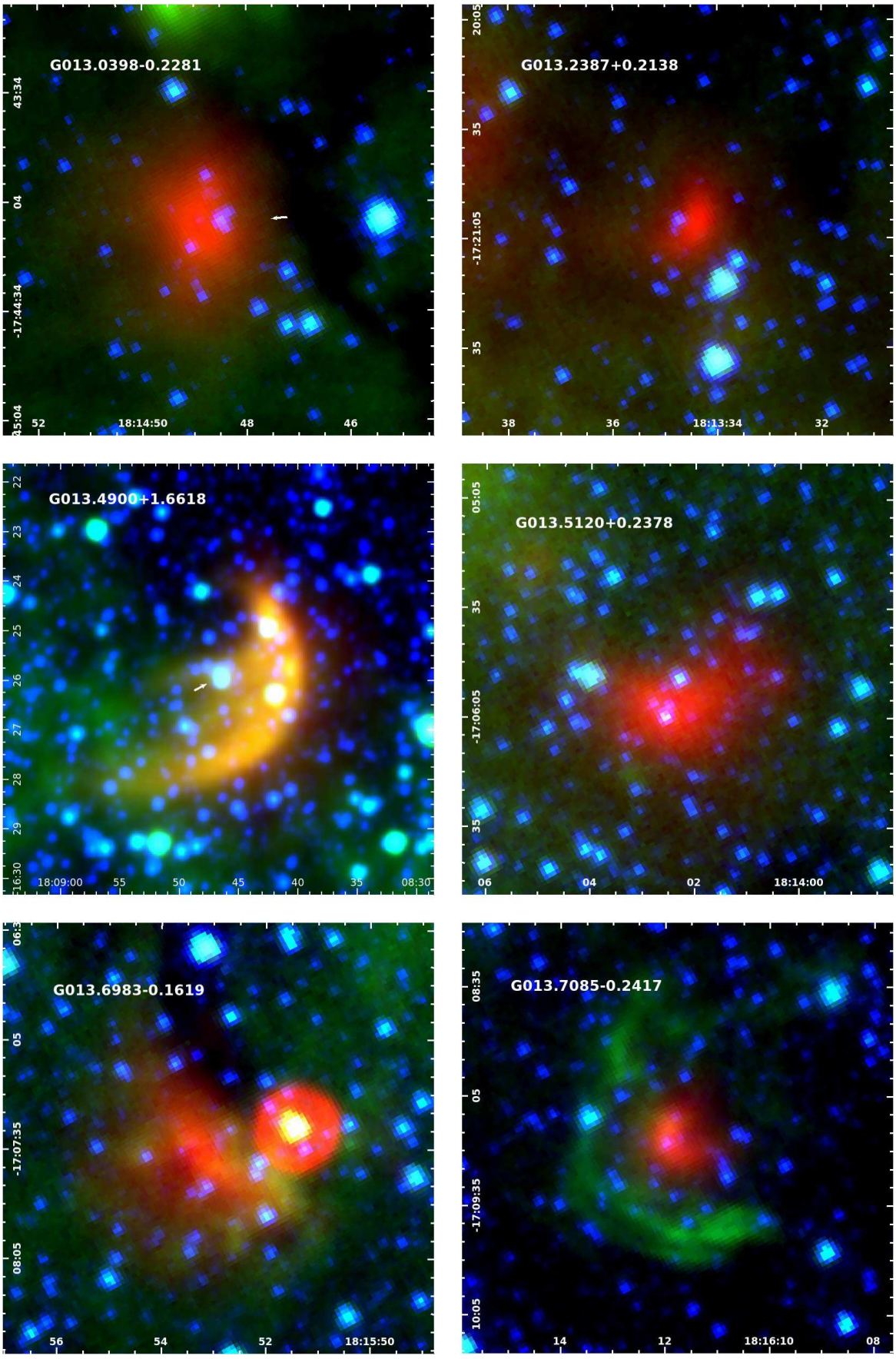
G013.0398-0.2281
43:34
04
-17:44:34
52
18:14:50
48
46
G013.2387+0.2138
20:05
35
-17:21:05
35
38
36
18:13:34
32
G013.4900+1.6618
22
23
24
25
26
27
28
29
18:09:00
55
50
45
40
35
08:30
G013.5120+0.2378
05:05
35
-17:06:05
35
06
04
02
18:14:00
G013.6983-0.1619
06:3
05
-17:07:35
08:05
56
54
52
18:15:50
G013.7085-0.2417
08:35
05
-17:09:35
10:05
14
12
18:16:10
08

Figure A7.

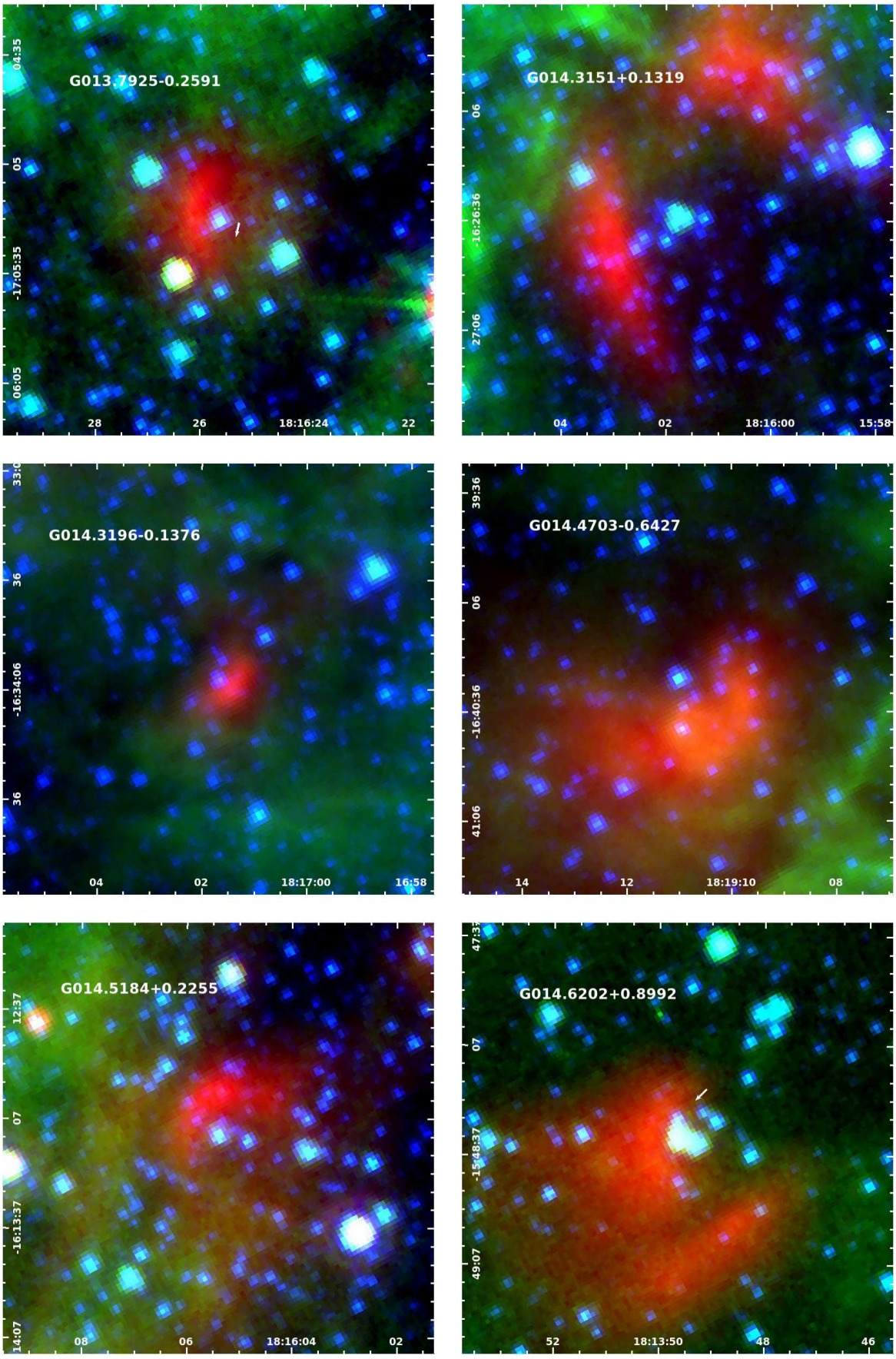
G013.7925-0.2591
04:35
05
-17:05:35
06:05
28
26
18:16:24
22
G014.3151+0.1319
06
-16:26:36
27:06
04
02
18:16:00
15:58
G014.3196-0.1376
33:0
36
-16:34:06
36
04
02
18:17:00
16:58
G014.4703-0.6427
39:36
06
-16:40:36
41:06
14
12
18:19:10
08
G014.5184+0.2255
12:37
07
-16:13:37
14:07
08
06
18:16:04
02
G014.6202+0.8992
47:3
07
-15:48:37
49:07
52
18:13:50
48
46

Figure A8.

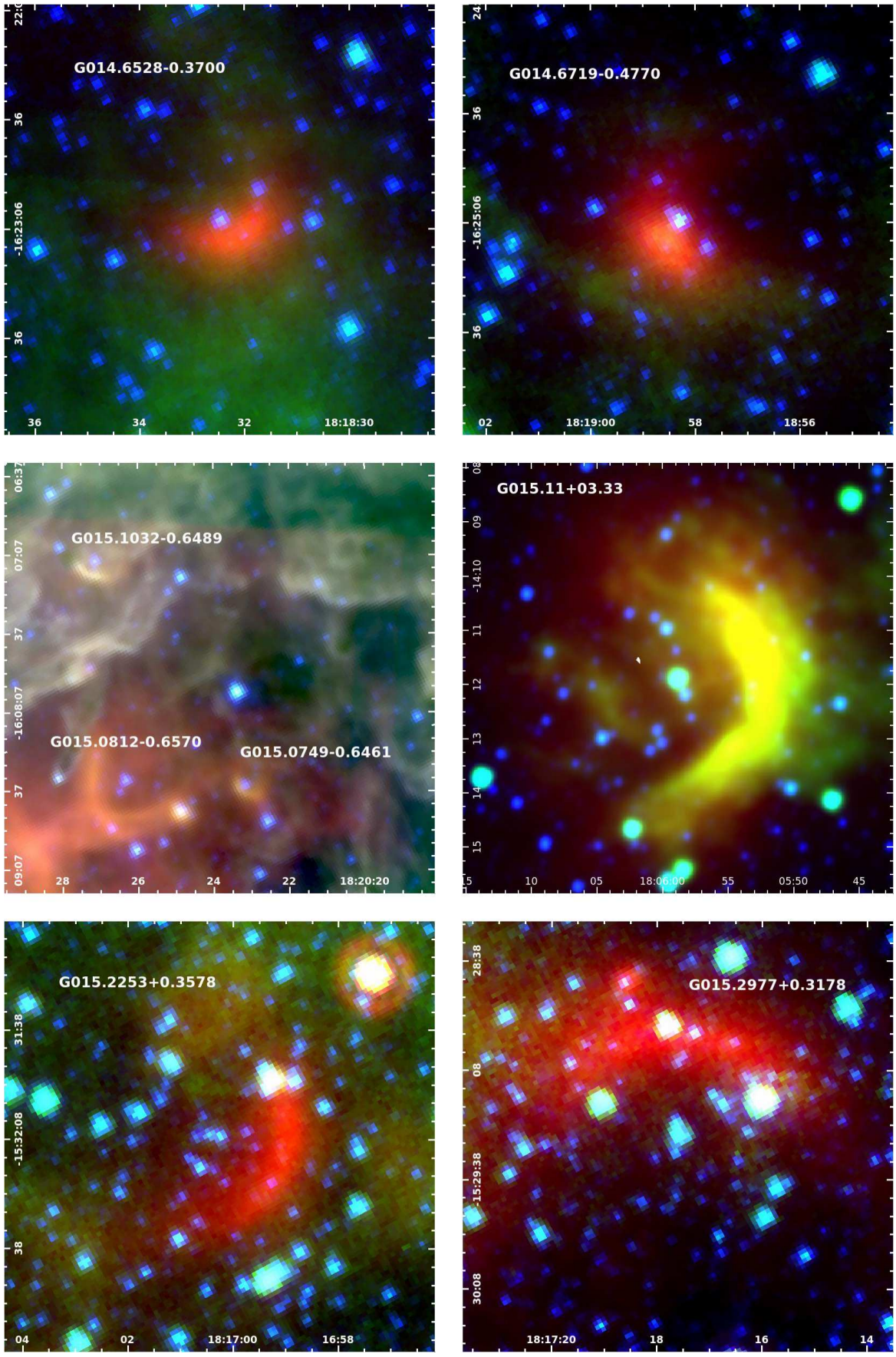
G014.6528-0.3700
G014.6719-0.4770
G015.1032-0.6489
G015.0812-0.6570
G015.0749-0.6461
G015.11+03.33
G015.2253+0.3578
G015.2977+0.3178

Figure A9.

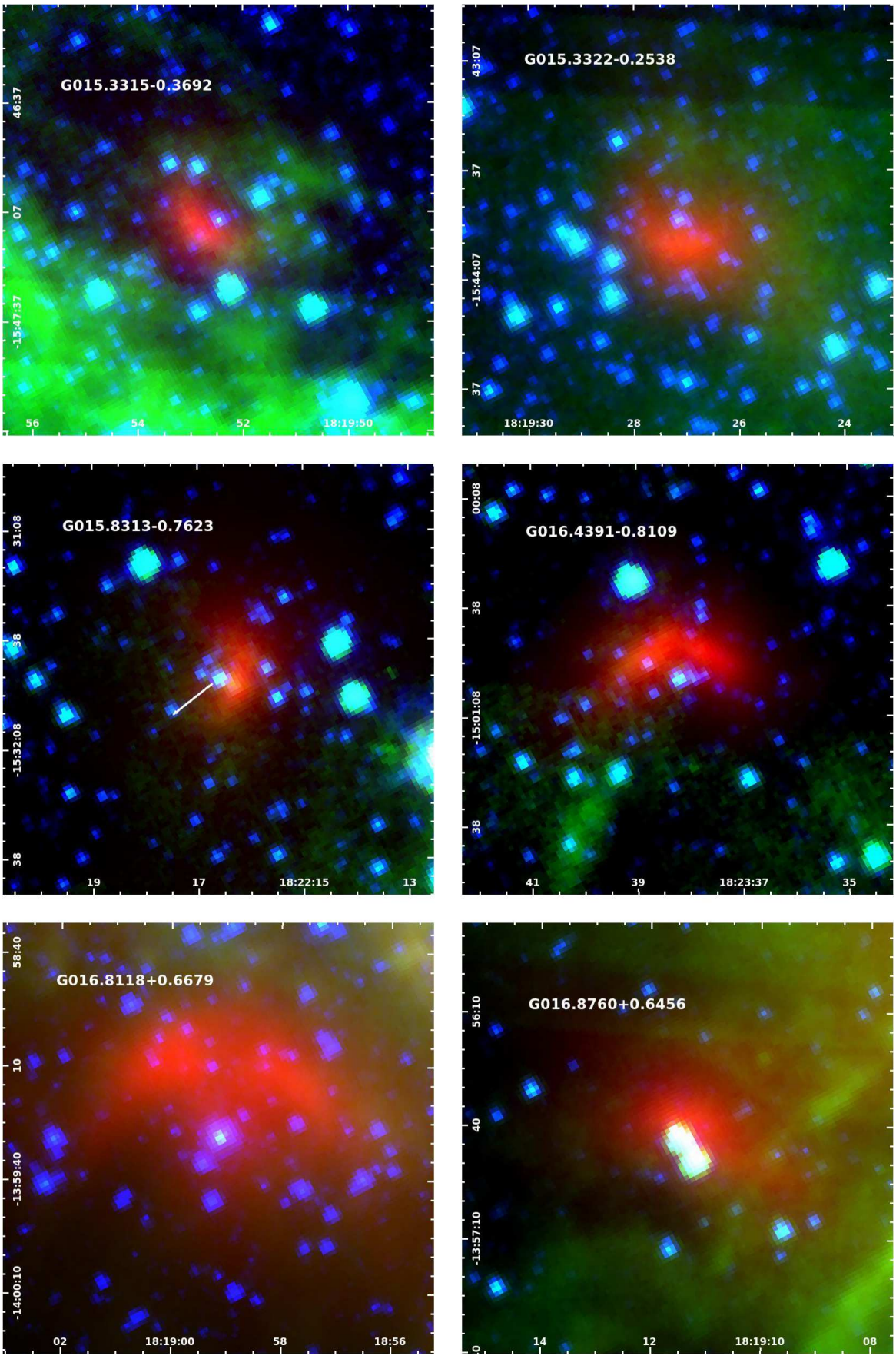
G015.3315-0.3692
G015.3322-0.2538
G015.8313-0.7623
G016.4391-0.8109
G016.8118+0.6679
G016.8760+0.6456

Figure A10.

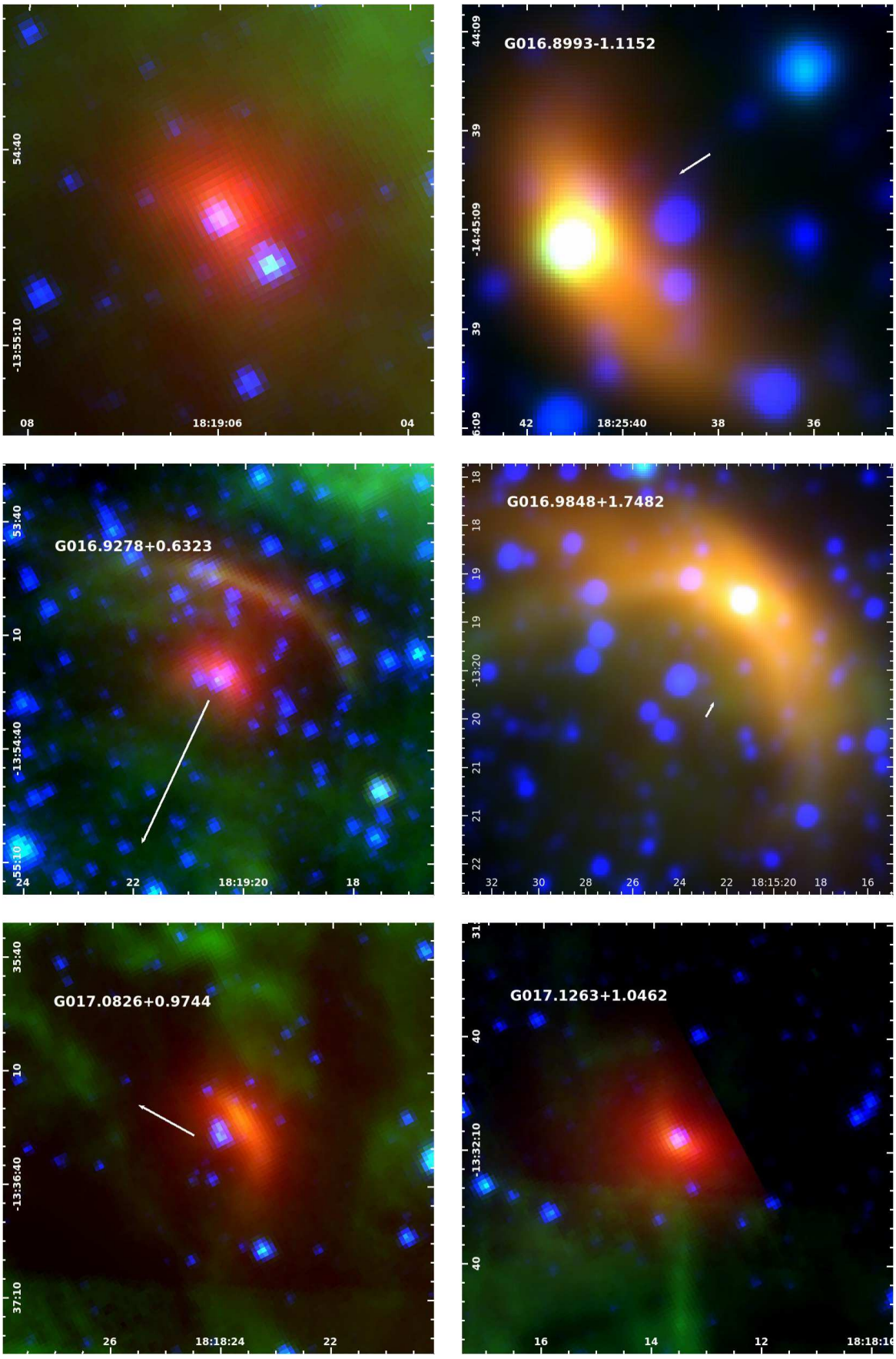
G016.8993-1.1152
G016.9278+0.6323
G016.9848+1.7482
G017.0826+0.9744
G017.1263+1.0462

Figure A11.

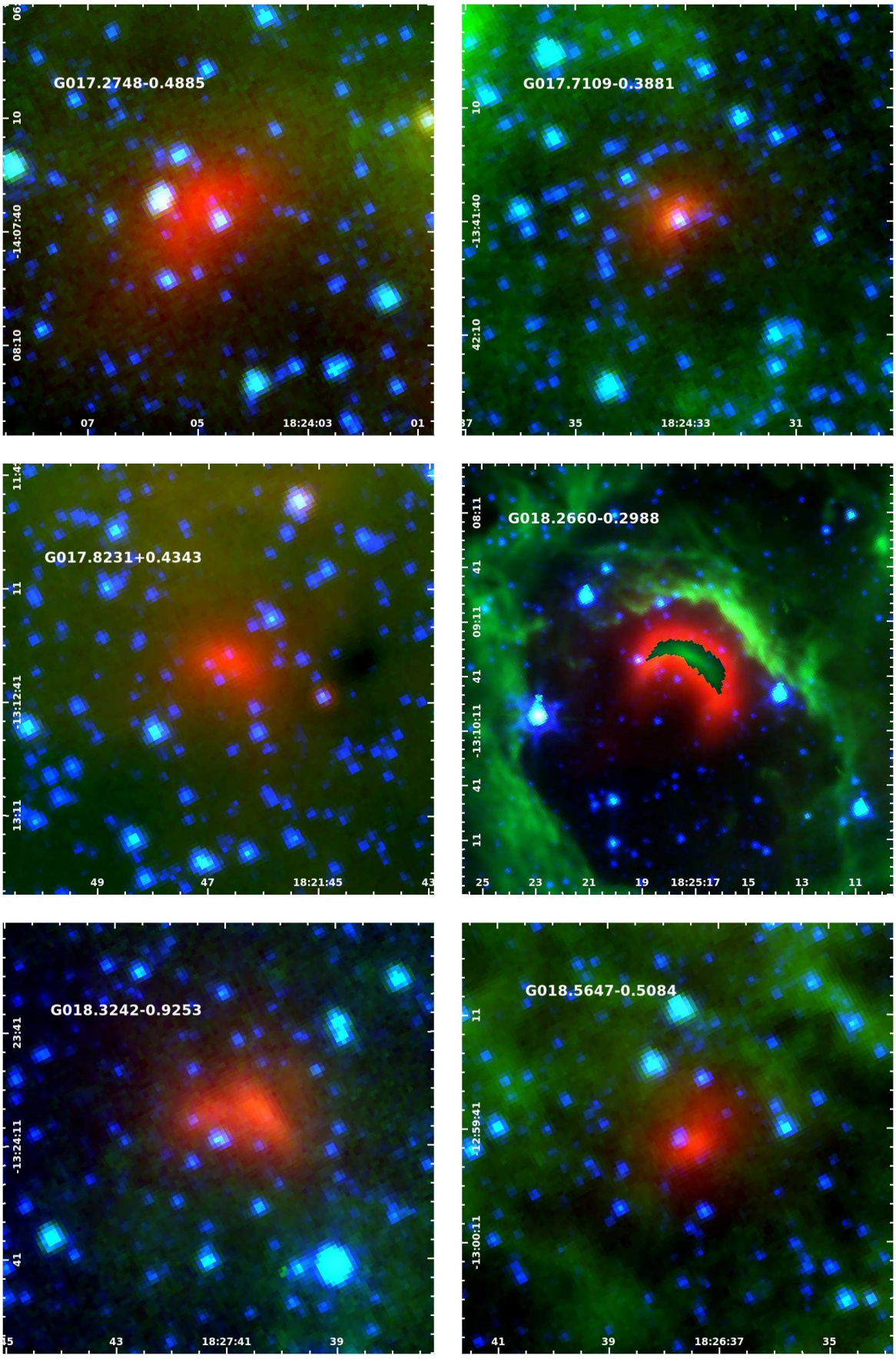
G017.2748-0.4885
G017.7109-0.3881
G017.8231+0.4343
G018.2660-0.2988
G018.3242-0.9253
G018.5647-0.5084

Figure A12.

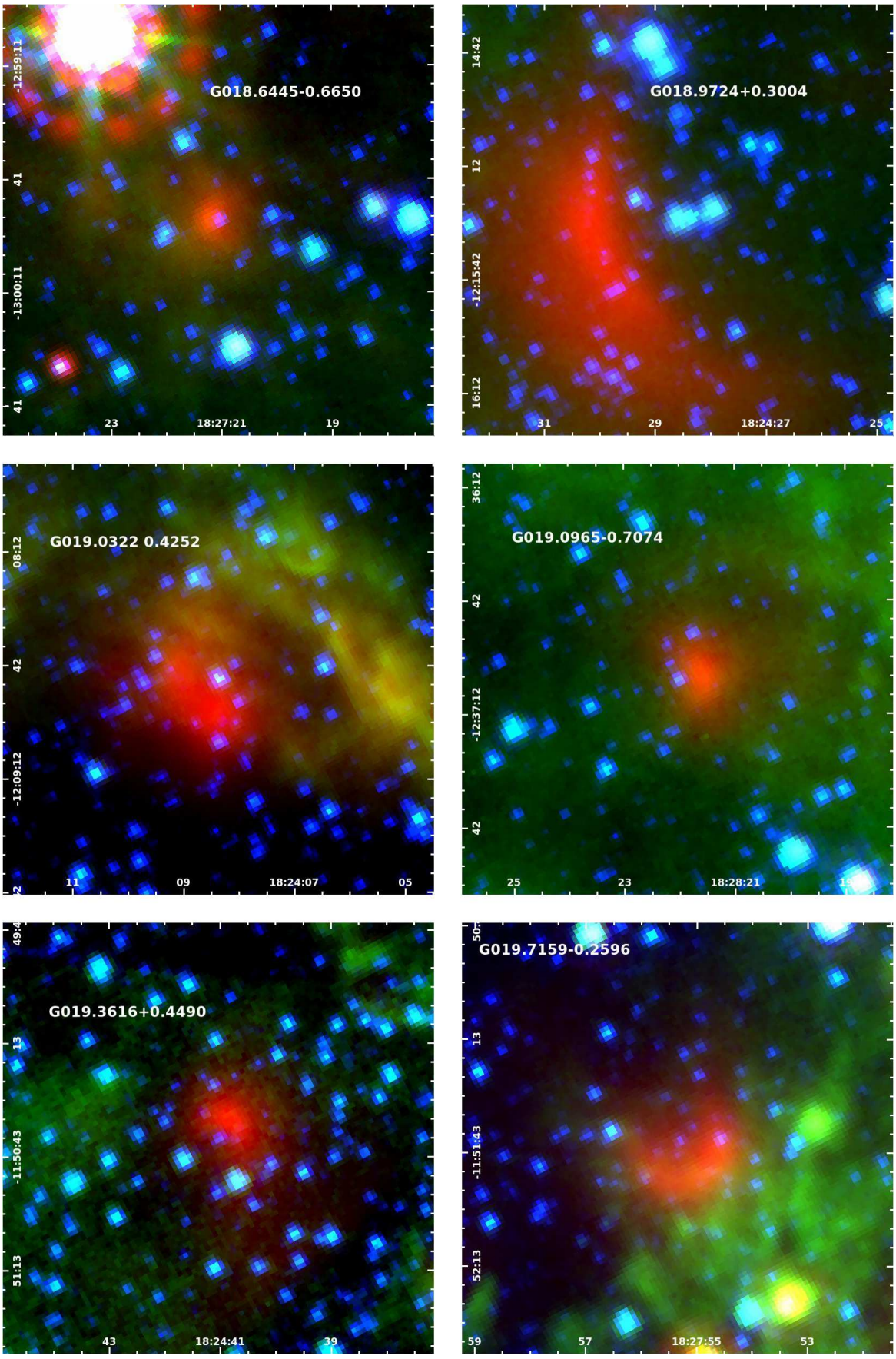
G018.6445-0.6650
-12:59:11
41
-13:00:11
41
23
18:27:21
19
G018.9724+0.3004
14:42
12
-12:15:42
16:12
31
29
18:24:27
25
G019.0322 0.4252
08:12
42
-12:09:12
11
09
18:24:07
05
G019.0965-0.7074
36:12
42
-12:37:12
42
25
23
18:28:21
G019.3616+0.4490
13
-11:50:43
51:13
43
18:24:41
39
G019.7159-0.2596
13
-11:51:43
52:13
59
57
18:27:55
53

Figure A13.

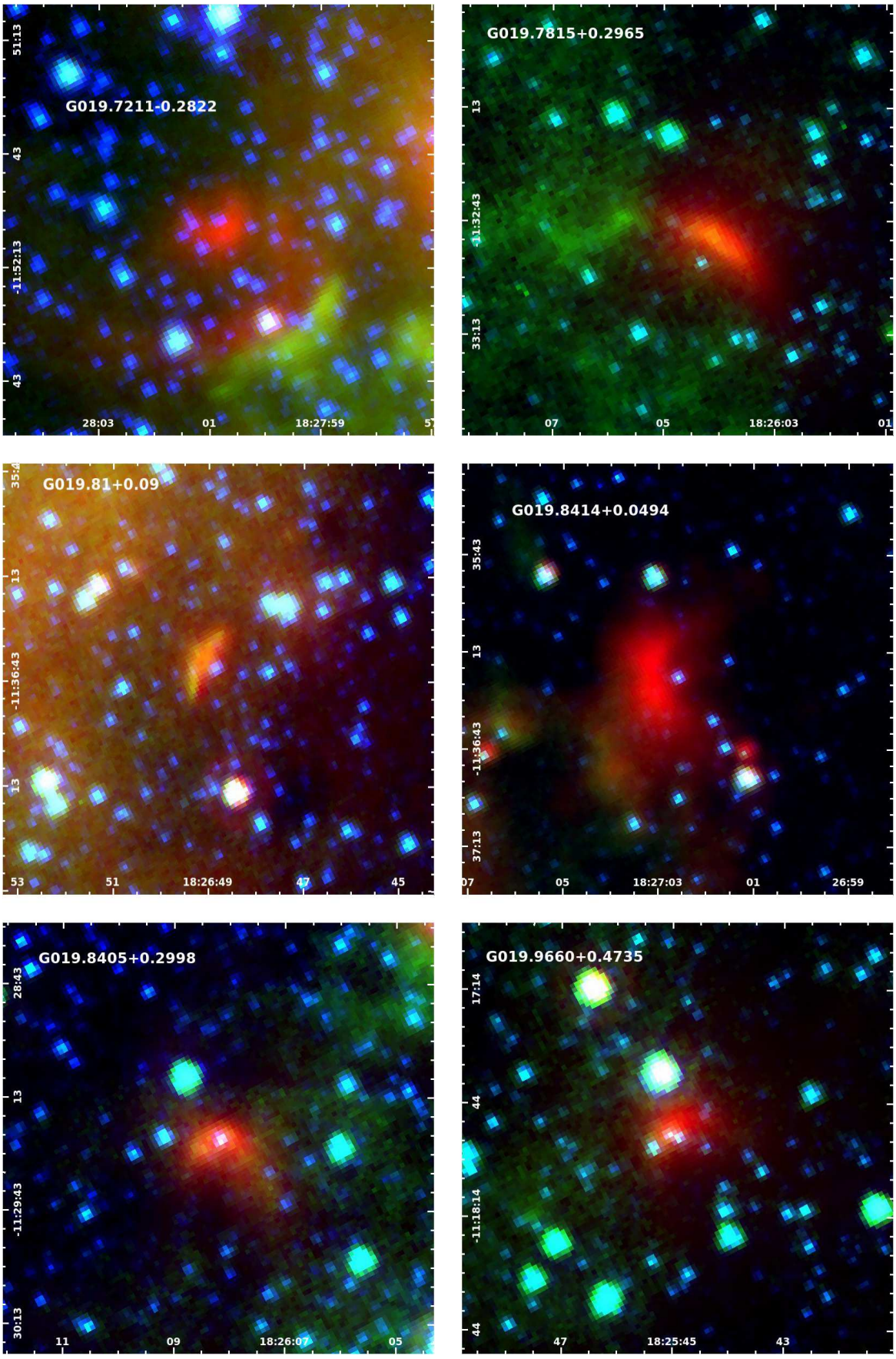
G019.7211-0.2822
51:13
43
-11:52:13
43
28:03
01
18:27:59
G019.7815+0.2965
13
-11:32:43
33:13
07
05
18:26:03
01
G019.81+0.09
35:0
13
-11:36:43
13
53
51
18:26:49
47
45
G019.8414+0.0494
35:43
13
-11:36:43
37:13
07
05
18:27:03
01
26:59
G019.8405+0.2998
28:43
13
-11:29:43
30:13
11
09
18:26:07
05
G019.9660+0.4735
17:14
44
-11:18:14
44
47
18:25:45
43

Figure A14.

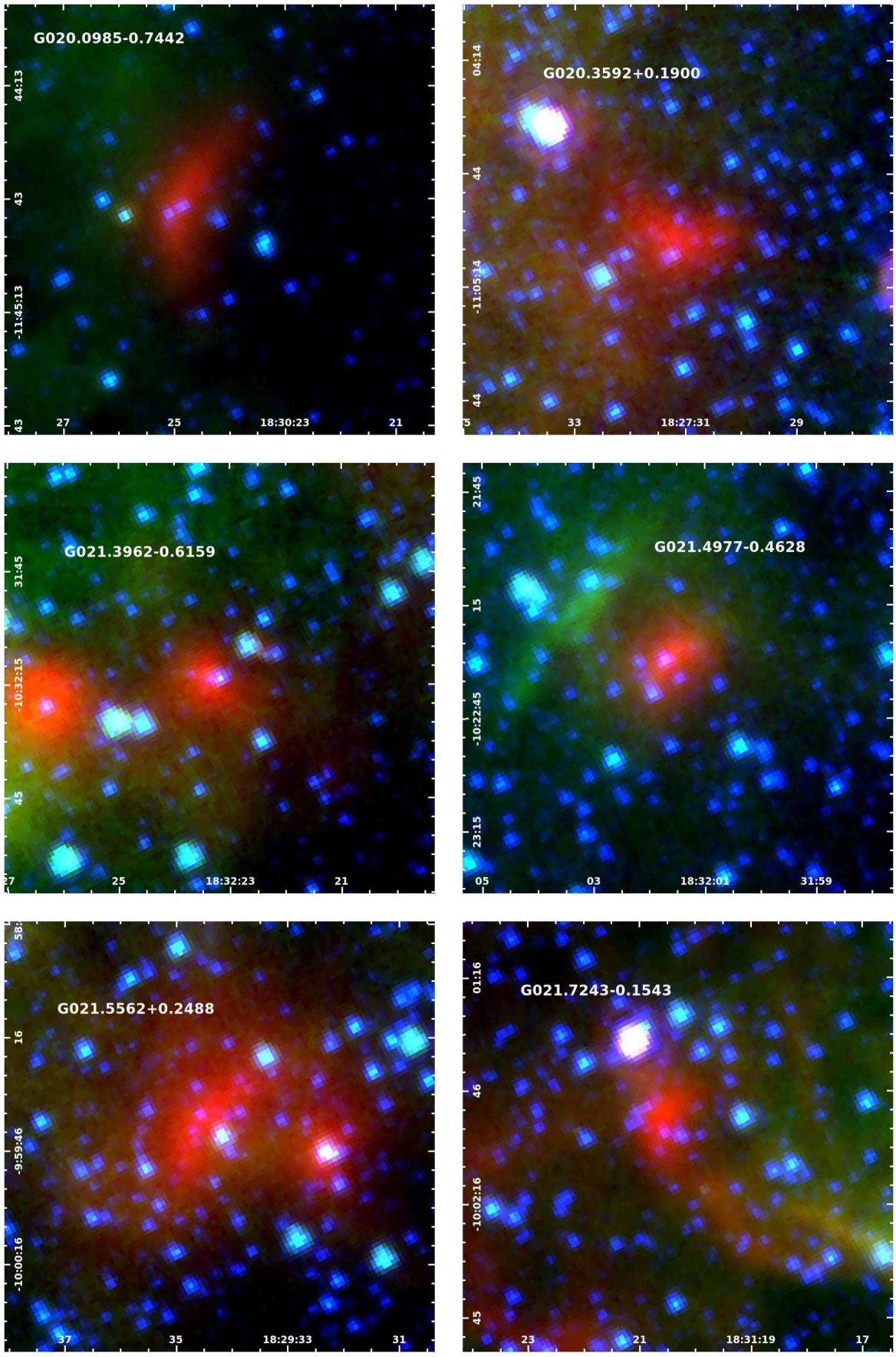
G020.0985-0.7442
44:13
43
-11:45:13
43
27
25
18:30:23
21
G020.3592+0.1900
04:14
44
-11:05:14
44
33
18:27:31
29
G021.3962-0.6159
31:45
-10:32:15
45
27
25
18:32:23
21
G021.4977-0.4628
21:45
15
-10:22:45
23:15
05
03
18:32:01
31:59
G021.5562+0.2488
16
-9:59:46
-10:00:16
37
35
18:29:33
31
G021.7243-0.1543
01:16
46
-10:02:16
45
23
21
18:31:19
17

Figure A15.

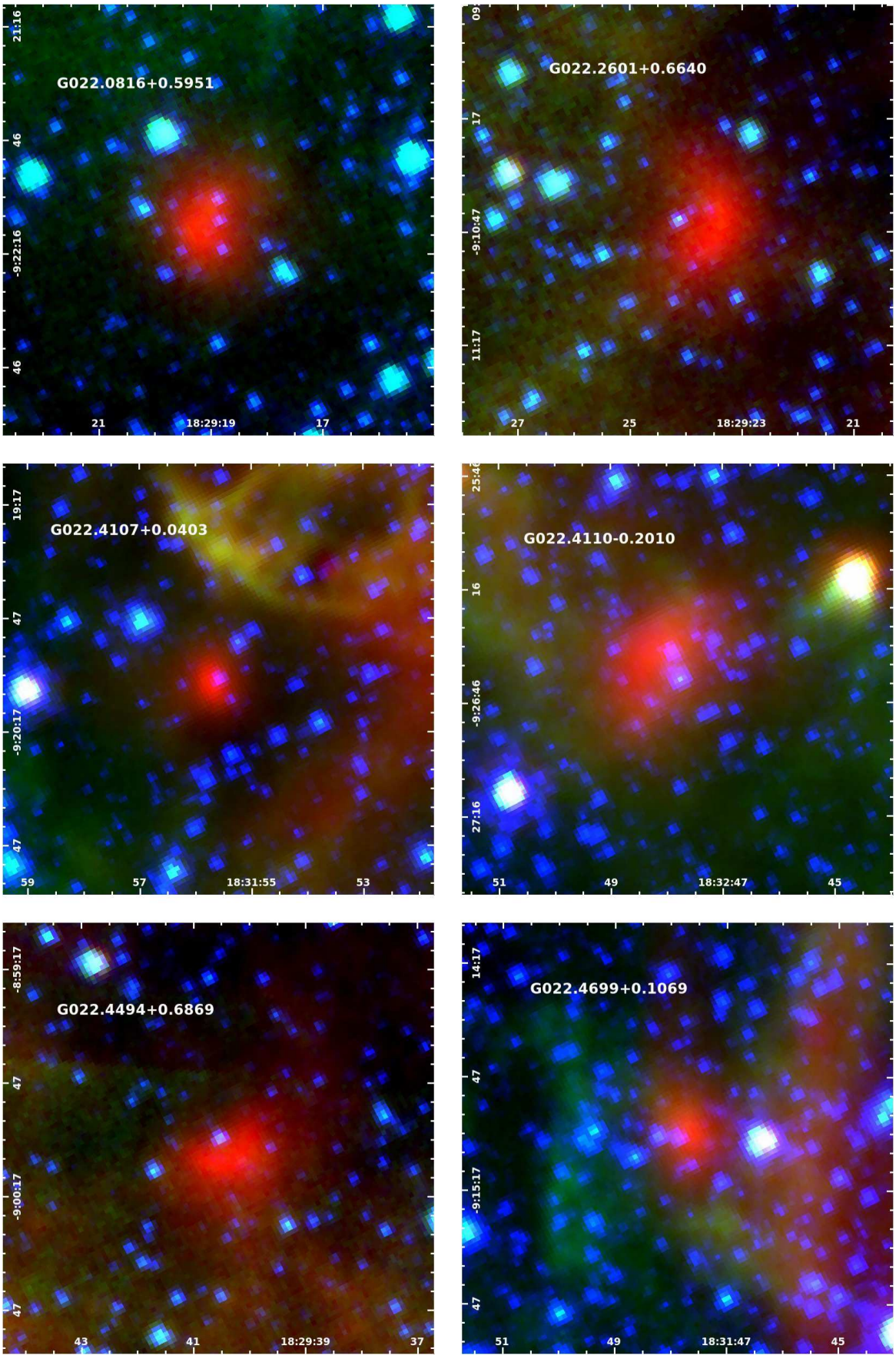
G022.0816+0.5951
21:16
46
-9:22:16
46
21
18:29:19
17
G022.2601+0.6640
09
17
-9:10:47
11:17
27
25
18:29:23
21
G022.4107+0.0403
19:17
47
-9:20:17
47
59
57
18:31:55
53
G022.4110-0.2010
25:46
16
-9:26:46
27:16
51
49
18:32:47
45
G022.4494+0.6869
-8:59:17
47
-9:00:17
47
43
41
18:29:39
37
G022.4699+0.1069
14:17
47
-9:15:17
47
51
49
18:31:47
45

Figure A16.

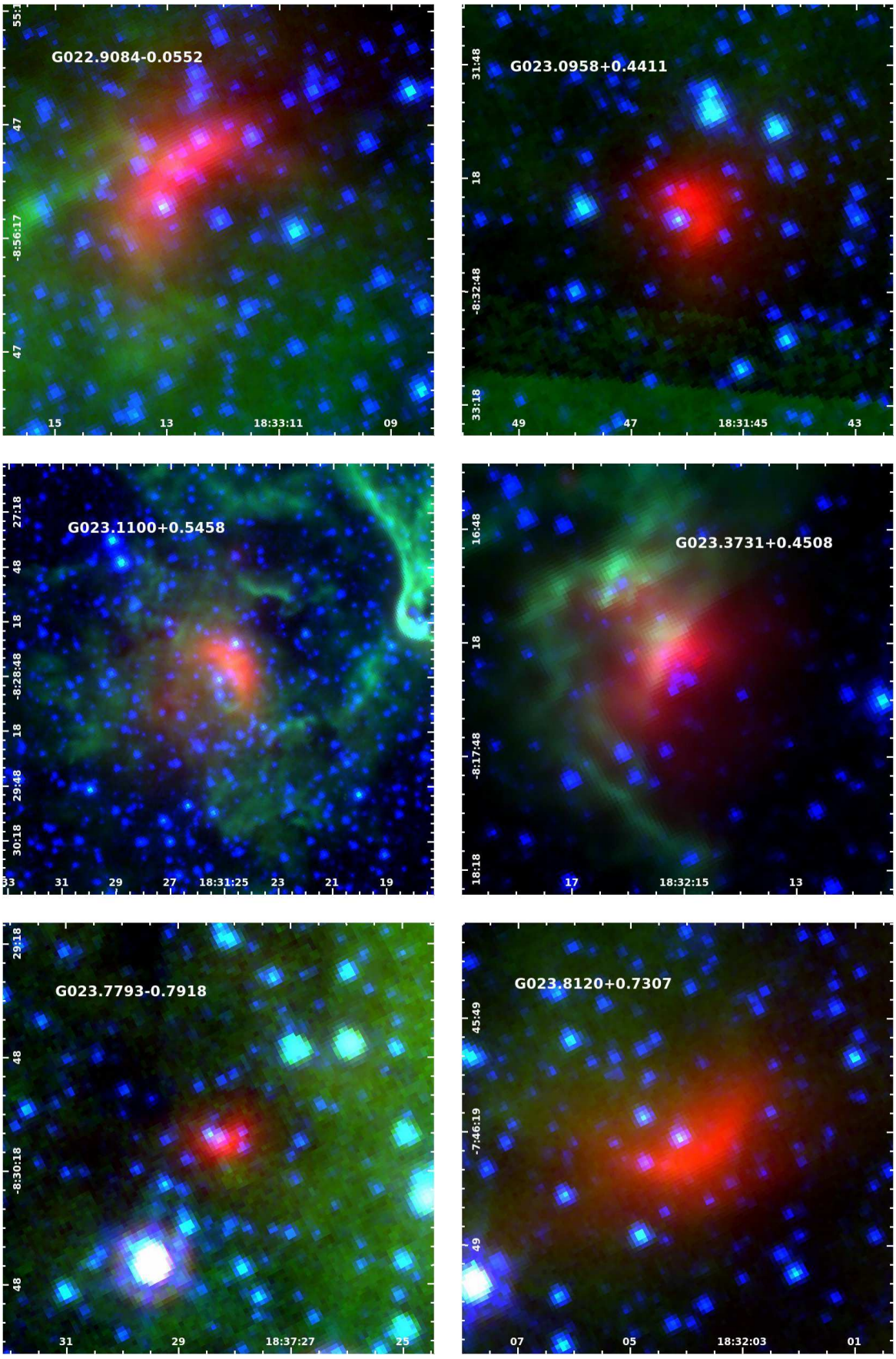
G022.9084-0.0552
G023.0958+0.4411
G023.1100+0.5458
G023.3731+0.4508
G023.7793-0.7918
G023.8120+0.7307

Figure A17.

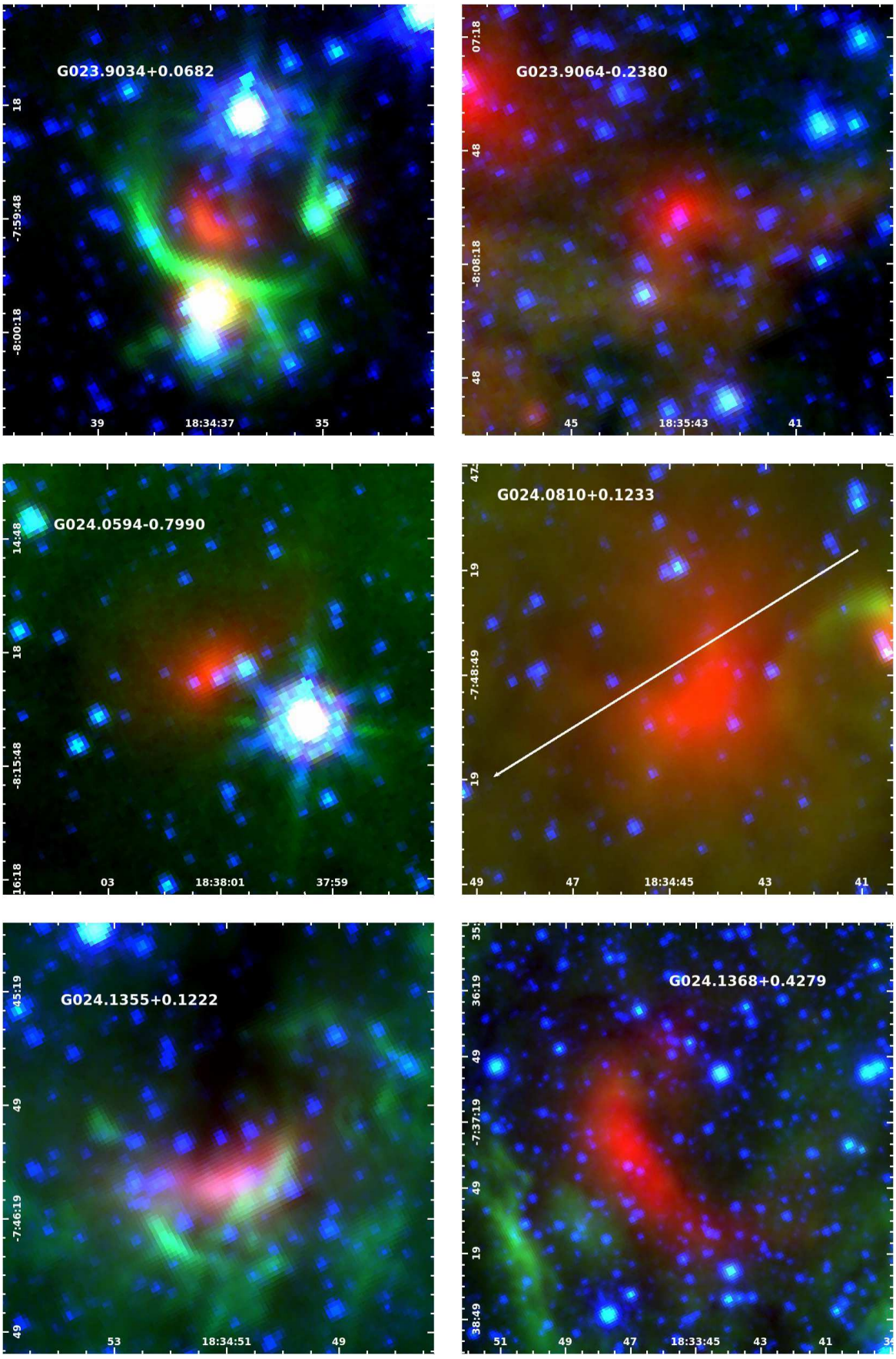
G023.9034+0.0682
G023.9064-0.2380
G024.0594-0.7990
G024.0810+0.1233
G024.1355+0.1222
G024.1368+0.4279

Figure A18.

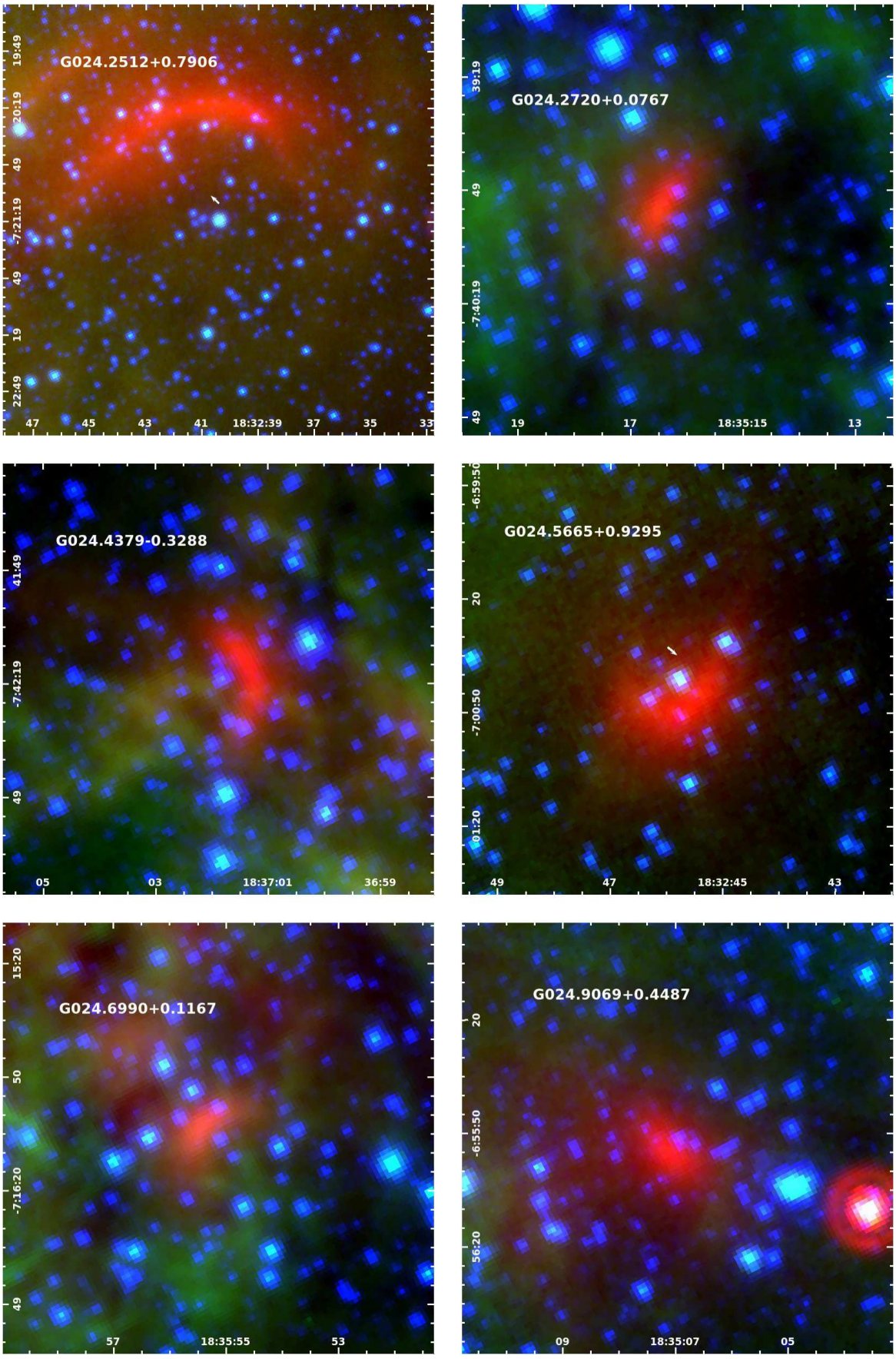
G024.2512+0.7906
19:49
20:19
49
-7:21:19
49
19
22:49
47
45
43
41
18:32:39
37
35
33
G024.2720+0.0767
39:19
49
-7:40:19
49
19
17
18:35:15
13
G024.4379-0.3288
41:49
-7:42:19
49
05
03
18:37:01
36:59
G024.5665+0.9295
-6:59:50
20
-7:00:50
01:20
49
47
18:32:45
43
G024.6990+0.1167
15:20
50
-7:16:20
49
57
18:35:55
53
G024.9069+0.4487
20
-6:55:50
56:20
09
18:35:07
05

Figure A19.

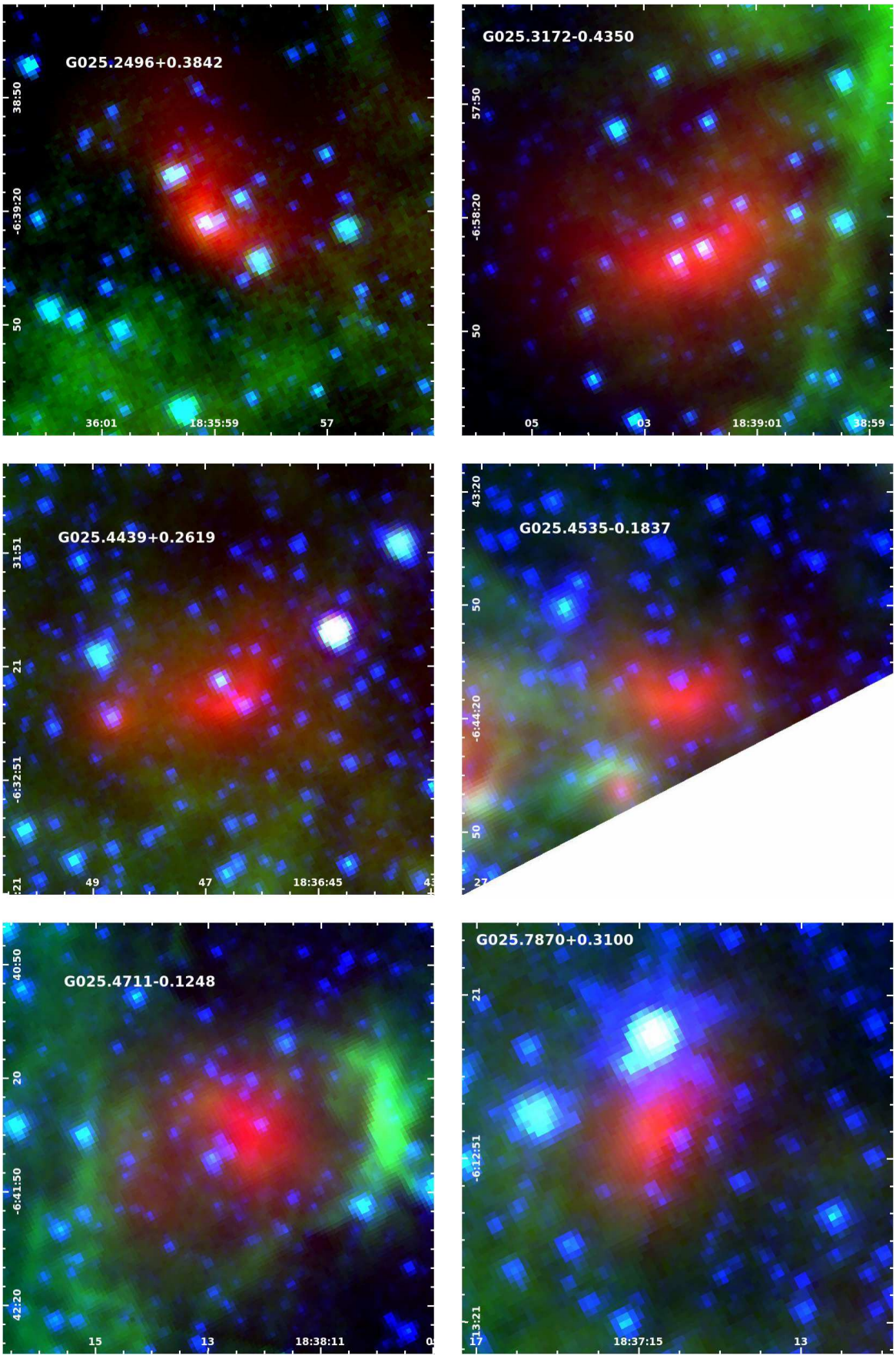
G025.2496+0.3842
38:50
-6:39:20
50
36:01
18:35:59
57
G025.3172-0.4350
57:50
-6:58:20
50
05
03
18:39:01
38:59
G025.4439+0.2619
31:51
21
-6:32:51
49
47
18:36:45
G025.4535-0.1837
43:20
50
-6:44:20
50
G025.4711-0.1248
40:50
20
-6:41:50
42:20
15
13
18:38:11
G025.7870+0.3100
21
-6:12:51
13:21
17
18:37:15
13

Figure A20.

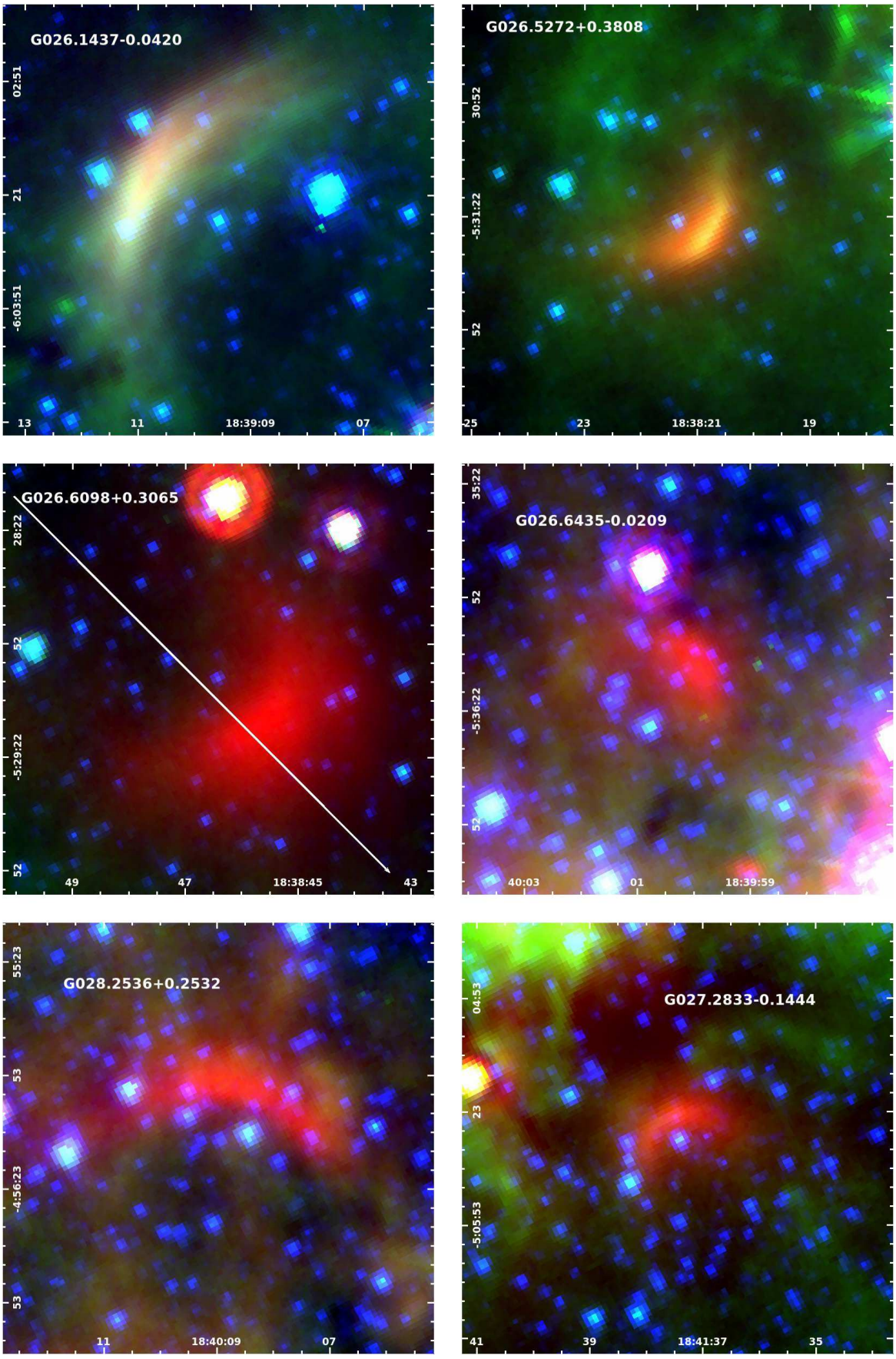
G026.1437-0.0420
02:51
21
-6:03:51
13
11
18:39:09
07
G026.5272+0.3808
30:52
-5:31:22
52
-25
23
18:38:21
19
G026.6098+0.3065
28:22
52
-5:29:22
52
49
47
18:38:45
43
G026.6435-0.0209
35:22
52
-5:36:22
52
40:03
01
18:39:59
G028.2536+0.2532
55:23
53
-4:56:23
53
11
18:40:09
07
G027.2833-0.1444
04:53
23
-5:05:53
41
39
18:41:37
35

Figure A21.

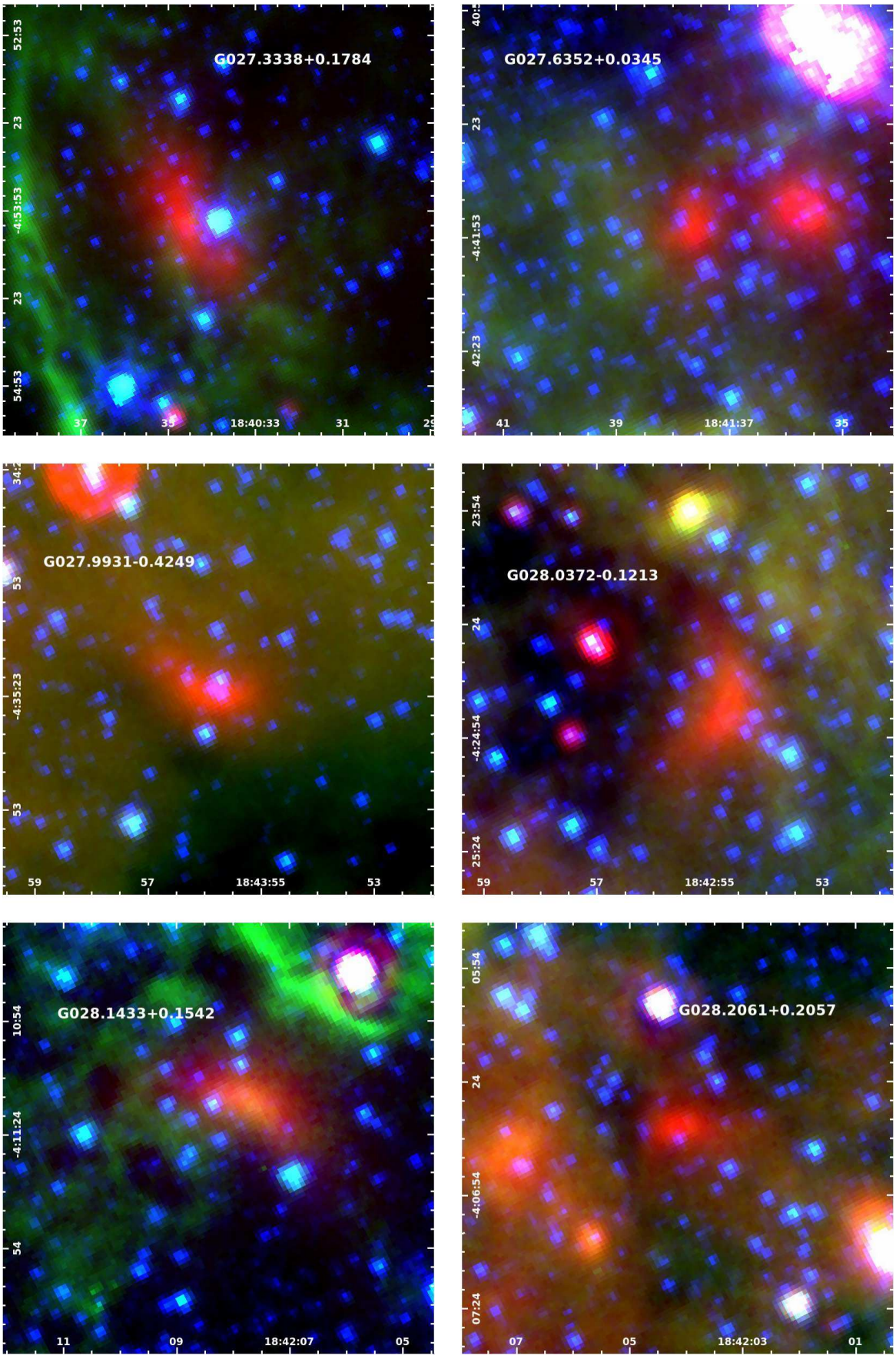
G027.3338+0.1784
G027.6352+0.0345
G027.9931-0.4249
G028.0372-0.1213
G028.1433+0.1542
G028.2061+0.2057

Figure A22.

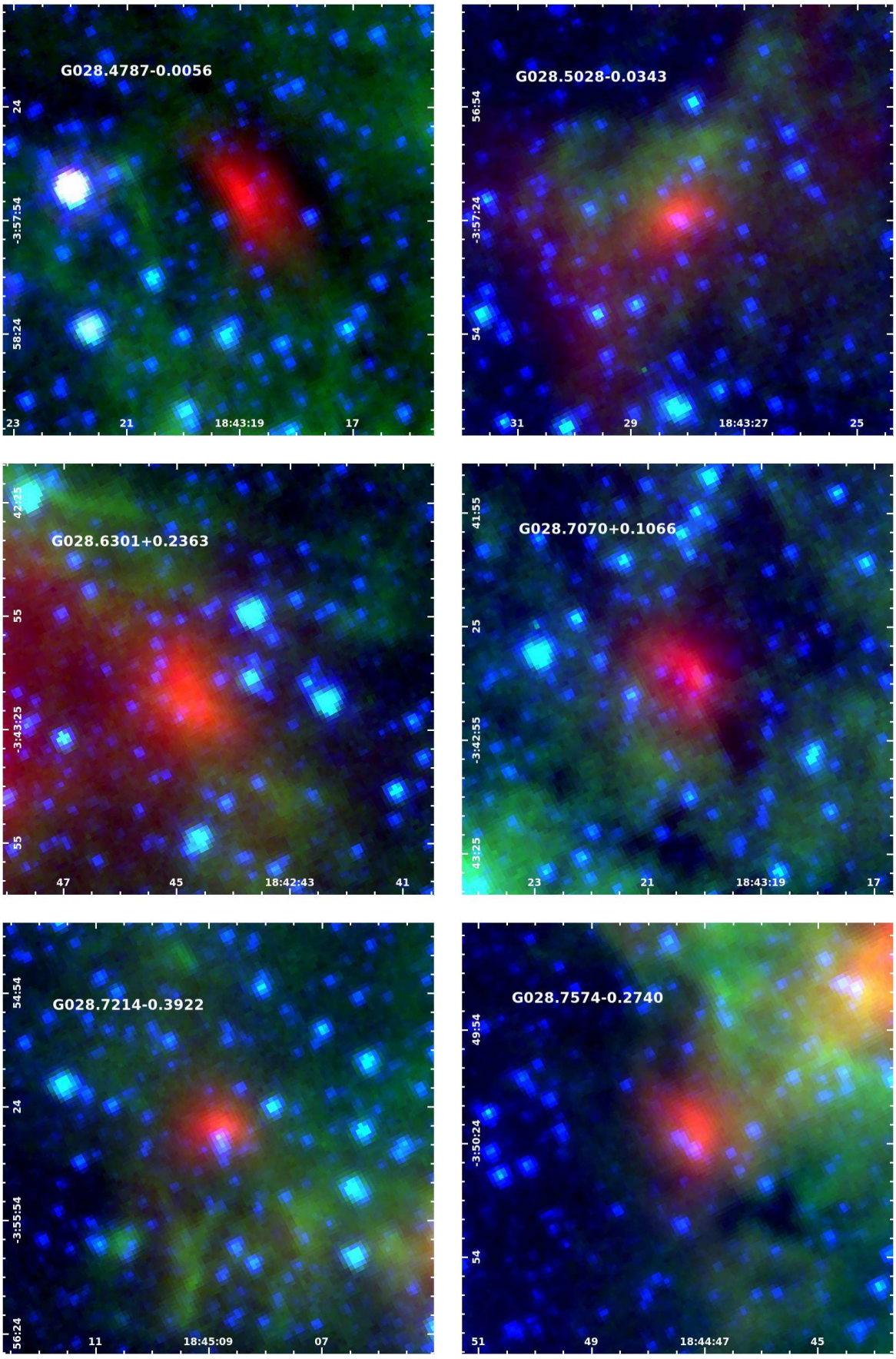
G028.4787-0.0056
24
-3:57:54
58:24
23
21
18:43:19
17
G028.5028-0.0343
56:54
-3:57:24
54
31
29
18:43:27
25
G028.6301+0.2363
42:25
55
-3:43:25
55
47
45
18:42:43
41
G028.7070+0.1066
41:55
25
-3:42:55
43:25
23
21
18:43:19
17
G028.7214-0.3922
54:54
24
-3:55:54
56:24
11
18:45:09
07
G028.7574-0.2740
49:54
-3:50:24
54
51
49
18:44:47
45

Figure A23.

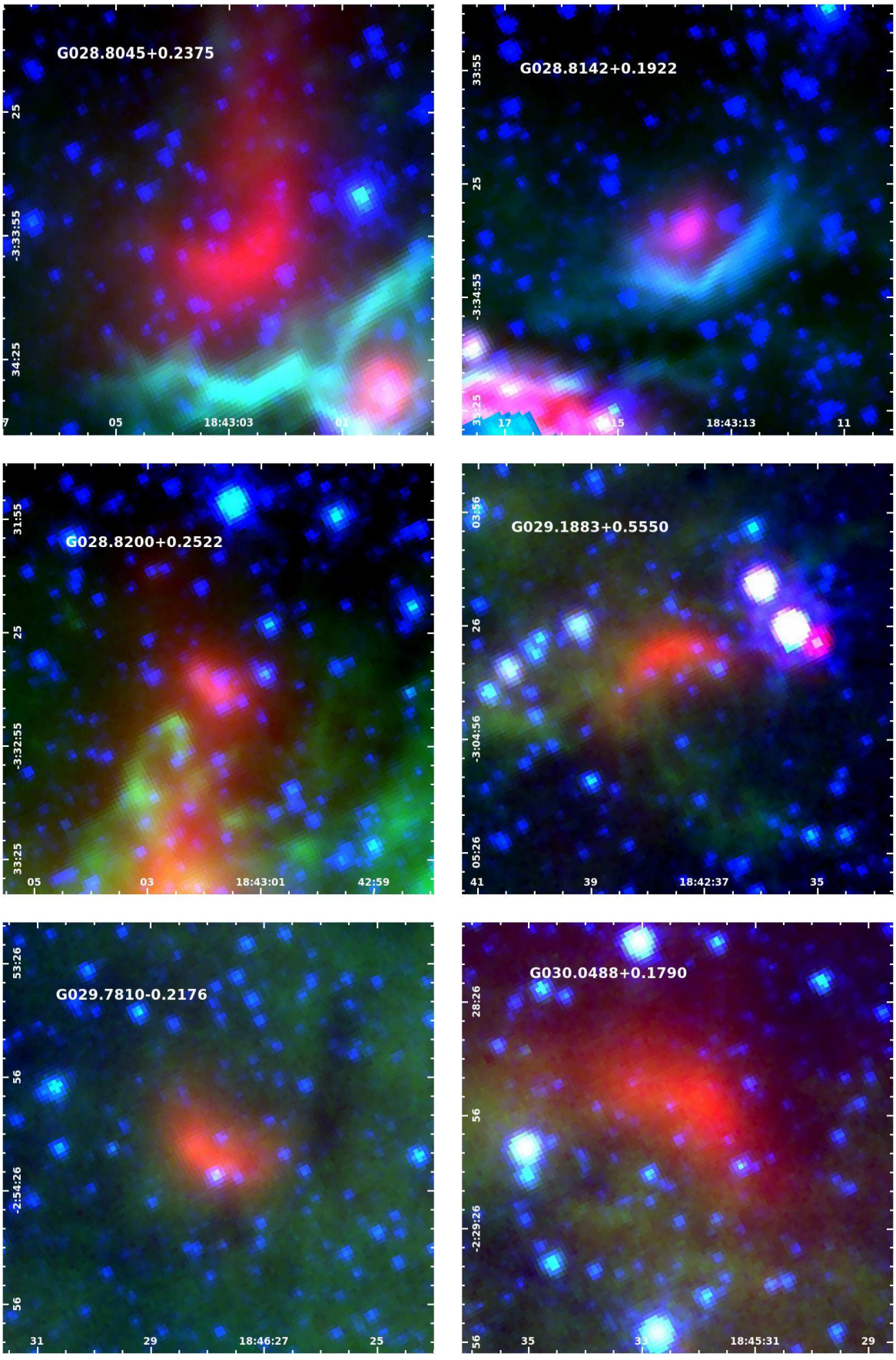
G028.8045+0.2375
G028.8142+0.1922
G028.8200+0.2522
G029.1883+0.5550
G029.7810-0.2176
G030.0488+0.1790

Figure A24.

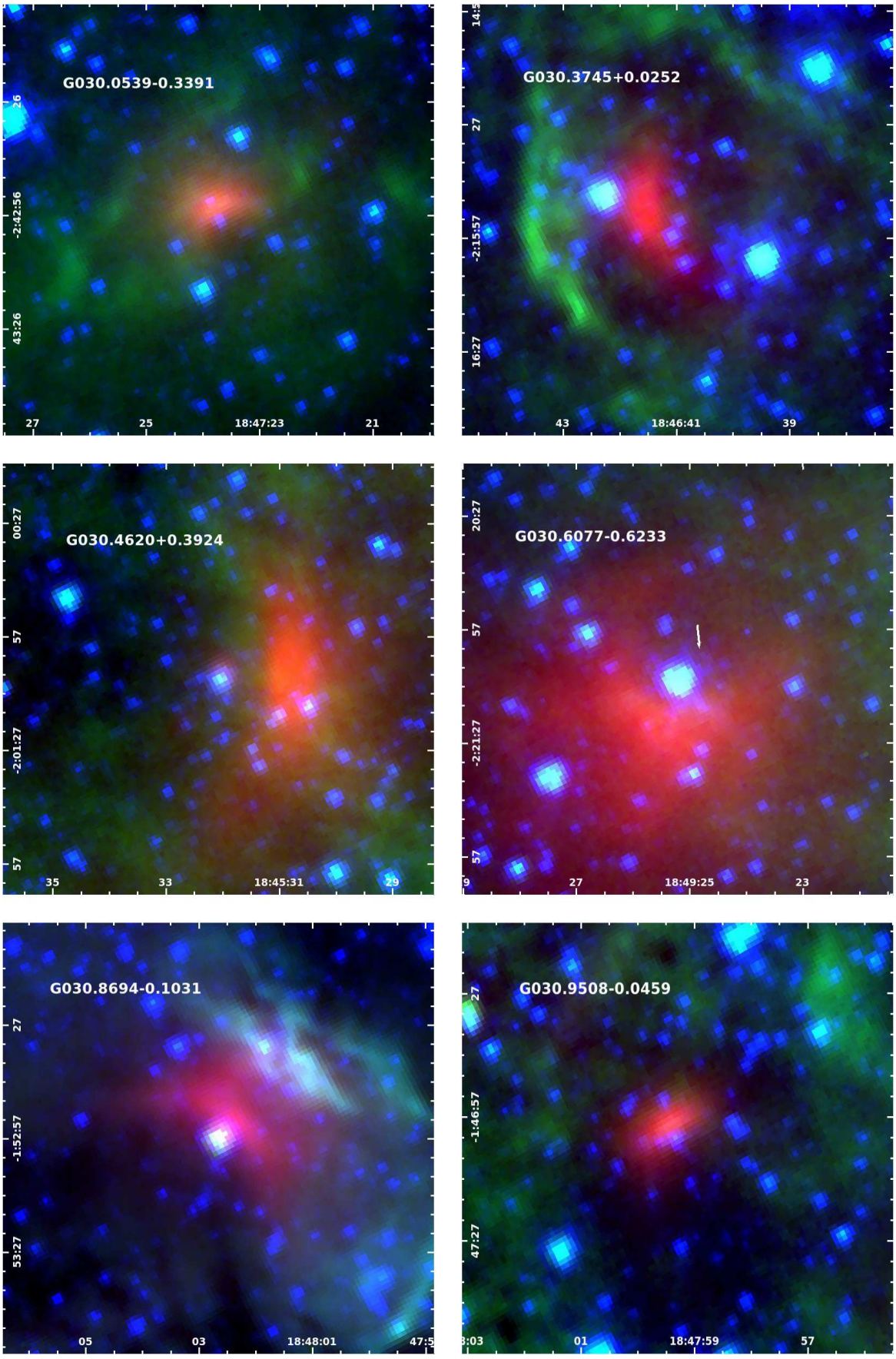
G030.0539-0.3391
26
-2:42:56
43:26
27
25
18:47:23
21
G030.3745+0.0252
27
-2:15:57
16:27
43
18:46:41
39
G030.4620+0.3924
00:27
57
-2:01:27
57
35
33
18:45:31
29
G030.6077-0.6233
20:27
57
-2:21:27
57
27
18:49:25
23
G030.8694-0.1031
27
-1:52:57
53:27
05
03
18:48:01
G030.9508-0.0459
27
-1:46:57
47:27
01
18:47:59
57

Figure A25.

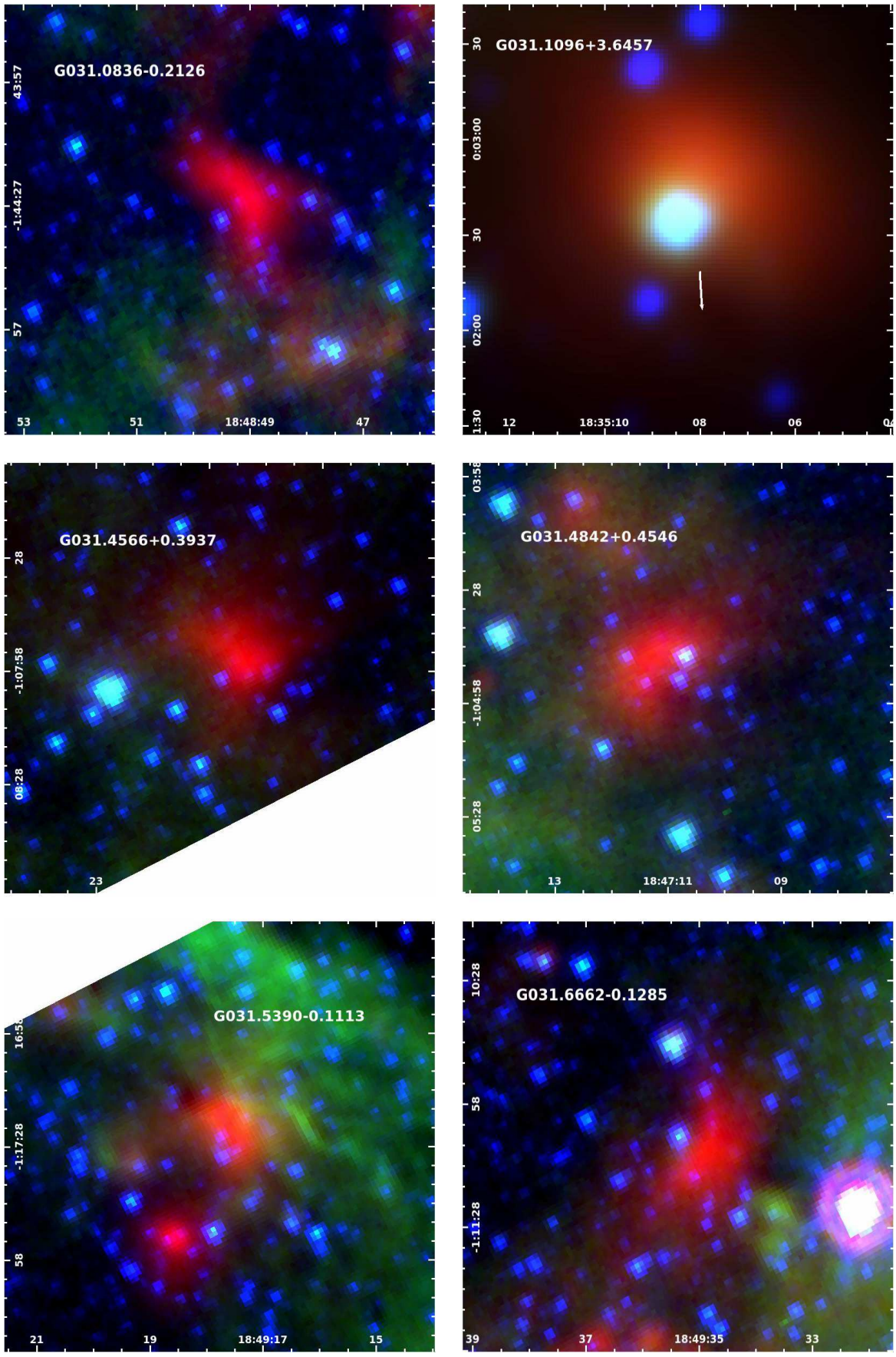
G031.0836-0.2126
43:57
-1:44:27
57
53
51
18:48:49
47
G031.1096+3.6457
30
0:03:00
30
02:00
1:30
12
18:35:10
08
06
G031.4566+0.3937
28
-1:07:58
08:28
23
G031.4842+0.4546
03:58
28
-1:04:58
05:28
13
18:47:11
09
G031.5390-0.1113
16:58
-1:17:28
58
21
19
18:49:17
15
G031.6662-0.1285
10:28
58
-1:11:28
39
37
18:49:35
33

Figure A26.

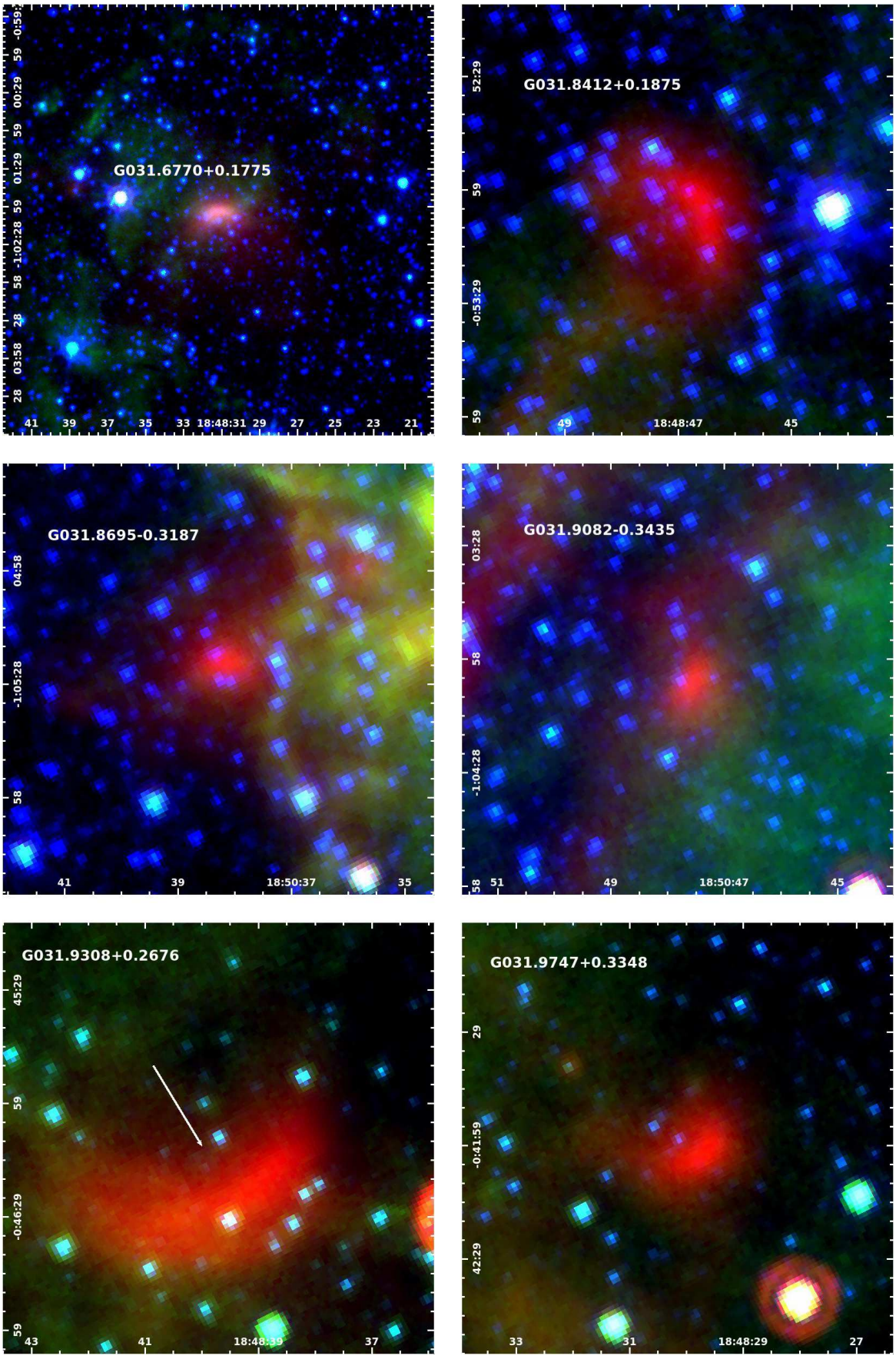
G031.6770+0.1775
G031.8412+0.1875
G031.8695-0.3187
G031.9082-0.3435
G031.9308+0.2676
G031.9747+0.3348

Figure A27.

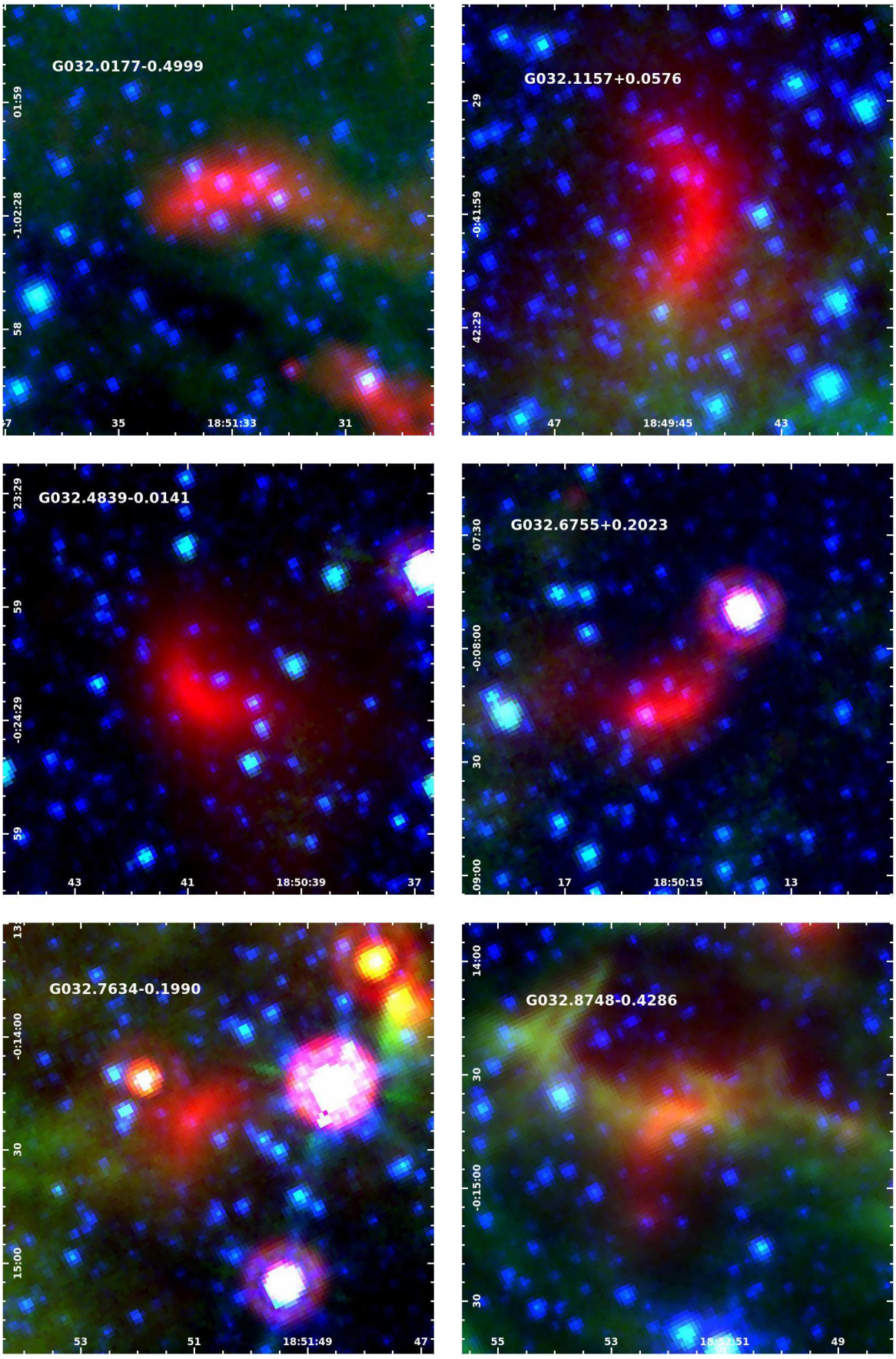
G032.0177-0.4999
01:59
-1:02:28
58
7
35
18:51:33
31
G032.1157+0.0576
29
-0:41:59
42:29
47
18:49:45
43
G032.4839-0.0141
23:29
59
-0:24:29
59
43
41
18:50:39
37
G032.6755+0.2023
07:30
-0:08:00
30
09:00
17
18:50:15
13
G032.7634-0.1990
13
-0:14:00
30
15:00
53
51
18:51:49
47
G032.8748-0.4286
14:00
30
-0:15:00
30
55
53
49

Figure A28.

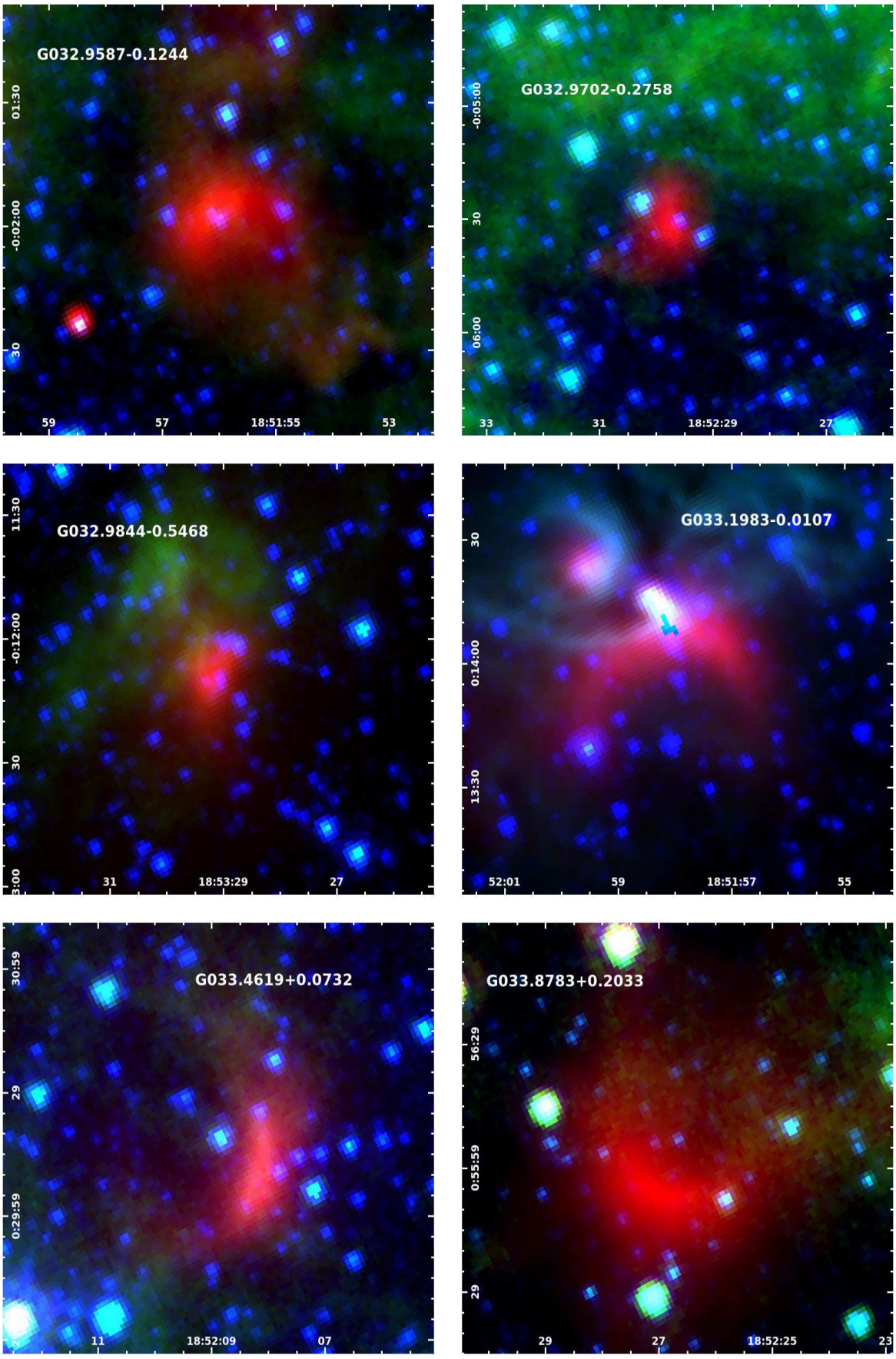
G032.9587-0.1244
01:30
-0:02:00
30
59
57
18:51:55
53
G032.9702-0.2758
-0:05:00
30
06:00
33
31
18:52:29
27
G032.9844-0.5468
11:30
-0:12:00
30
3:00
31
18:53:29
27
G033.1983-0.0107
30
0:14:00
13:30
52:01
59
18:51:57
55
G033.4619+0.0732
30:59
29
0:29:59
11
18:52:09
07
G033.8783+0.2033
56:29
0:55:59
29
29
27
18:52:25
23

Figure A29.

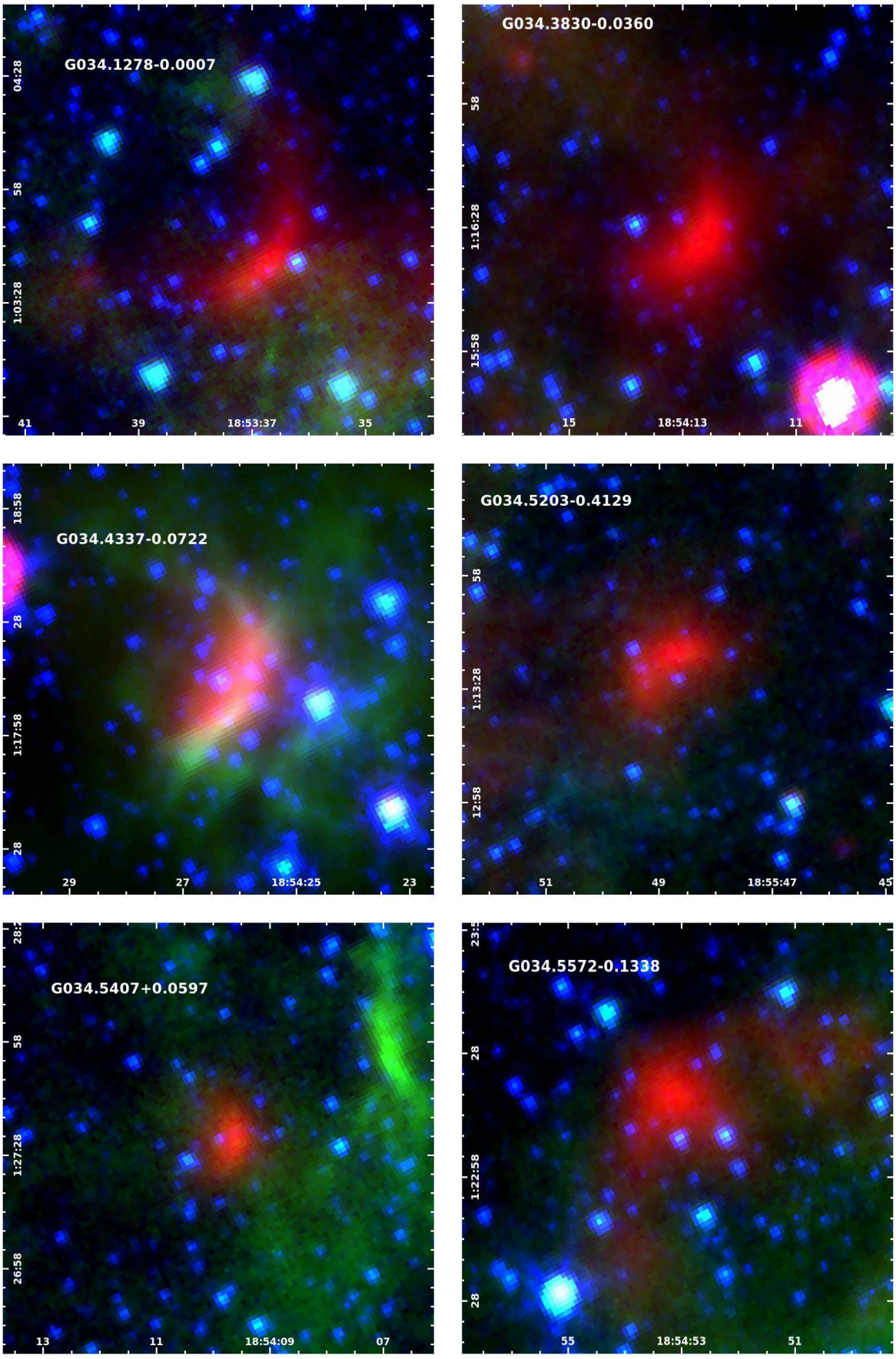
G034.1278-0.0007
04:28
58
1:03:28
41
39
18:53:37
35
G034.3830-0.0360
58
1:16:28
15:58
15
18:54:13
11
G034.4337-0.0722
18:58
28
1:17:58
28
29
27
18:54:25
23
G034.5203-0.4129
58
1:13:28
12:58
51
49
18:55:47
45
G034.5407+0.0597
58
1:27:28
26:58
13
11
18:54:09
07
G034.5572-0.1338
28
1:22:58
28
55
18:54:53
51

Figure A30.

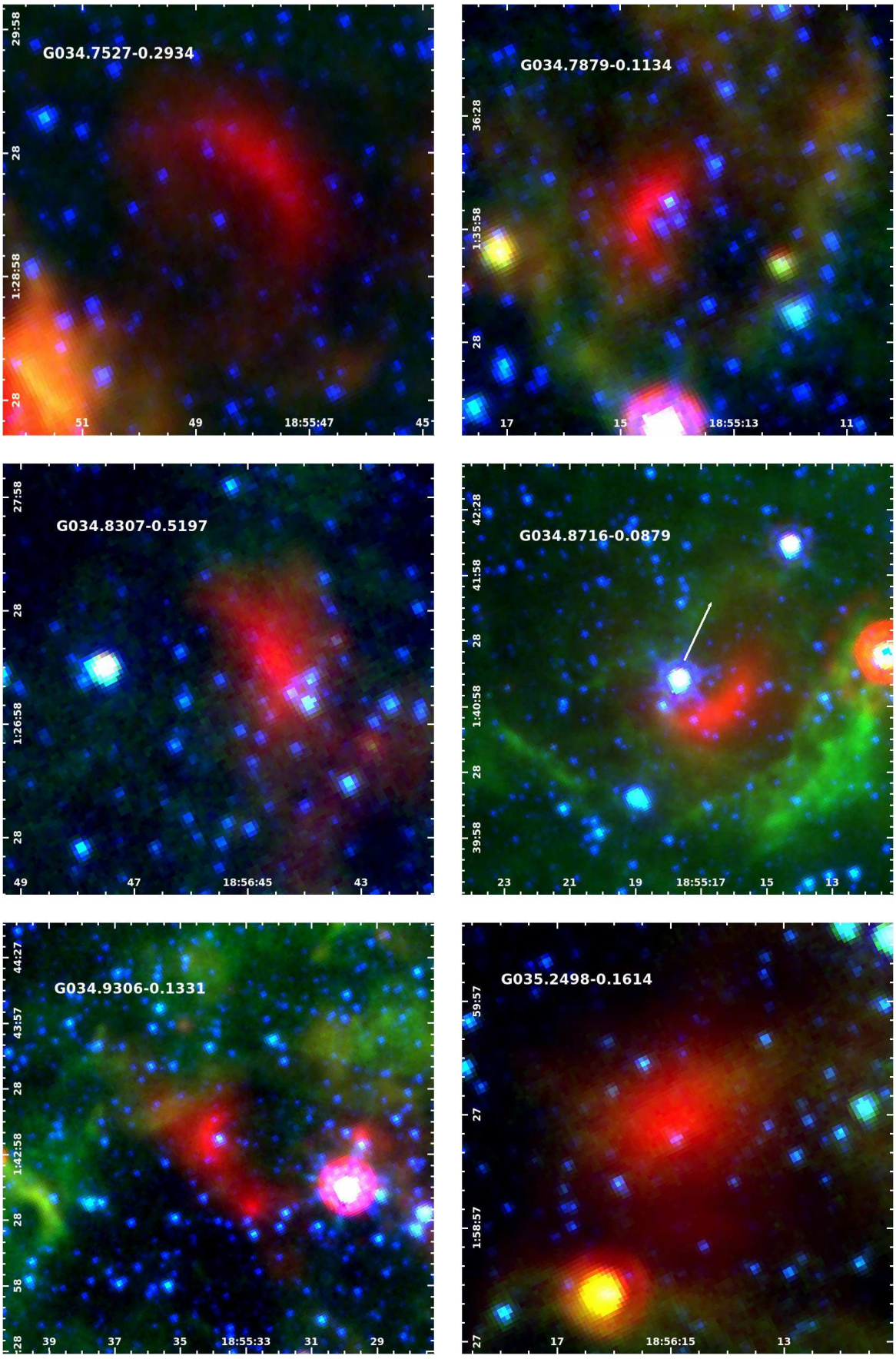
G034.7527-0.2934
29:58
28
1:28:58
28
51
49
18:55:47
45
G034.7879-0.1134
36:28
1:35:58
28
17
15
18:55:13
11
G034.8307-0.5197
27:58
28
1:26:58
28
49
47
18:56:45
43
G034.8716-0.0879
42:28
41:58
28
1:40:58
28
39:58
23
21
19
18:55:17
15
13
G034.9306-0.1331
44:27
43:57
28
1:42:58
28
58
28
39
37
35
18:55:33
31
29
G035.2498-0.1614
59:57
27
1:58:57
27
17
18:56:15
13

Figure A31.

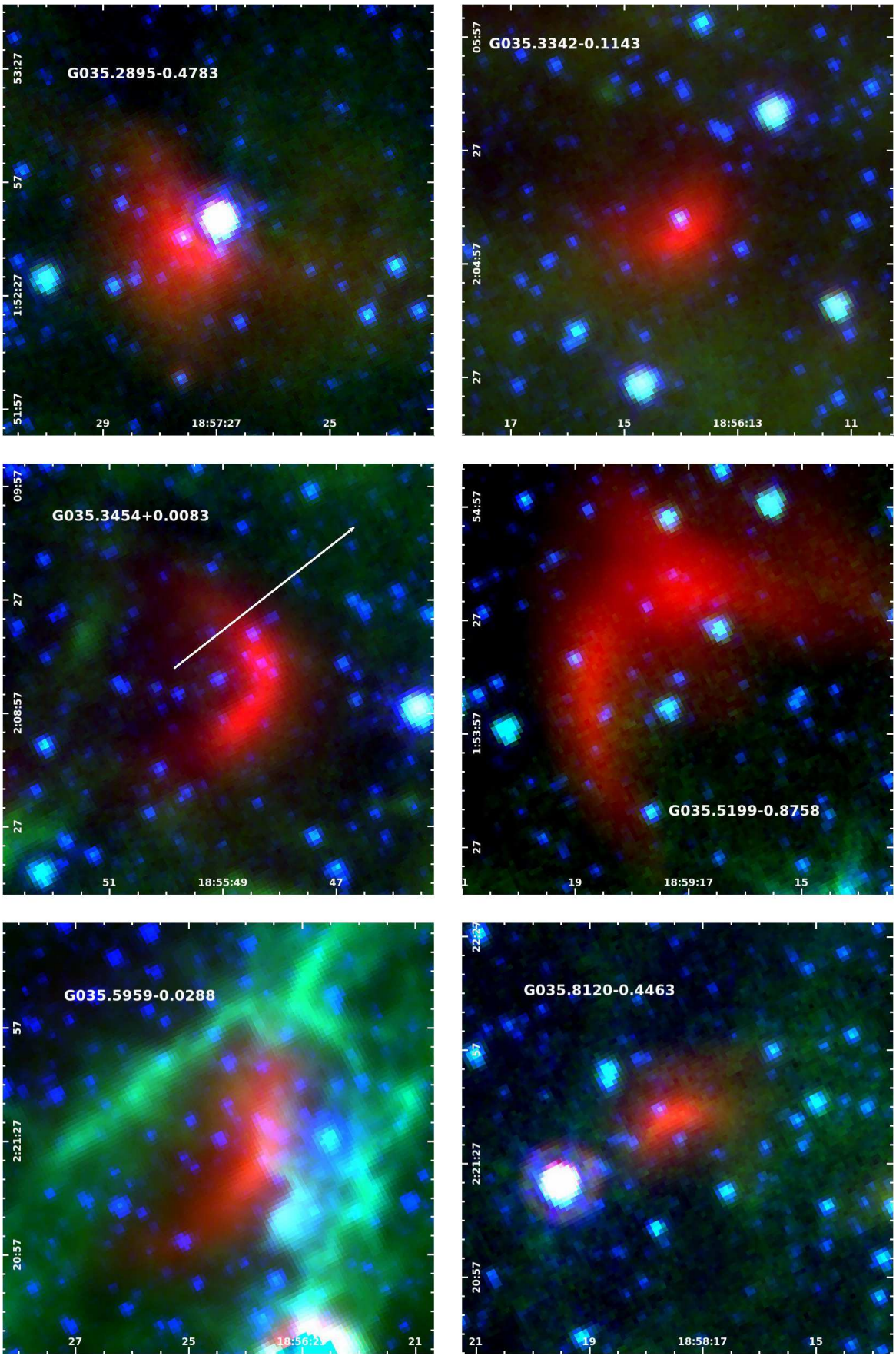
G035.2895-0.4783
G035.3342-0.1143
G035.3454+0.0083
G035.5199-0.8758
G035.5959-0.0288
G035.8120-0.4463

Figure A32.

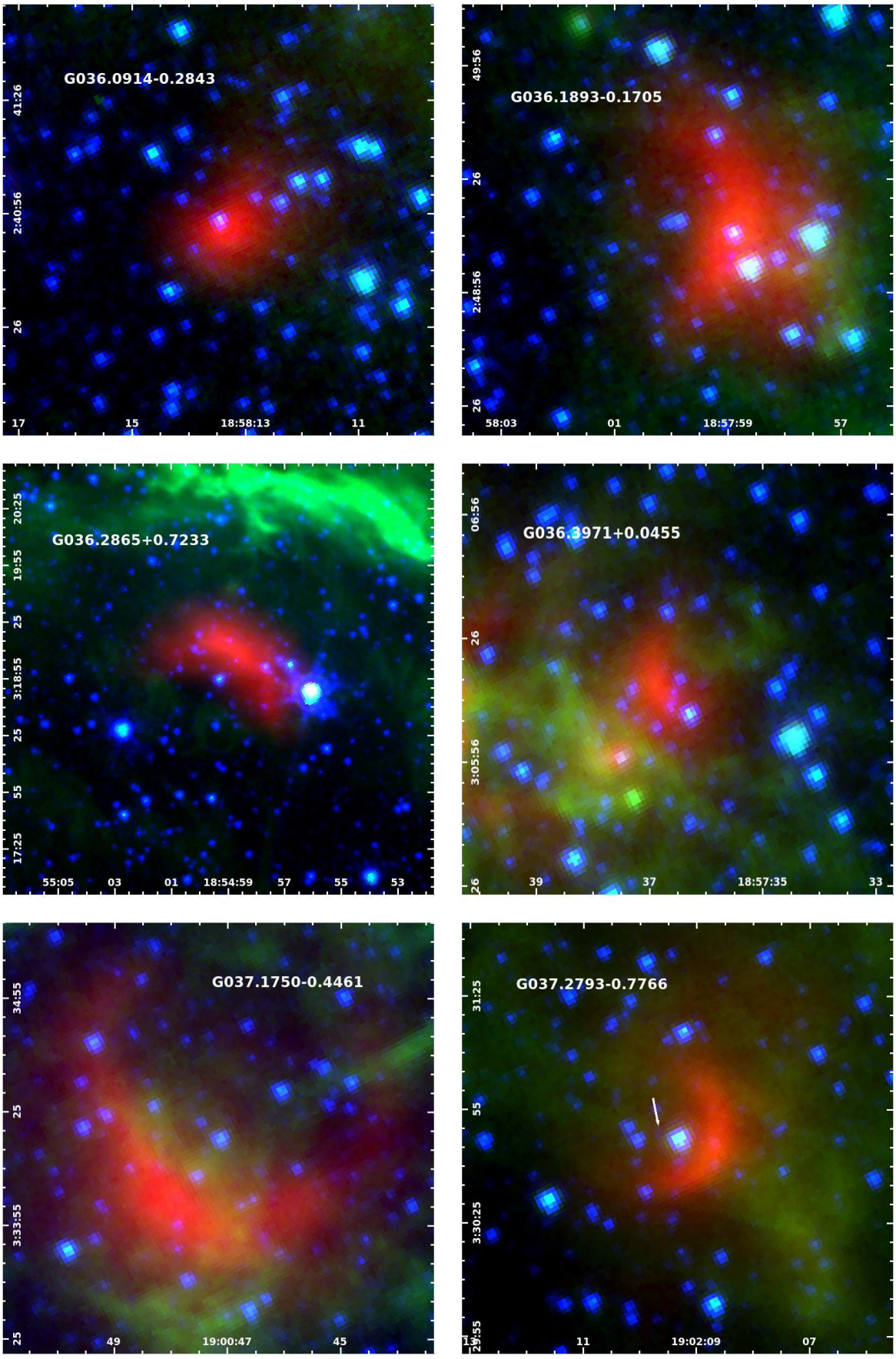
G036.0914-0.2843
41:26
2:40:56
26
17
15
18:58:13
11
G036.1893-0.1705
49:56
26
2:48:56
26
58:03
01
18:57:59
57
G036.2865+0.7233
20:25
19:55
25
3:18:55
25
55
17:25
55:05
03
01
18:54:59
57
55
53
G036.3971+0.0455
06:56
26
3:05:56
26
39
37
18:57:35
33
G037.1750-0.4461
34:55
25
3:33:55
25
49
19:00:47
45
G037.2793-0.7766
31:25
55
3:30:25
29:55
11
19:02:09
07

Figure A33.

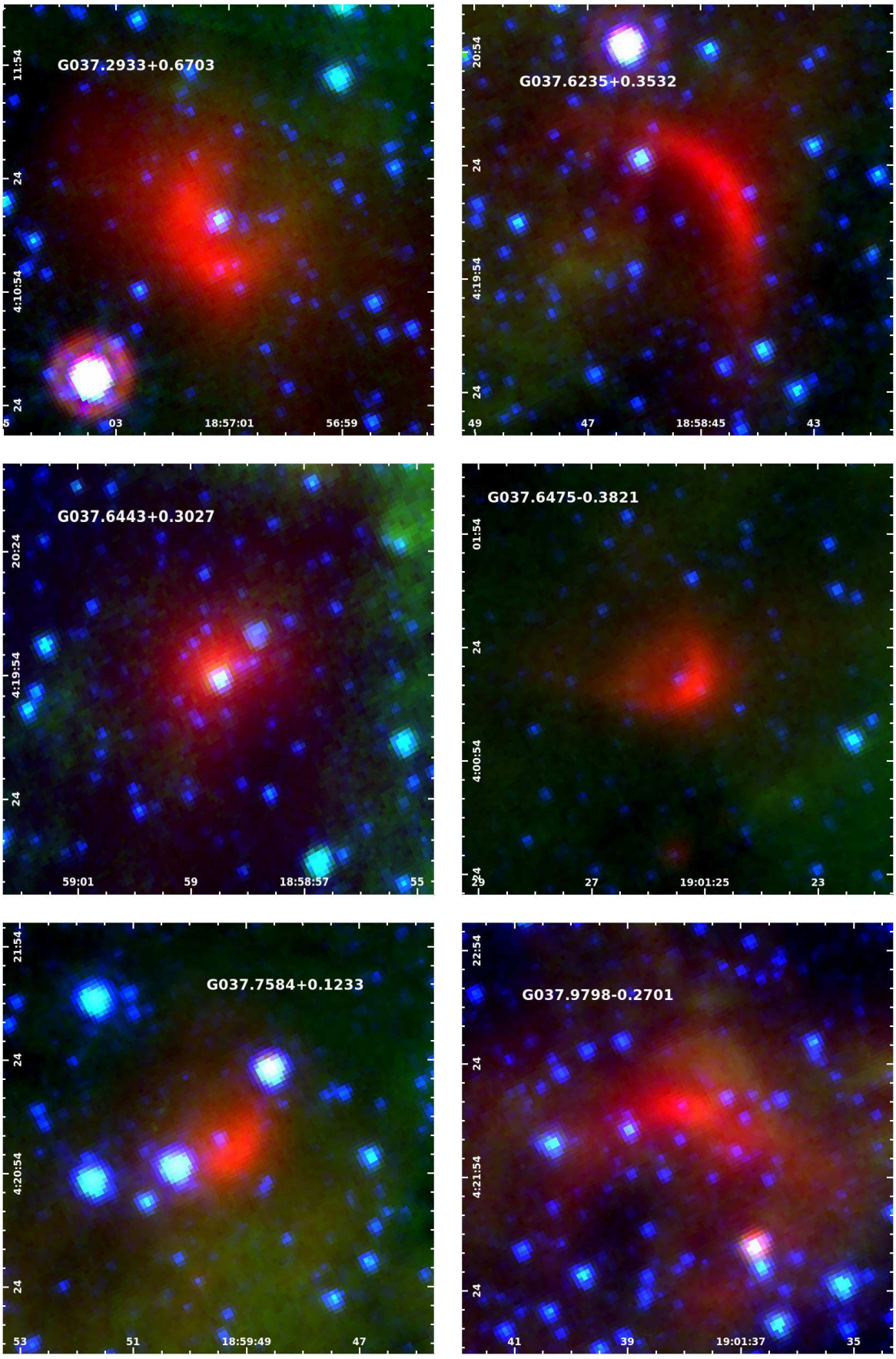
G037.2933+0.6703
11:54
24
4:10:54
24
5
03
18:57:01
56:59
G037.6235+0.3532
20:54
24
4:19:54
24
49
47
18:58:45
43
G037.6443+0.3027
20:24
4:19:54
24
59:01
59
18:58:57
55
G037.6475-0.3821
01:54
24
4:00:54
24
29
27
19:01:25
23
G037.7584+0.1233
21:54
24
4:20:54
24
53
51
18:59:49
47
G037.9798-0.2701
22:54
24
4:21:54
24
41
39
19:01:37
35

Figure A34.

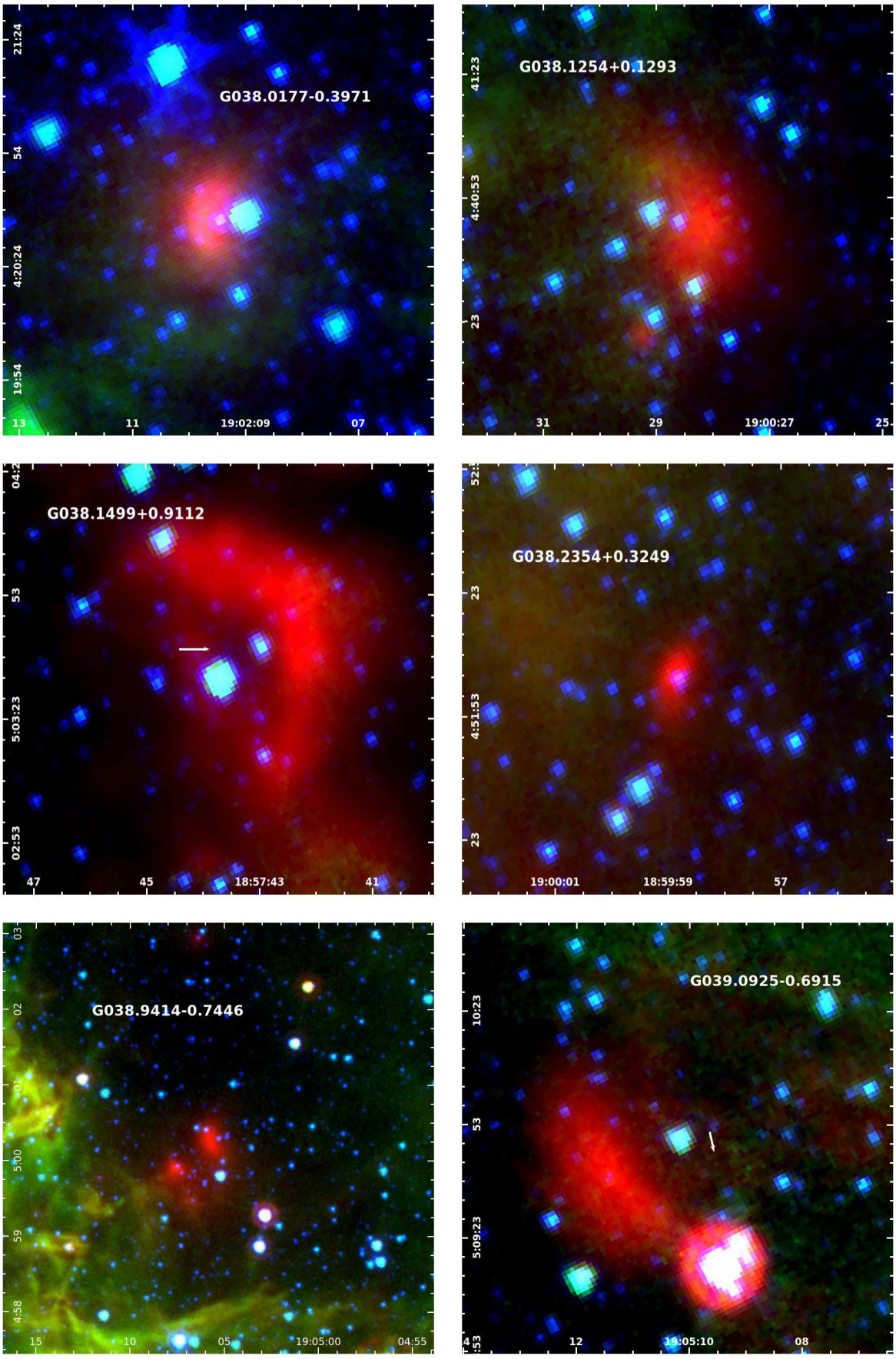
G038.0177-0.3971
21:24
54
4:20:24
19:54
13
11
19:02:09
07
G038.1254+0.1293
41:23
4:40:53
23
31
29
19:00:27
25
G038.1499+0.9112
53
5:03:23
02:53
47
45
18:57:43
41
G038.2354+0.3249
23
4:51:53
23
19:00:01
18:59:59
57
G038.9414-0.7446
03
02
01
5:00
59
4:58
15
10
05
19:05:00
04:55
G039.0925-0.6915
10:23
53
5:09:23
12
19:05:10
08

Figure A35.

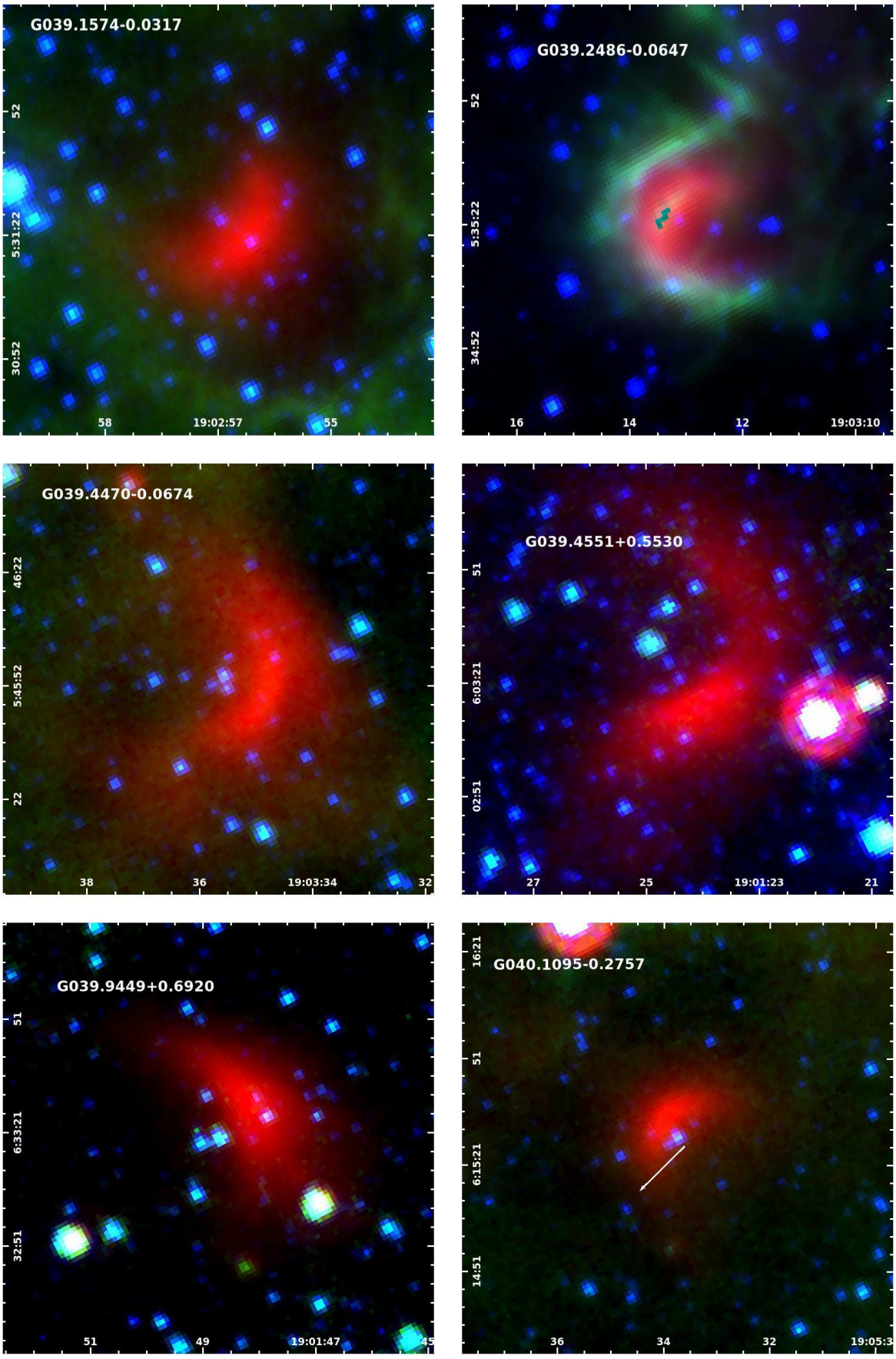
G039.1574-0.0317
52
5:31:22
30:52
58
19:02:57
55
G039.2486-0.0647
52
5:35:22
34:52
16
14
12
19:03:10
G039.4470-0.0674
46:22
5:45:52
22
38
36
19:03:34
32
G039.4551+0.5530
51
6:03:21
02:51
27
25
19:01:23
21
G039.9449+0.6920
51
6:33:21
32:51
51
49
19:01:47
45
G040.1095-0.2757
16:21
51
6:15:21
14:51
36
34
32
19:05:3

Figure A36.

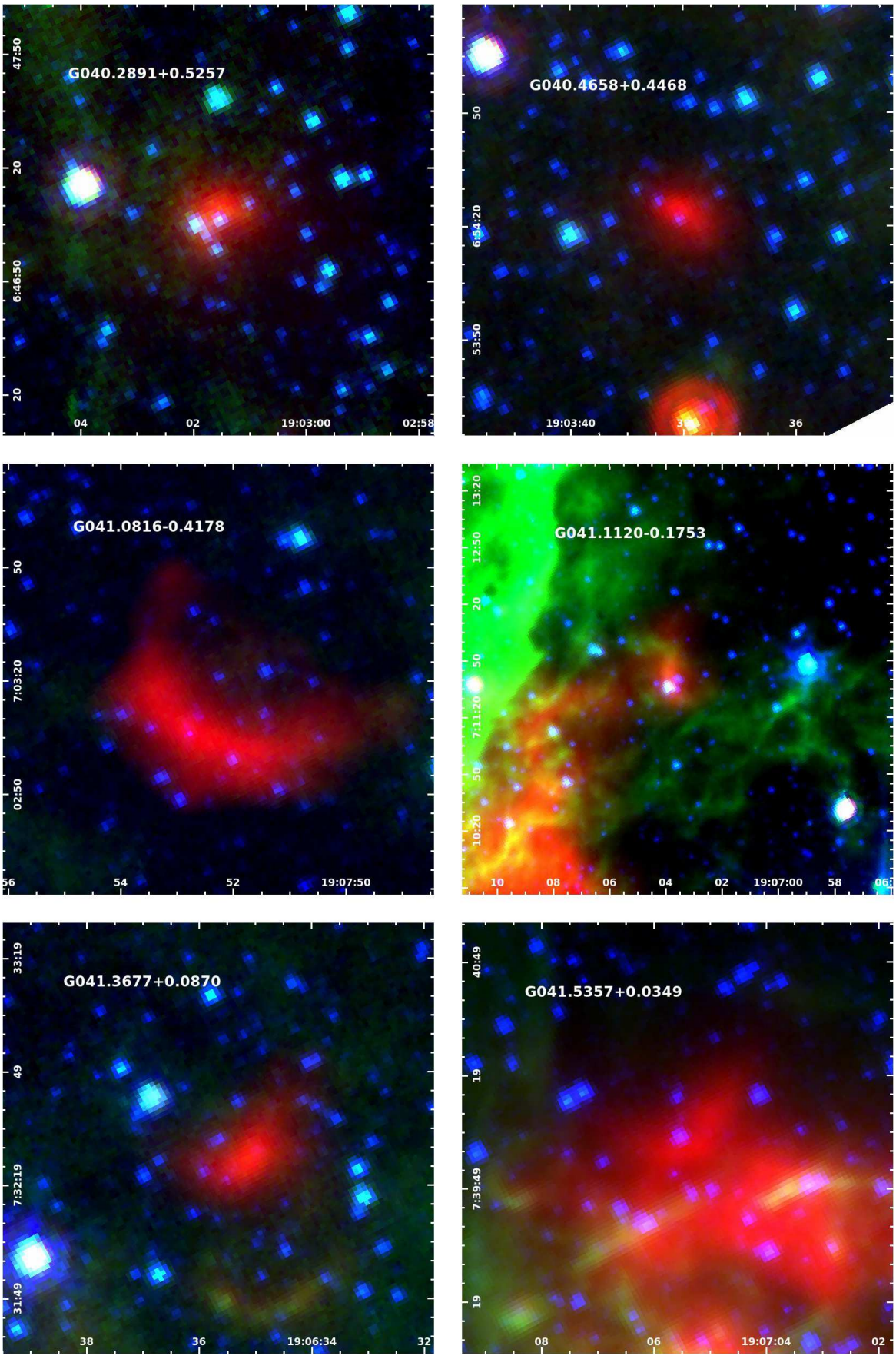
G040.2891+0.5257
47:50
20
6:46:50
20
04
02
19:03:00
02:58
G040.4658+0.4468
50
6:54:20
53:50
19:03:40
36
G041.0816-0.4178
50
7:03:20
02:50
56
54
52
19:07:50
G041.1120-0.1753
13:20
12:50
20
50
7:11:20
50
10:20
10
08
06
04
02
19:07:00
58
G041.3677+0.0870
33:19
49
7:32:19
31:49
38
36
19:06:34
32
G041.5357+0.0349
40:49
19
7:39:49
19
08
06
19:07:04
02

Figure A37.

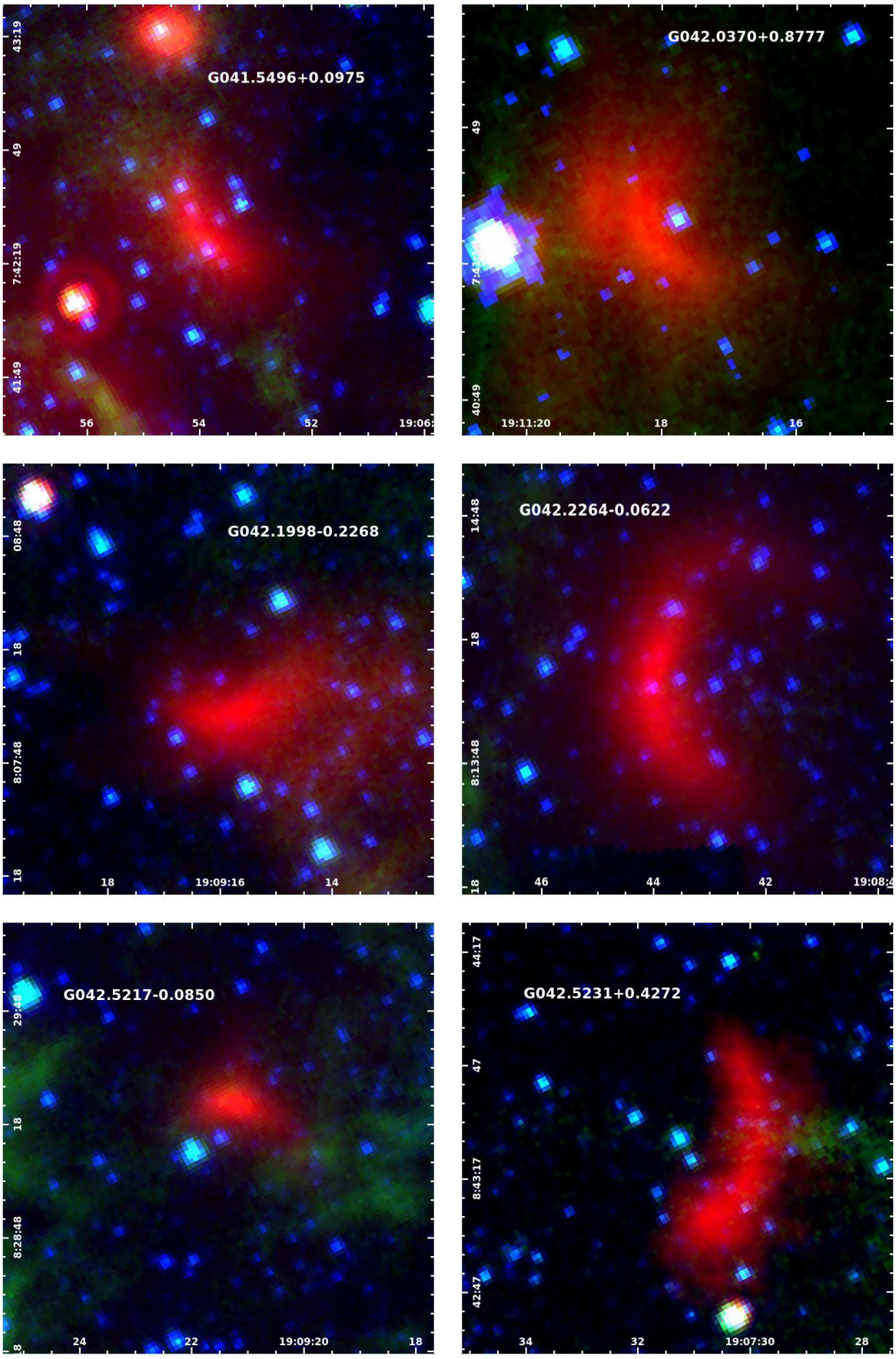
G041.5496+0.0975
43:19
49
7:42:19
41:49
56
54
52
19:06:
G042.0370+0.8777
49
40:49
19:11:20
18
16
G042.1998-0.2268
08:48
18
8:07:48
18
18
19:09:16
14
G042.2264-0.0622
14:48
18
8:13:48
18
46
44
42
19:08:4
G042.5217-0.0850
29:48
18
8:28:48
24
22
19:09:20
18
G042.5231+0.4272
44:17
47
8:43:17
42:47
34
32
19:07:30
28

Figure A38.

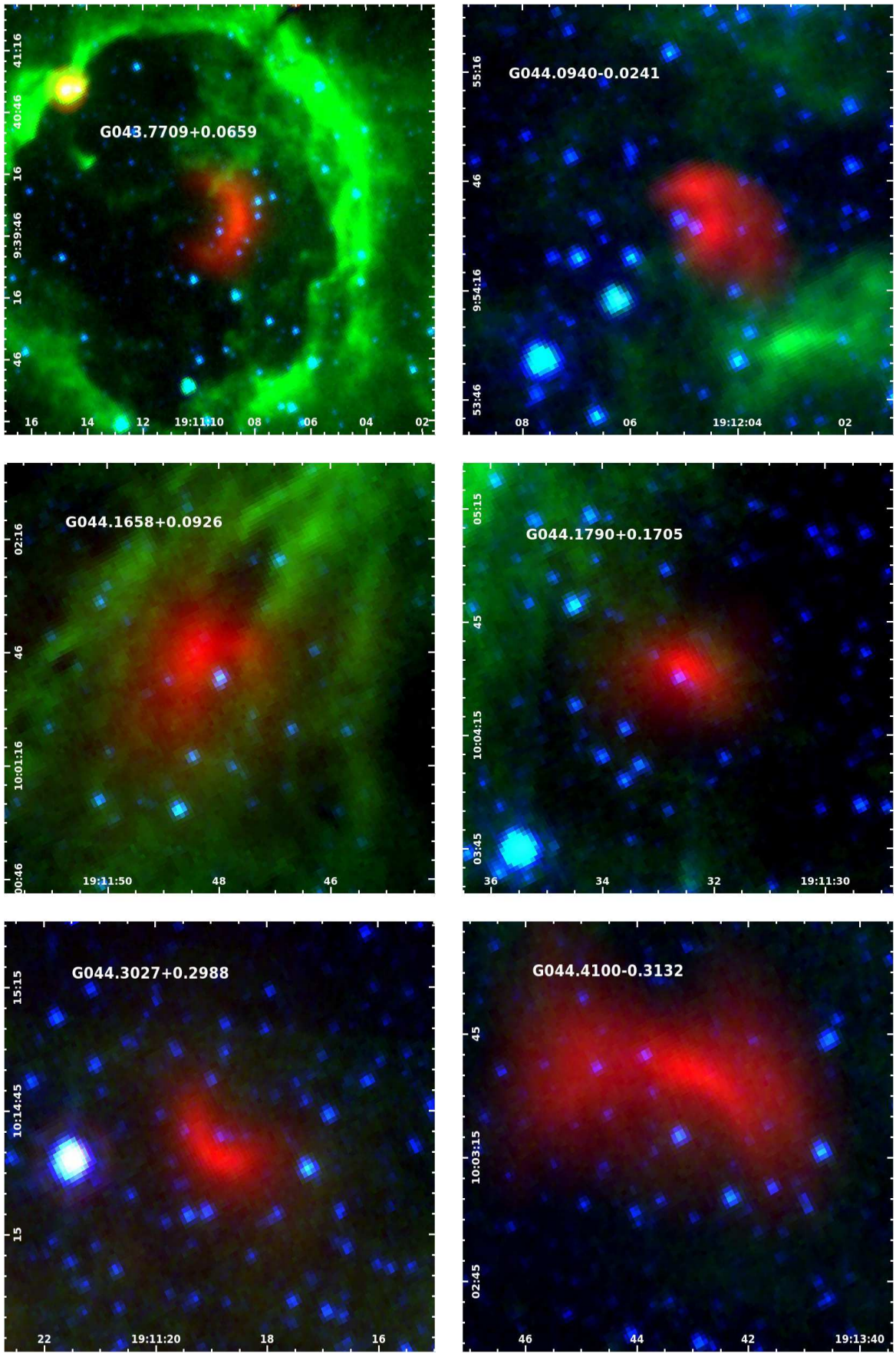
G043.7709+0.0659
G044.0940-0.0241
G044.1658+0.0926
G044.1790+0.1705
G044.3027+0.2988
G044.4100-0.3132

Figure A39.

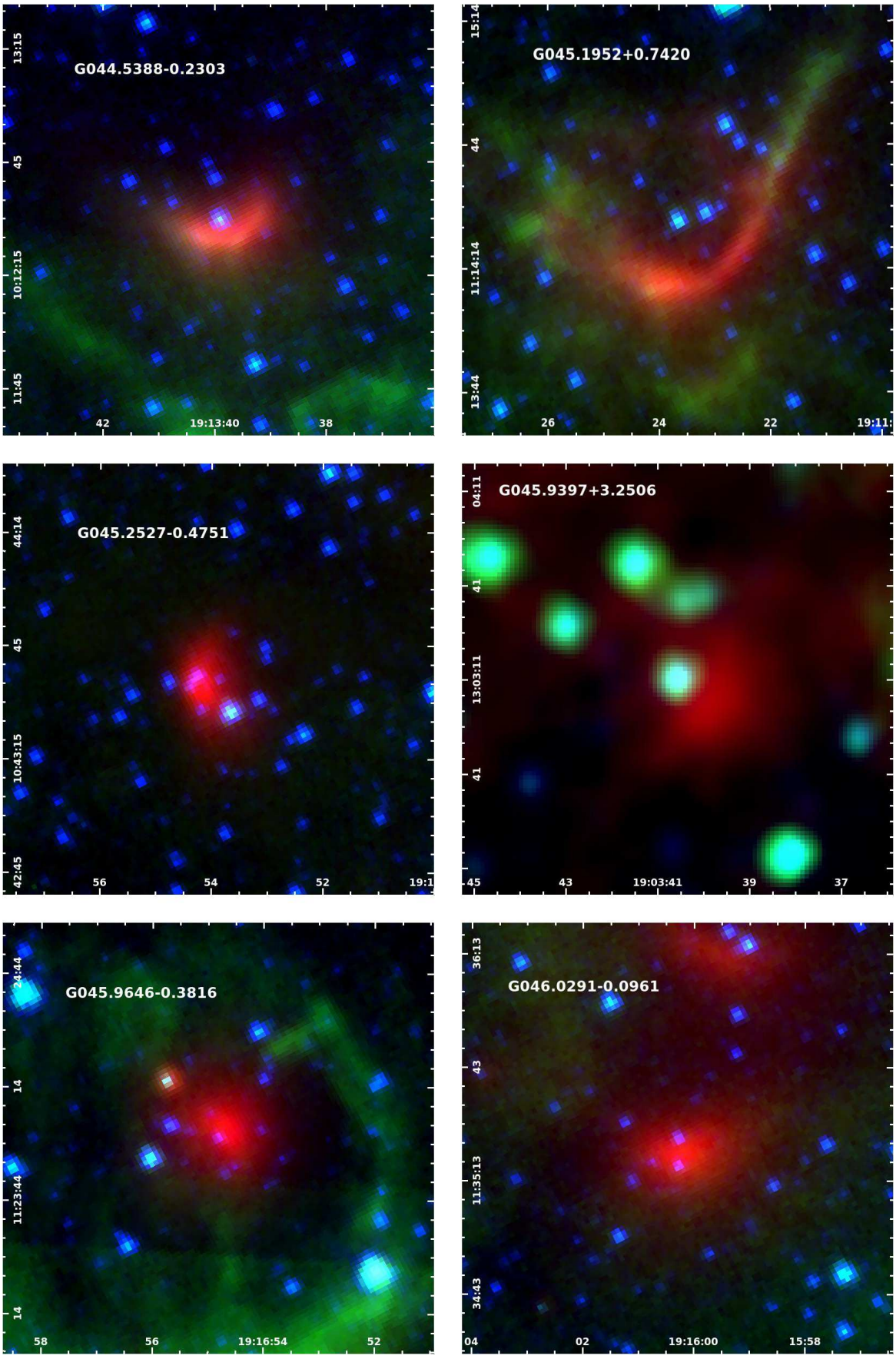
G044.5388-0.2303
13:15
45
10:12:15
11:45
42
19:13:40
38
G045.1952+0.7420
15:14
44
11:14:14
13:44
26
24
22
19:11:
G045.2527-0.4751
44:14
45
10:43:15
42:45
56
54
52
19:1
G045.9397+3.2506
04:11
41
13:03:11
41
45
43
19:03:41
39
37
G045.9646-0.3816
24:44
14
11:23:44
14
58
56
19:16:54
52
G046.0291-0.0961
36:13
43
11:35:13
34:43
04
02
19:16:00
15:58

Figure A40.

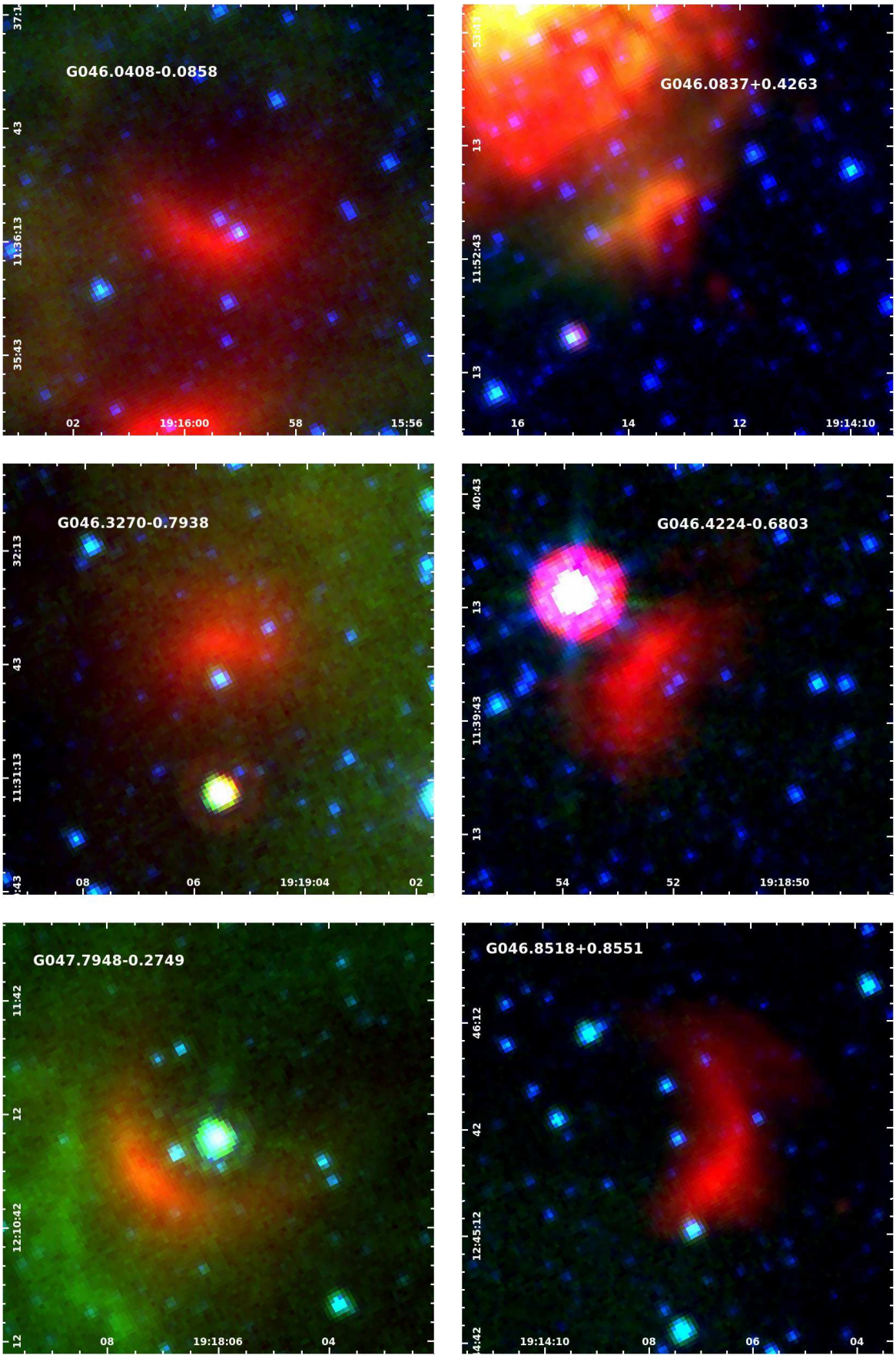
G046.0408-0.0858
37:1
43
11:36:13
35:43
02
19:16:00
58
15:56
G046.0837+0.4263
53:43
13
11:52:43
13
16
14
12
19:14:10
G046.3270-0.7938
32:13
43
11:31:13
:43
08
06
19:19:04
02
G046.4224-0.6803
40:43
13
11:39:43
13
54
52
19:18:50
G047.7948-0.2749
11:42
12
12:10:42
12
08
19:18:06
04
G046.8518+0.8551
46:12
42
12:45:12
4:42
19:14:10
08
06
04

Figure A41.

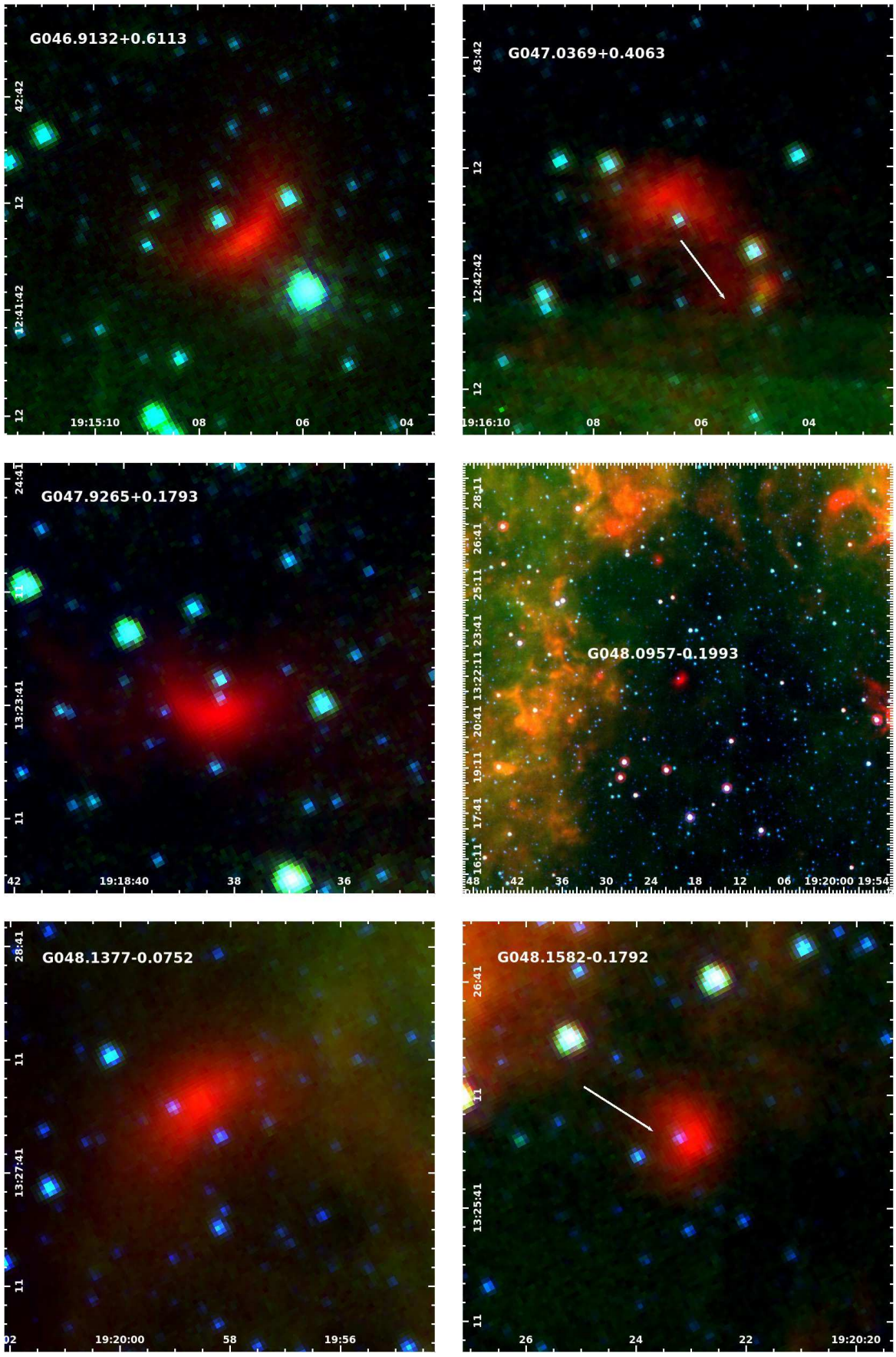
G046.9132+0.6113
42:42
12
12:41:42
12
19:15:10
08
06
04
G047.0369+0.4063
43:42
12
12:42:42
12
19:16:10
08
06
04
G047.9265+0.1793
24:41
11
13:23:41
11
42
19:18:40
38
36
G048.0957-0.1993
28:11
26:41
25:11
23:41
13:22:11
20:41
19:11
17:41
16:11
48
42
36
30
24
18
12
06
19:20:00
19:54
G048.1377-0.0752
28:41
11
13:27:41
11
02
19:20:00
58
19:56
G048.1582-0.1792
26:41
11
13:25:41
11
26
24
22
19:20:20

Figure A42.

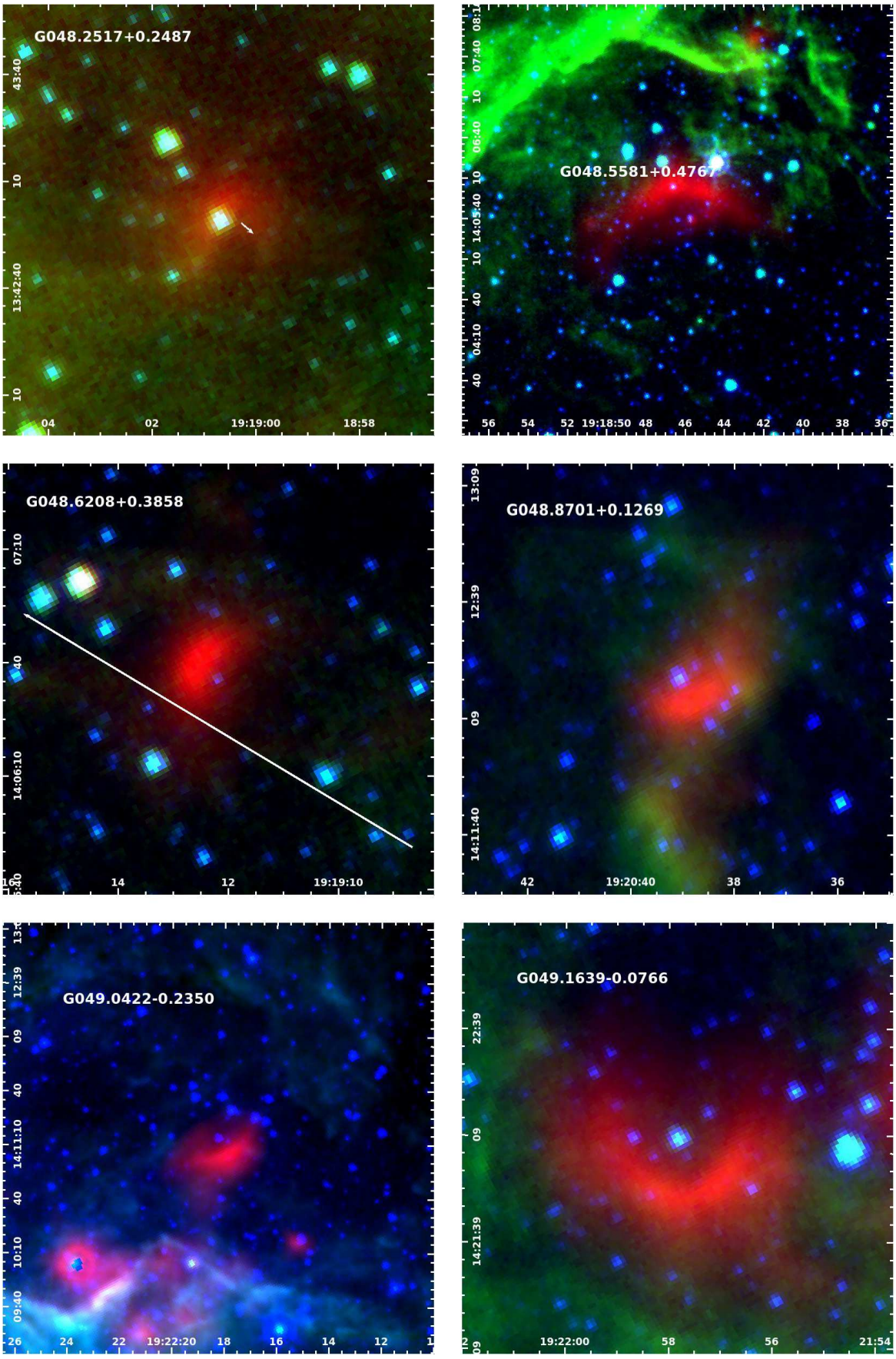
G048.2517+0.2487
G048.5581+0.4767
G048.6208+0.3858
G048.8701+0.1269
G049.0422-0.2350
G049.1639-0.0766

Figure A43.

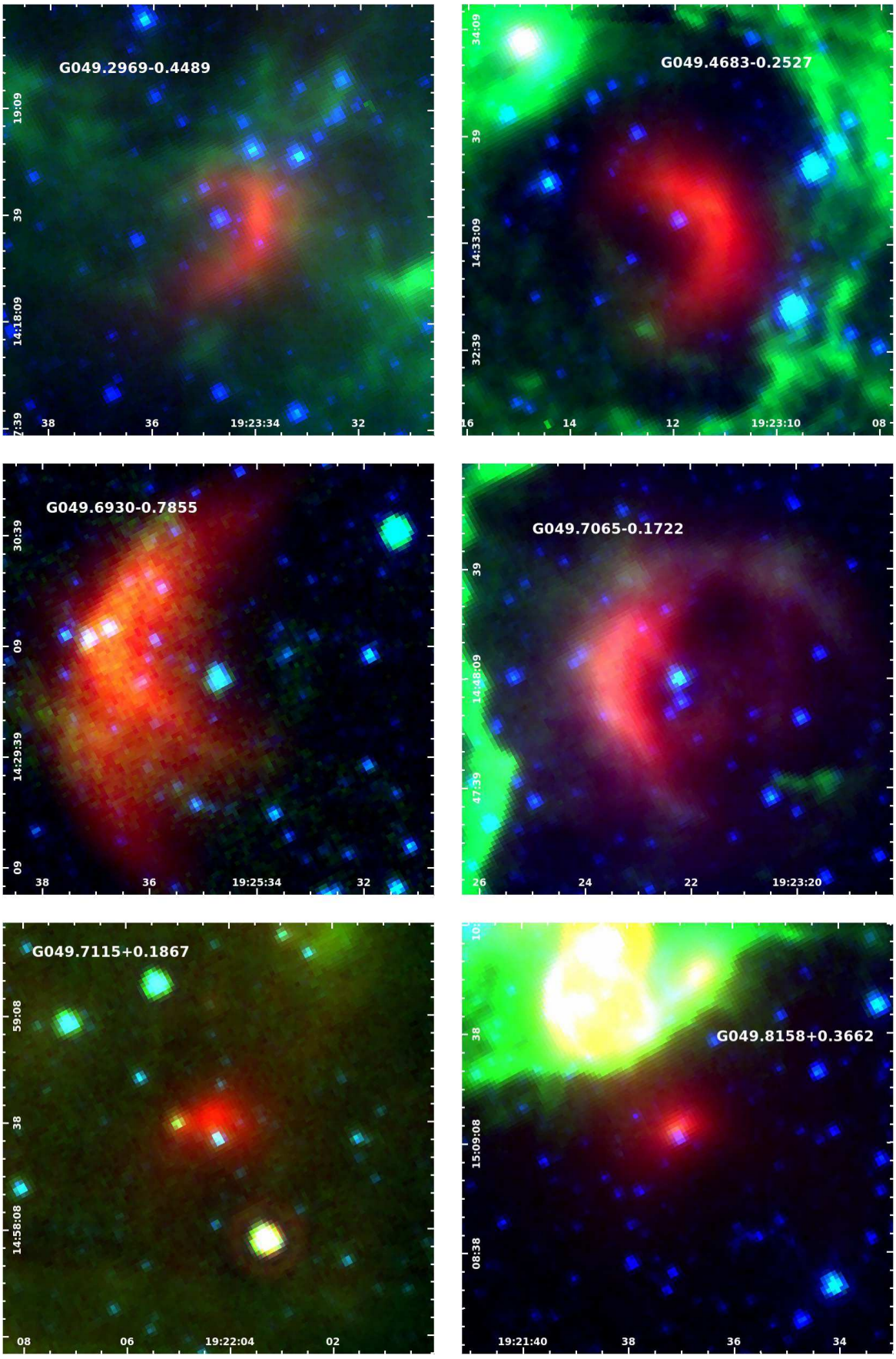
G049.2969-0.4489
19:09
39
14:18:09
7:39
38
36
19:23:34
32
G049.4683-0.2527
34:09
39
14:33:09
32:39
16
14
12
19:23:10
08
G049.6930-0.7855
30:39
09
14:29:39
09
38
36
19:25:34
32
G049.7065-0.1722
39
14:48:09
47:39
26
24
22
19:23:20
G049.7115+0.1867
59:08
38
14:58:08
08
06
19:22:04
02
G049.8158+0.3662
38
15:09:08
08:38
19:21:40
38
36
34

Figure A44.

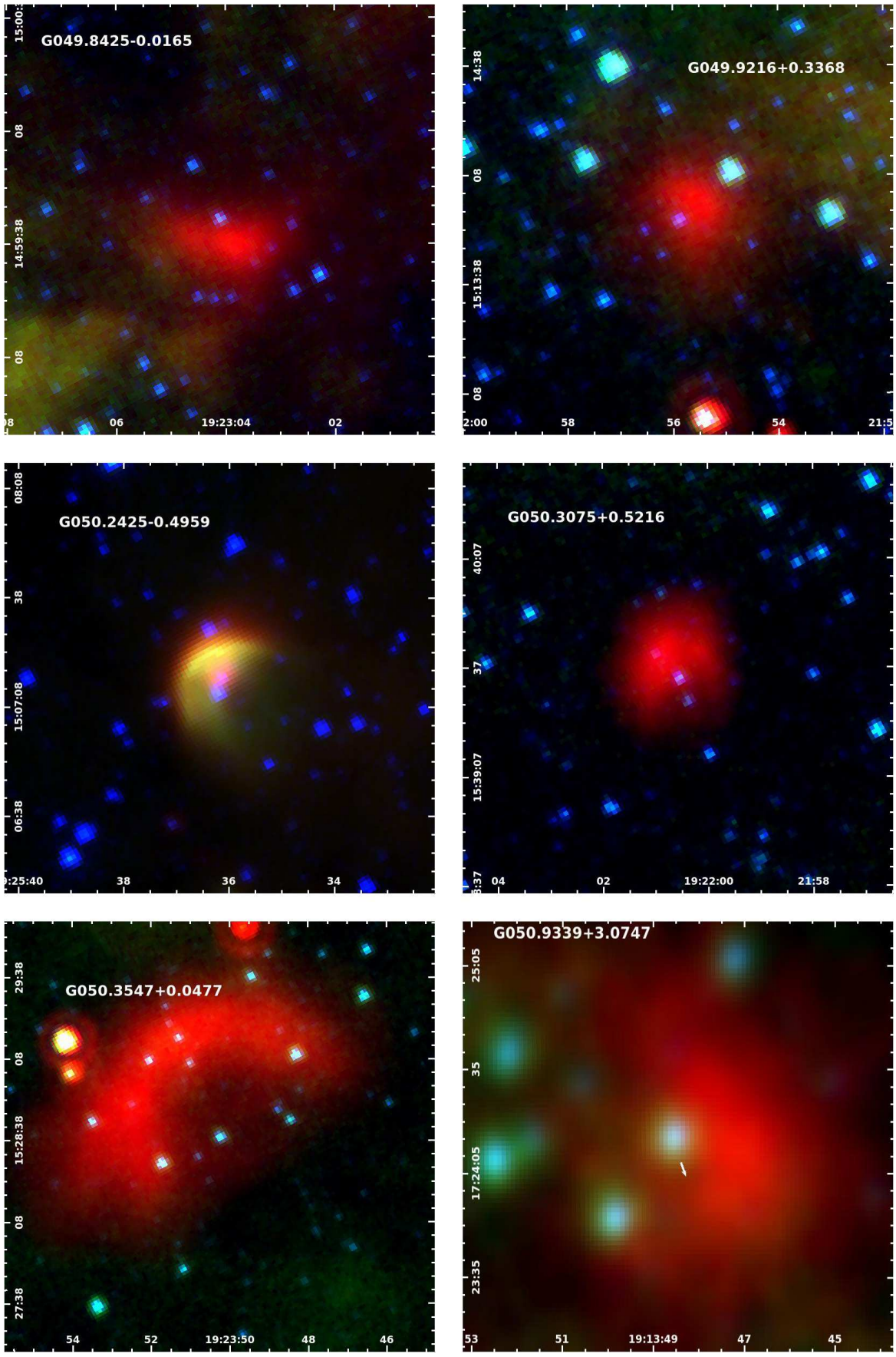
G049.8425-0.0165
G049.9216+0.3368
G050.2425-0.4959
G050.3075+0.5216
G050.3547+0.0477
G050.9339+3.0747

Figure A45.

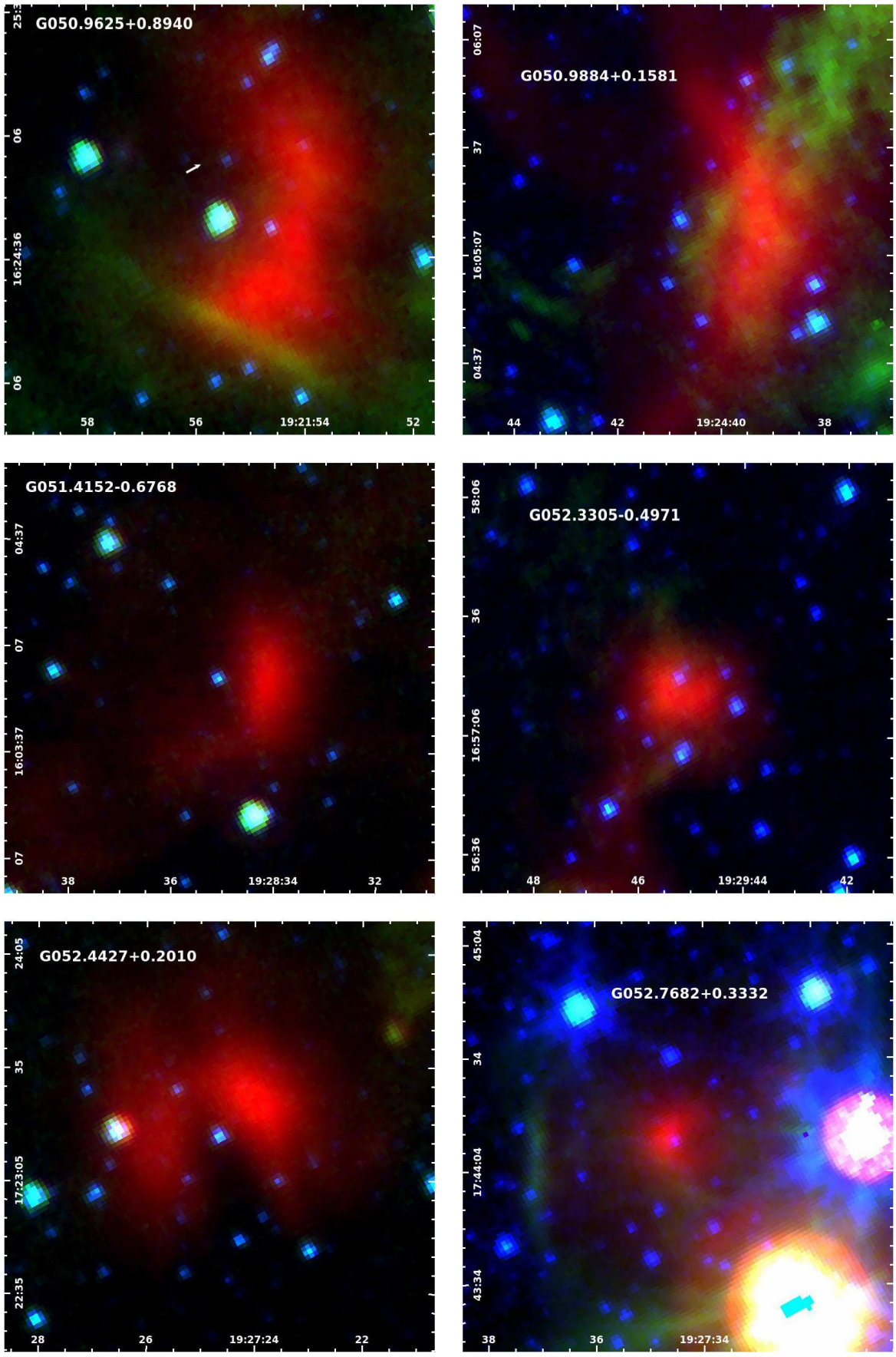
G050.9625+0.8940
25:3
06
16:24:36
06
58
56
19:21:54
52
G050.9884+0.1581
06:07
37
16:05:07
04:37
44
42
19:24:40
38
G051.4152-0.6768
04:37
07
16:03:37
07
38
36
19:28:34
32
G052.3305-0.4971
58:06
36
16:57:06
56:36
48
46
19:29:44
42
G052.4427+0.2010
24:05
35
17:23:05
22:35
28
26
19:27:24
22
G052.7682+0.3332
45:04
34
17:44:04
43:34
38
36
19:27:34

Figure A46.

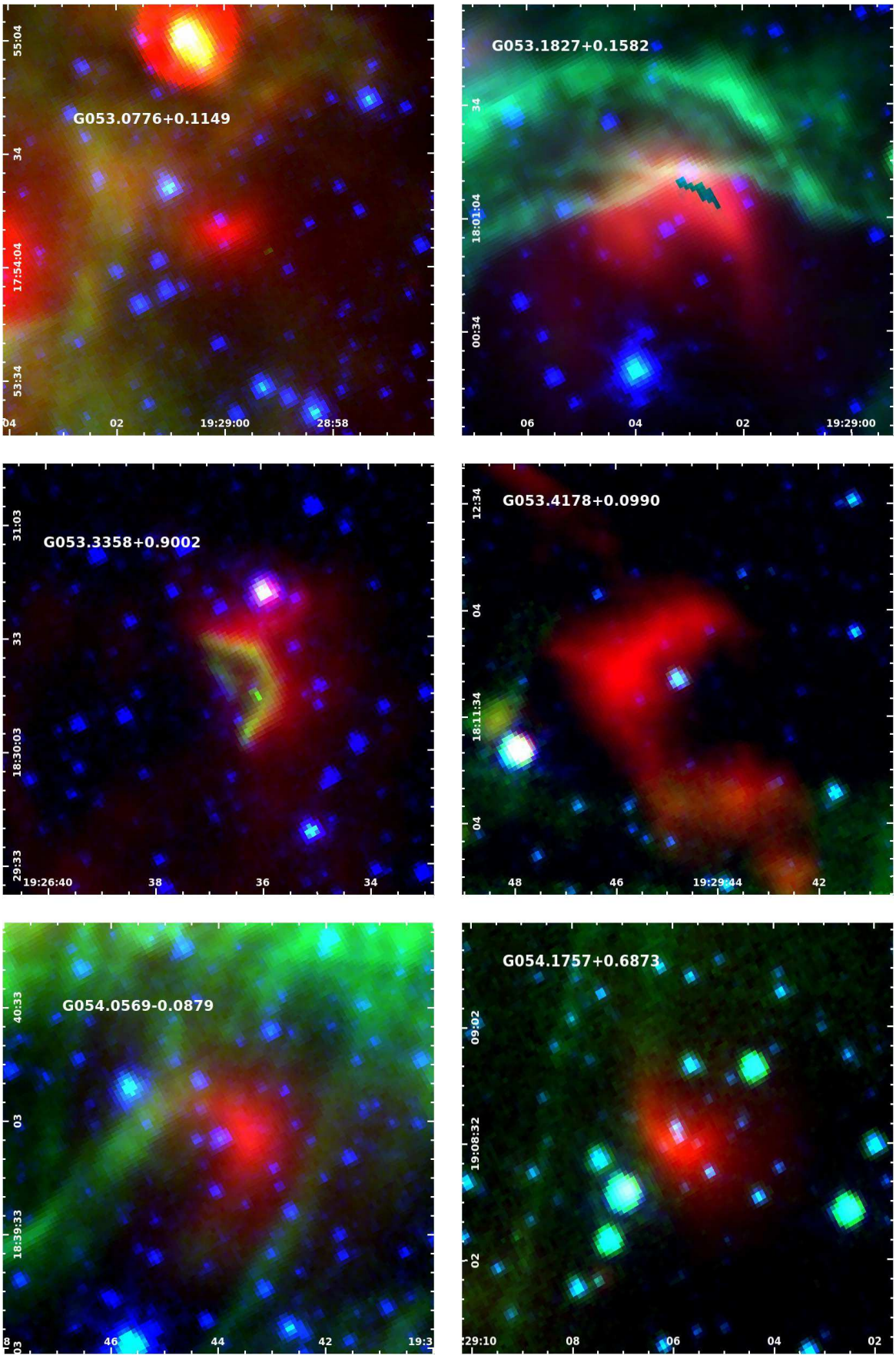
G053.0776+0.1149
55:04
34
17:54:04
53:34
04
02
19:29:00
28:58
G053.1827+0.1582
34
18:01:04
00:34
06
04
02
19:29:00
G053.3358+0.9002
31:03
33
18:30:03
29:33
19:26:40
38
36
34
G053.4178+0.0990
12:34
04
18:11:34
04
48
46
19:29:44
42
G054.0569-0.0879
40:33
03
18:39:33
46
44
42
G054.1757+0.6873
09:02
19:08:32
02
08
06
04
02

Figure A47.

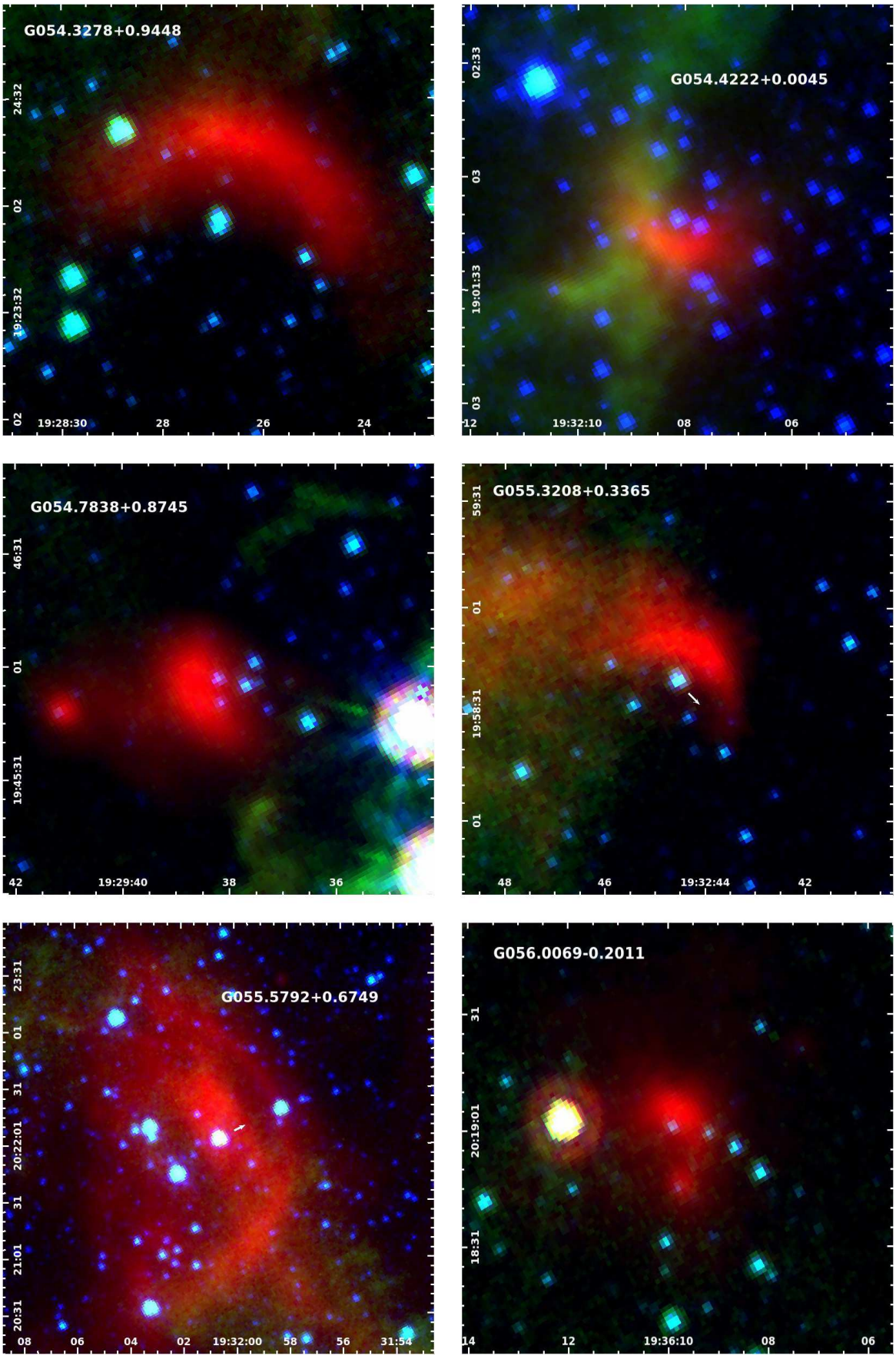
G054.3278+0.9448
24:32
02
19:23:32
02
19:28:30
28
26
24
G054.4222+0.0045
02:33
03
19:01:33
03
12
19:32:10
08
06
G054.7838+0.8745
46:31
01
19:45:31
42
19:29:40
38
36
G055.3208+0.3365
59:31
01
19:58:31
01
48
46
19:32:44
42
G055.5792+0.6749
23:31
01
31
20:22:01
31
21:01
20:31
08
06
04
02
19:32:00
58
56
31:54
G056.0069-0.2011
31
20:19:01
18:31
14
12
19:36:10
08
06

Figure A48.

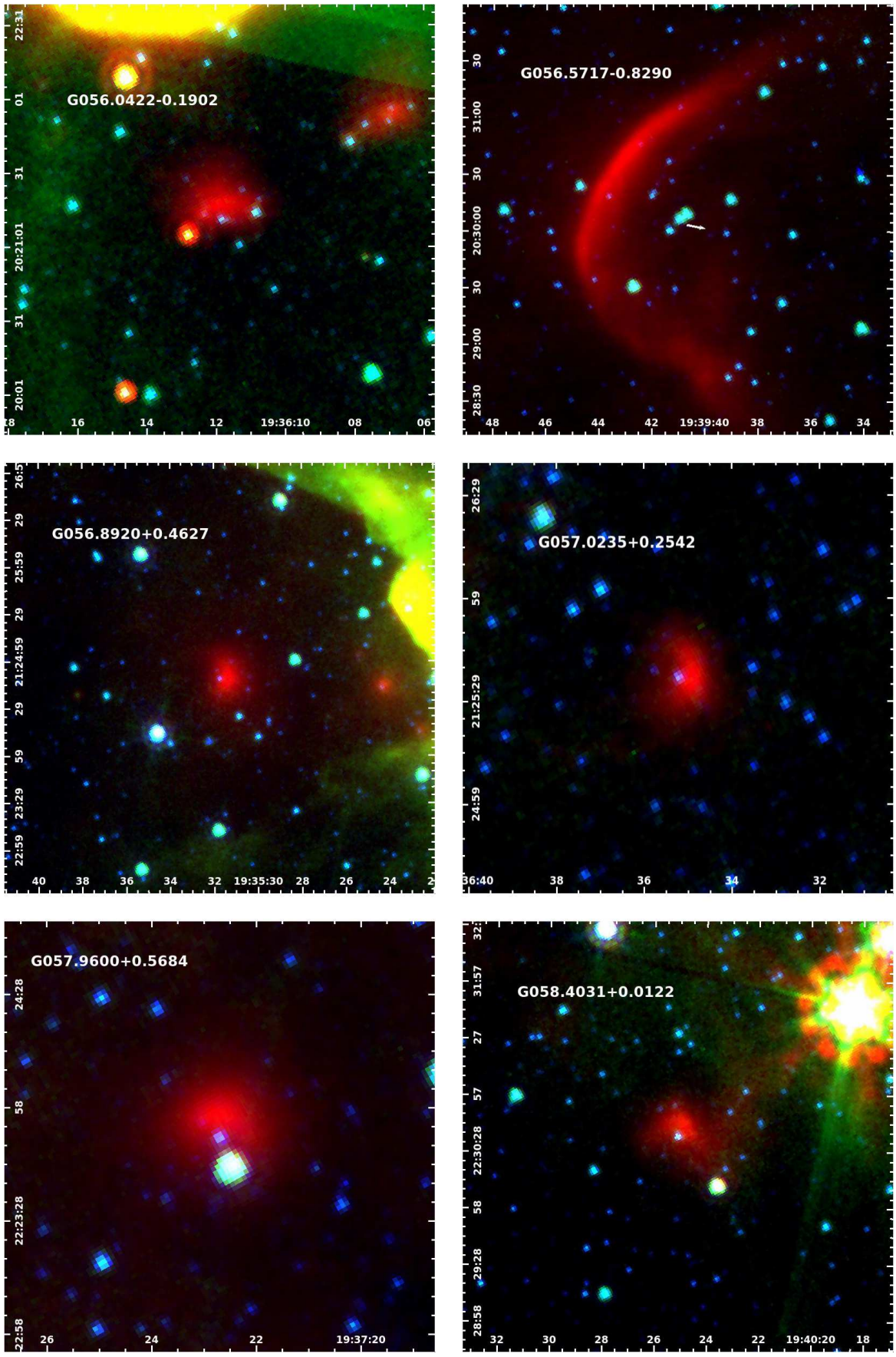
G056.0422-0.1902
G056.5717-0.8290
G056.8920+0.4627
G057.0235+0.2542
G057.9600+0.5684
G058.4031+0.0122

Figure A49.

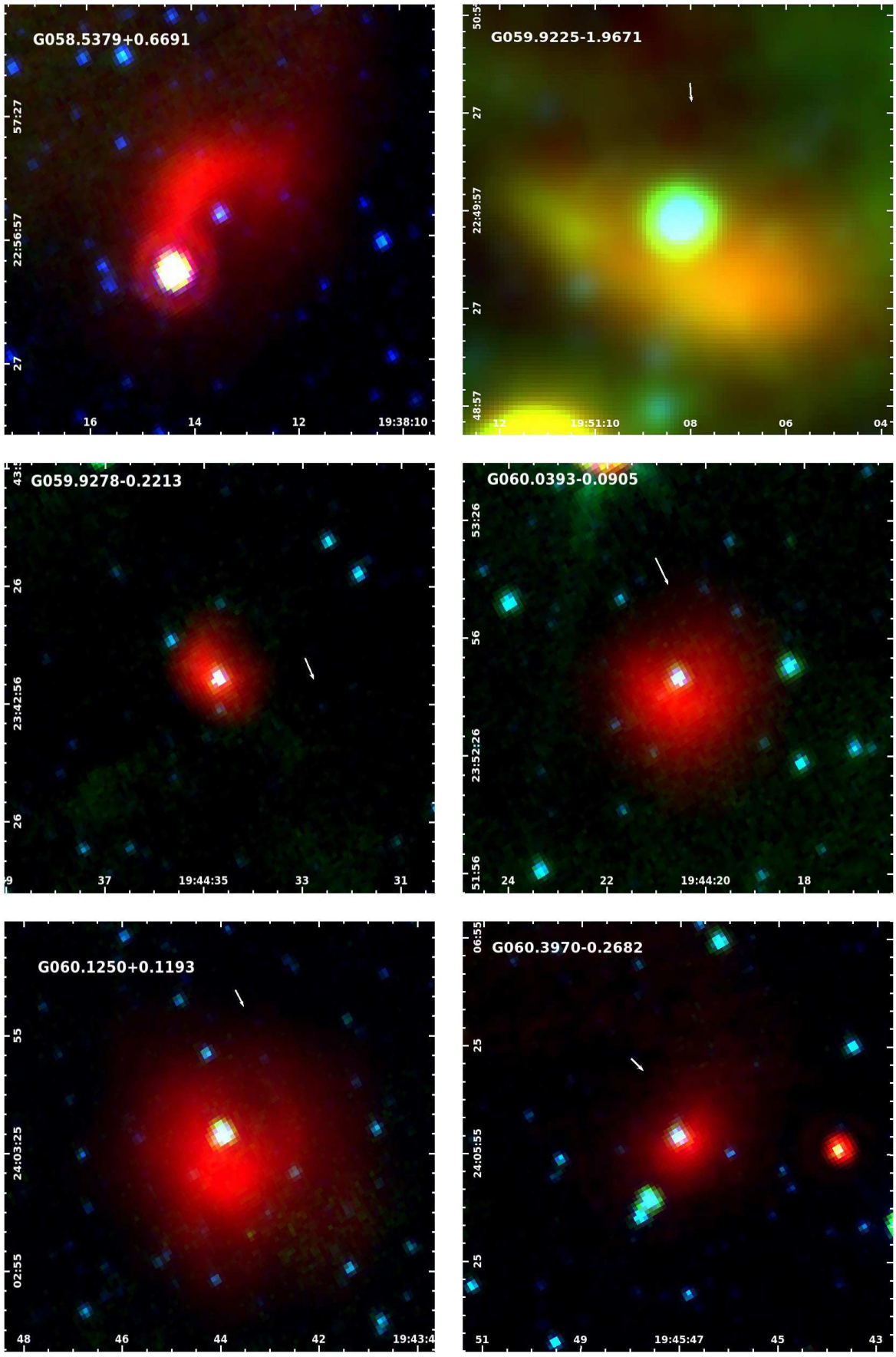
G058.5379+0.6691
57:27
22:56:57
27
16
14
12
19:38:10
G059.9225-1.9671
50:5
27
22:49:57
27
48:57
12
19:51:10
08
06
04
G059.9278-0.2213
43:
26
23:42:56
26
9
37
19:44:35
33
31
G060.0393-0.0905
53:26
56
23:52:26
51:56
24
22
19:44:20
18
G060.1250+0.1193
55
24:03:25
02:55
48
46
44
42
19:43:4
G060.3970-0.2682
06:55
25
24:05:55
25
51
49
19:45:47
45
43

Figure A50.

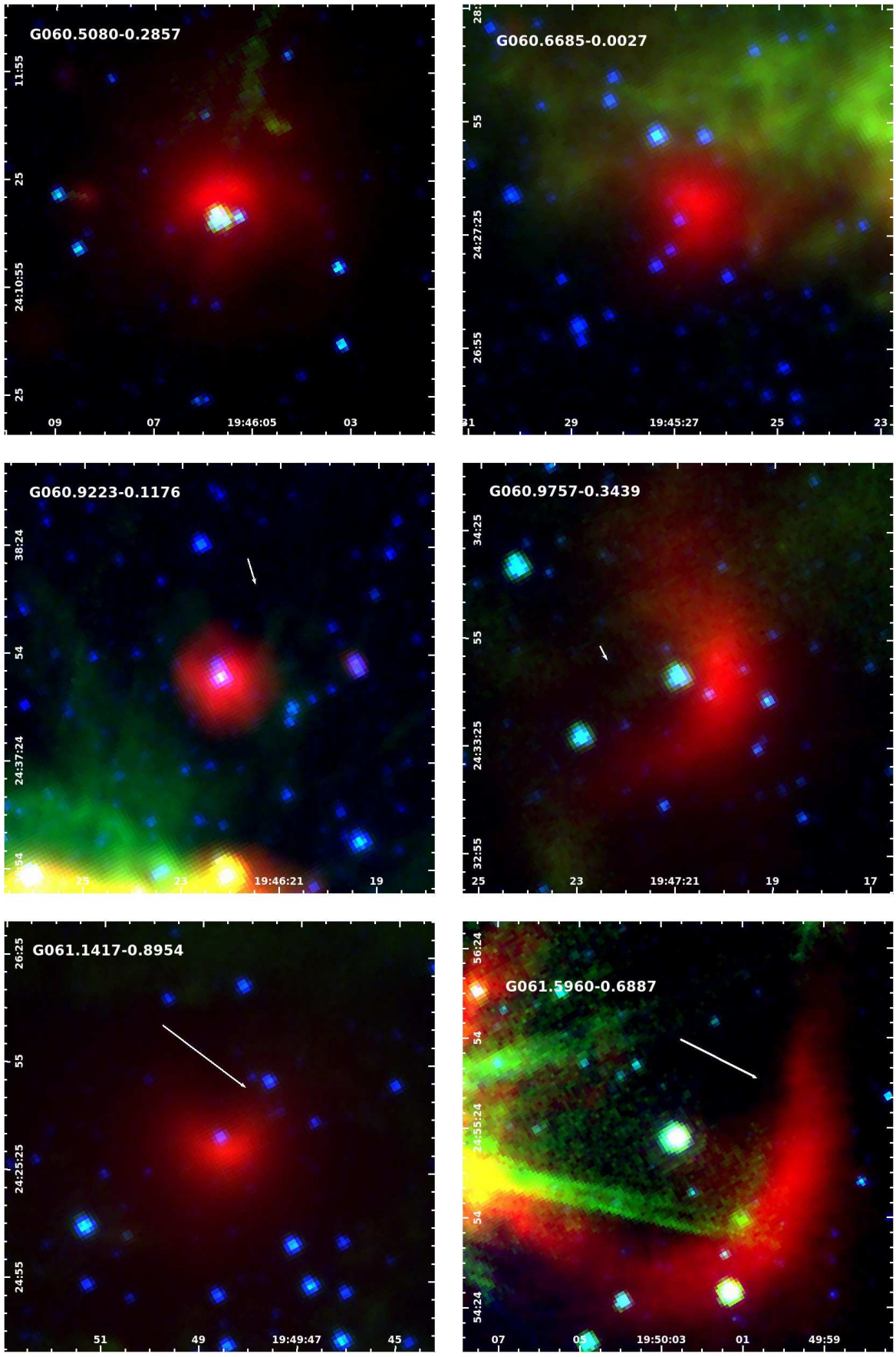
G060.5080-0.2857
11:55
25
24:10:55
25
09
07
19:46:05
03
G060.6685-0.0027
55
24:27:25
26:55
29
19:45:27
25
23
G060.9223-0.1176
38:24
54
24:37:24
25
23
19:46:21
19
G060.9757-0.3439
34:25
55
24:33:25
32:55
25
23
19:47:21
19
17
G061.1417-0.8954
26:25
55
24:25:25
24:55
51
49
19:49:47
45
G061.5960-0.6887
56:24
54
24:55:24
54:24
07
05
19:50:03
01
49:59

Figure A51.

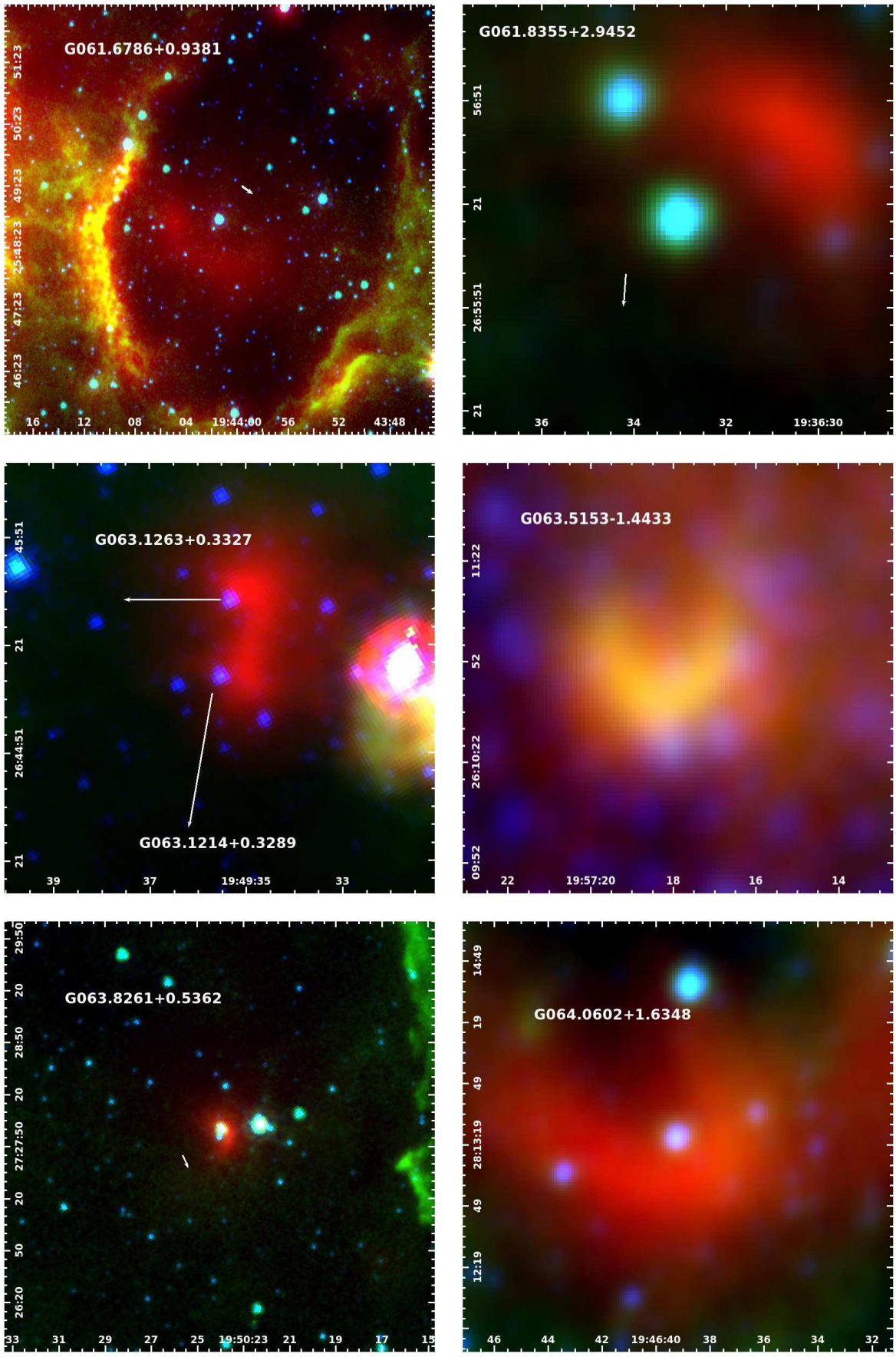
G061.6786+0.9381
G061.8355+2.9452
G063.1263+0.3327
G063.1214+0.3289
G063.5153-1.4433
G063.8261+0.5362
G064.0602+1.6348

Figure A52.

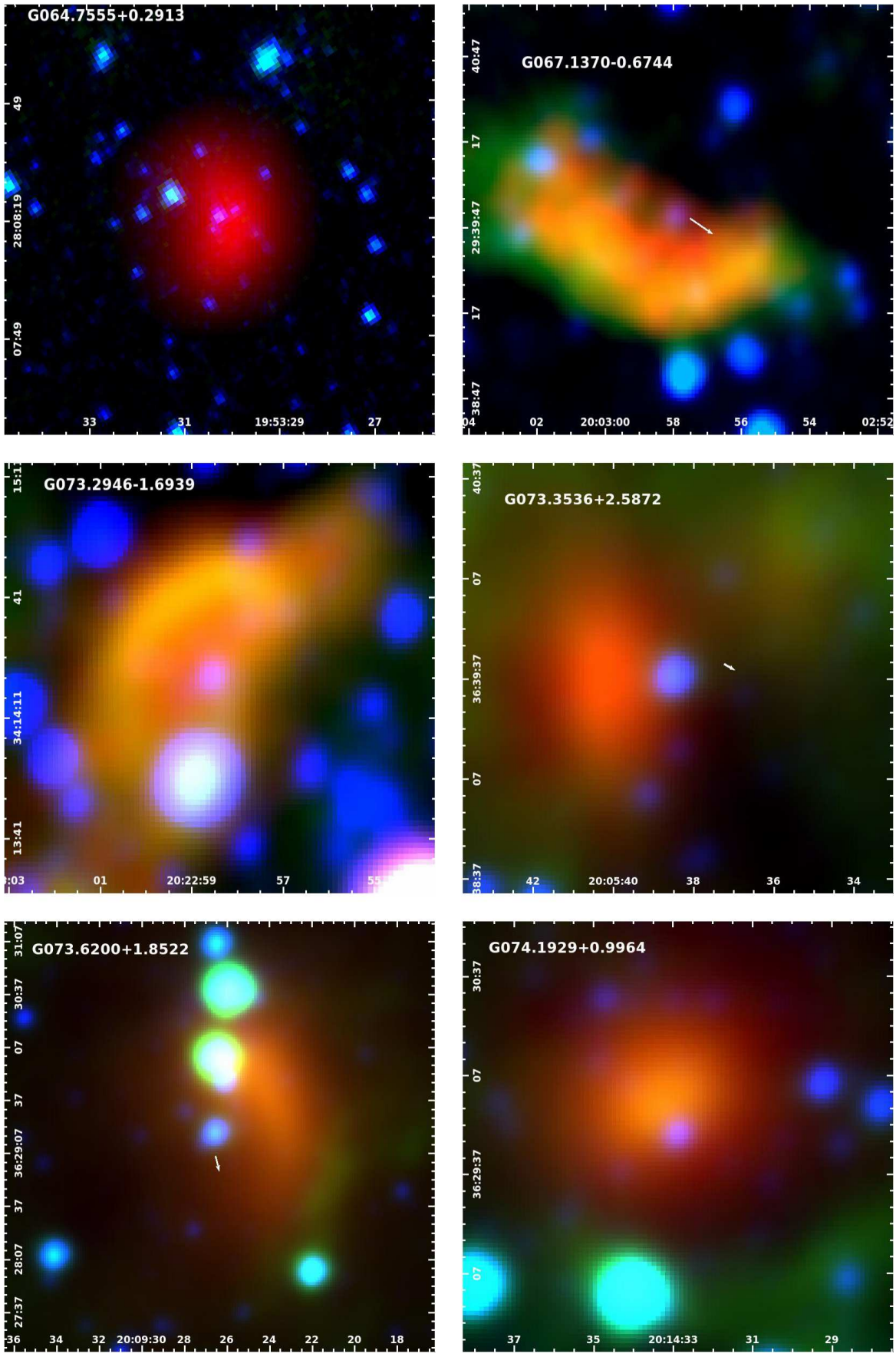
G064.7555+0.2913
49
28:08:19
07:49
33
31
19:53:29
27
G067.1370-0.6744
40:47
17
29:39:47
17
38:47
04
02
20:03:00
58
56
54
02:52
G073.2946-1.6939
15:1
41
34:14:11
13:41
:03
01
20:22:59
57
55
G073.3536+2.5872
40:37
07
36:39:37
07
38:37
42
20:05:40
38
36
34
G073.6200+1.8522
31:07
30:37
07
37
36:29:07
37
28:07
27:37
36
34
32
20:09:30
28
26
24
22
20
18
G074.1929+0.9964
30:37
07
36:29:37
07
37
35
20:14:33
31
29

Figure A53.

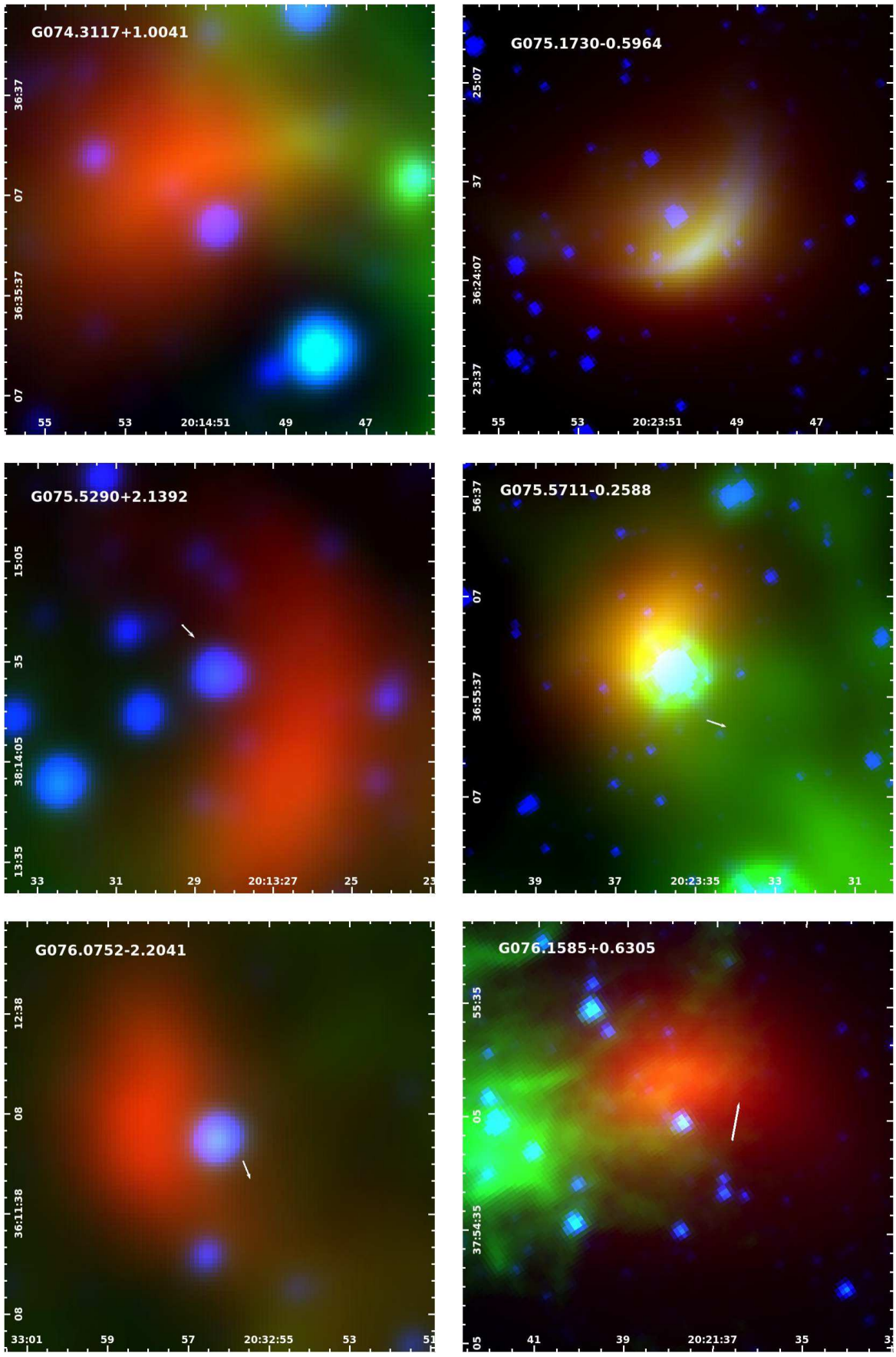
G074.3117+1.0041
36:37
07
36:35:37
07
55
53
20:14:51
49
47
G075.1730-0.5964
25:07
37
36:24:07
23:37
55
53
20:23:51
49
47
G075.5290+2.1392
15:05
35
38:14:05
13:35
33
31
29
20:13:27
25
G075.5711-0.2588
56:37
07
36:55:37
07
39
37
20:23:35
33
31
G076.0752-2.2041
12:38
08
36:11:38
08
33:01
59
57
20:32:55
53
G076.1585+0.6305
55:35
05
37:54:35
05
41
39
20:21:37
35

Figure A54.

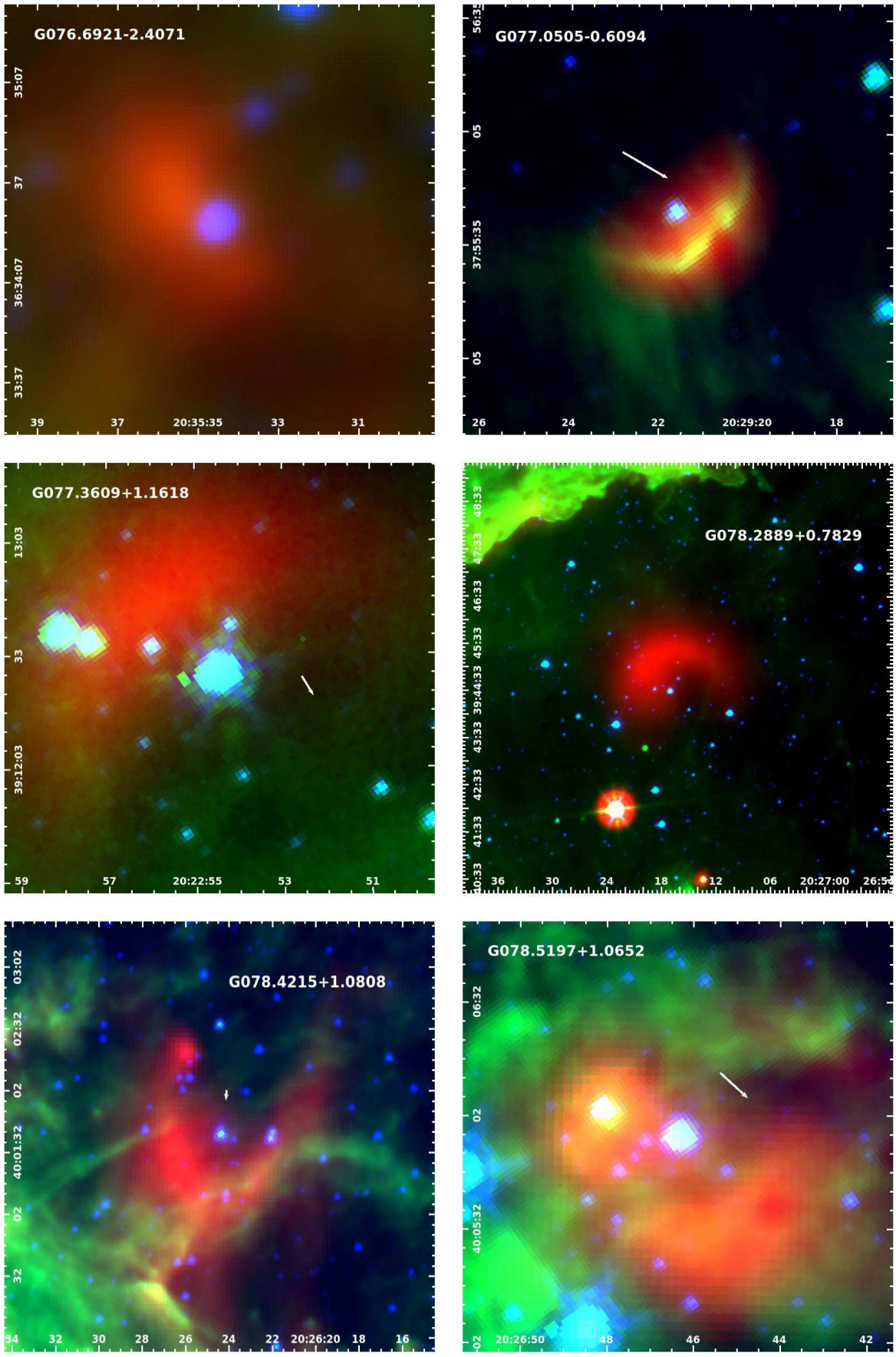
G076.6921-2.4071
35:07
37
36:34:07
33:37
39
37
20:35:35
33
31
G077.0505-0.6094
56:35
05
37:55:35
05
26
24
22
20:29:20
18
G077.3609+1.1618
13:03
33
39:12:03
59
57
20:22:55
53
51
G078.2889+0.7829
48:33
47:33
46:33
45:33
39:44:33
43:33
42:33
41:33
40:33
36
30
24
18
12
06
20:27:00
G078.4215+1.0808
03:02
02:32
02
40:01:32
02
32
34
32
30
28
26
24
22
20:26:20
18
16
G078.5197+1.0652
06:32
02
40:05:32
02
20:26:50
48
46
44
42

Figure A55.

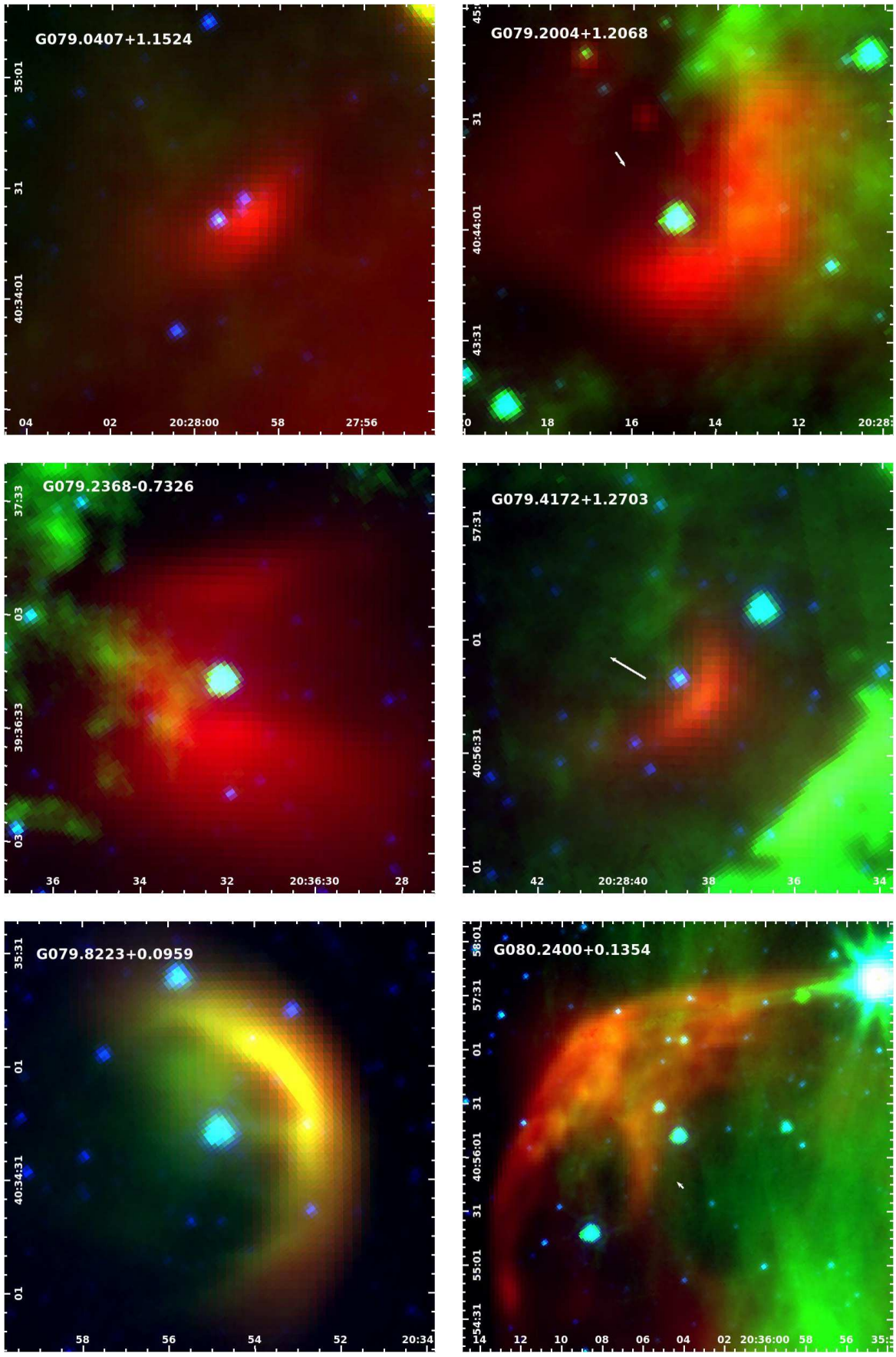
G079.0407+1.1524
35:01
31
40:34:01
04
02
20:28:00
58
27:56
G079.2004+1.2068
31
40:44:01
43:31
18
16
14
12
G079.2368-0.7326
37:33
03
39:36:33
03
36
34
32
20:36:30
28
G079.4172+1.2703
57:31
01
40:56:31
01
42
20:28:40
38
36
34
G079.8223+0.0959
35:31
01
40:34:31
01
58
56
54
52
20:34
G080.2400+0.1354
58:01
57:31
01
31
40:56:01
31
55:01
54:31
14
12
10
08
06
04
02
20:36:00
58
56

Figure A56.

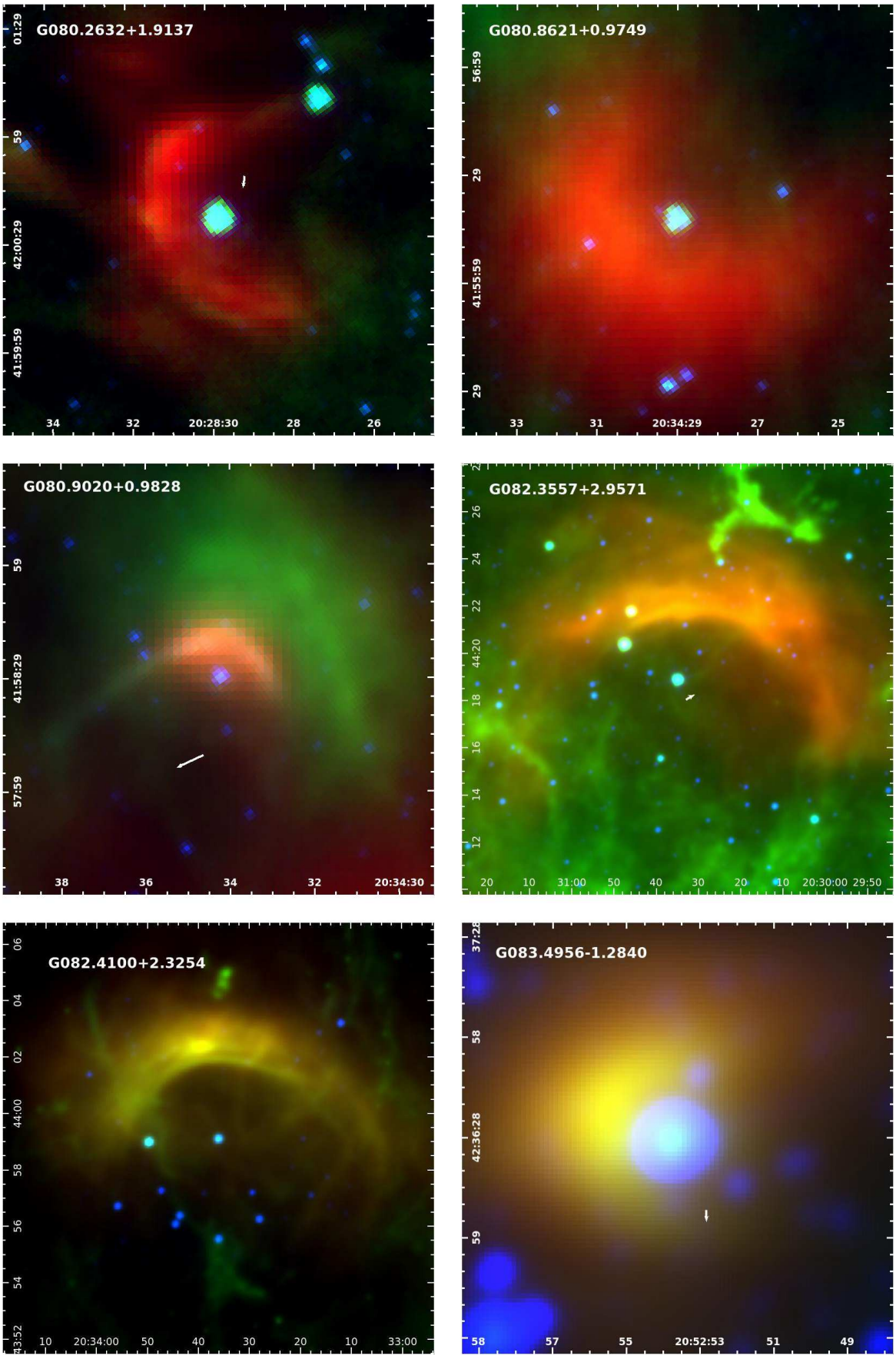
G080.2632+1.9137
01:29
59
42:00:29
41:59:59
34
32
20:28:30
28
26
G080.8621+0.9749
56:59
29
41:55:59
29
33
31
20:34:29
27
25
G080.9020+0.9828
59
41:58:29
57:59
38
36
34
32
20:34:30
G082.3557+2.9571
26
24
22
44:20
18
16
14
12
20
10
31:00
50
40
30
20
10
20:30:00
29:50
G082.4100+2.3254
06
04
02
44:00
58
56
54
43:52
10
20:34:00
50
40
30
20
10
33:00
G083.4956-1.2840
37:28
58
42:36:28
59
58
57
55
20:52:53
51
49

Figure A57.

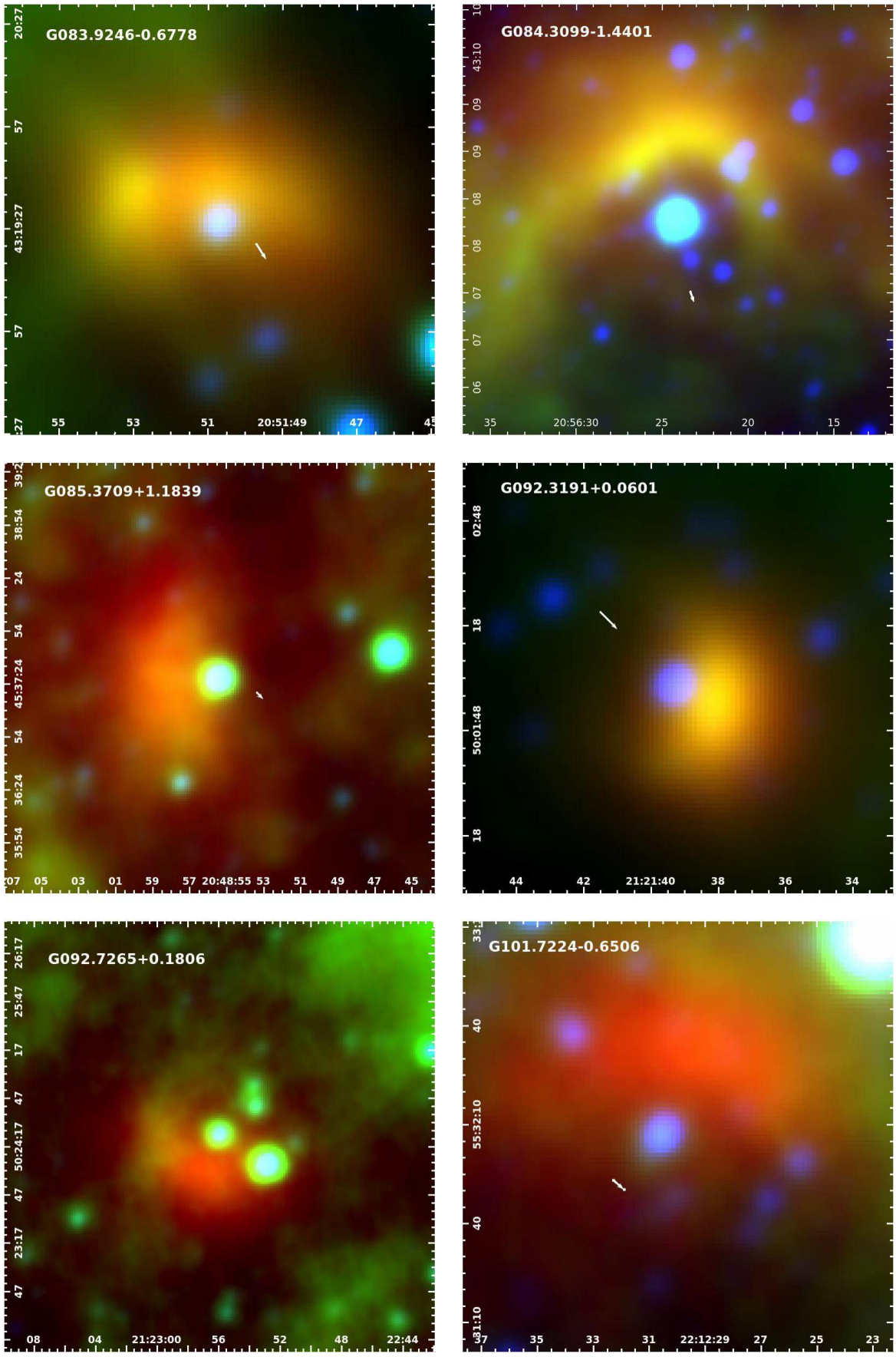
G083.9246-0.6778
G084.3099-1.4401
G085.3709+1.1839
G092.3191+0.0601
G092.7265+0.1806
G101.7224-0.6506

Figure A58.

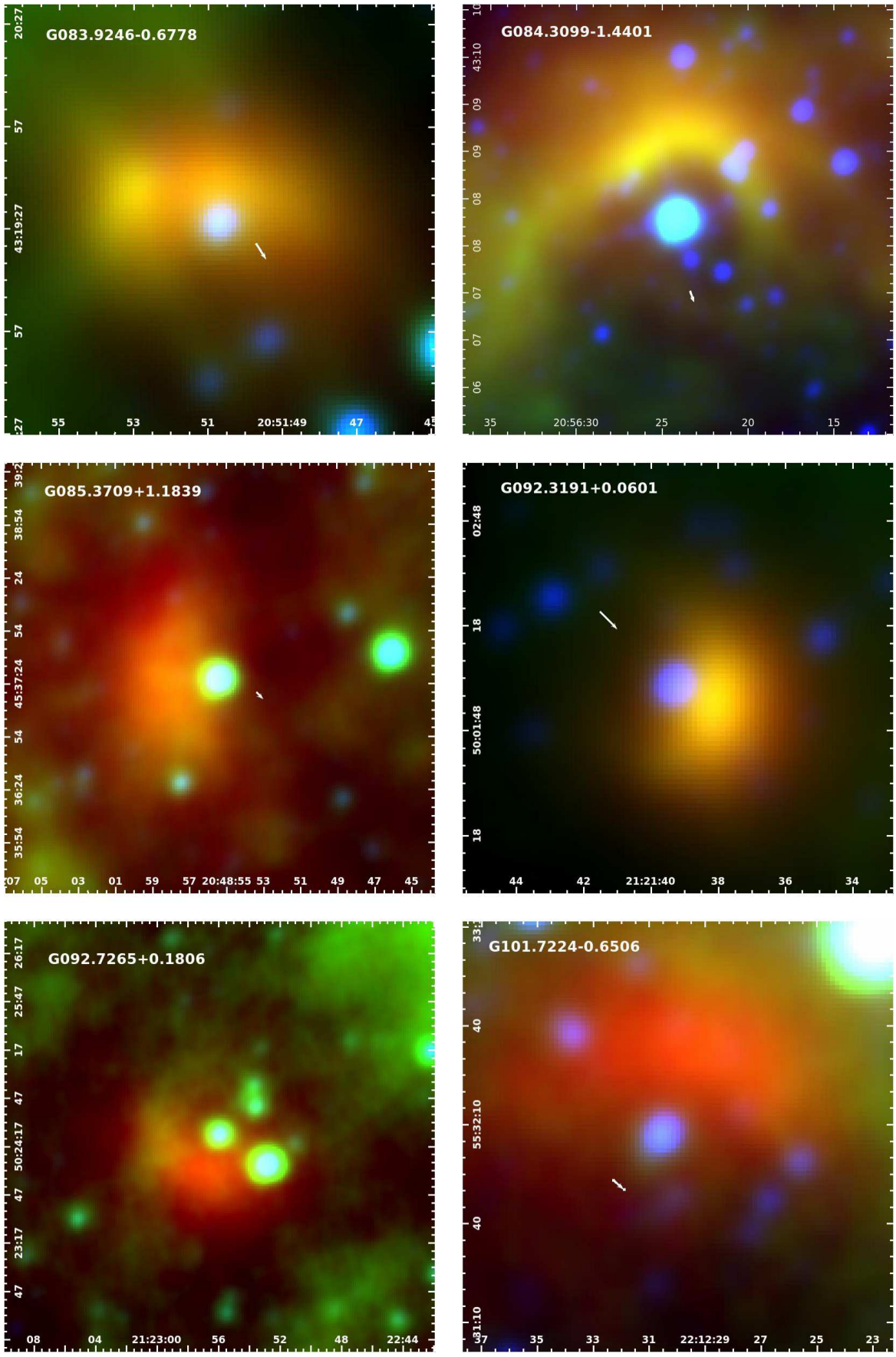
G083.9246-0.6778
G084.3099-1.4401
G085.3709+1.1839
G092.3191+0.0601
G092.7265+0.1806
G101.7224-0.6506

Figure A59.

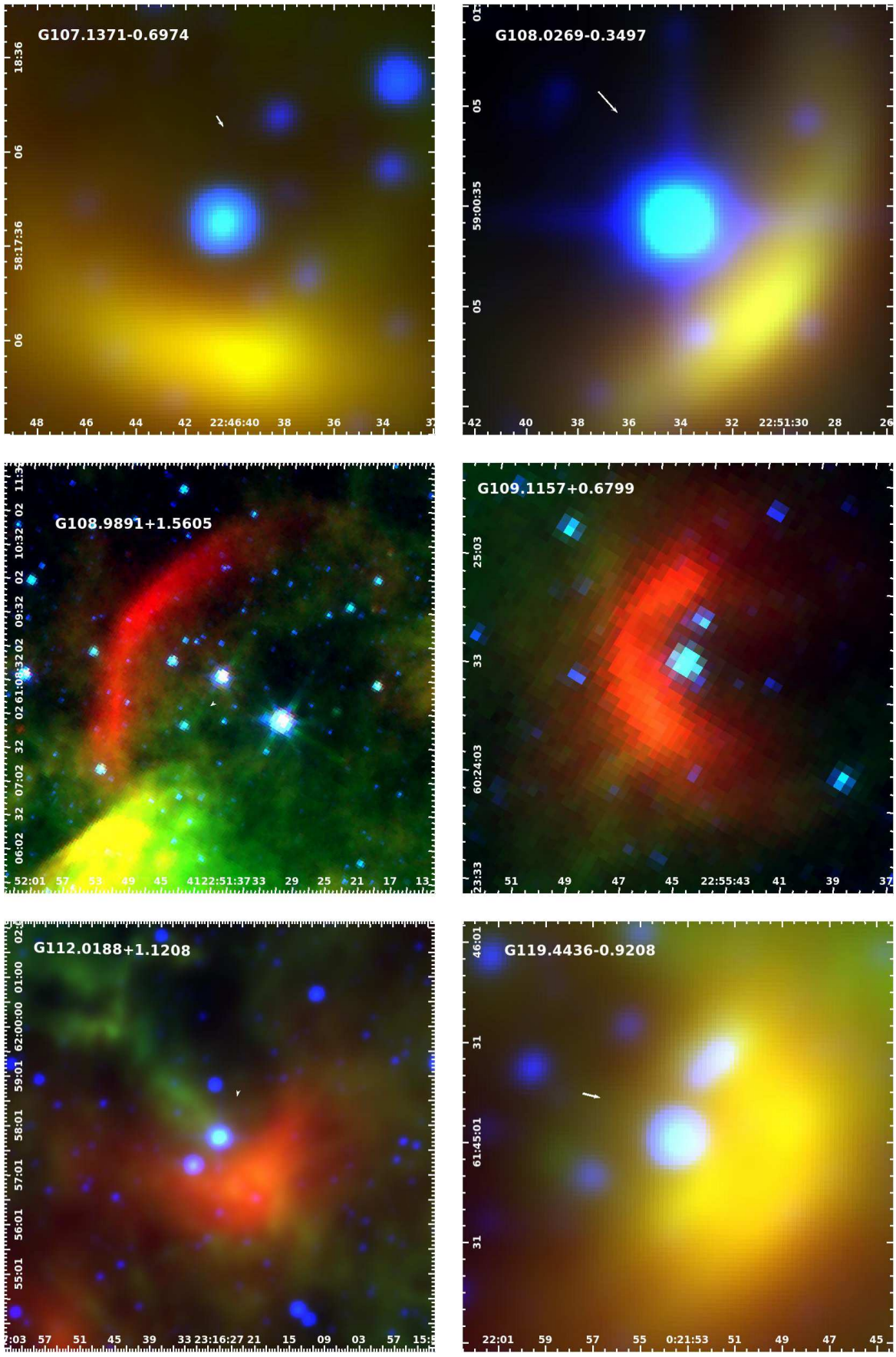
G107.1371-0.6974
G108.0269-0.3497
G108.9891+1.5605
G109.1157+0.6799
G112.0188+1.1208
G119.4436-0.9208

Figure A60.

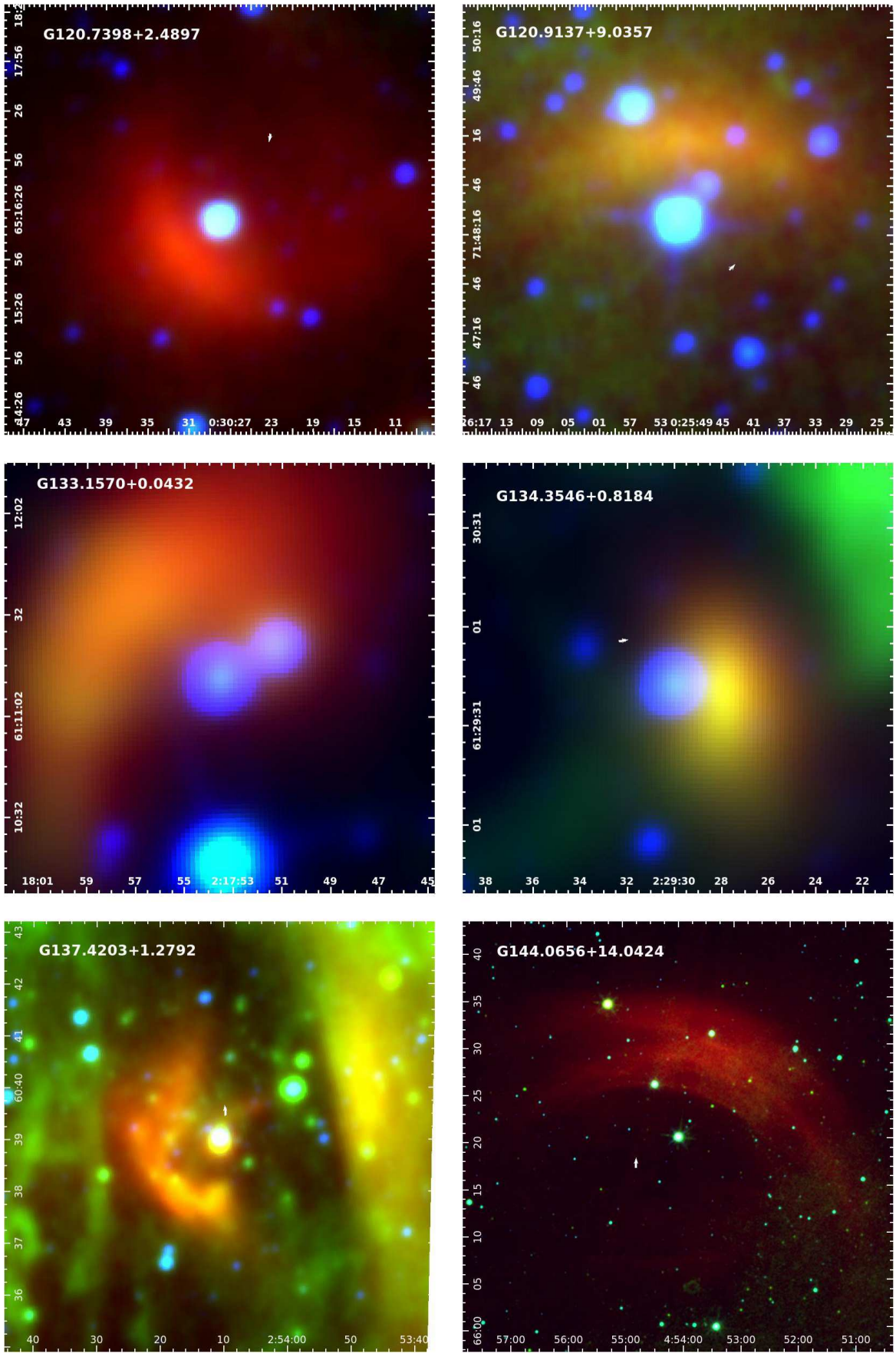
G120.7398+2.4897
G120.9137+9.0357
G133.1570+0.0432
G134.3546+0.8184
G137.4203+1.2792
G144.0656+14.0424

Figure A61.

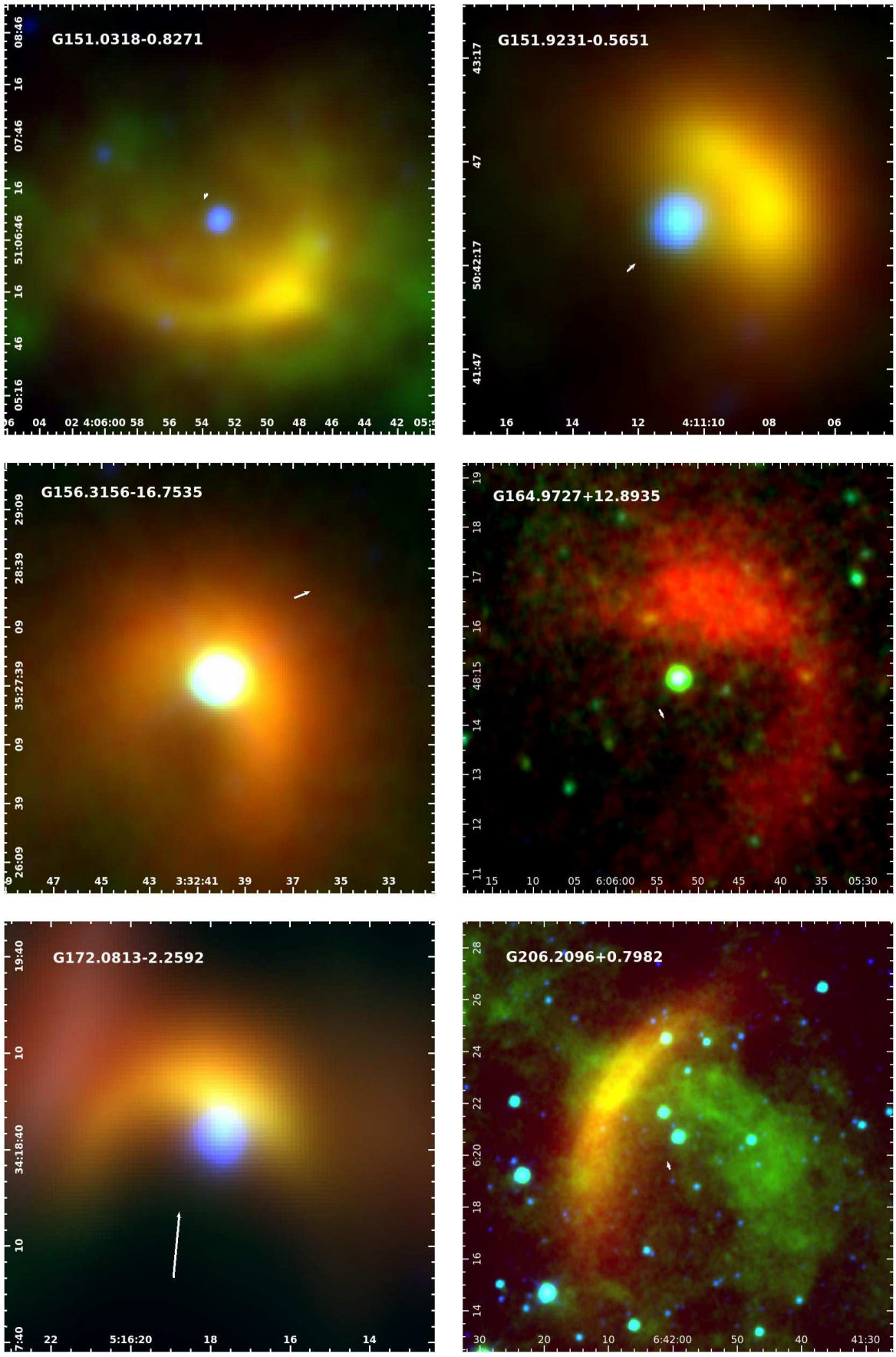
G151.0318-0.8271
G151.9231-0.5651
G156.3156-16.7535
G164.9727+12.8935
G172.0813-2.2592
G206.2096+0.7982

Figure A62.

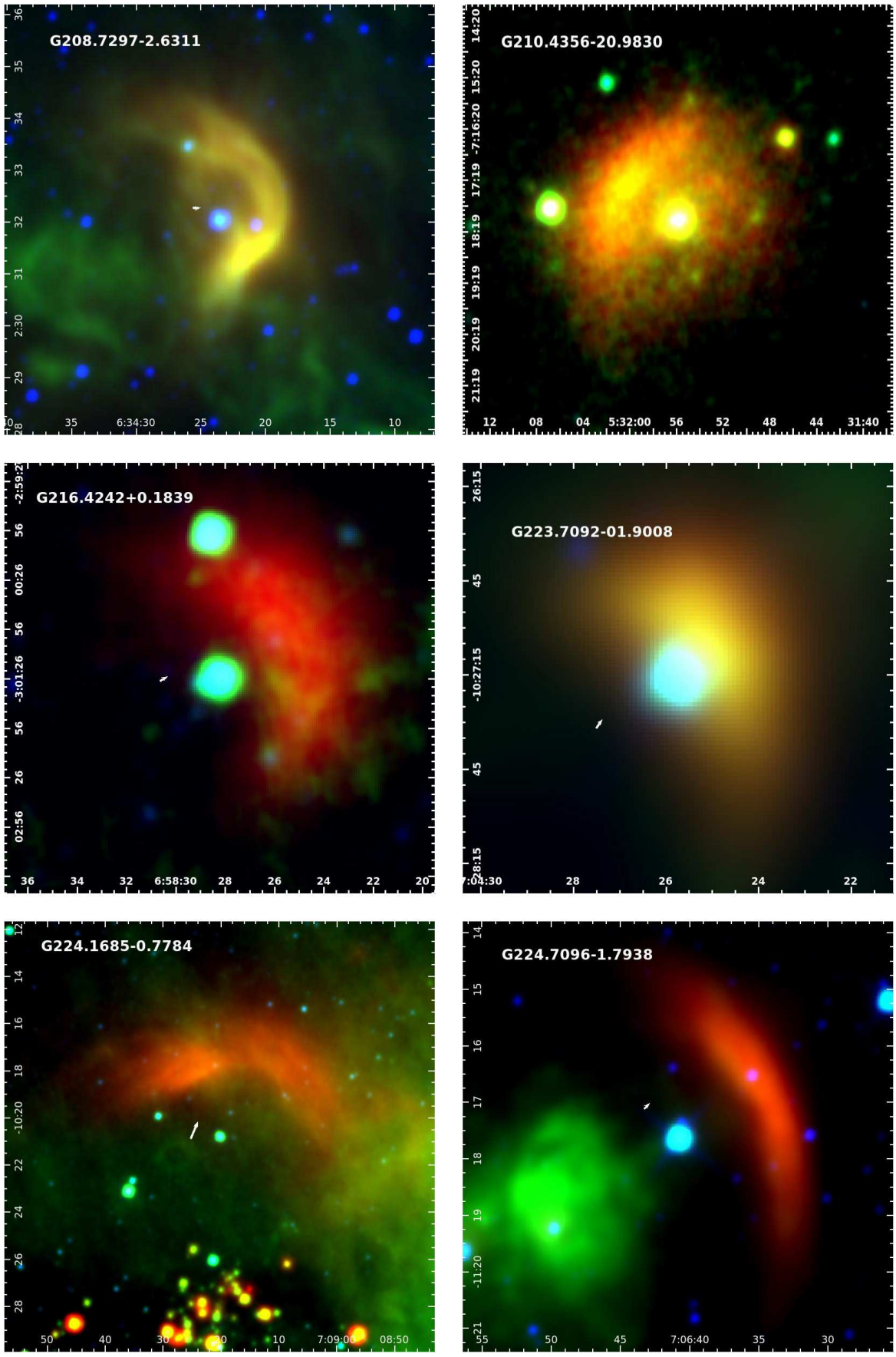
G208.7297-2.6311
G210.4356-20.9830
G216.4242+0.1839
G223.7092-01.9008
G224.1685-0.7784
G224.7096-1.7938

Figure A63.

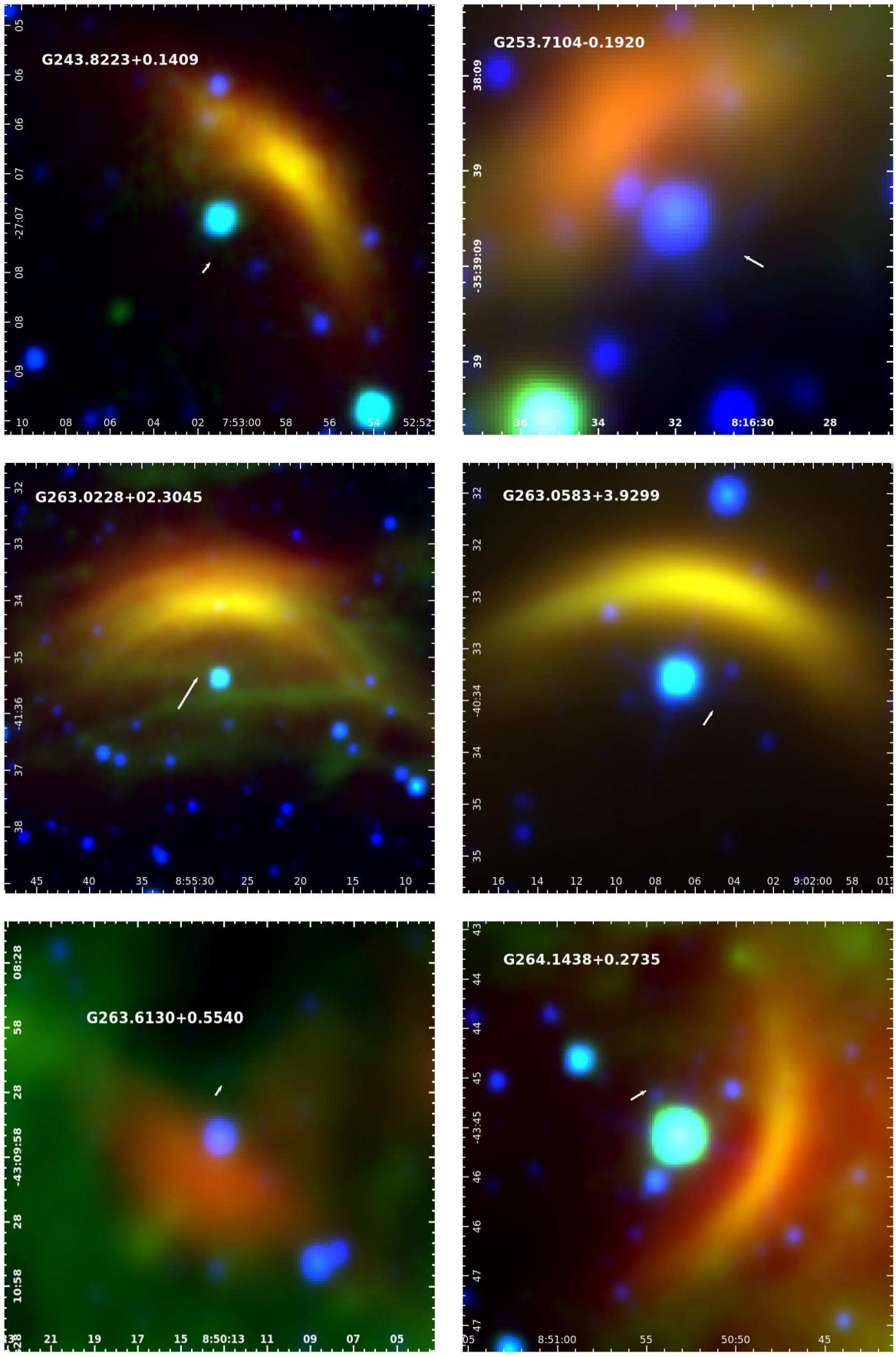
G243.8223+0.1409
G253.7104-0.1920
G263.0228+02.3045
G263.0583+3.9299
G263.6130+0.5540
G264.1438+0.2735

Figure A64.

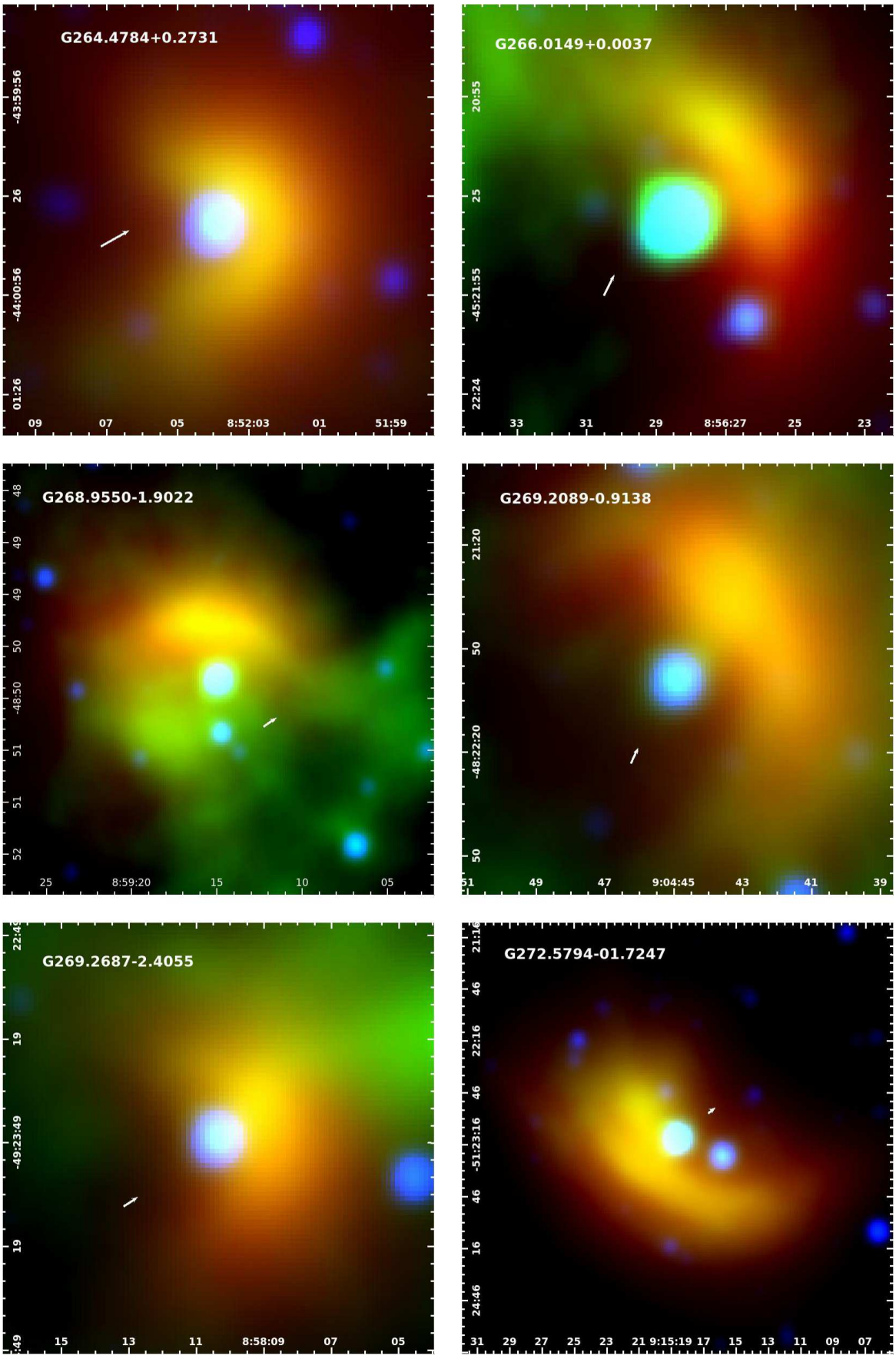
G264.4784+0.2731
G266.0149+0.0037
G268.9550-1.9022
G269.2089-0.9138
G269.2687-2.4055
G272.5794-01.7247

Figure A65.

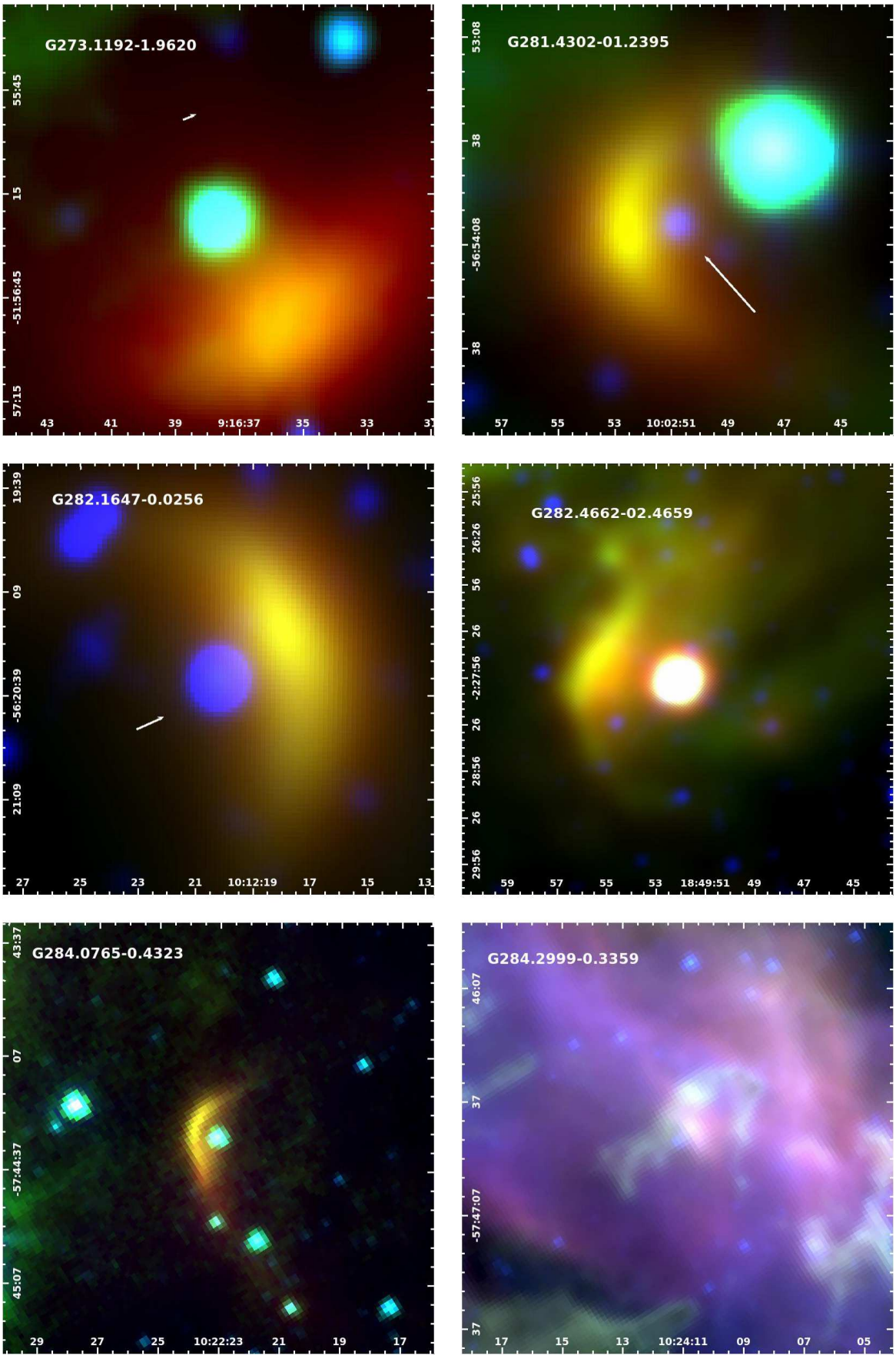
G273.1192-1.9620
55:45
15
-51:56:45
57:15
43
41
39
9:16:37
35
33
G281.4302-01.2395
53:08
38
-56:54:08
38
57
55
53
10:02:51
49
47
45
G282.1647-0.0256
19:39
09
-56:20:39
21:09
27
25
23
21
10:12:19
17
15
13
G282.4662-02.4659
25:56
26:26
56
26
-2:27:56
26
28:56
26
29:56
59
57
55
53
18:49:51
49
47
45
G284.0765-0.4323
43:37
07
-57:44:37
45:07
29
27
25
10:22:23
21
19
17
G284.2999-0.3359
46:07
37
-57:47:07
37
17
15
13
10:24:11
09
07
05

Figure A66.

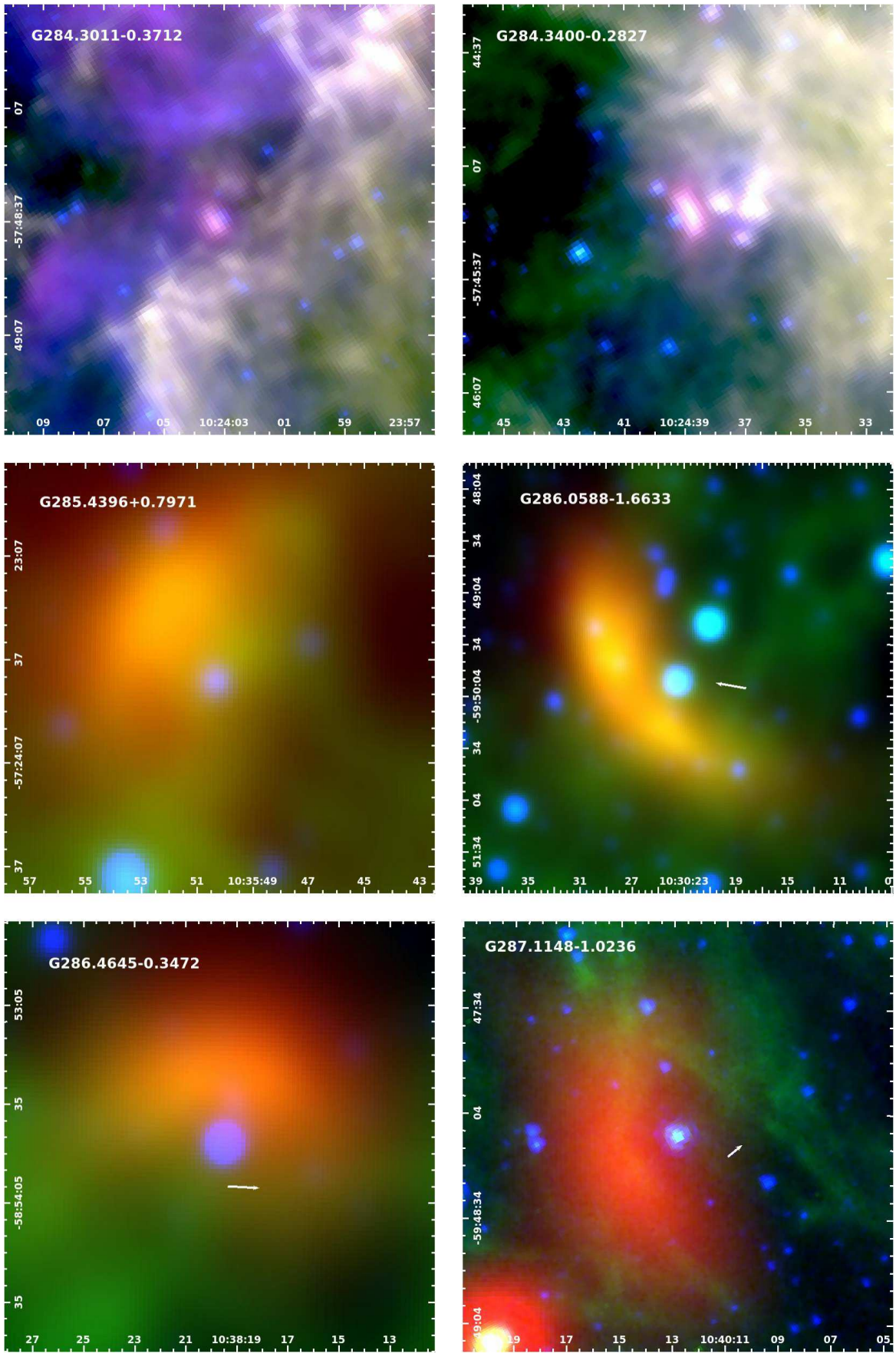
G284.3011-0.3712
G284.3400-0.2827
G285.4396+0.7971
G286.0588-1.6633
G286.4645-0.3472
G287.1148-1.0236

Figure A67.

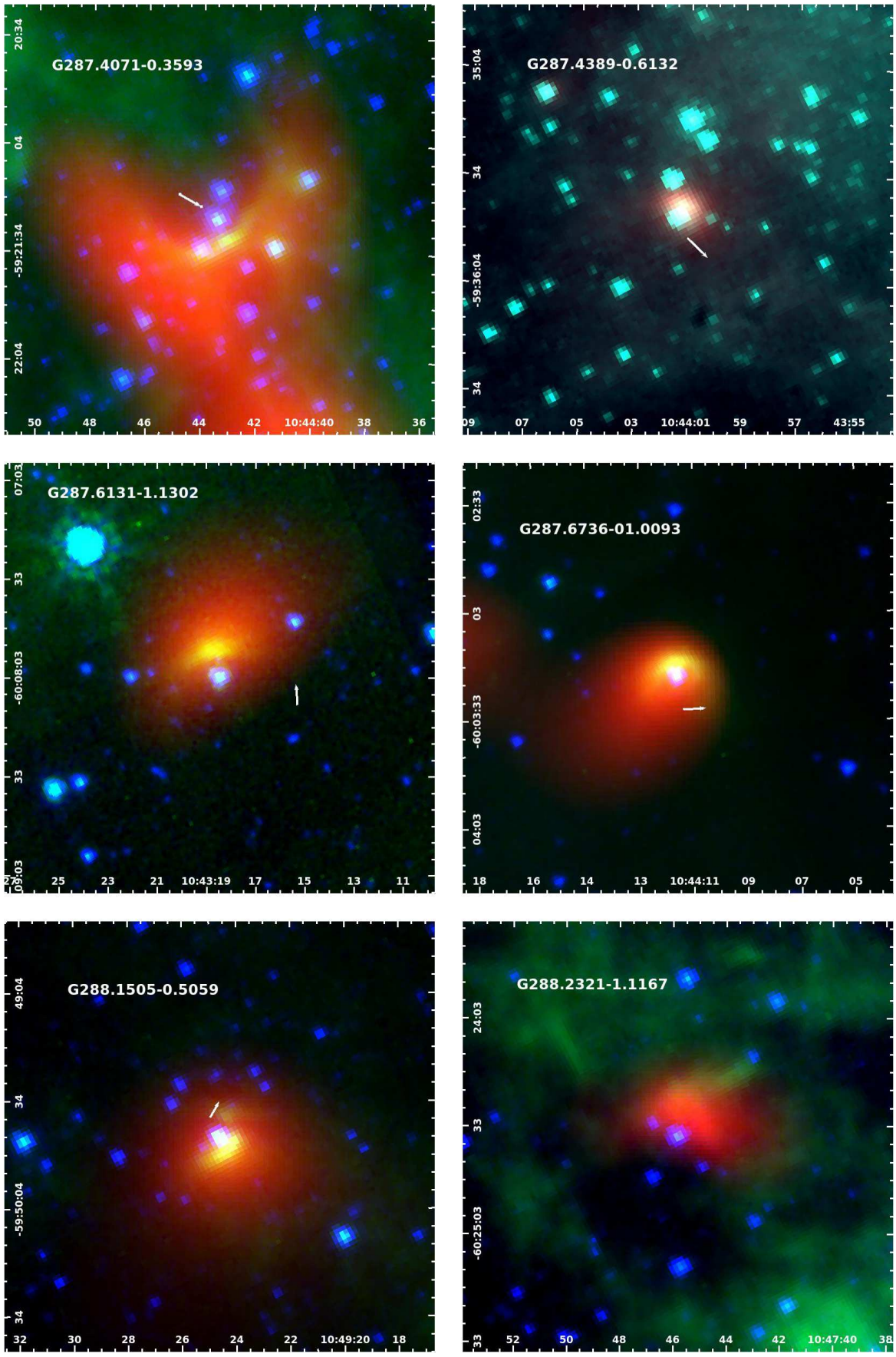
G287.4071-0.3593
G287.4389-0.6132
G287.6131-1.1302
G287.6736-01.0093
G288.1505-0.5059
G288.2321-1.1167

Figure A68.

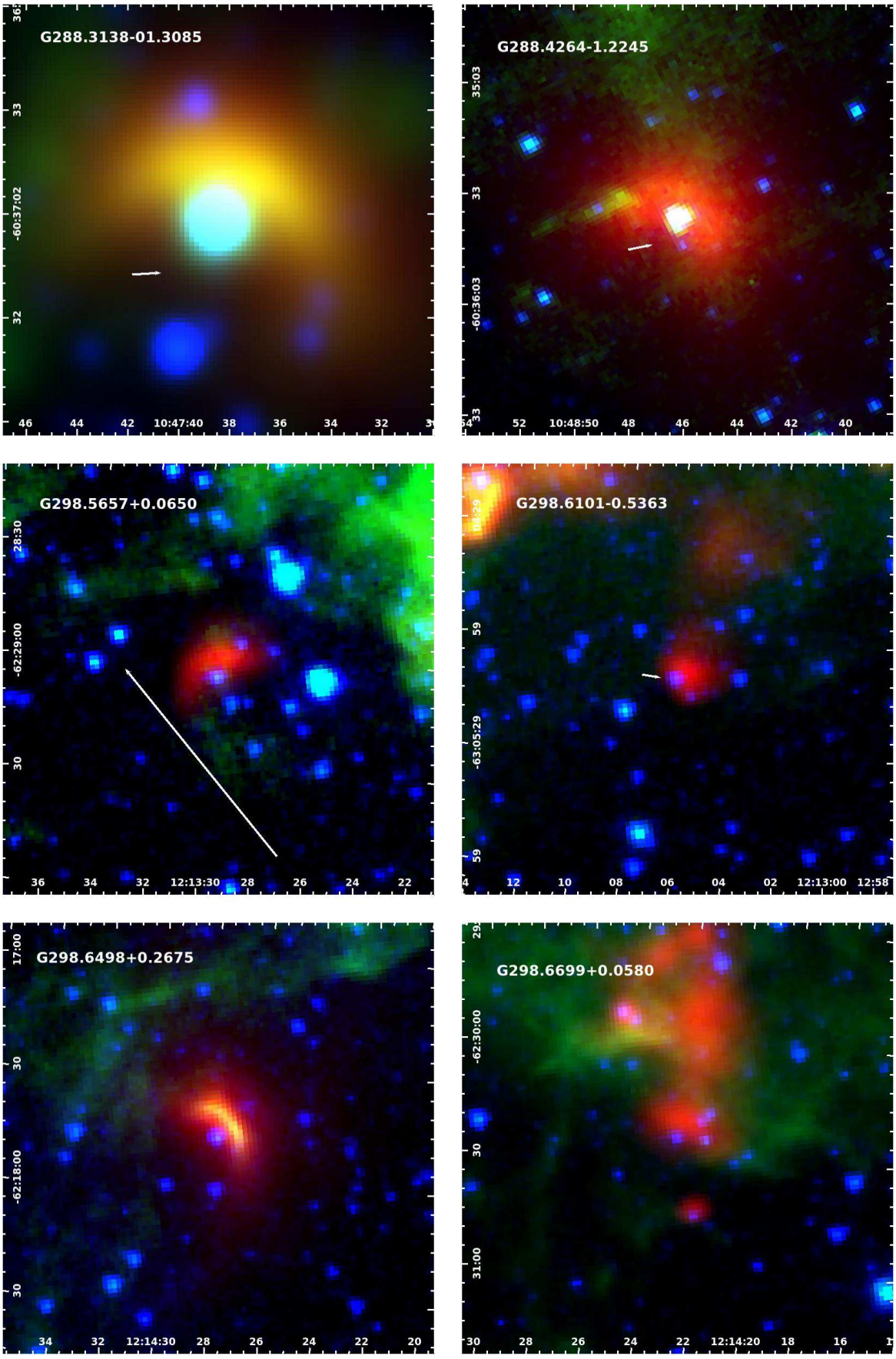
G288.3138-01.3085
G288.4264-1.2245
G298.5657+0.0650
G298.6101-0.5363
G298.6498+0.2675
G298.6699+0.0580

Figure A69.

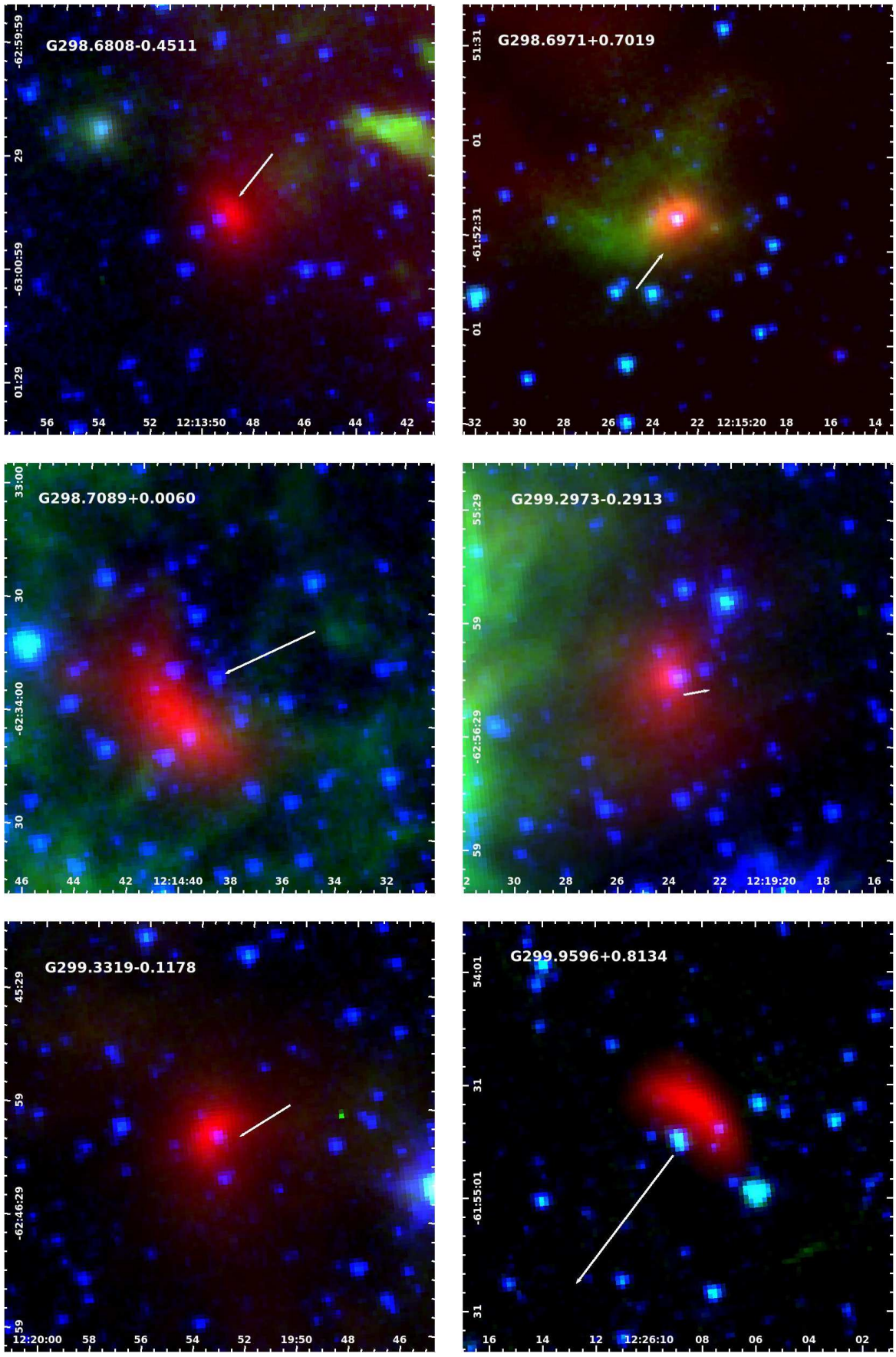
G298.6808-0.4511
G298.6971+0.7019
G298.7089+0.0060
G299.2973-0.2913
G299.3319-0.1178
G299.9596+0.8134

Figure A70.

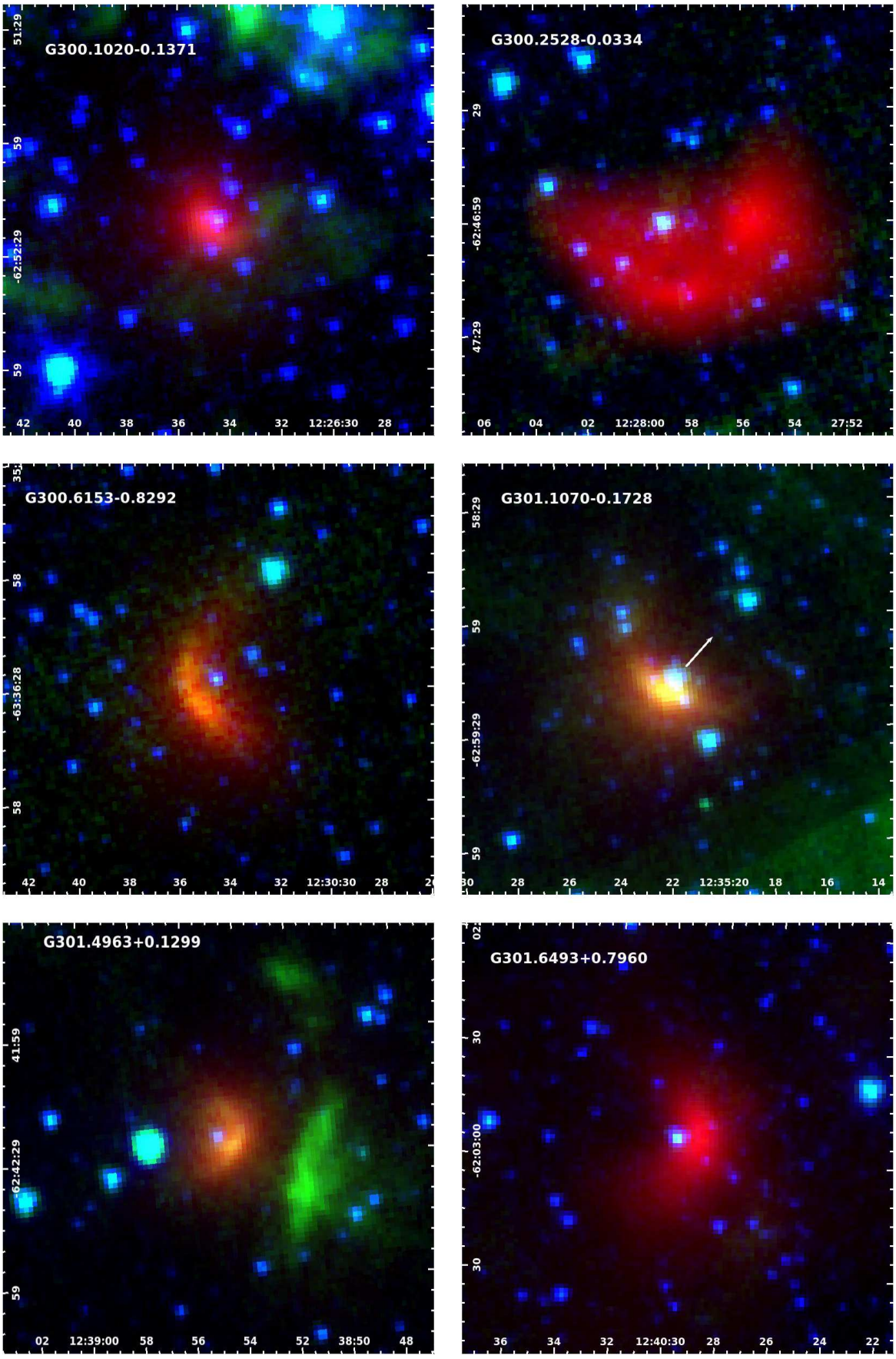
G300.1020-0.1371
51:29
59
-62:52:29
59
42 40 38 36 34 32 12:26:30 28
G300.2528-0.0334
29
-62:46:59
47:29
06 04 02 12:28:00 58 56 54 27:52
G300.6153-0.8292
58
-63:36:28
58
42 40 38 36 34 32 12:30:30 28
G301.1070-0.1728
58:29
59
-62:59:29
59
30 28 26 24 22 12:35:20 18 16 14
G301.4963+0.1299
41:59
-62:42:29
59
02 12:39:00 58 56 54 52 38:50 48
G301.6493+0.7960
30
-62:03:00
30
36 34 32 12:40:30 28 26 24 22

Figure A71.

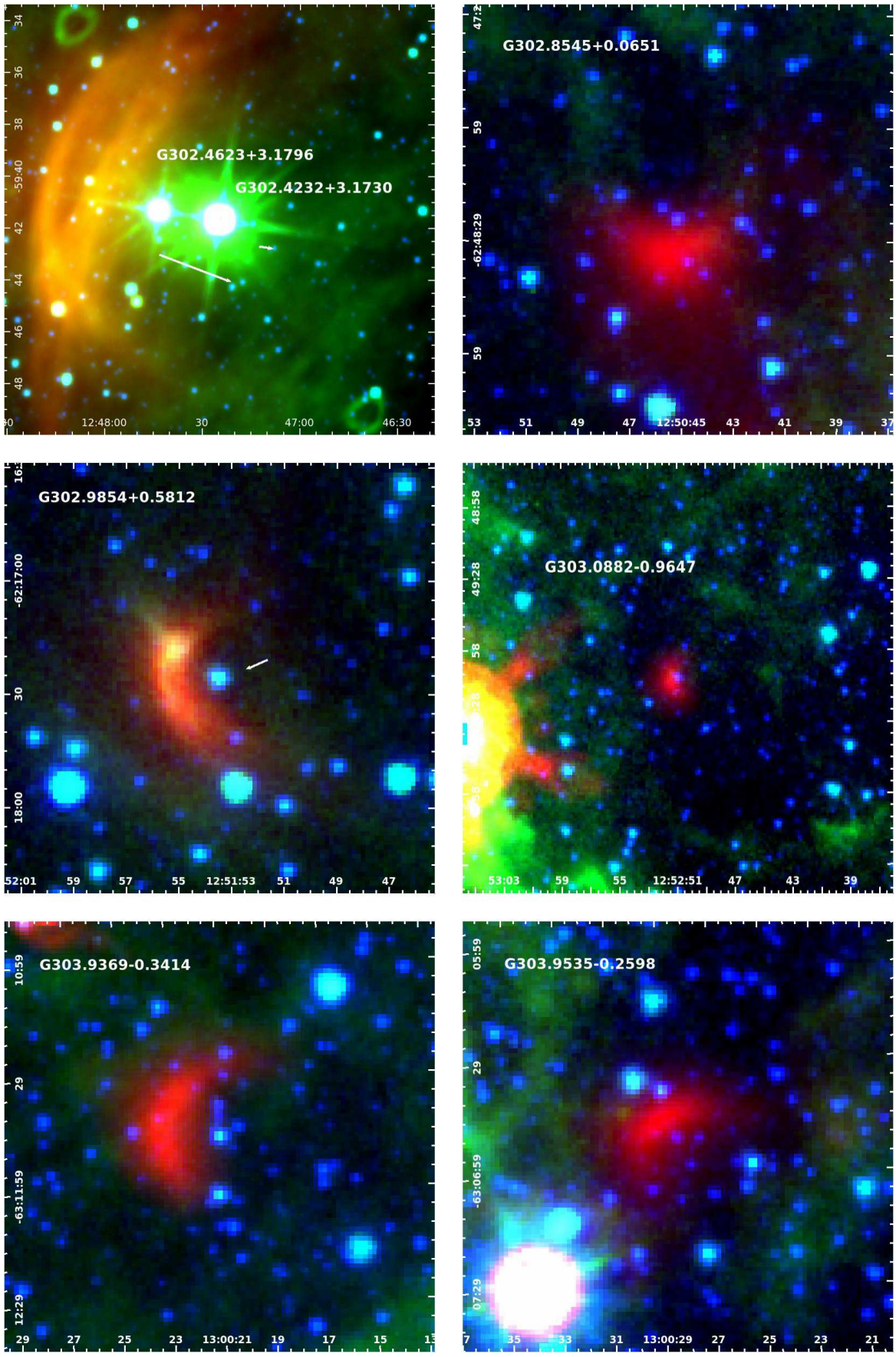
G302.4623+3.1796
G302.4232+3.1730
G302.8545+0.0651
G302.9854+0.5812
G303.0882-0.9647
G303.9369-0.3414
G303.9535-0.2598

Figure A72.

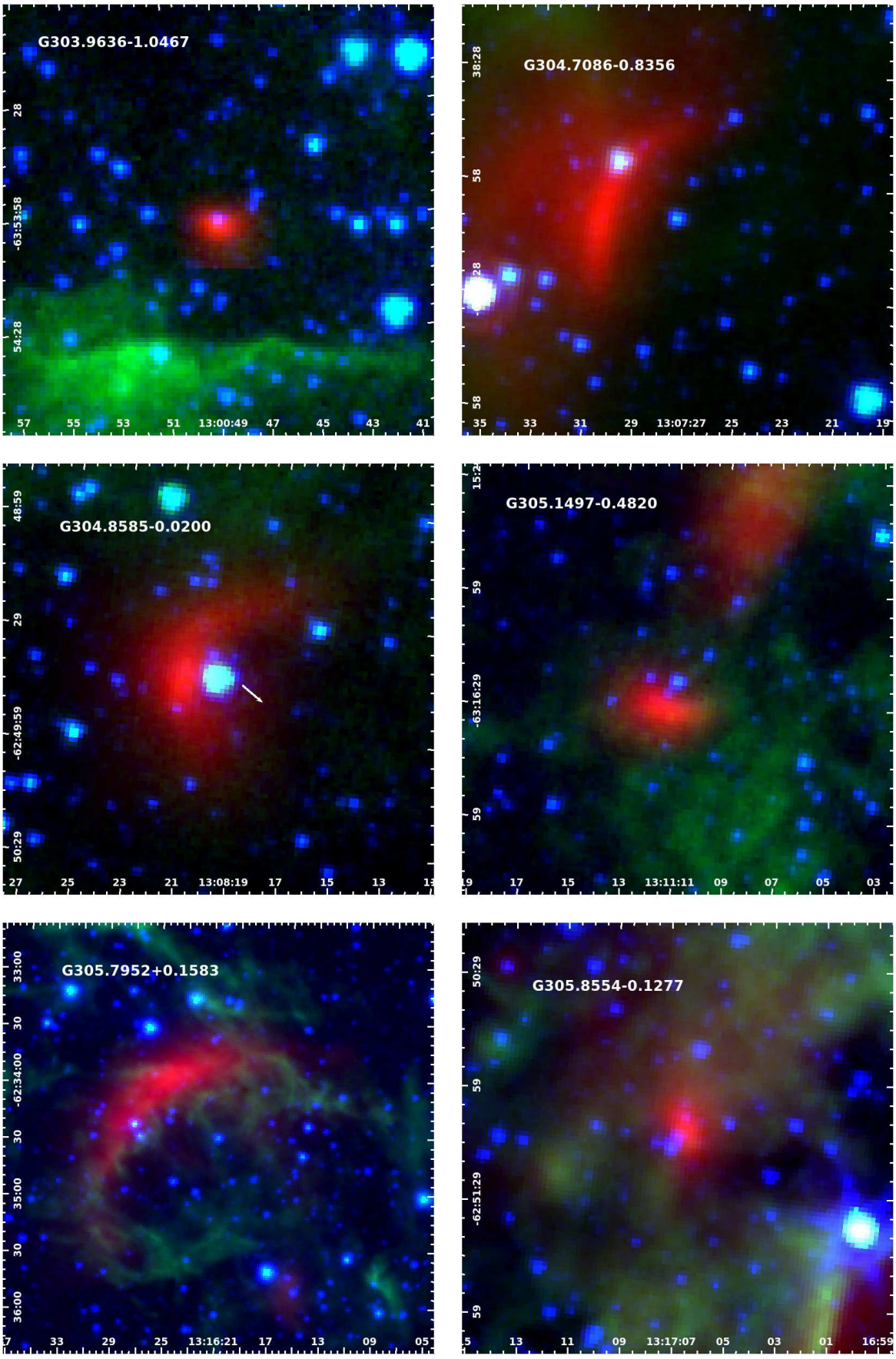
G303.9636-1.0467
G304.7086-0.8356
G304.8585-0.0200
G305.1497-0.4820
G305.7952+0.1583
G305.8554-0.1277

Figure A73.

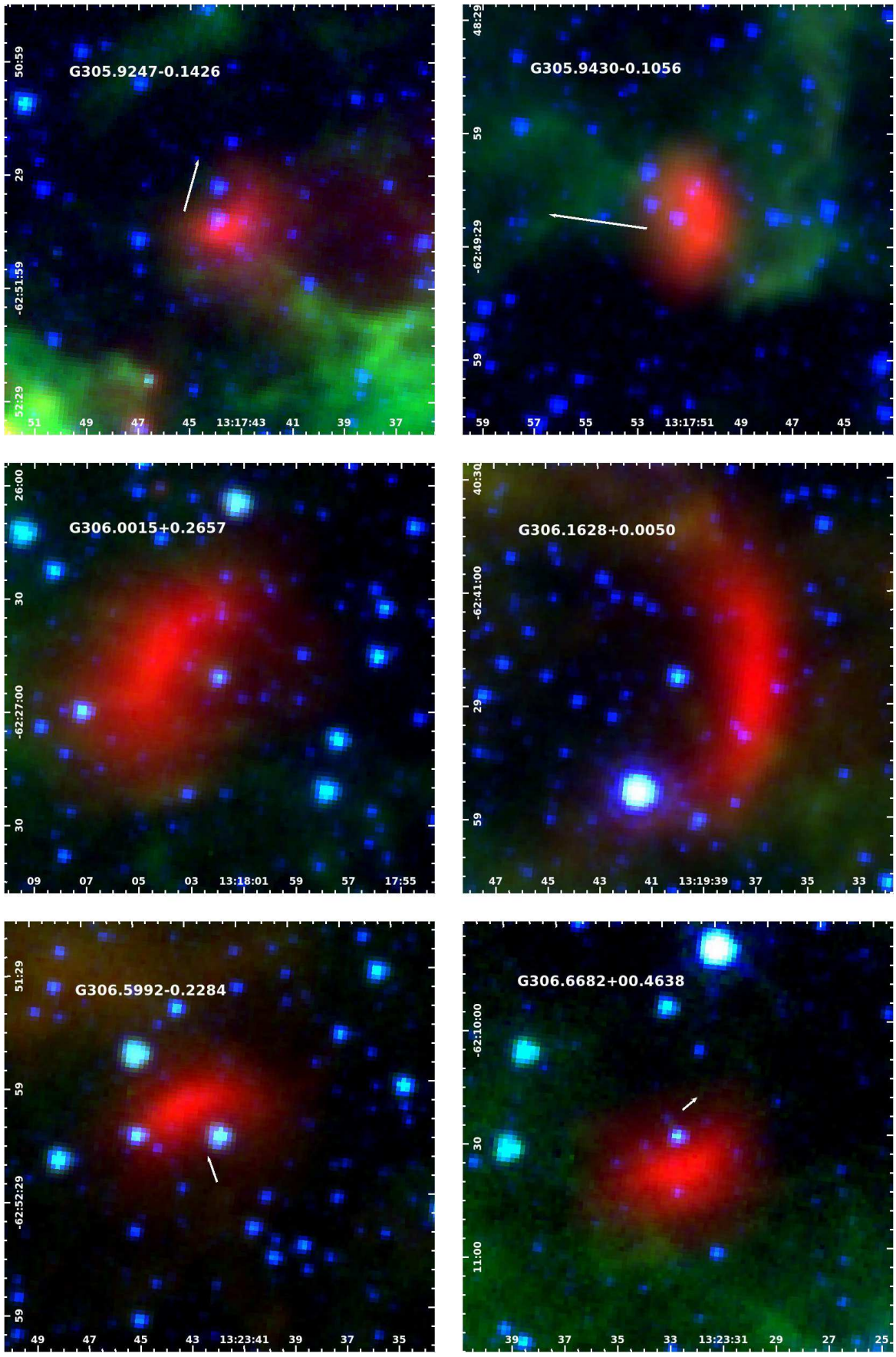
G305.9247-0.1426
G305.9430-0.1056
G306.0015+0.2657
G306.1628+0.0050
G306.5992-0.2284
G306.6682+00.4638

Figure A74.

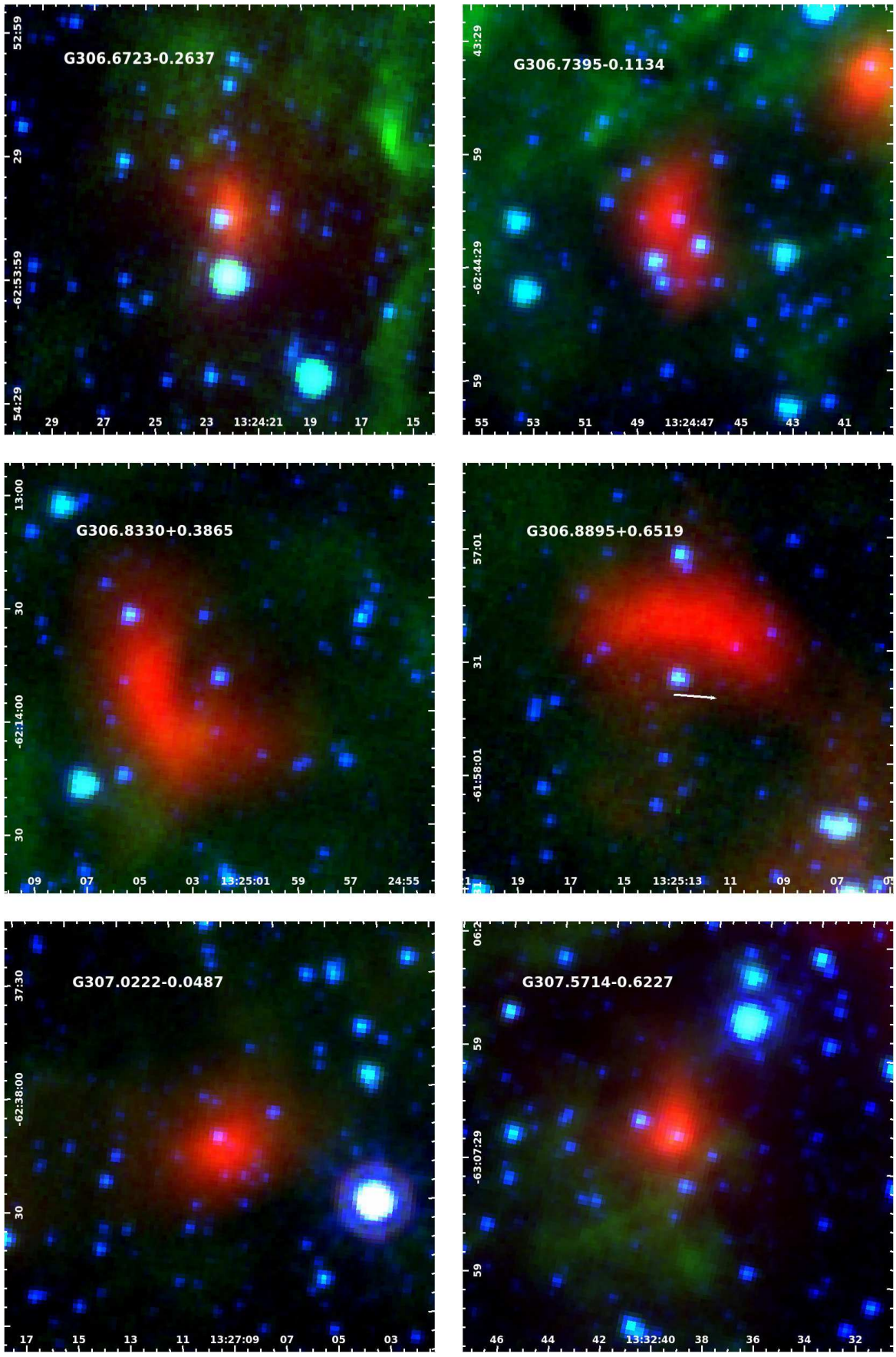
G306.6723-0.2637
52:59
29
-62:53:59
54:29
29 27 25 23 13:24:21 19 17 15
G306.7395-0.1134
43:29
59
-62:44:29
59
55 53 51 49 13:24:47 45 43 41
G306.8330+0.3865
13:00
30
-62:14:00
30
09 07 05 03 13:25:01 59 57 24:55
G306.8895+0.6519
57:01
31
-61:58:01
19 17 15 13:25:13 11 09 07
G307.0222-0.0487
37:30
-62:38:00
30
17 15 13 11 13:27:09 07 05 03
G307.5714-0.6227
59
-63:07:29
59
46 44 42 13:32:40 38 36 34 32

Figure A75.

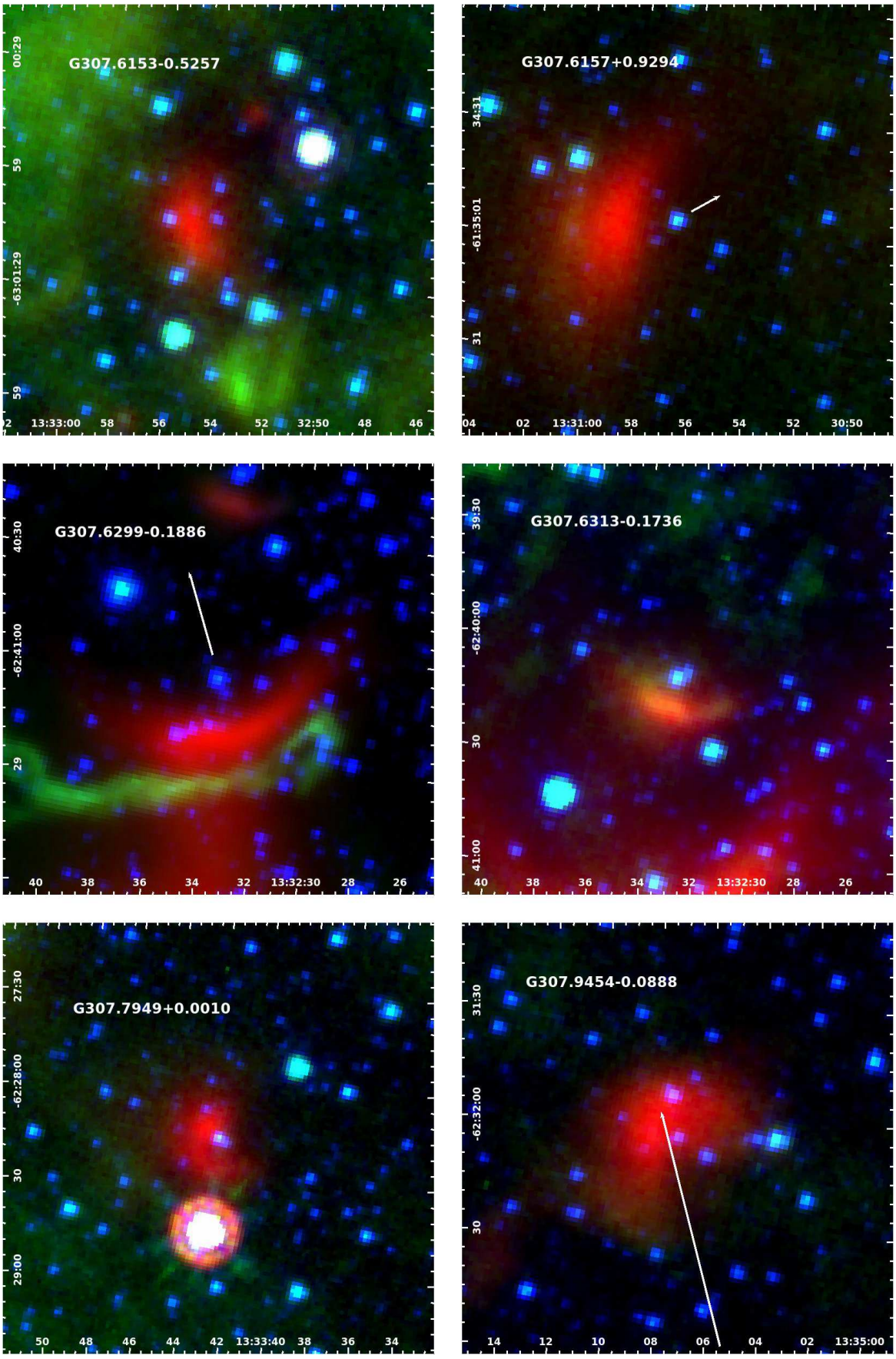
G307.6153-0.5257
G307.6157+0.9294
G307.6299-0.1886
G307.6313-0.1736
G307.7949+0.0010
G307.9454-0.0888

Figure A76.

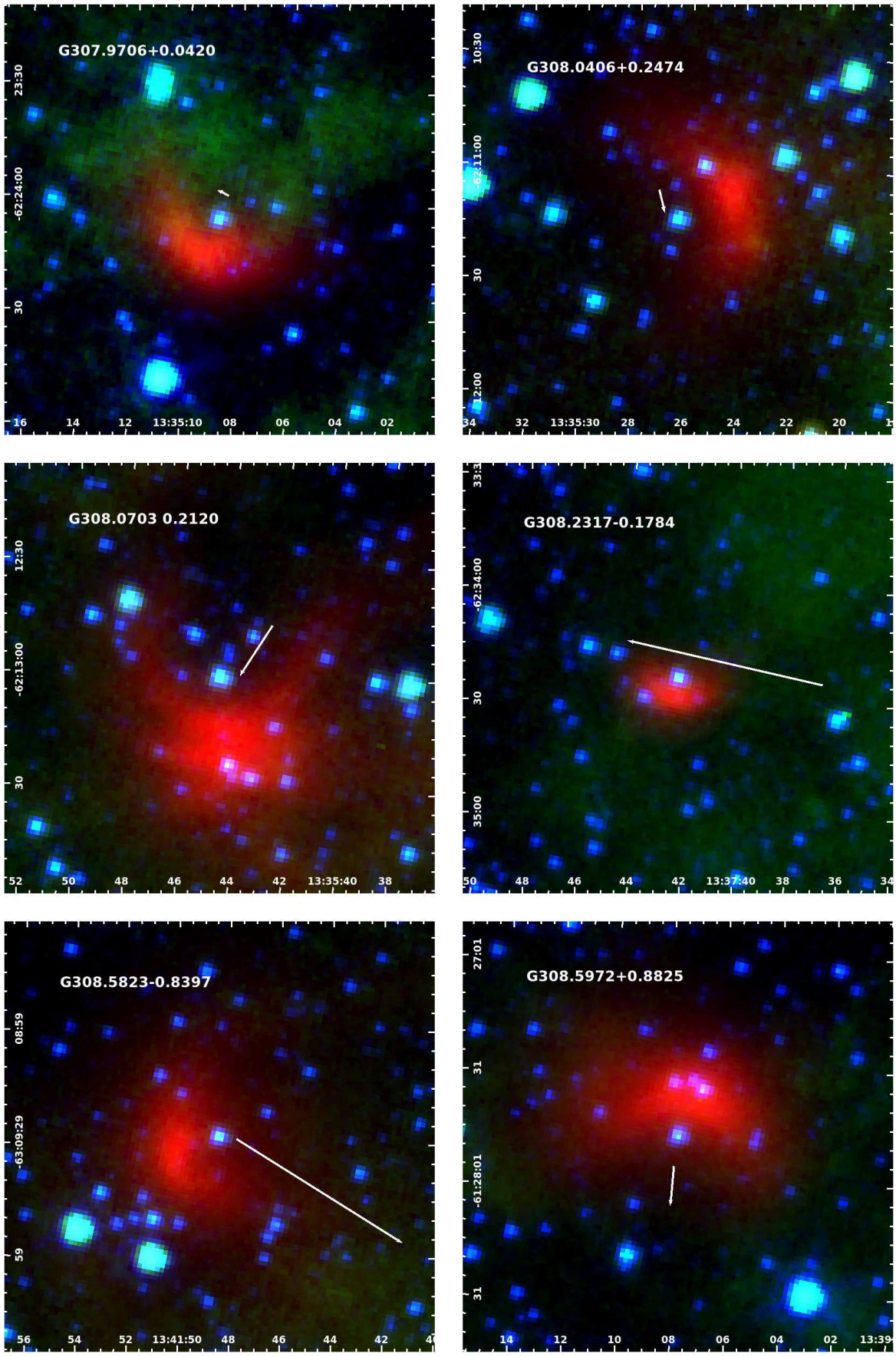
G307.9706+0.0420
G308.0406+0.2474
G308.0703 0.2120
G308.2317-0.1784
G308.5823-0.8397
G308.5972+0.8825

Figure A77.

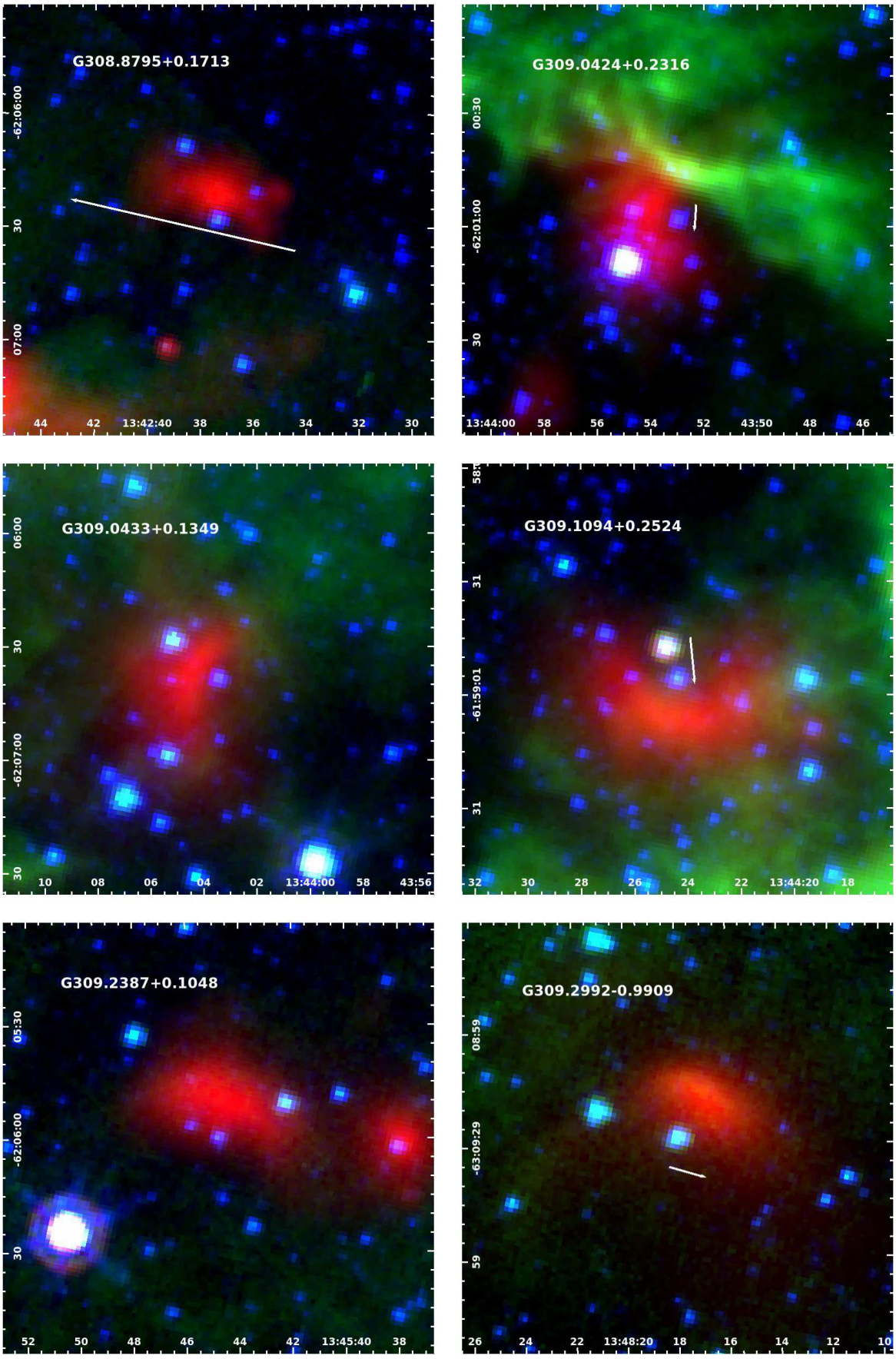
G308.8795+0.1713
-62:06:00
30
07:00
44
42
13:42:40
38
36
34
32
30
G309.0424+0.2316
00:30
-62:01:00
30
13:44:00
58
56
54
52
43:50
48
46
G309.0433+0.1349
06:00
30
-62:07:00
30
10
08
06
04
02
13:44:00
58
43:56
G309.1094+0.2524
58
31
-61:59:01
31
32
30
28
26
24
22
13:44:20
18
G309.2387+0.1048
05:30
-62:06:00
30
52
50
48
46
44
42
13:45:40
38
G309.2992-0.9909
08:59
-63:09:29
59
26
24
22
13:48:20
18
16
14
12
10

Figure A78.

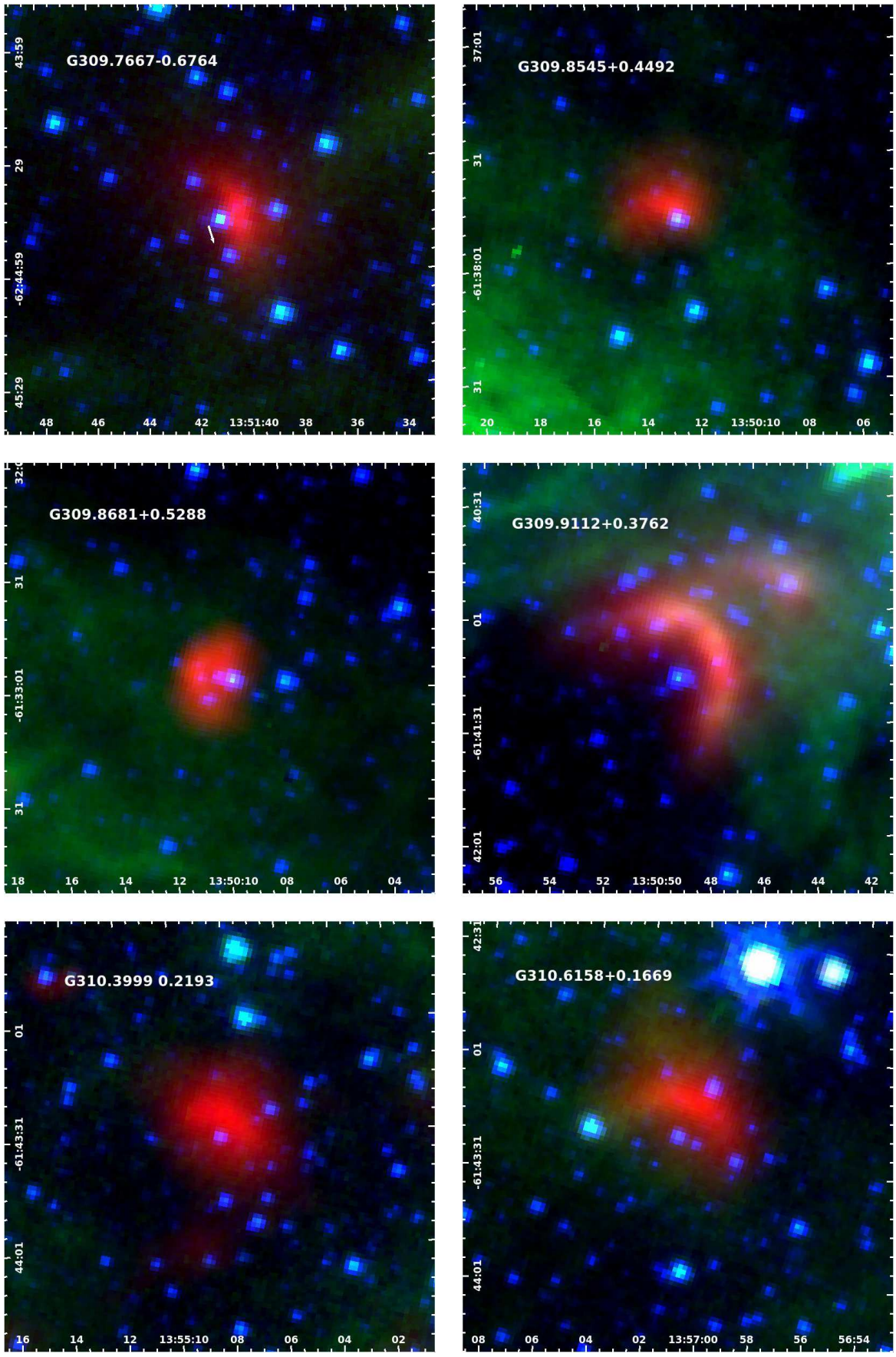
G309.7667-0.6764
43:59
29
-62:44:59
45:29
48 46 44 42 13:51:40 38 36 34
G309.8545+0.4492
37:01
31
-61:38:01
31
20 18 16 14 12 13:50:10 08 06
G309.8681+0.5288
31
-61:33:01
31
18 16 14 12 13:50:10 08 06 04
G309.9112+0.3762
40:31
01
-61:41:31
42:01
56 54 52 13:50:50 48 46 44 42
G310.3999 0.2193
01
-61:43:31
44:01
16 14 12 13:55:10 08 06 04 02
G310.6158+0.1669
42:31
01
-61:43:31
44:01
08 06 04 02 13:57:00 58 56 56:54

Figure A79.

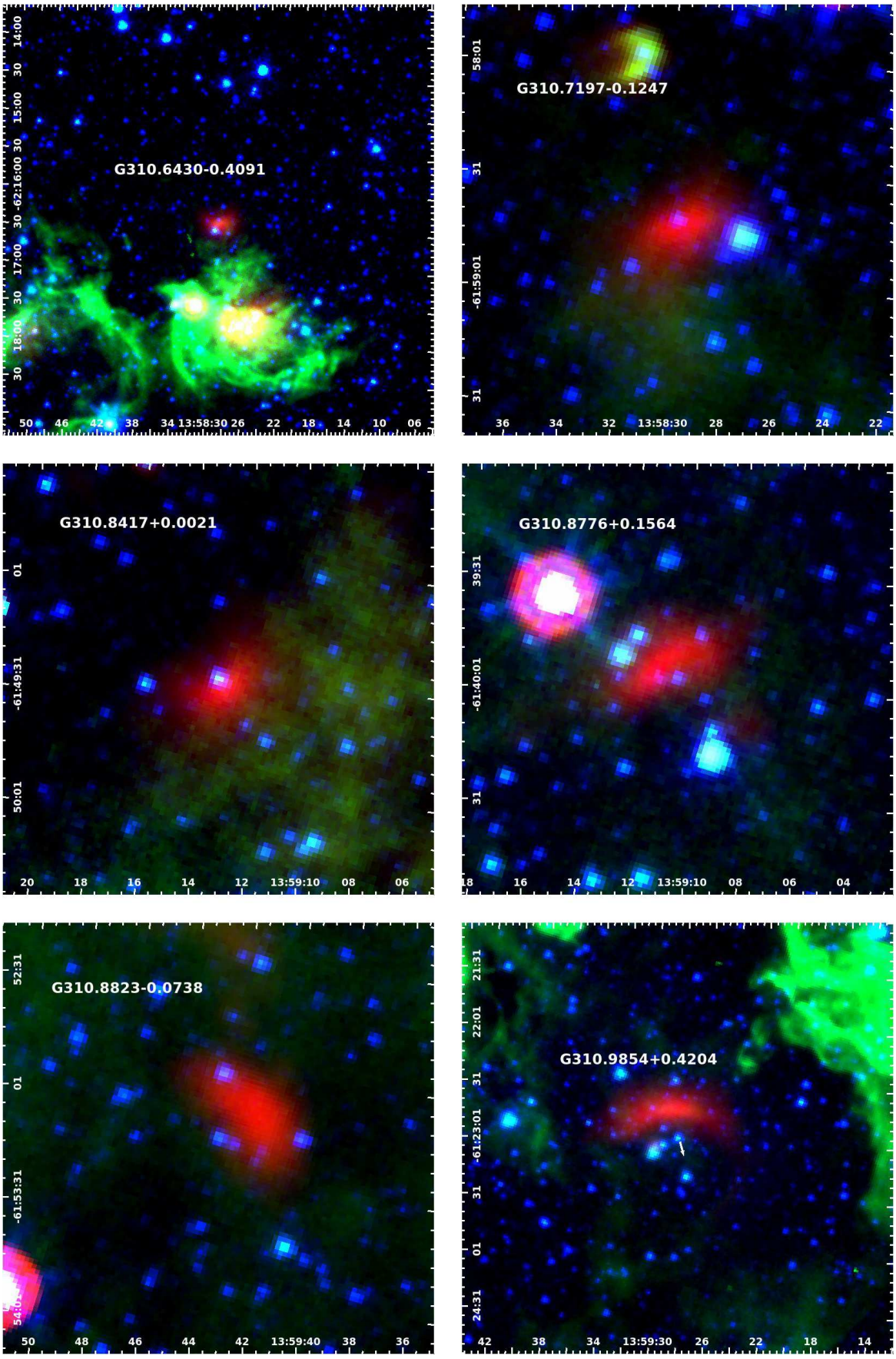
G310.6430-0.4091
G310.7197-0.1247
G310.8417+0.0021
G310.8776+0.1564
G310.8823-0.0738
G310.9854+0.4204

Figure A80.

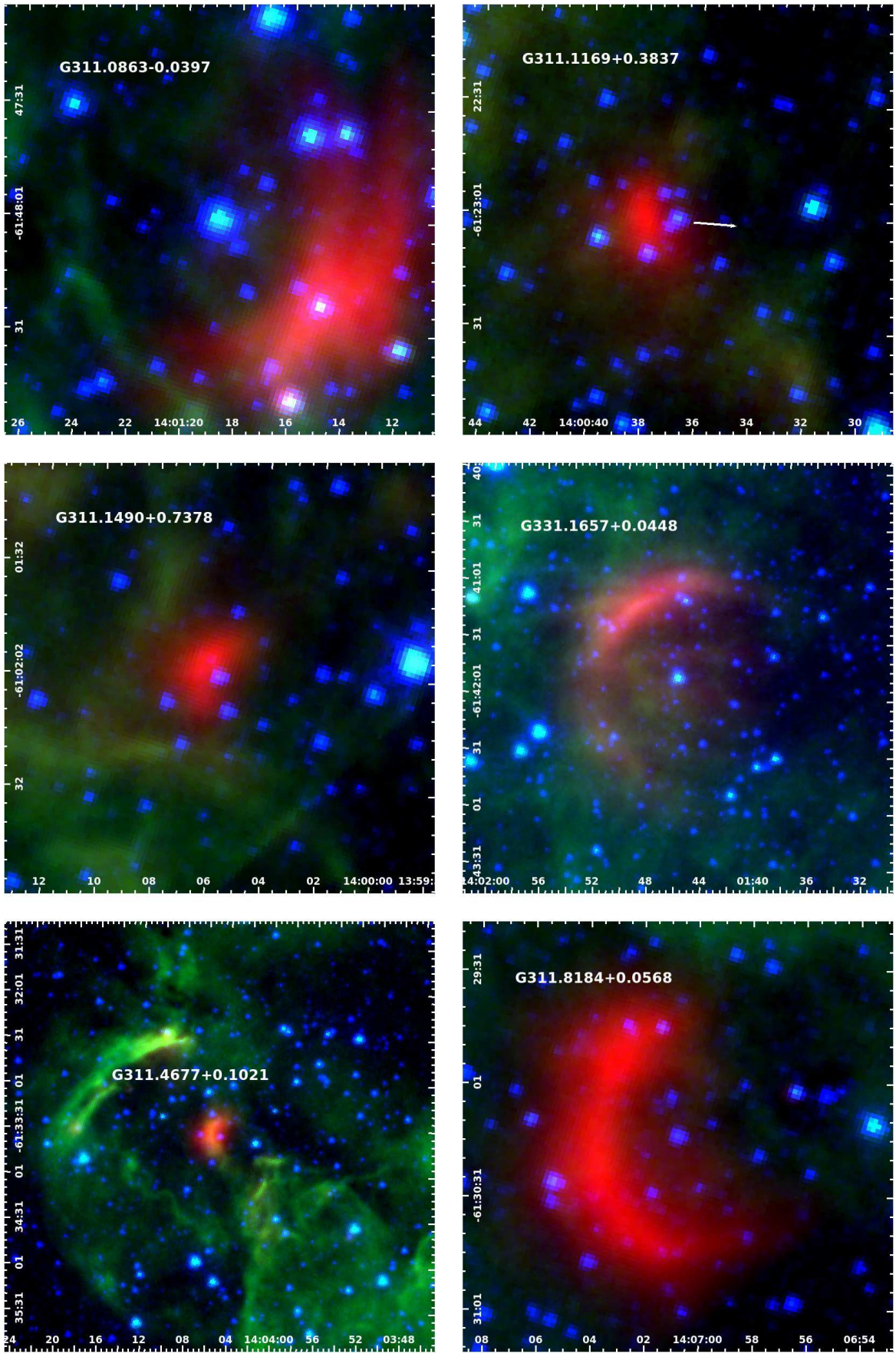
G311.0863-0.0397
G311.1169+0.3837
G311.1490+0.7378
G331.1657+0.0448
G311.4677+0.1021
G311.8184+0.0568

Figure A81.

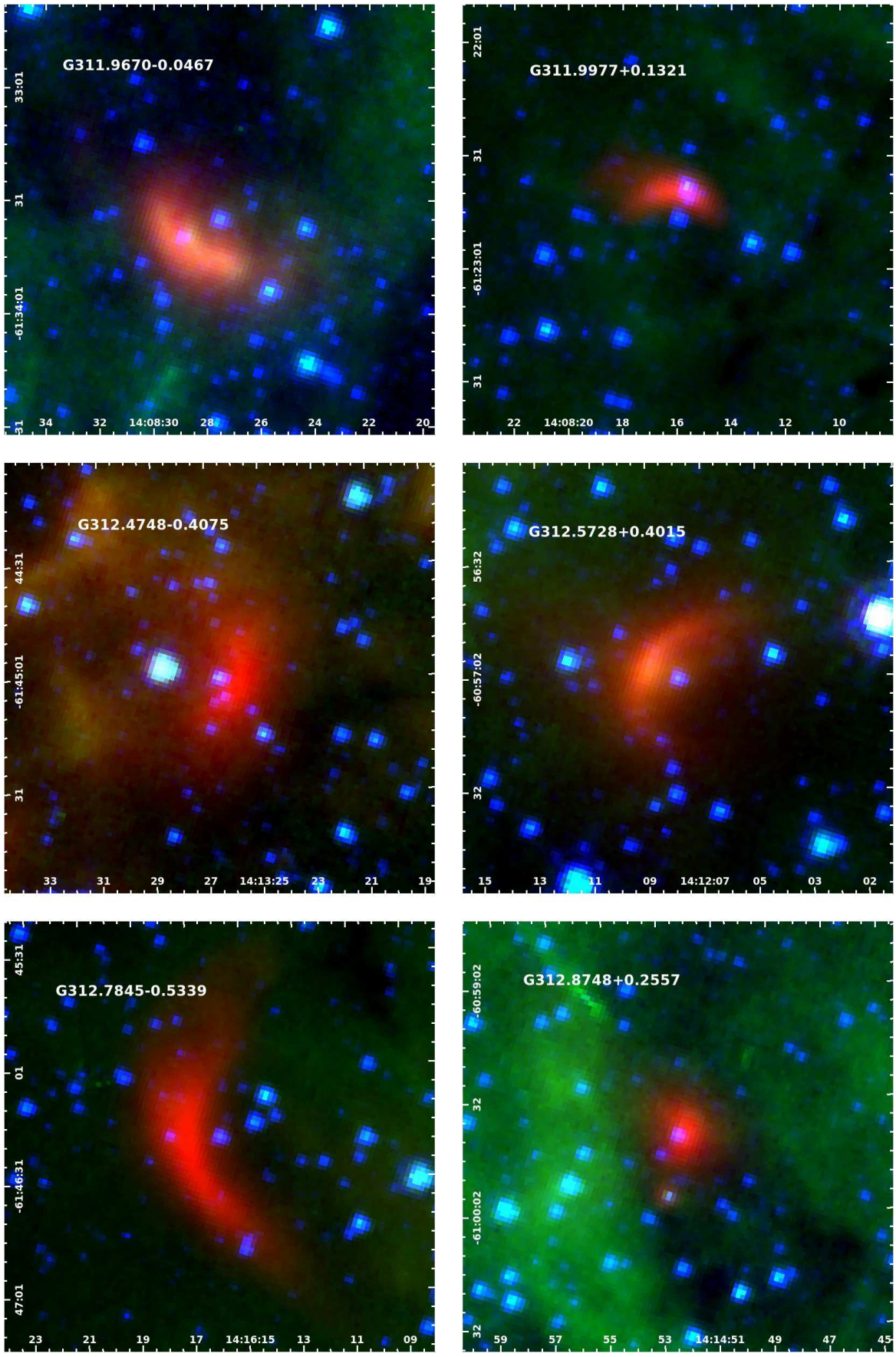
G311.9670-0.0467
33:01
31
-61:34:01
31
34
32
14:08:30
28
26
24
22
20
G311.9977+0.1321
22:01
31
-61:23:01
31
22
14:08:20
18
16
14
12
10
G312.4748-0.4075
44:31
-61:45:01
31
33
31
29
27
14:13:25
23
21
19
G312.5728+0.4015
56:32
-60:57:02
32
15
13
11
09
14:12:07
05
03
02
G312.7845-0.5339
45:31
01
-61:46:31
47:01
23
21
19
17
14:16:15
13
11
09
G312.8748+0.2557
-60:59:02
32
-61:00:02
32
59
57
55
53
14:14:51
49
47
45

Figure A82.

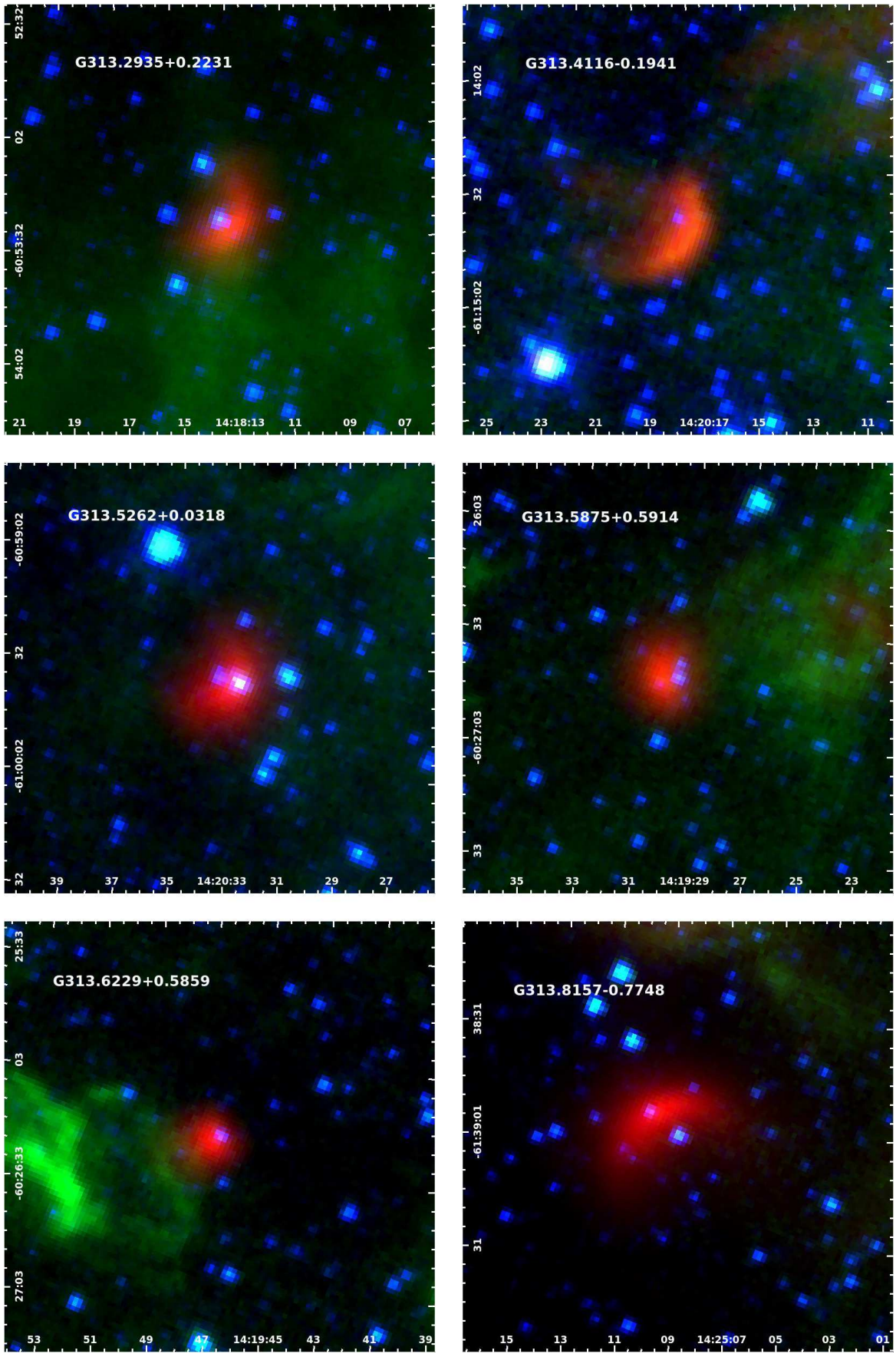
G313.2935+0.2231
52:32
02
-60:53:32
54:02
21 19 17 15 14:18:13 11 09 07
G313.4116-0.1941
14:02
32
-61:15:02
25 23 21 19 14:20:17 15 13 11
G313.5262+0.0318
-60:59:02
32
-61:00:02
32 39 37 35 14:20:33 31 29 27
G313.5875+0.5914
26:03
33
-60:27:03
33 35 33 31 14:19:29 27 25 23
G313.6229+0.5859
25:33
03
-60:26:33
27:03
53 51 49 47 14:19:45 43 41 39
G313.8157-0.7748
38:31
-61:39:01
31
15 13 11 09 14:25:07 05 03 01

Figure A83.

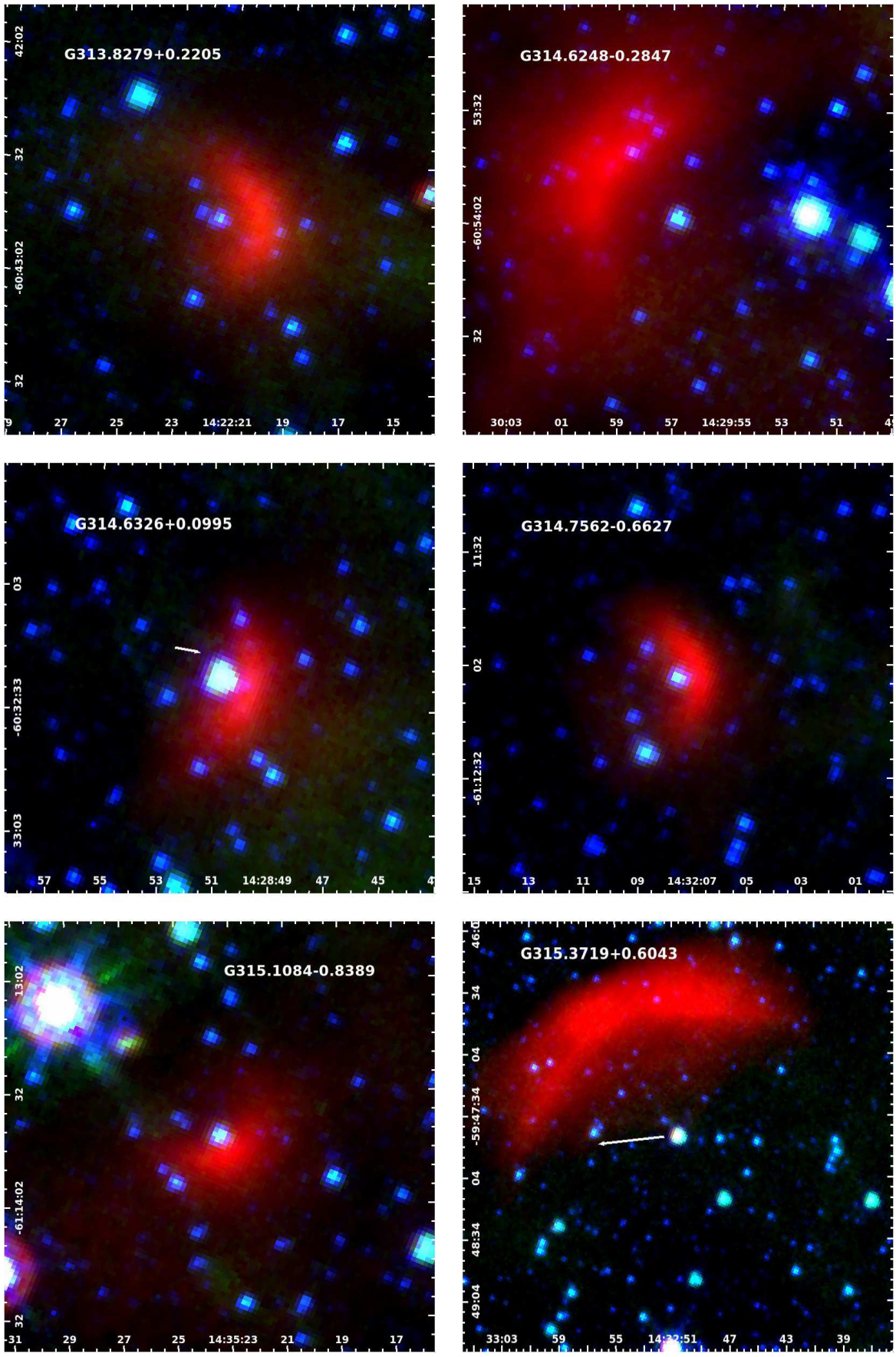
G313.8279+0.2205
G314.6248-0.2847
G314.6326+0.0995
G314.7562-0.6627
G315.1084-0.8389
G315.3719+0.6043

Figure A84.

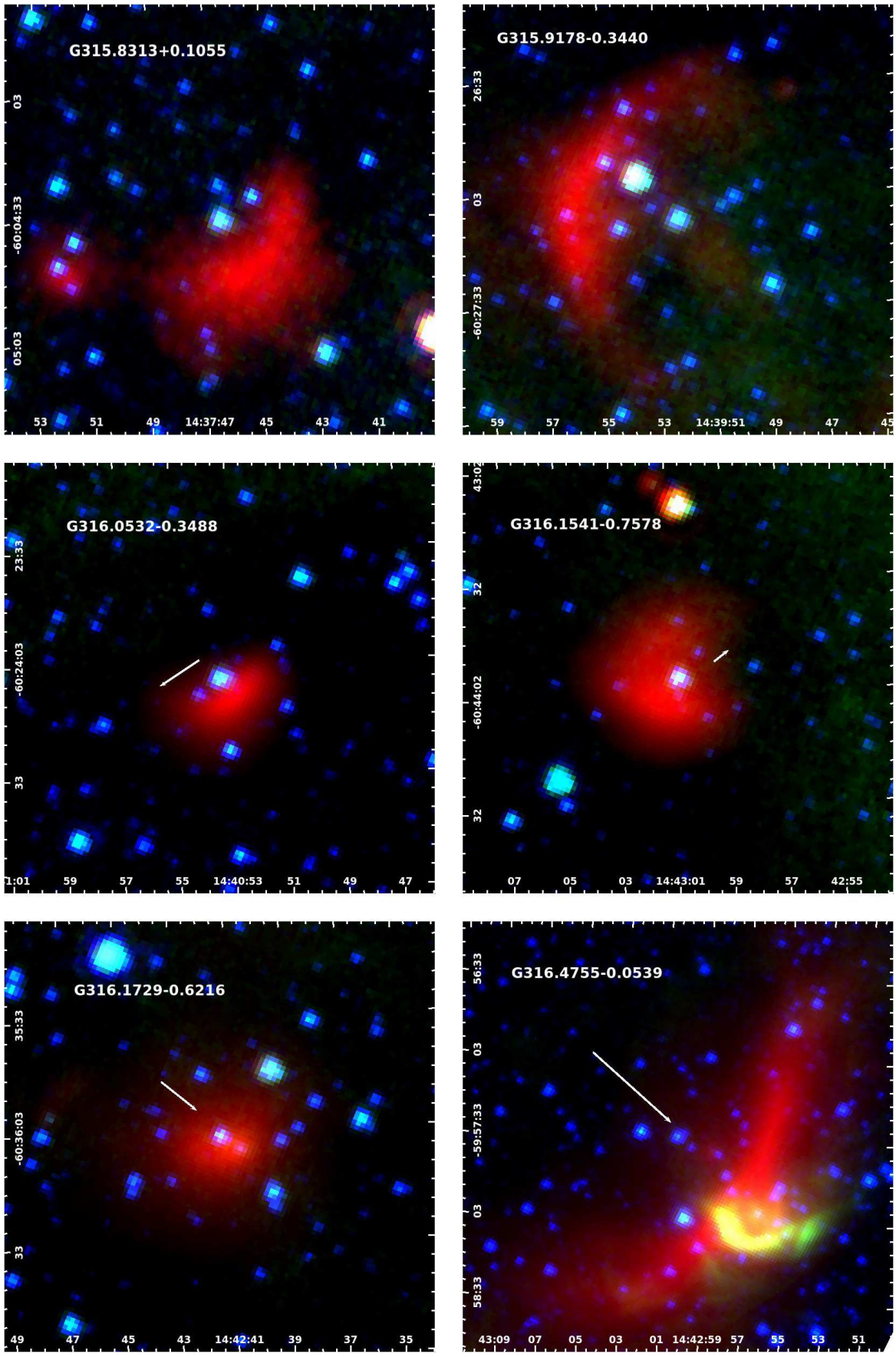
G315.8313+0.1055
G315.9178-0.3440
G316.0532-0.3488
G316.1541-0.7578
G316.1729-0.6216
G316.4755-0.0539

Figure A85.

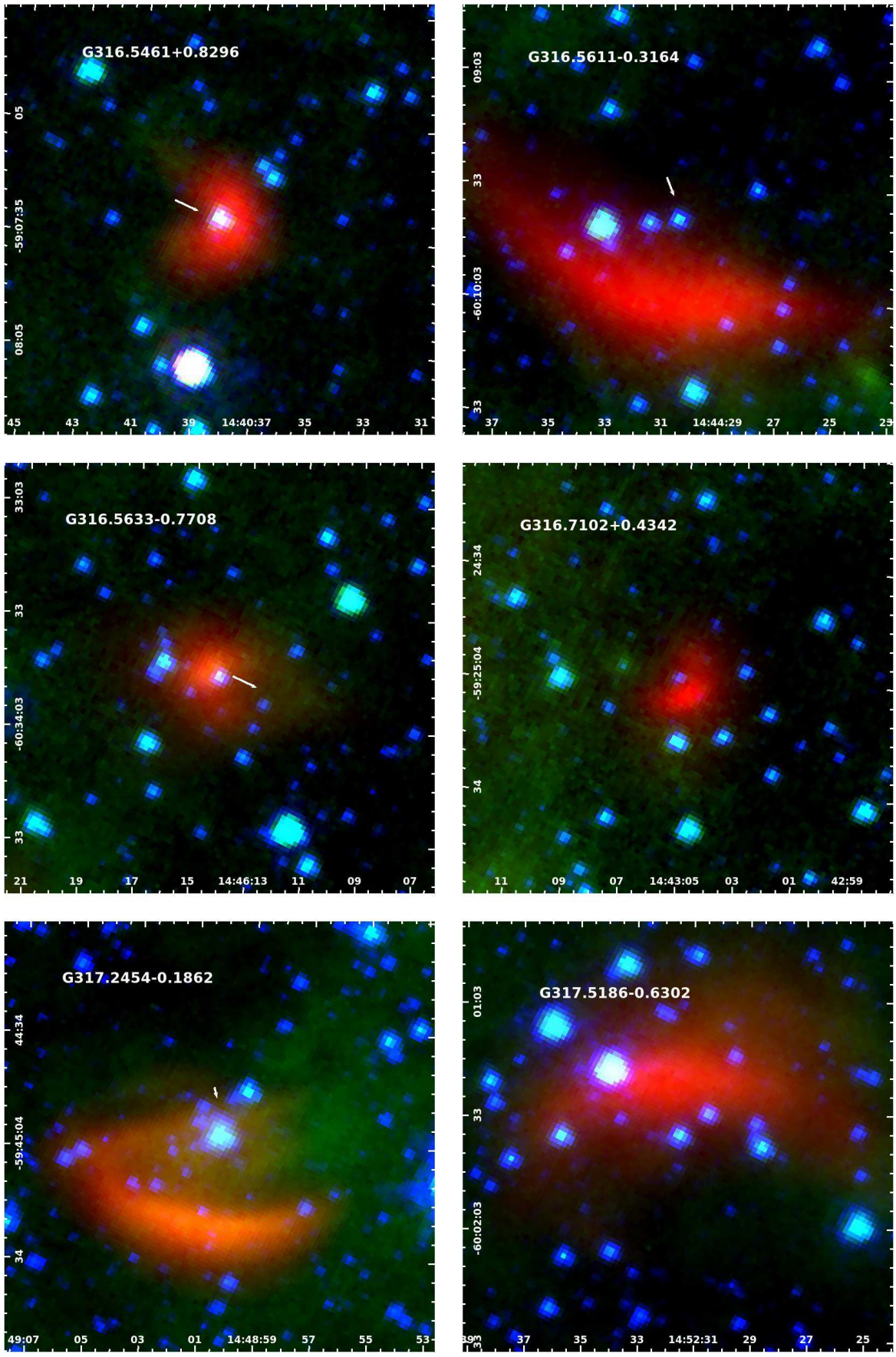
G316.5461+0.8296
G316.5611-0.3164
G316.5633-0.7708
G316.7102+0.4342
G317.2454-0.1862
G317.5186-0.6302

Figure A86.

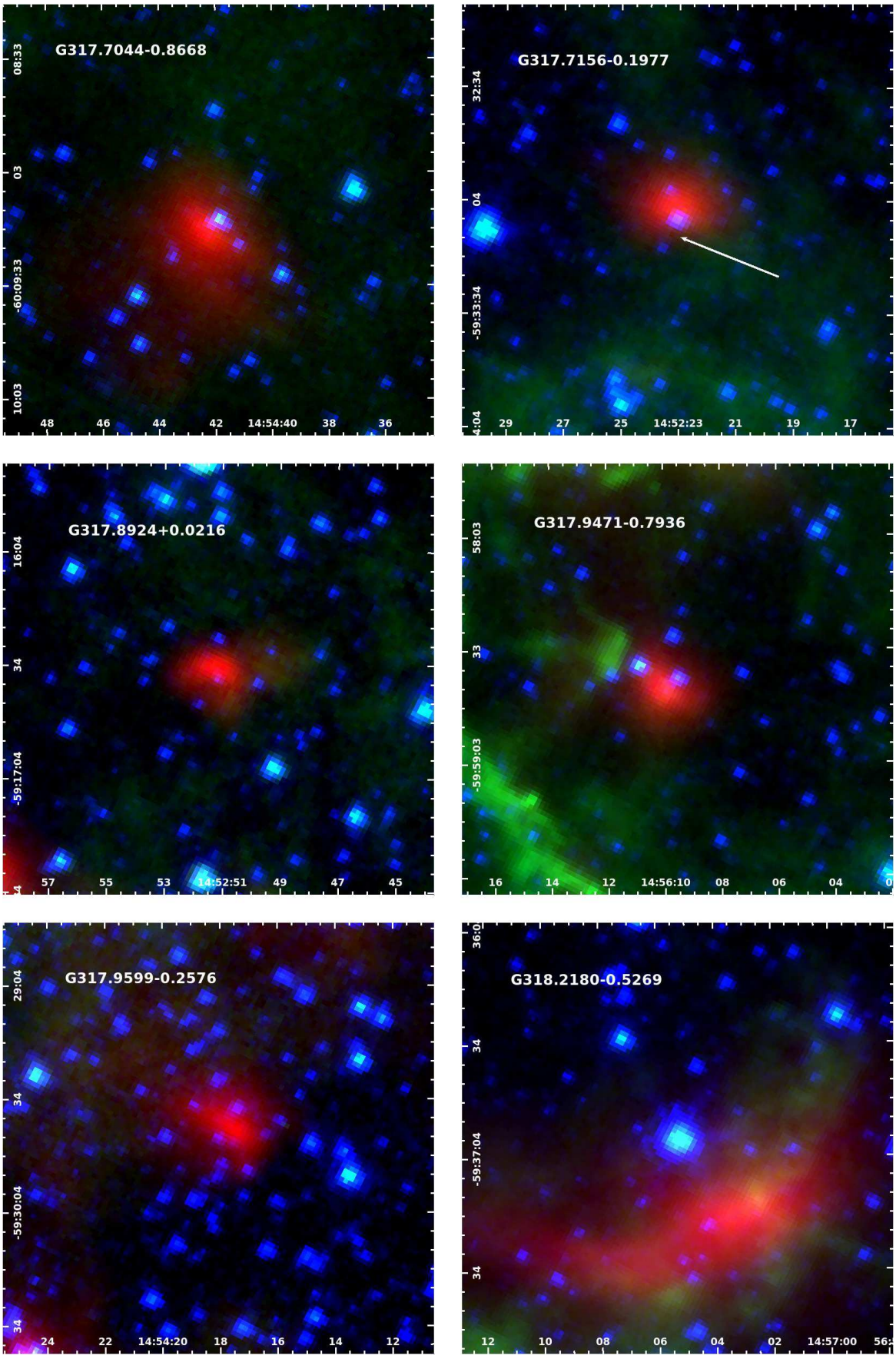
G317.7044-0.8668
08:33
03
-60:09:33
10:03
48
46
44
42
14:54:40
38
36
G317.7156-0.1977
32:34
04
-59:33:34
4:04
29
27
25
14:52:23
21
19
17
G317.8924+0.0216
16:04
34
-59:17:04
57
55
53
14:52:51
49
47
45
G317.9471-0.7936
58:03
33
-59:59:03
16
14
12
14:56:10
08
06
04
G317.9599-0.2576
29:04
34
-59:30:04
34
24
22
14:54:20
18
16
14
12
G318.2180-0.5269
36:0
34
-59:37:04
34
12
10
08
06
04
02
14:57:00

Figure A87.

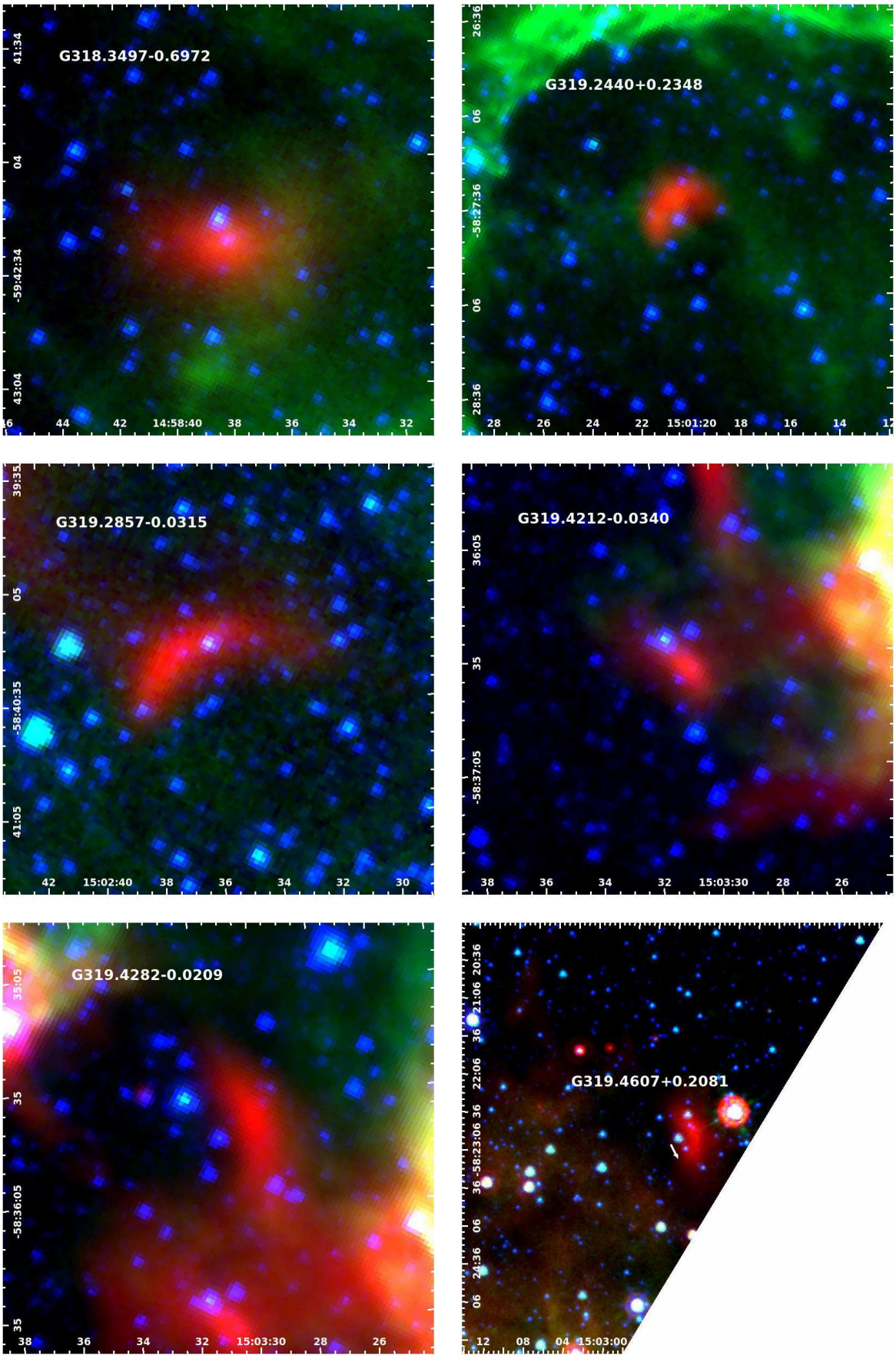
G318.3497-0.6972
G319.2440+0.2348
G319.2857-0.0315
G319.4212-0.0340
G319.4282-0.0209
G319.4607+0.2081

Figure A88.

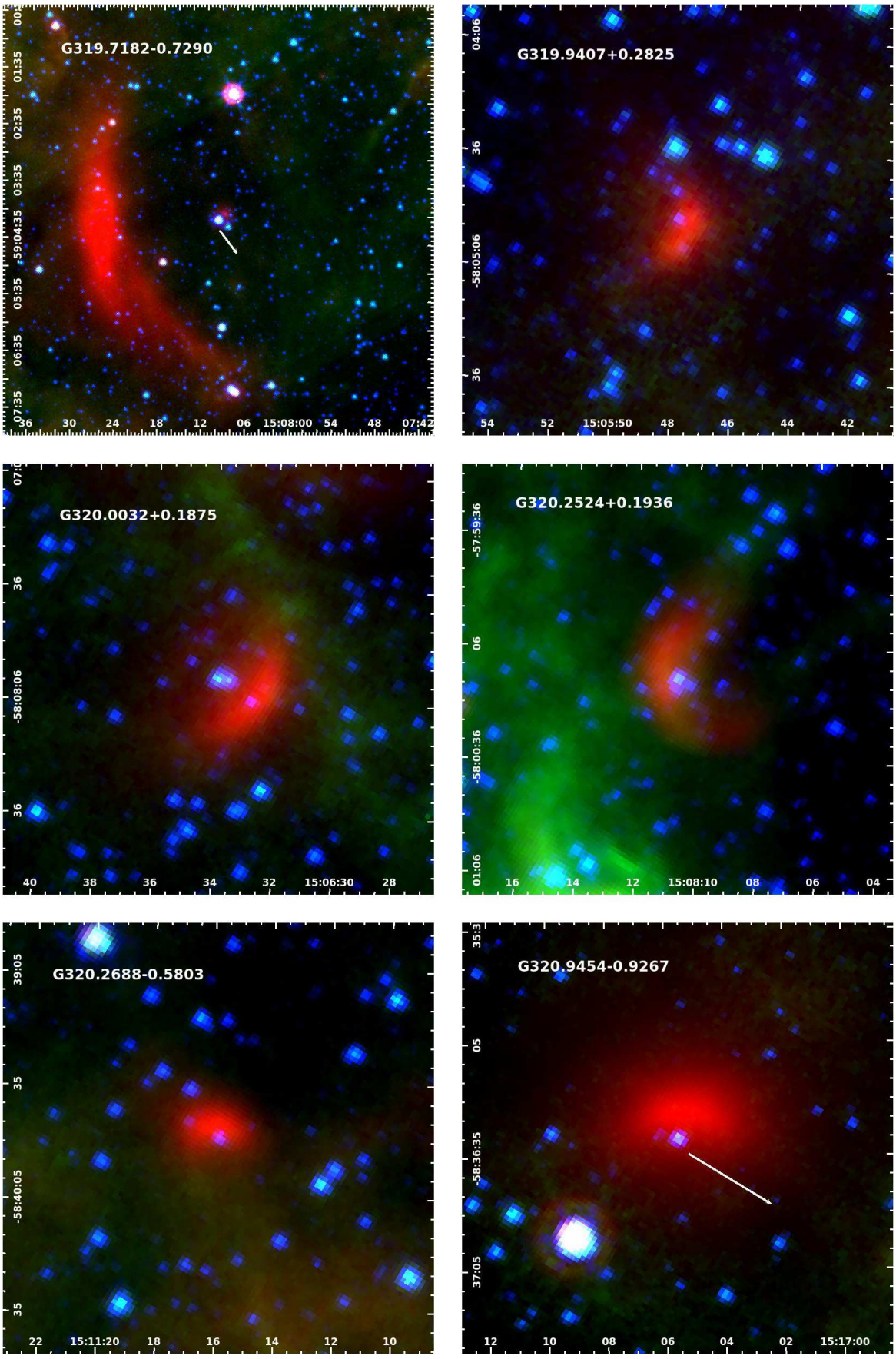
G319.7182-0.7290
G319.9407+0.2825
G320.0032+0.1875
G320.2524+0.1936
G320.2688-0.5803
G320.9454-0.9267

Figure A89.

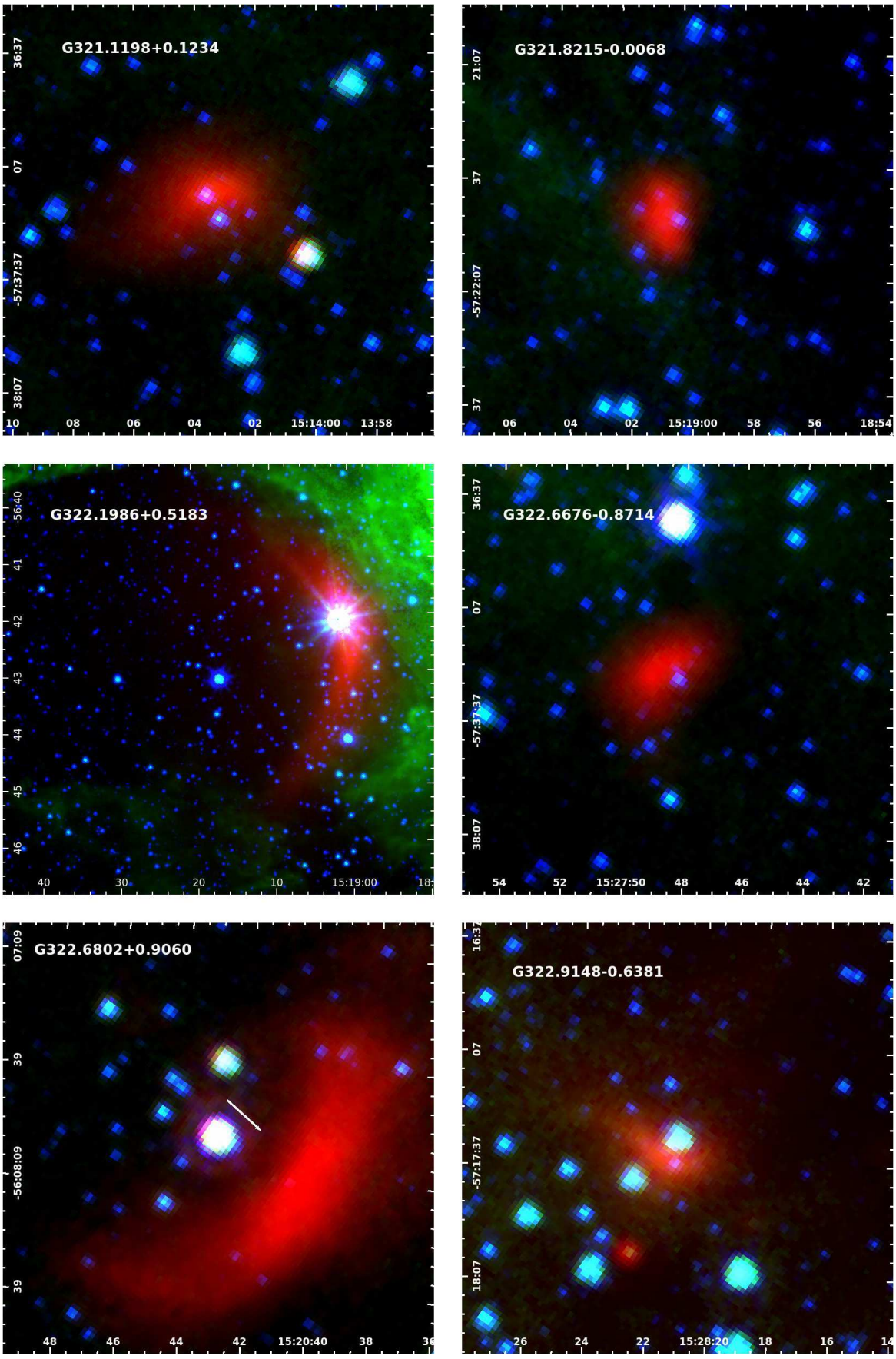
G321.1198+0.1234
G321.8215-0.0068
G322.1986+0.5183
G322.6676-0.8714
G322.6802+0.9060
G322.9148-0.6381

Figure A90.

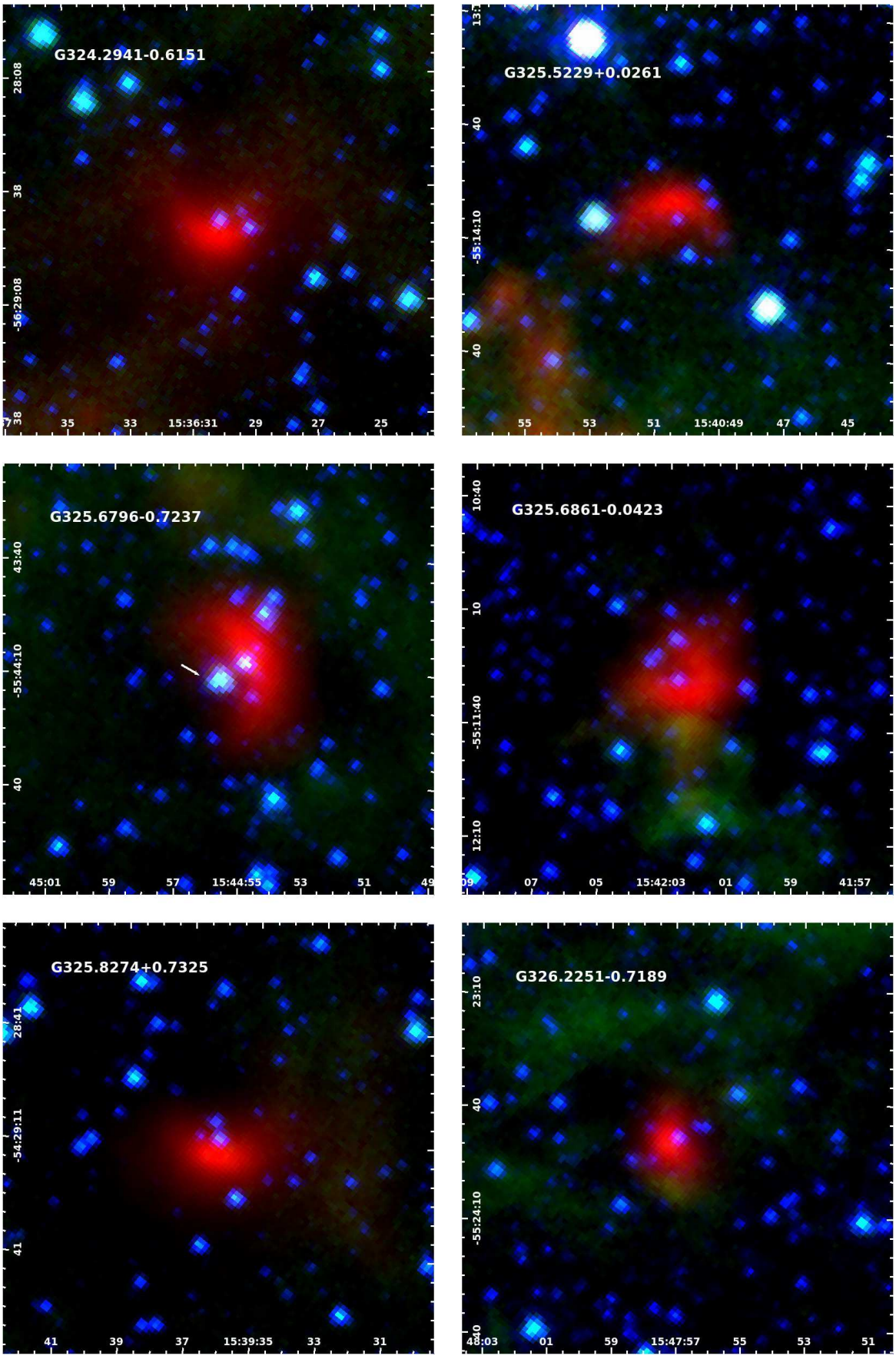
G324.2941-0.6151
28:08
38
-56:29:08
38
35
33
15:36:31
29
27
25
G325.5229+0.0261
40
-55:14:10
40
55
53
51
15:40:49
47
45
G325.6796-0.7237
43:40
-55:44:10
40
45:01
59
57
15:44:55
53
51
G325.6861-0.0423
10:40
10
-55:11:40
12:10
09
07
05
15:42:03
01
59
41:57
G325.8274+0.7325
28:41
-54:29:11
41
41
39
37
15:39:35
33
31
G326.2251-0.7189
23:10
40
-55:24:10
40
48:03
01
59
15:47:57
55
53
51

Figure A91.

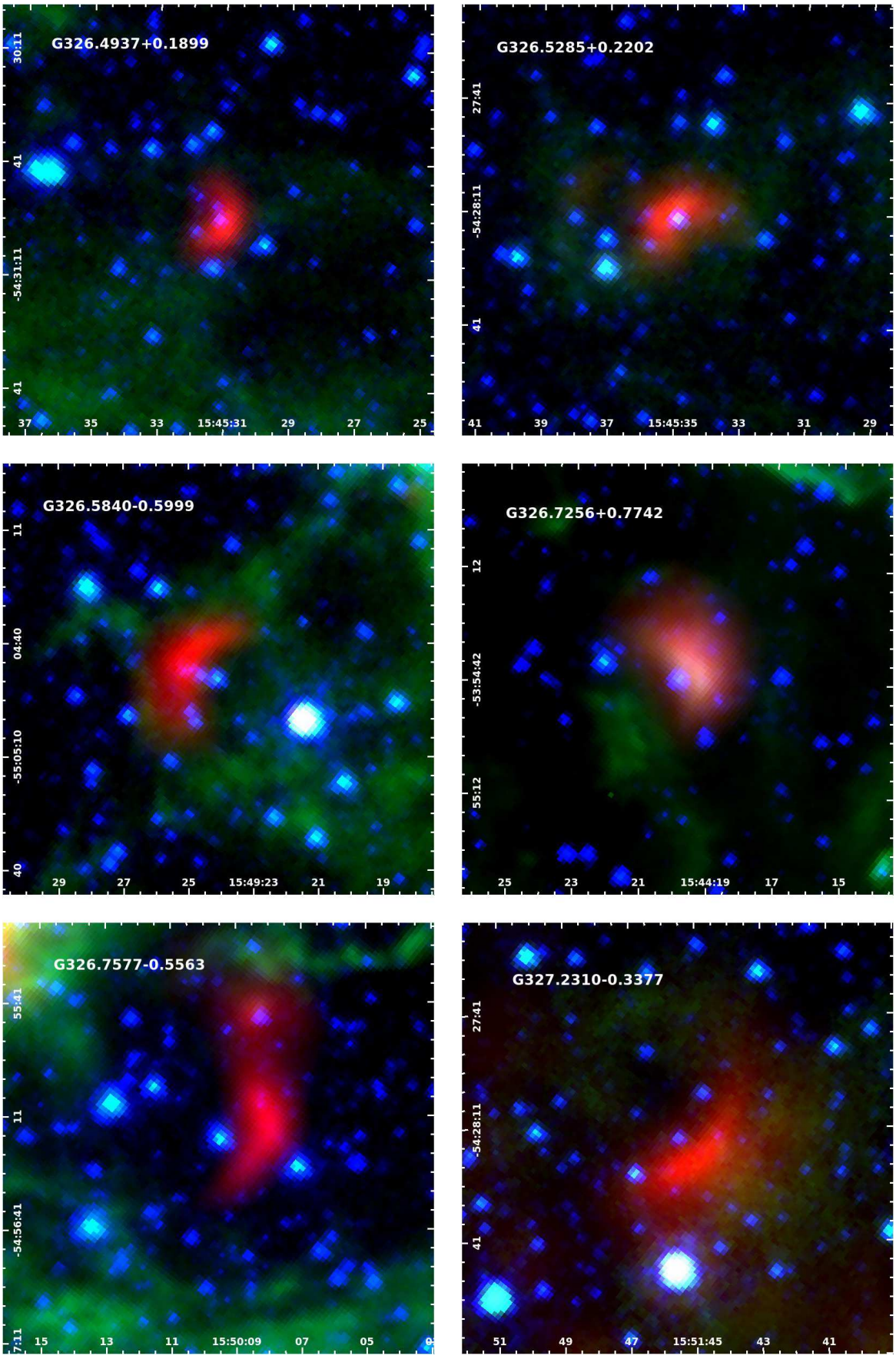
G326.4937+0.1899
30:11
41
-54:31:11
41
37
35
33
15:45:31
29
27
25
G326.5285+0.2202
27:41
-54:28:11
41
41
39
37
15:45:35
33
31
29
G326.5840-0.5999
11
04:40
-55:05:10
40
29
27
25
15:49:23
21
19
G326.7256+0.7742
12
-53:54:42
55:12
25
23
21
15:44:19
17
15
G326.7577-0.5563
55:41
11
-54:56:41
7:11
15
13
11
15:50:09
07
05
G327.2310-0.3377
27:41
-54:28:11
41
51
49
47
15:51:45
43
41

Figure A92.

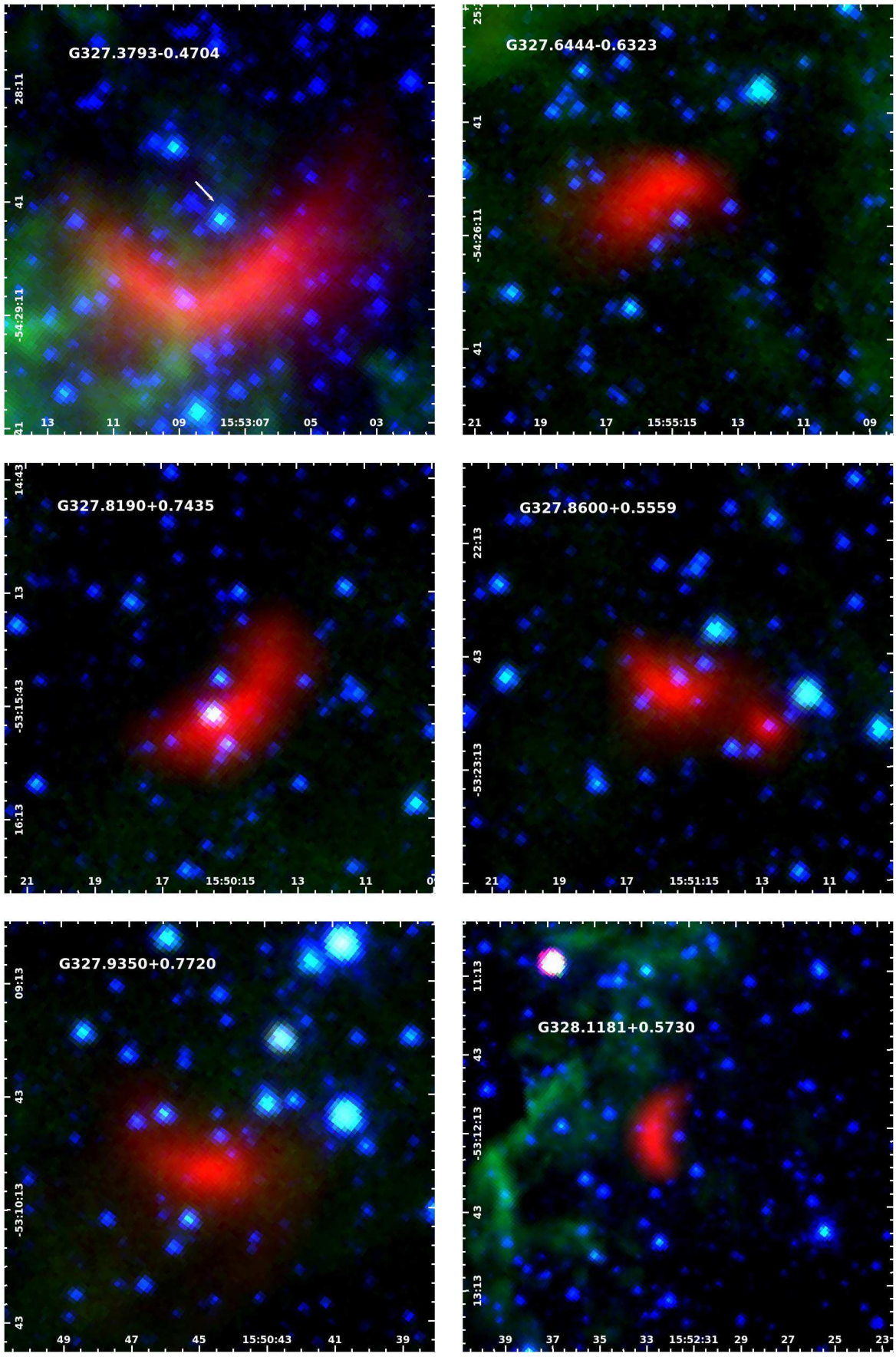
G327.3793-0.4704
G327.6444-0.6323
G327.8190+0.7435
G327.8600+0.5559
G327.9350+0.7720
G328.1181+0.5730

Figure A93.

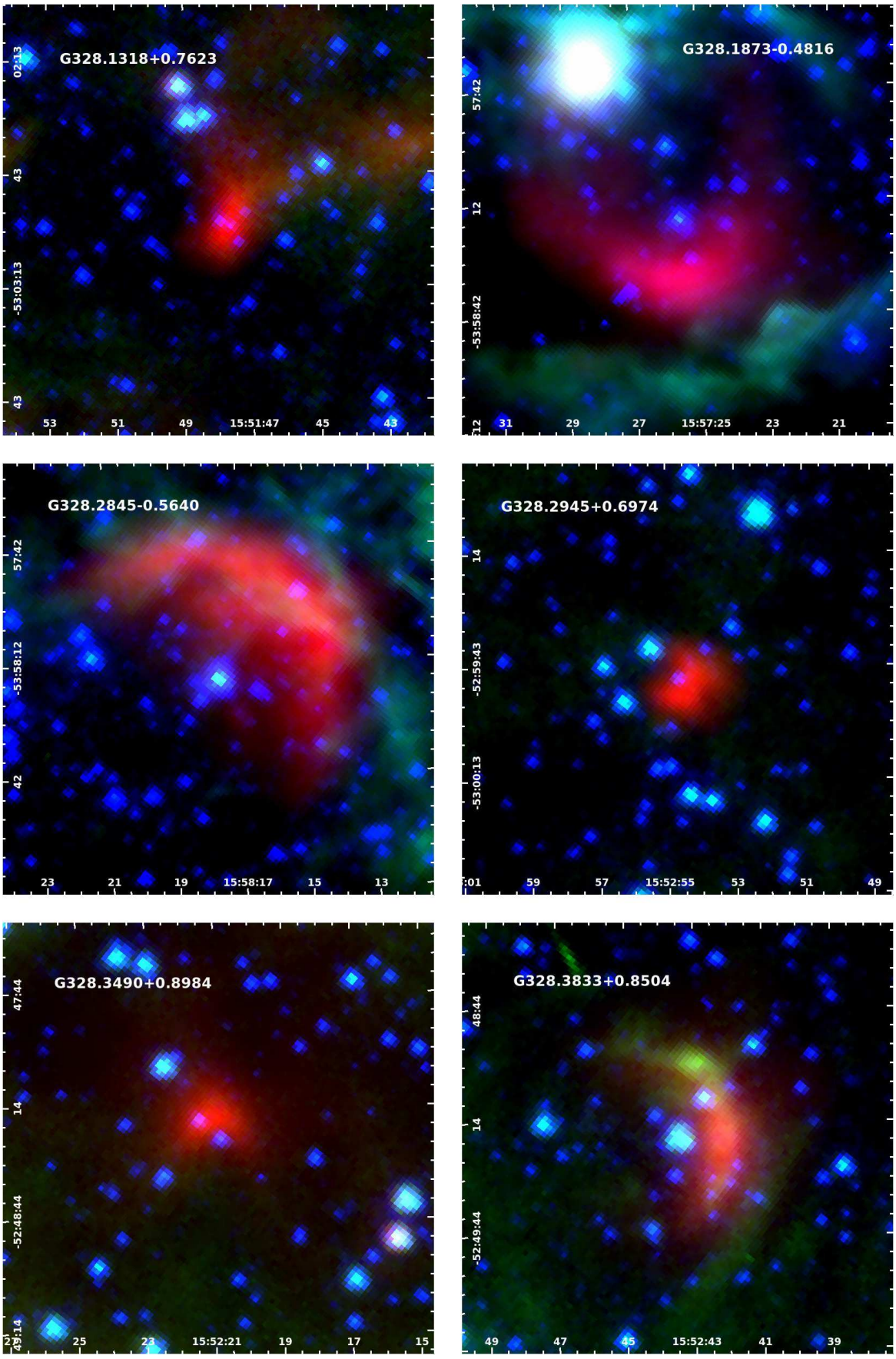
G328.1318+0.7623
02:13
43
-53:03:13
43
53
51
49
15:51:47
45
43
G328.1873-0.4816
57:42
12
-53:58:42
12
31
29
27
15:57:25
23
21
G328.2845-0.5640
57:42
-53:58:12
42
23
21
19
15:58:17
15
13
G328.2945+0.6974
14
-52:59:43
-53:00:13
01
59
57
15:52:55
53
51
49
G328.3490+0.8984
47:44
14
-52:48:44
29:14
25
23
15:52:21
19
17
15
G328.3833+0.8504
48:44
14
-52:49:44
49
47
45
15:52:43
41
39

Figure A94.

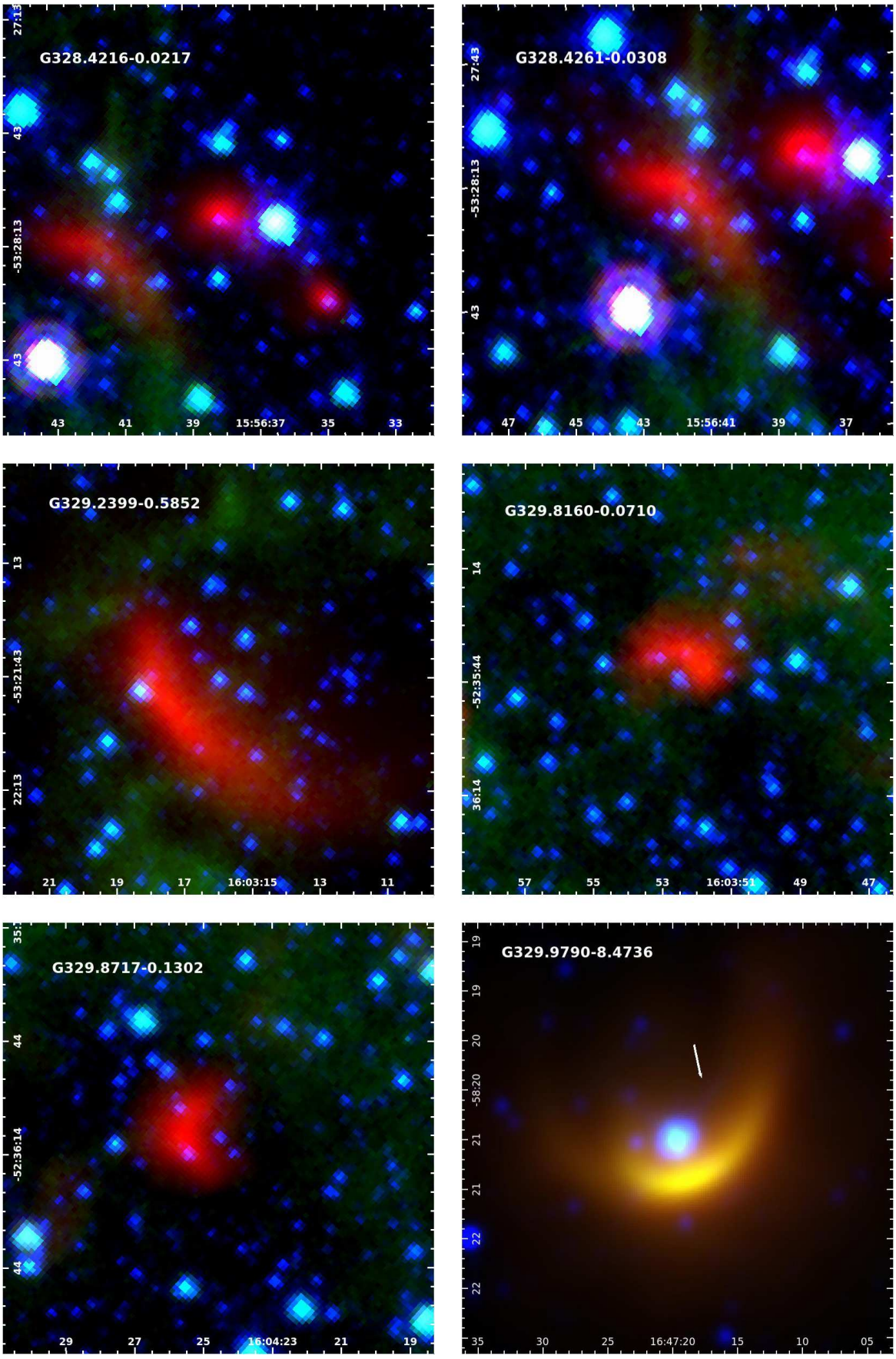
G328.4216-0.0217
G328.4261-0.0308
G329.2399-0.5852
G329.8160-0.0710
G329.8717-0.1302
G329.9790-8.4736

Figure A95.

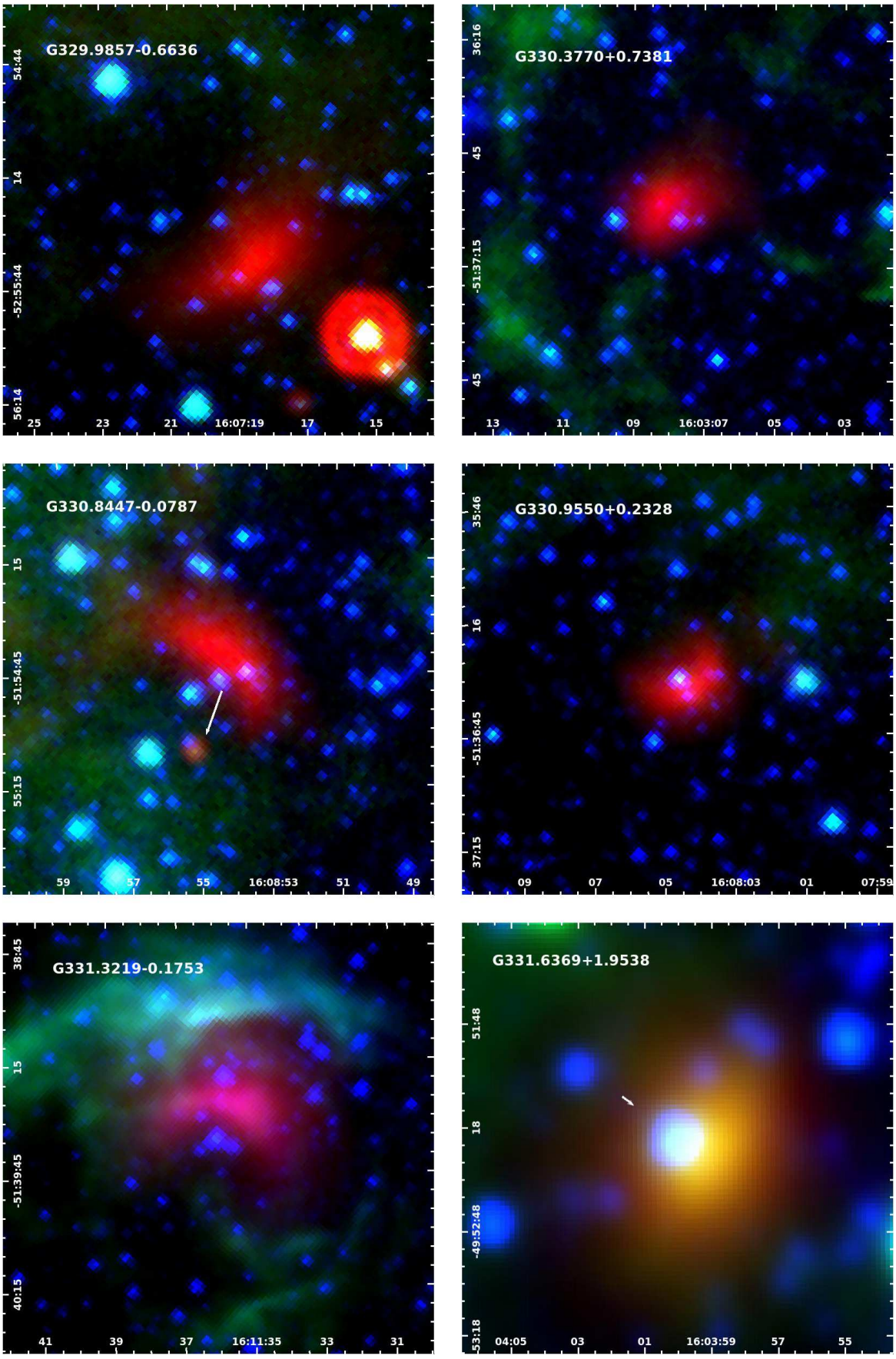
G329.9857-0.6636
54:44
14
-52:55:44
56:14
25
23
21
16:07:19
17
15
G330.3770+0.7381
36:16
45
-51:37:15
45
13
11
09
16:03:07
05
03
G330.8447-0.0787
15
-51:54:45
55:15
59
57
55
16:08:53
51
49
G330.9550+0.2328
35:46
16
-51:36:45
37:15
09
07
05
16:08:03
01
07:59
G331.3219-0.1753
38:45
15
-51:39:45
40:15
41
39
37
16:11:35
33
31
G331.6369+1.9538
51:48
18
-49:52:48
53:18
04:05
03
01
16:03:59
57
55

Figure A96.

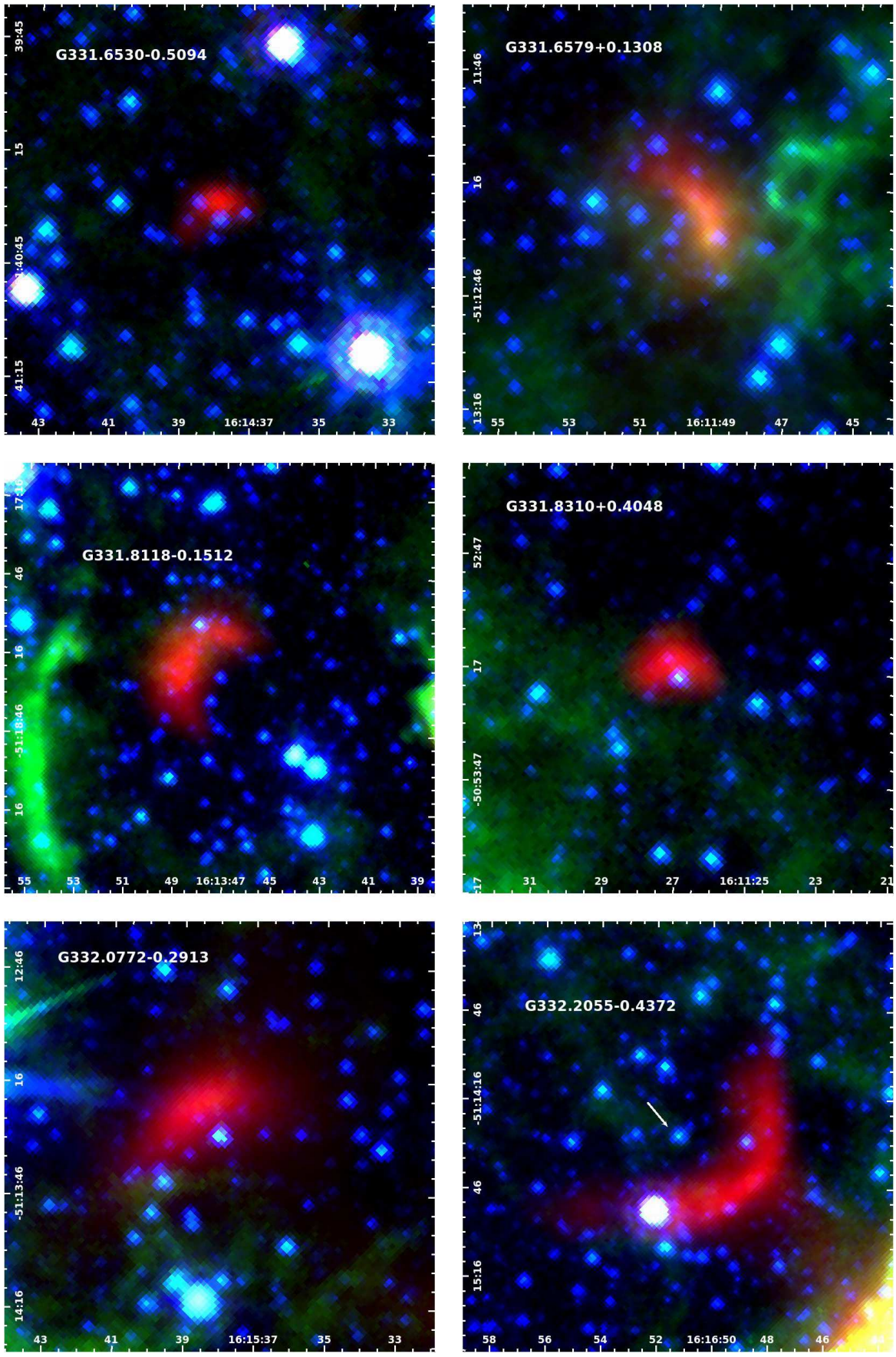
G331.6530-0.5094
G331.6579+0.1308
G331.8118-0.1512
G331.8310+0.4048
G332.0772-0.2913
G332.2055-0.4372

Figure A97.

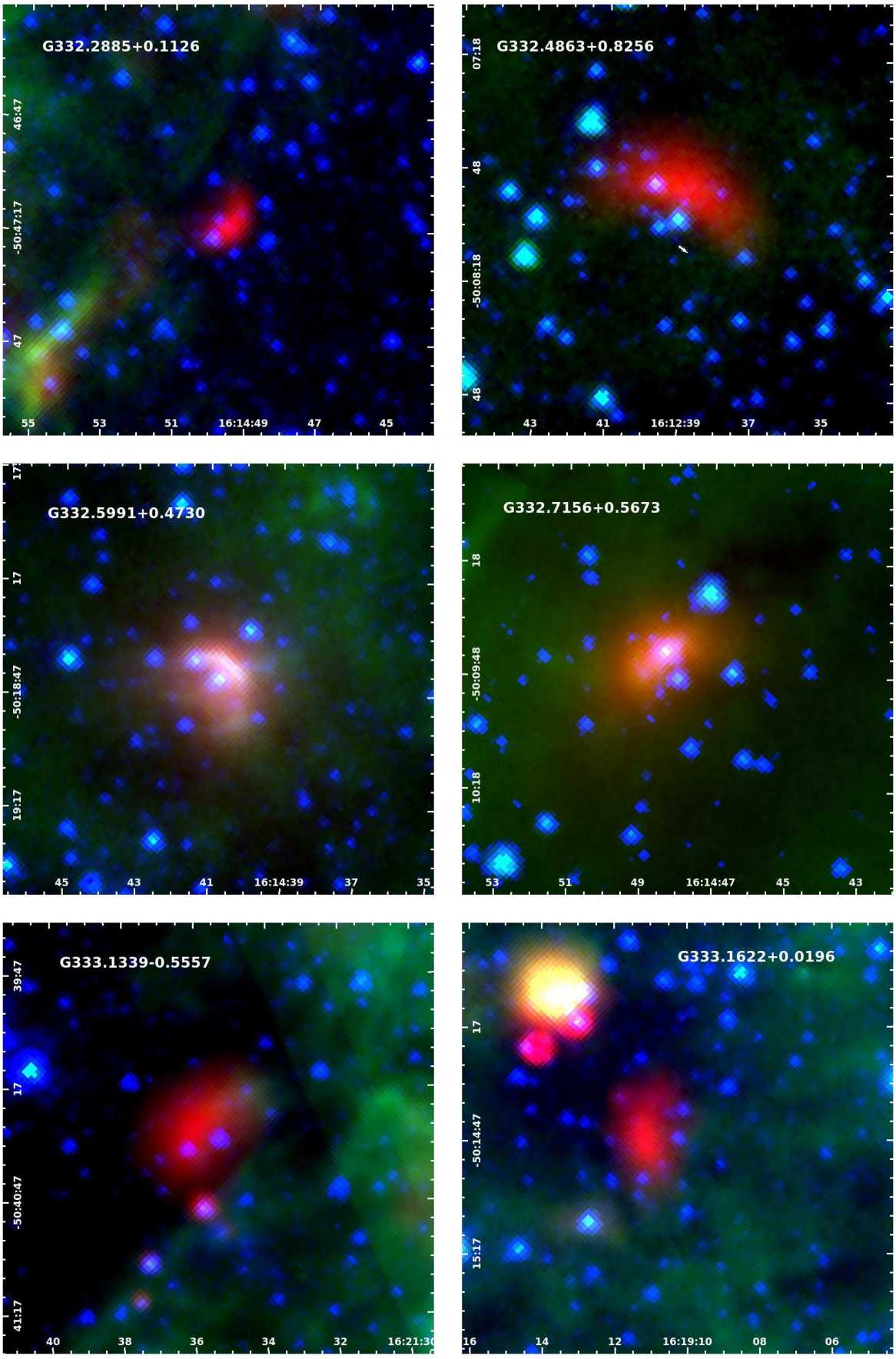
G332.2885+0.1126
G332.4863+0.8256
G332.5991+0.4730
G332.7156+0.5673
G333.1339-0.5557
G333.1622+0.0196

Figure A98.

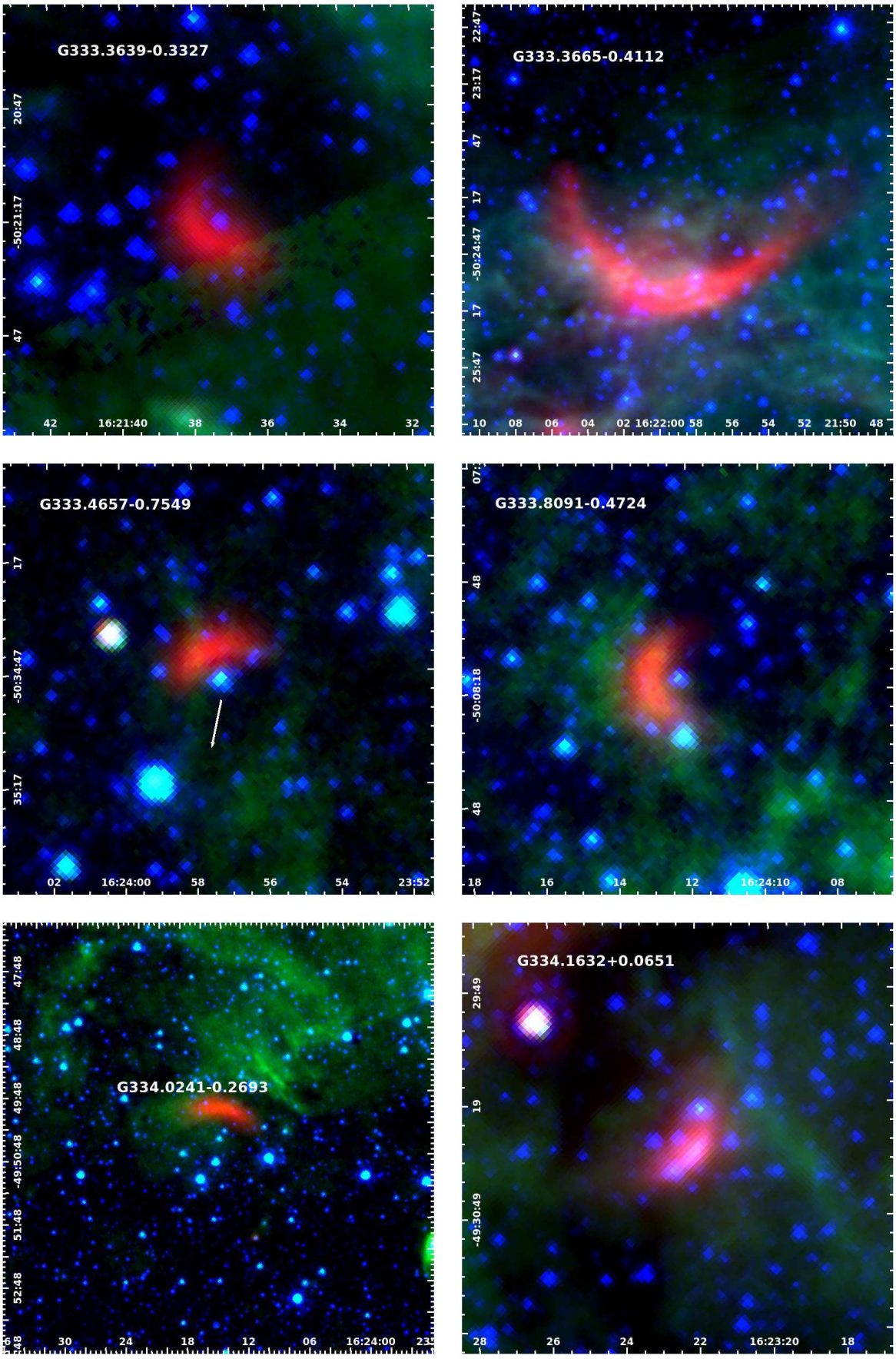
G333.3639-0.3327
G333.3665-0.4112
G333.4657-0.7549
G333.8091-0.4724
G334.0241-0.2693
G334.1632+0.0651

Figure A99.

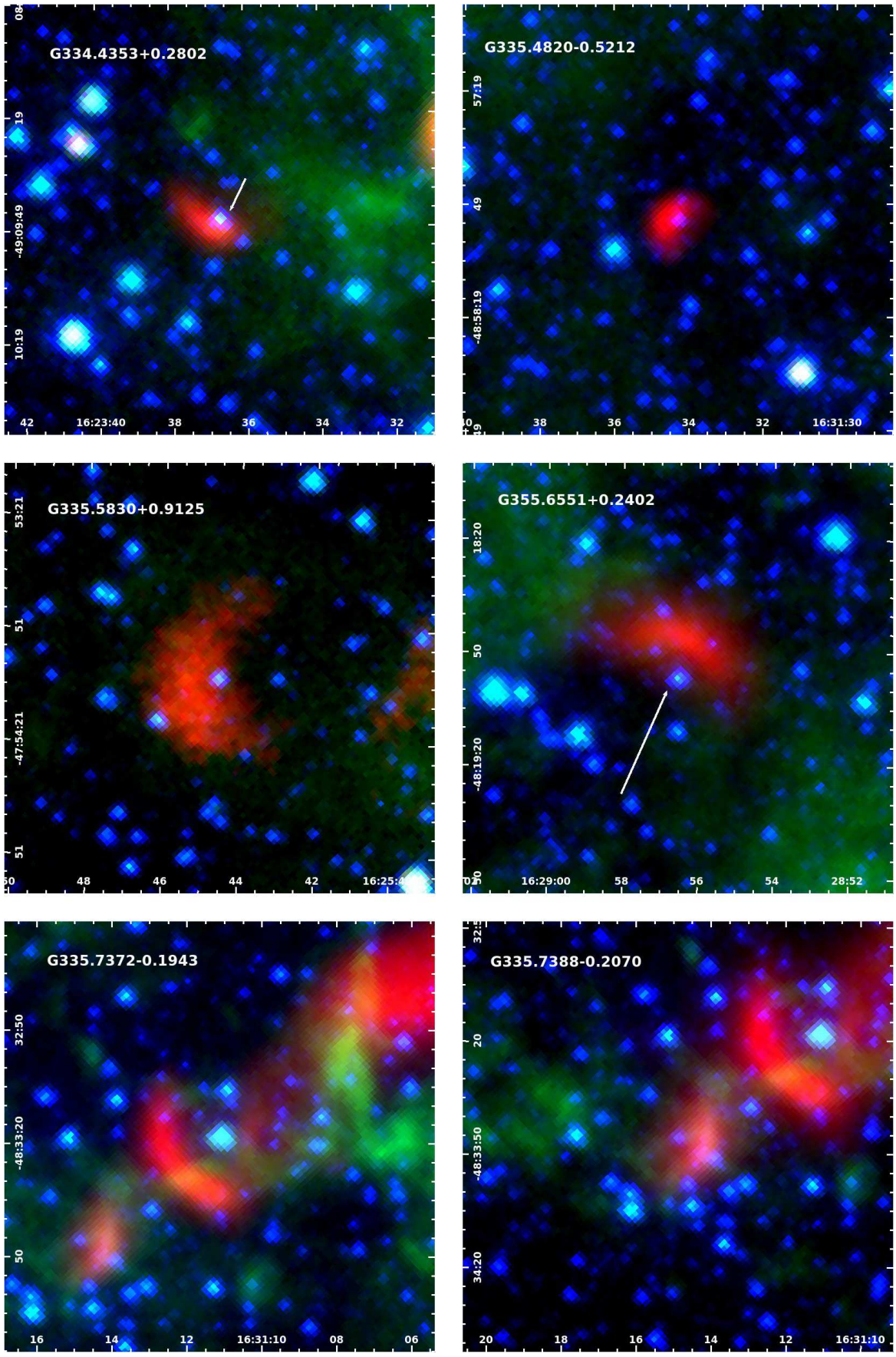
G334.4353+0.2802
G335.4820-0.5212
G335.5830+0.9125
G355.6551+0.2402
G335.7372-0.1943
G335.7388-0.2070

Figure A100.

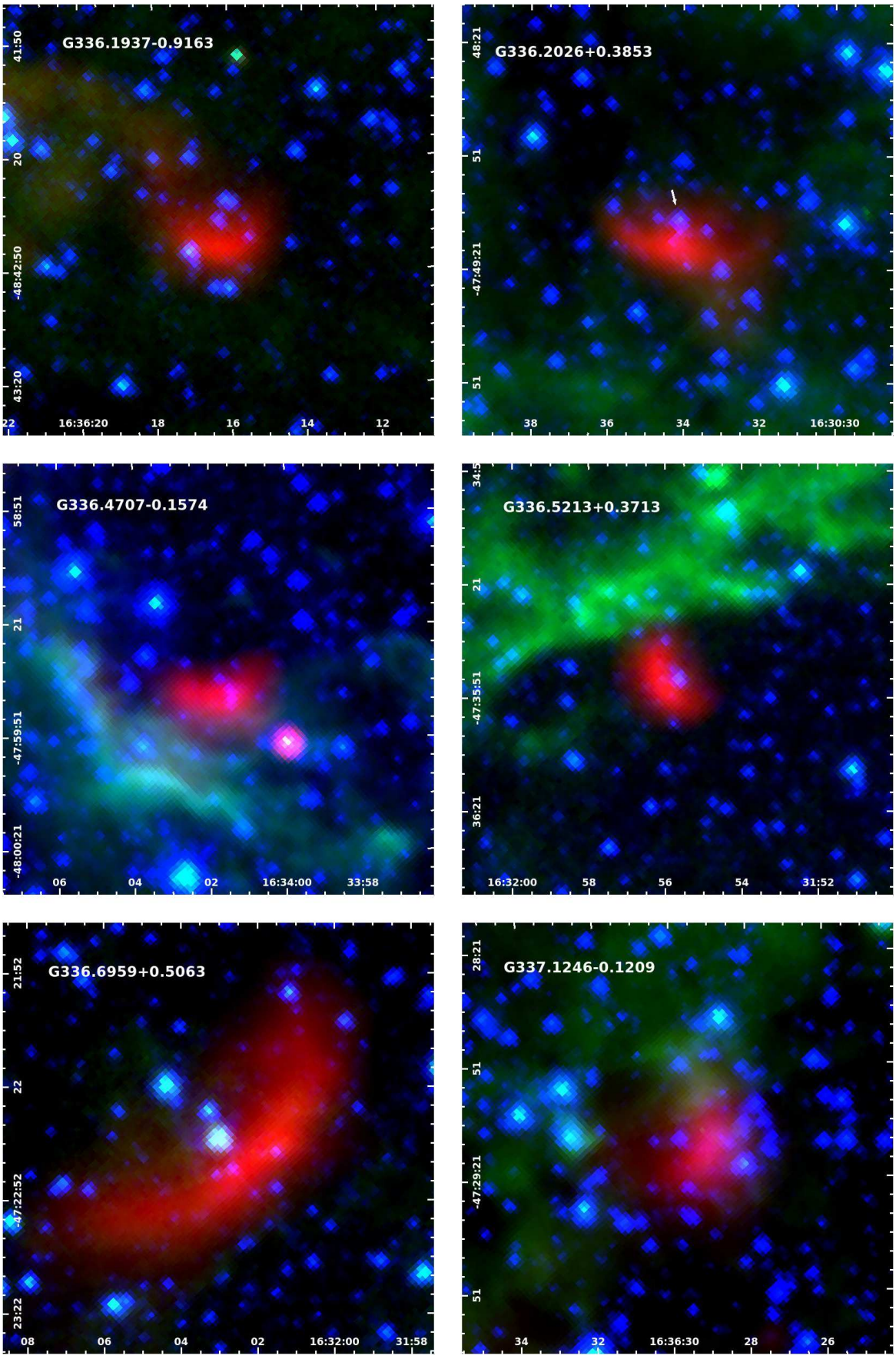
G336.1937-0.9163
41:50
20
-48:42:50
43:20
22
16:36:20
18
16
14
12
G336.2026+0.3853
48:21
51
-47:49:21
51
38
36
34
32
16:30:30
G336.4707-0.1574
58:51
21
-47:59:51
-48:00:21
06
04
02
16:34:00
33:58
G336.5213+0.3713
34:5
21
-47:35:51
36:21
16:32:00
58
56
54
31:52
G336.6959+0.5063
21:52
22
-47:22:52
23:22
08
06
04
02
16:32:00
31:58
G337.1246-0.1209
28:21
51
-47:29:21
51
34
32
16:36:30
28
26

Figure A101.

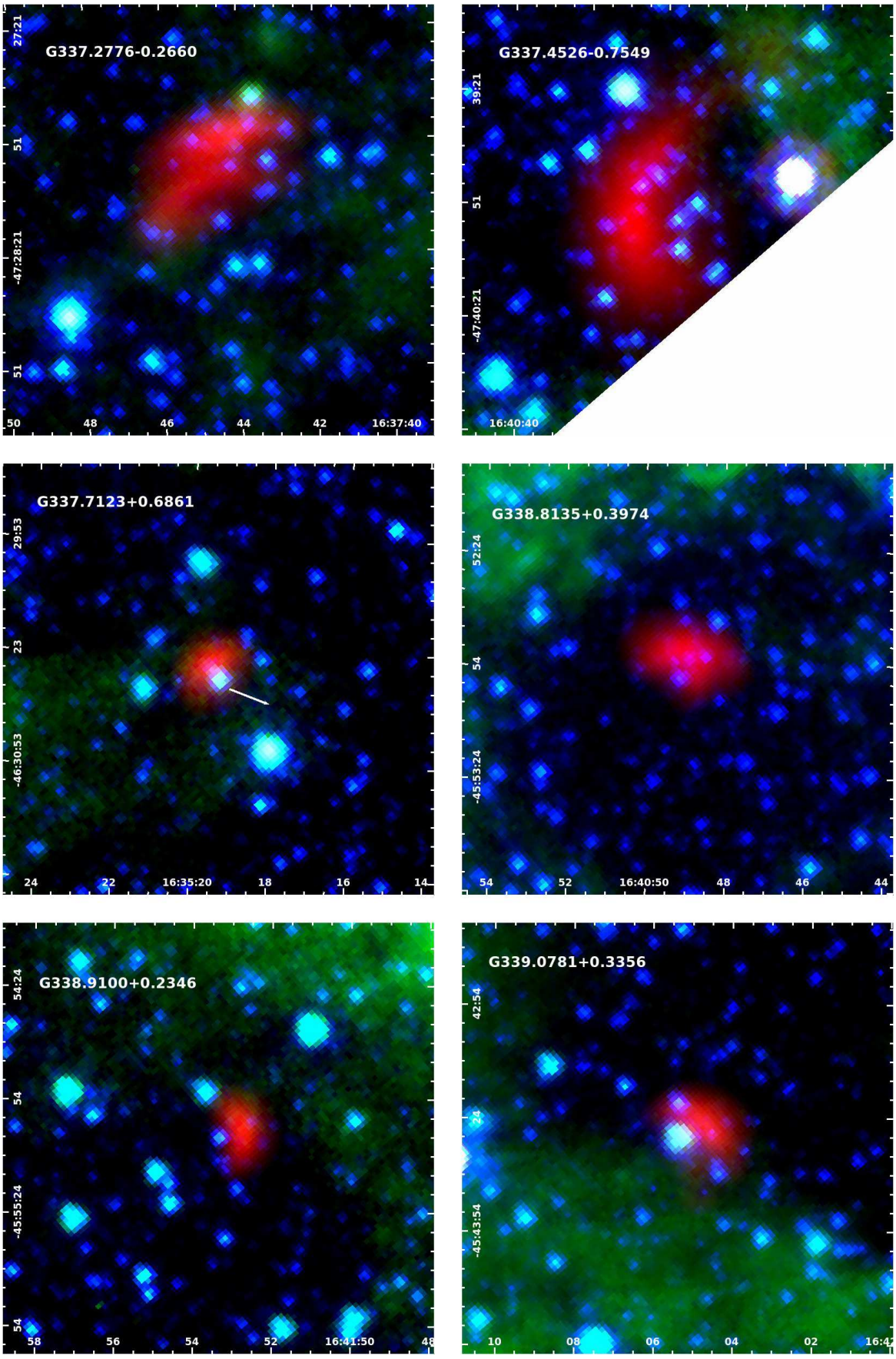
G337.2776-0.2660
27:21
51
-47:28:21
51
50
48
46
44
42
16:37:40
G337.4526-0.7549
39:21
51
-47:40:21
16:40:40
G337.7123+0.6861
29:53
23
-46:30:53
24
22
16:35:20
18
16
14
G338.8135+0.3974
52:24
54
-45:53:24
54
52
16:40:50
48
46
44
G338.9100+0.2346
54:24
54
-45:55:24
54
58
56
54
52
16:41:50
48
G339.0781+0.3356
42:54
24
-45:43:54
10
08
06
04
02
16:4

Figure A102.

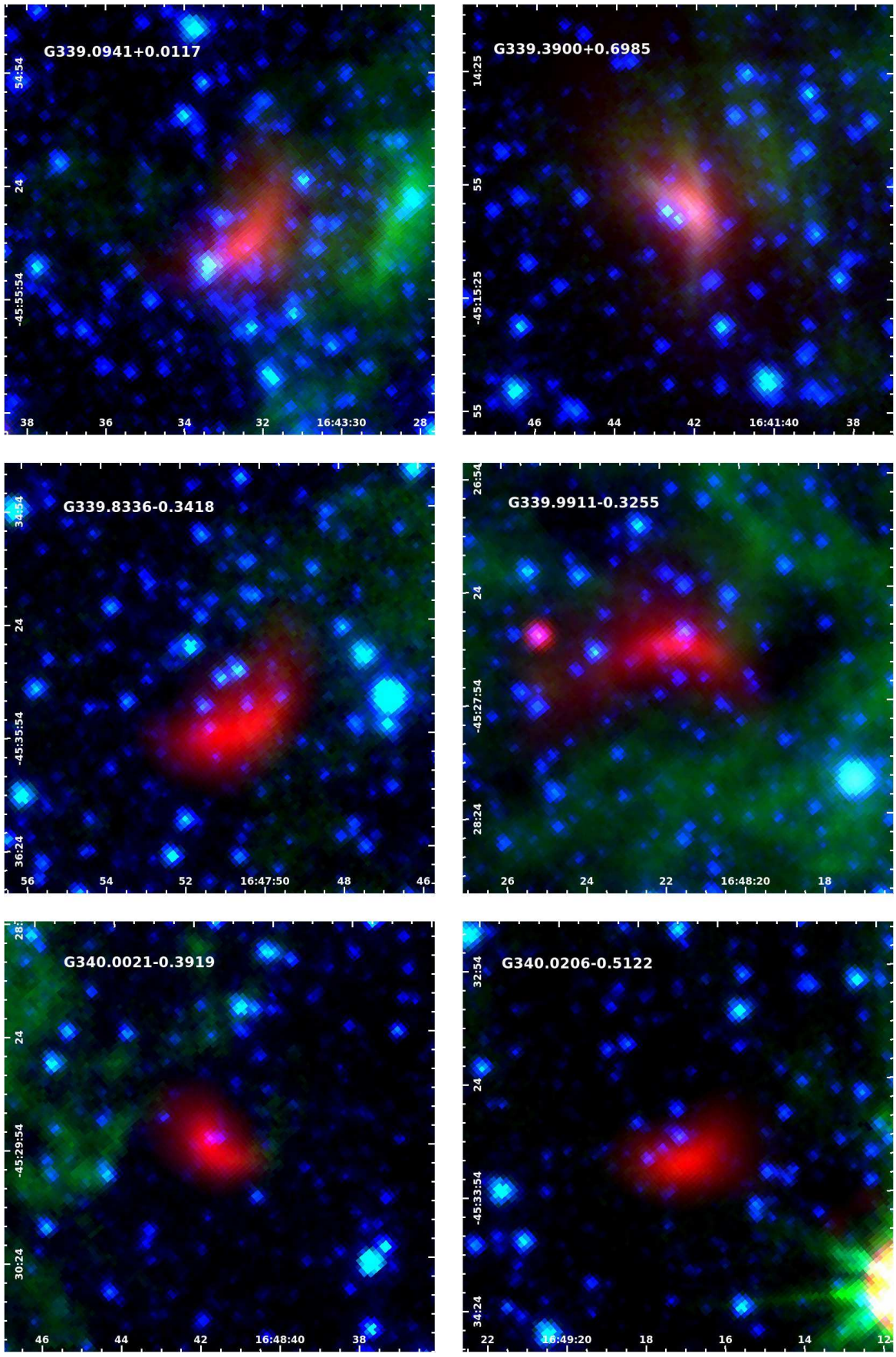
G339.0941+0.0117
54:54
24
-45:55:54
38
36
34
32
16:43:30
28
G339.3900+0.6985
14:25
55
-45:15:25
55
46
44
42
16:41:40
38
G339.8336-0.3418
34:54
24
-45:35:54
36:24
56
54
52
16:47:50
48
46
G339.9911-0.3255
26:54
24
-45:27:54
28:24
26
24
22
16:48:20
18
G340.0021-0.3919
24
-45:29:54
30:24
46
44
42
16:48:40
38
G340.0206-0.5122
32:54
24
-45:33:54
34:24
22
16:49:20
18
16
14

Figure A103.

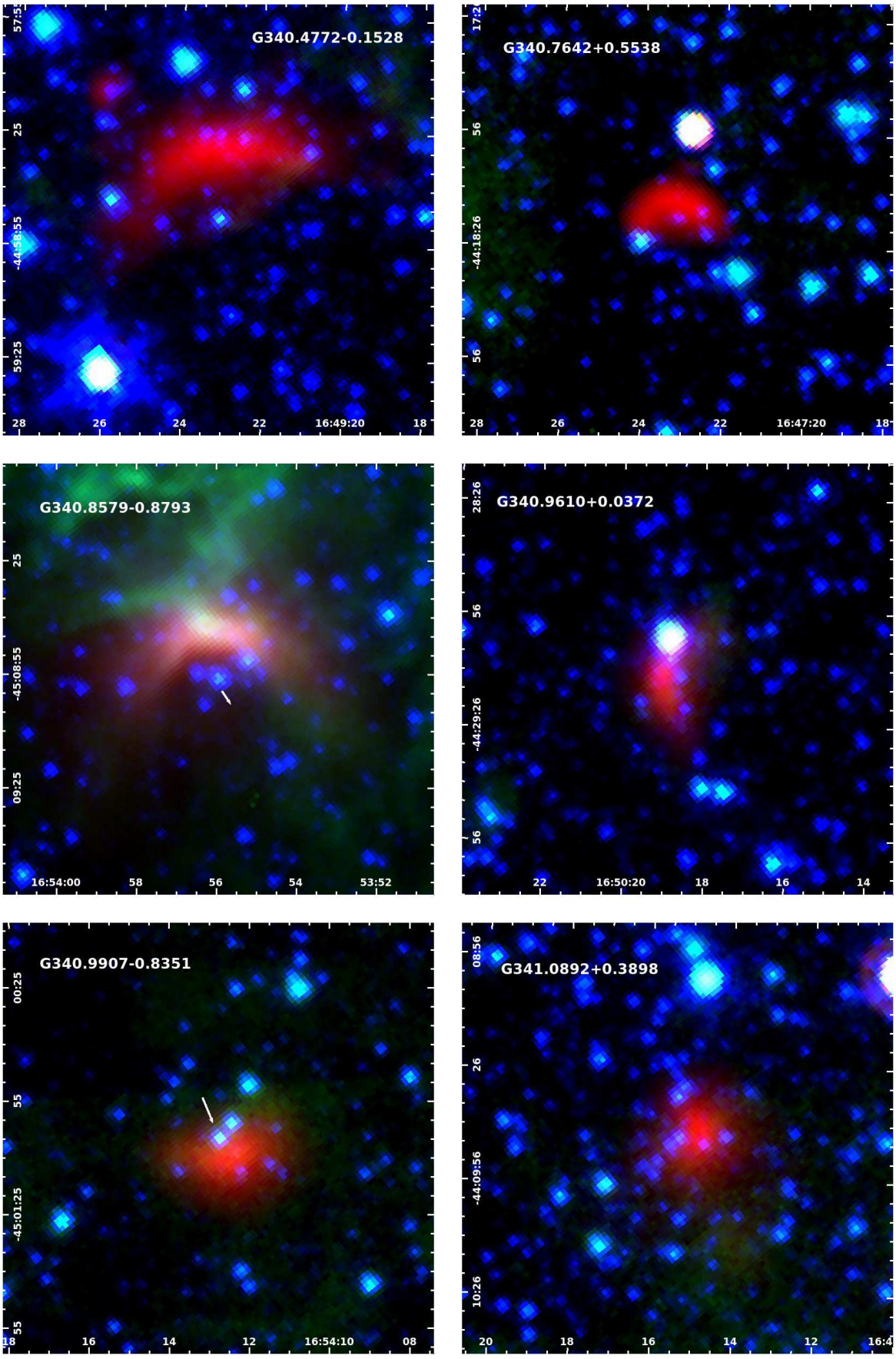
G340.4772-0.1528
G340.7642+0.5538
G340.8579-0.8793
G340.9610+0.0372
G340.9907-0.8351
G341.0892+0.3898

Figure A104.

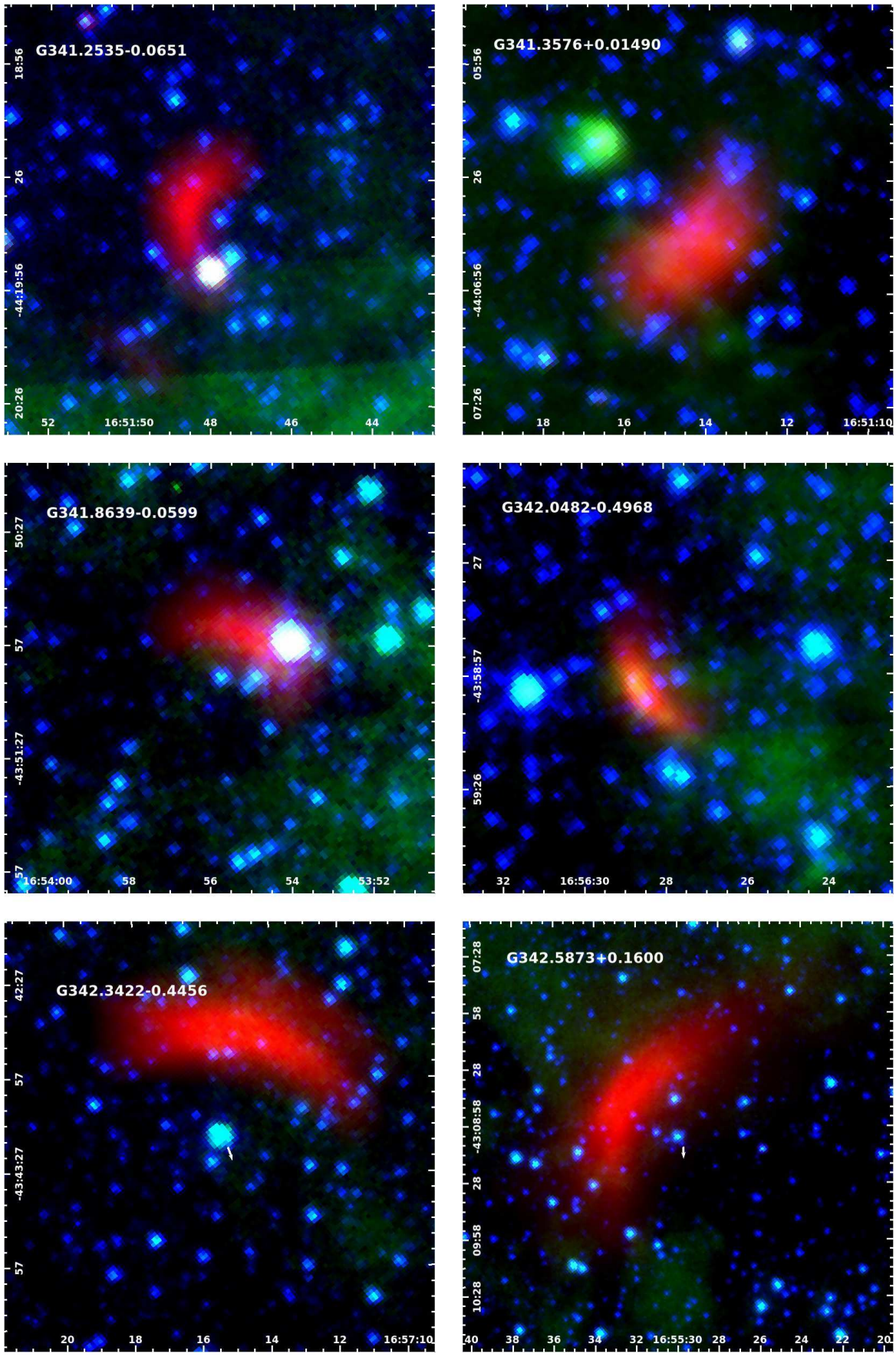
G341.2535-0.0651
18:56
26
-44:19:56
20:26
52
16:51:50
48
46
44
G341.3576+0.01490
05:56
26
-44:06:56
07:26
18
16
14
12
16:51:10
G341.8639-0.0599
50:27
57
-43:51:27
57
16:54:00
58
56
54
53:52
G342.0482-0.4968
27
-43:58:57
59:26
32
16:56:30
28
26
24
G342.3422-0.4456
42:27
57
-43:43:27
57
20
18
16
14
12
16:57:10
G342.5873+0.1600
07:28
58
28
-43:08:58
28
09:58
10:28
40
38
36
34
32
16:55:30
28
26
24
22
20

Figure A105.

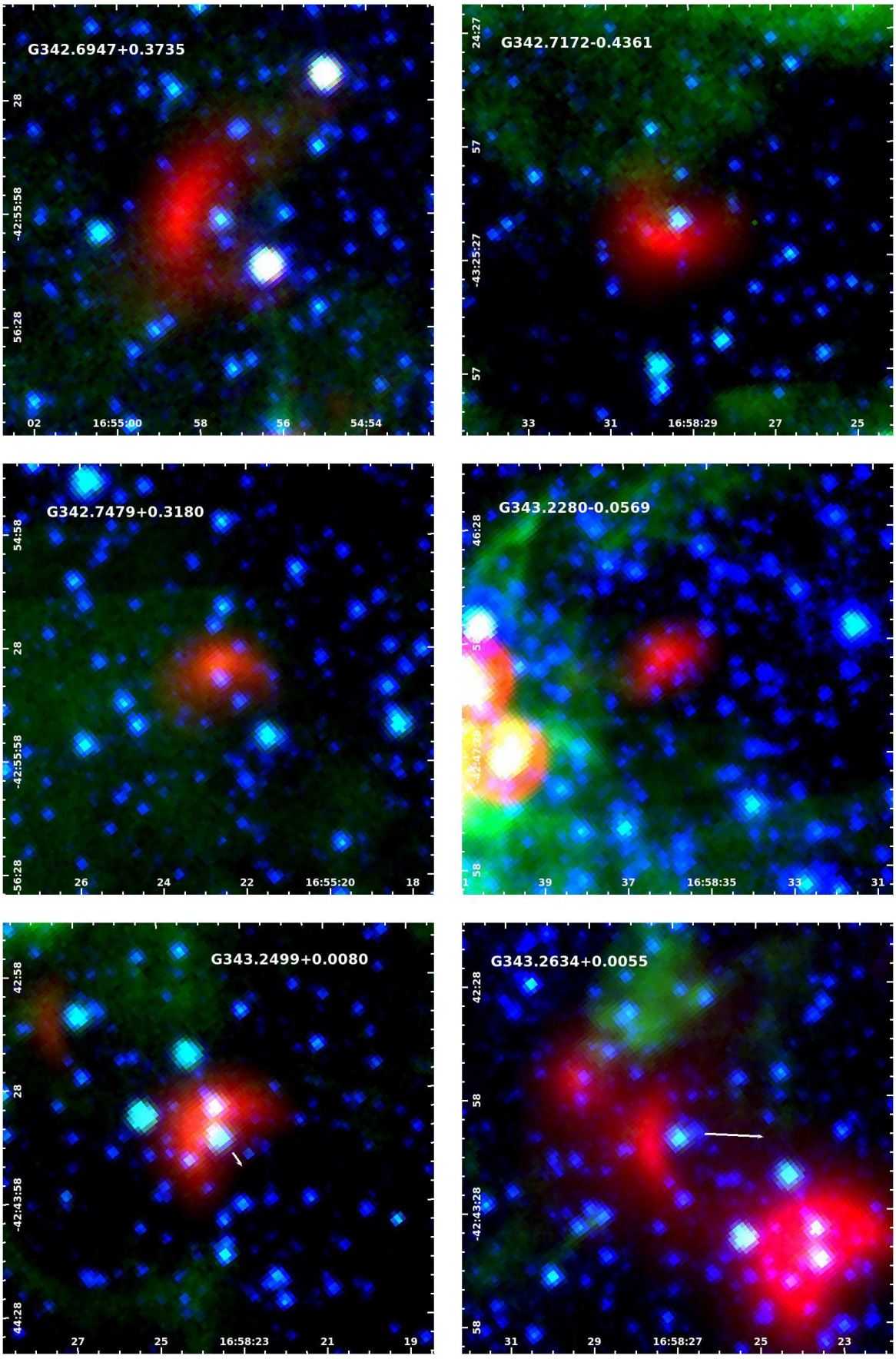
G342.6947+0.3735
G342.7172-0.4361
G342.7479+0.3180
G343.2280-0.0569
G343.2499+0.0080
G343.2634+0.0055

Figure A106.

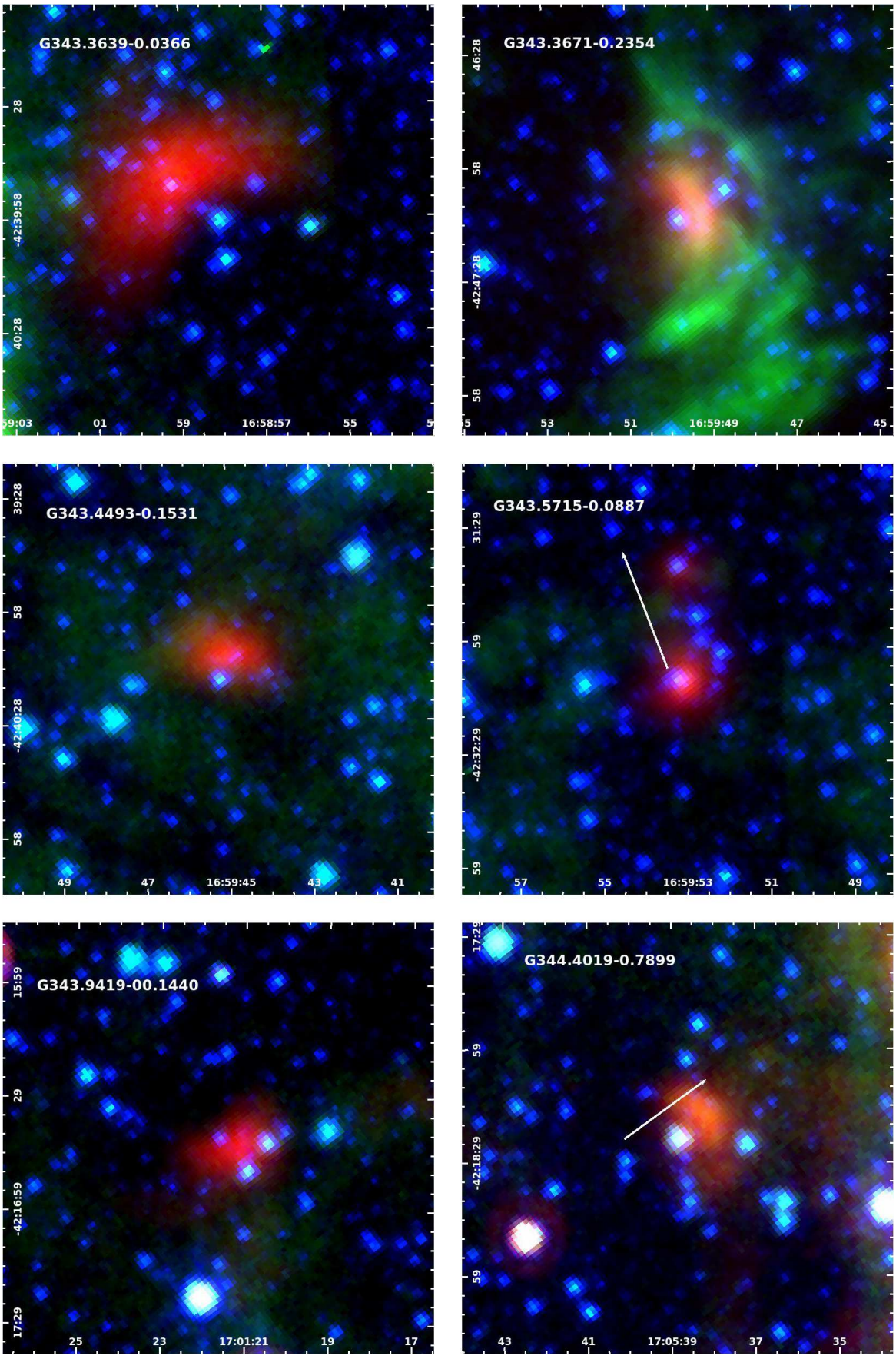
G343.3639-0.0366
G343.3671-0.2354
G343.4493-0.1531
G343.5715-0.0887
G343.9419-00.1440
G344.4019-0.7899

Figure A107.

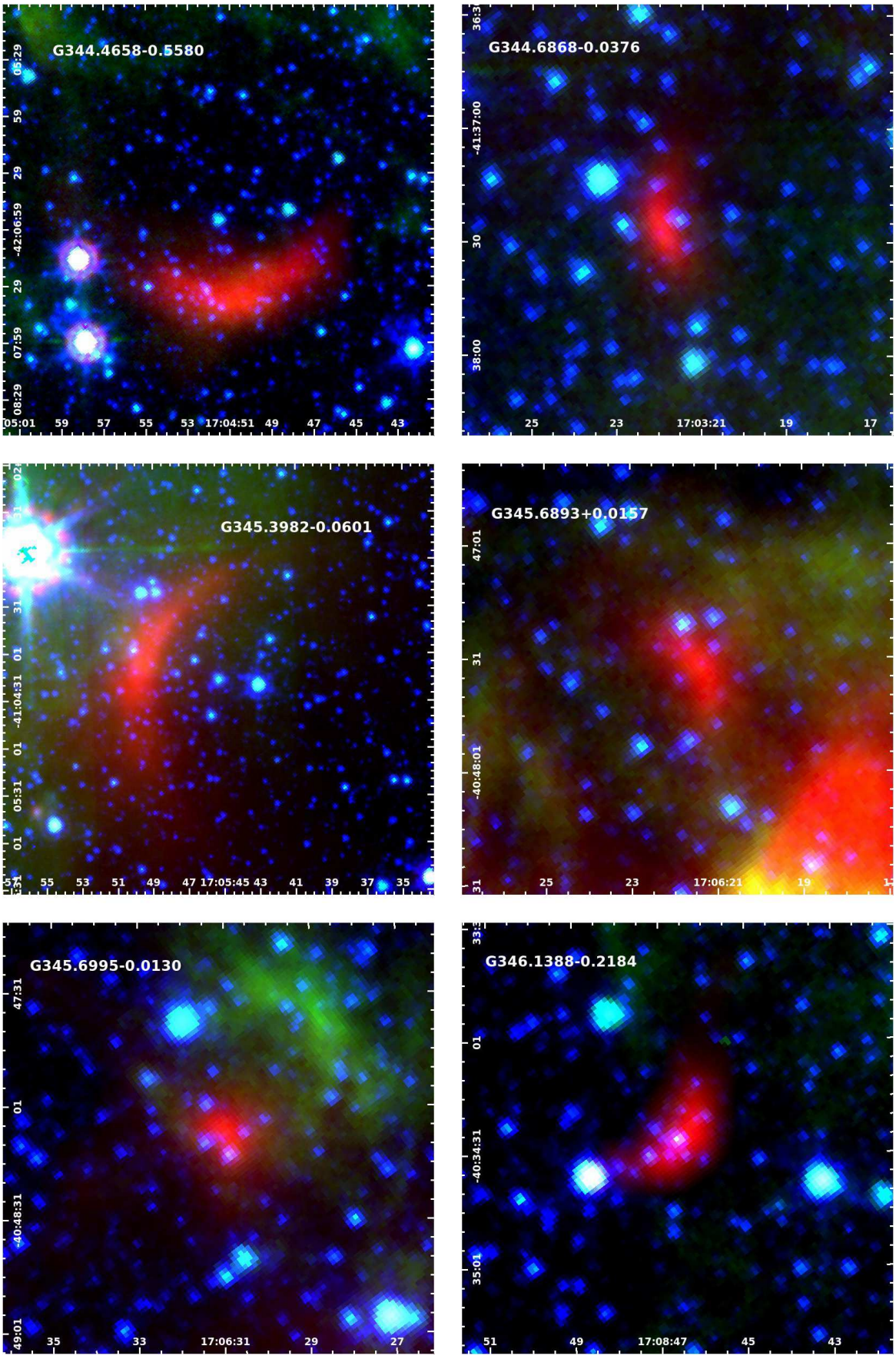
G344.4658-0.5580
G344.6868-0.0376
G345.3982-0.0601
G345.6893+0.0157
G345.6995-0.0130
G346.1388-0.2184

Figure A108.

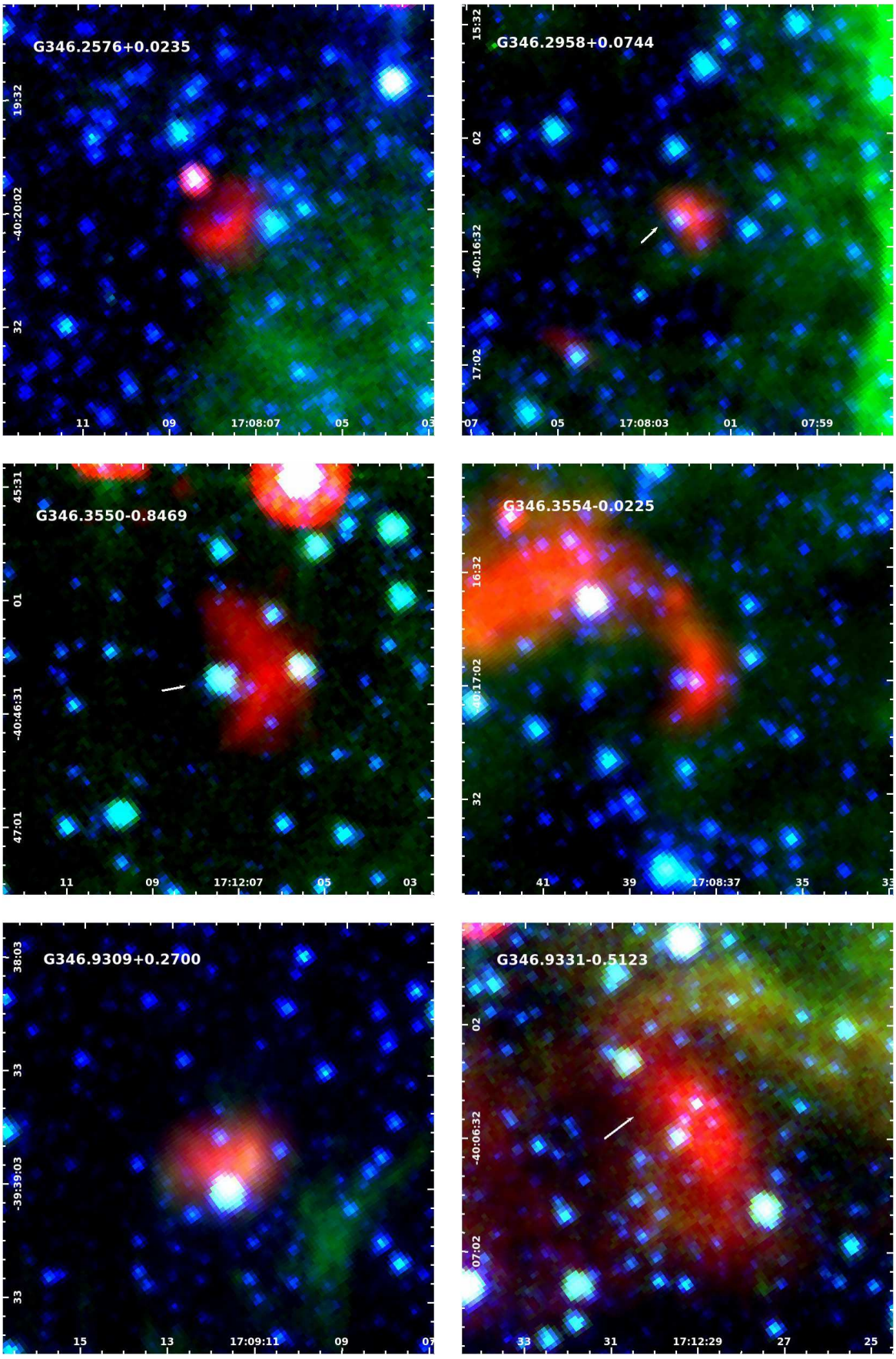
G346.2576+0.0235
G346.2958+0.0744
G346.3550-0.8469
G346.3554-0.0225
G346.9309+0.2700
G346.9331-0.5123

Figure A109.

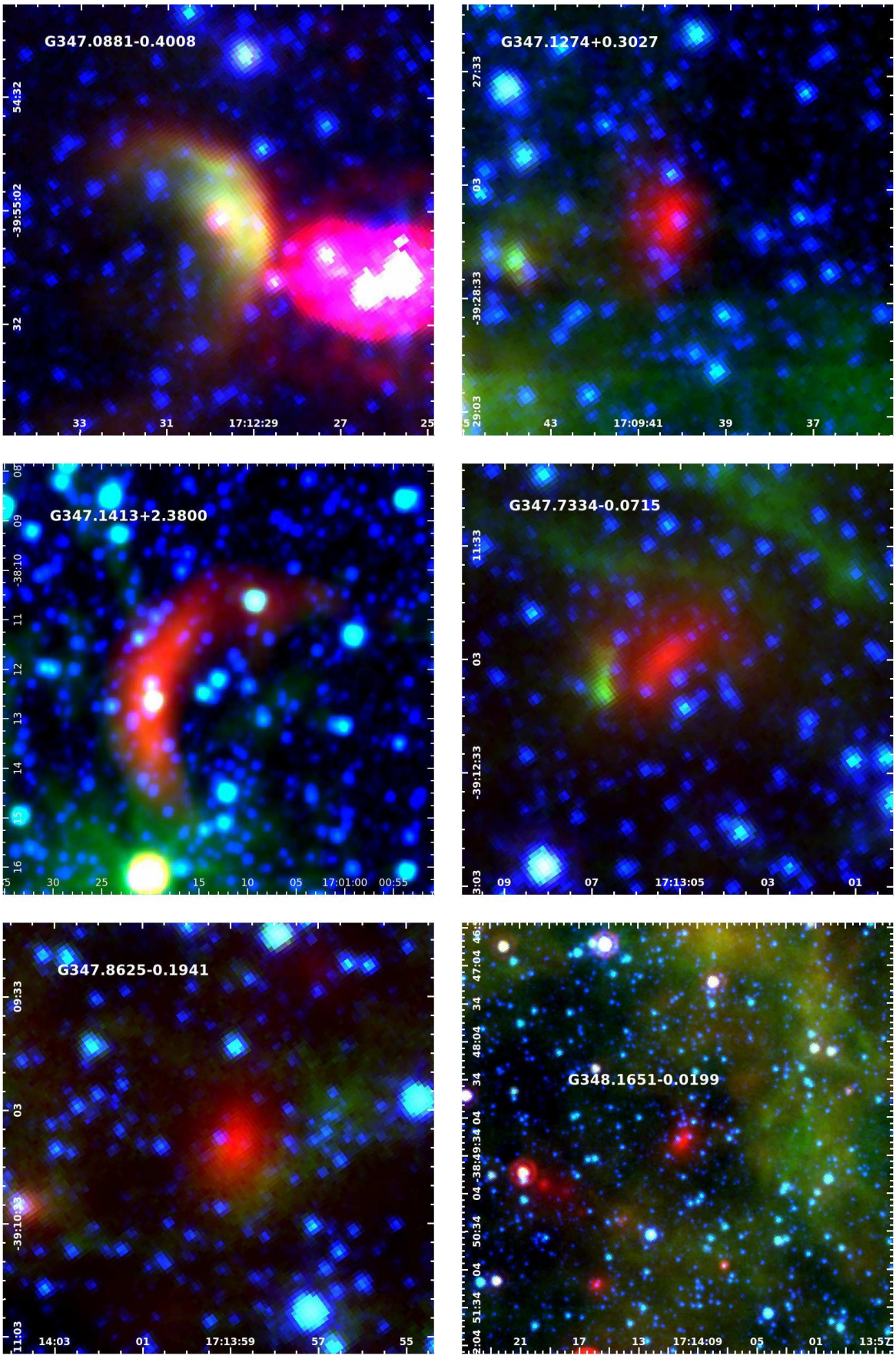
G347.0881-0.4008
G347.1274+0.3027
G347.1413+2.3800
G347.7334-0.0715
G347.8625-0.1941
G348.1651-0.0199

Figure A110.

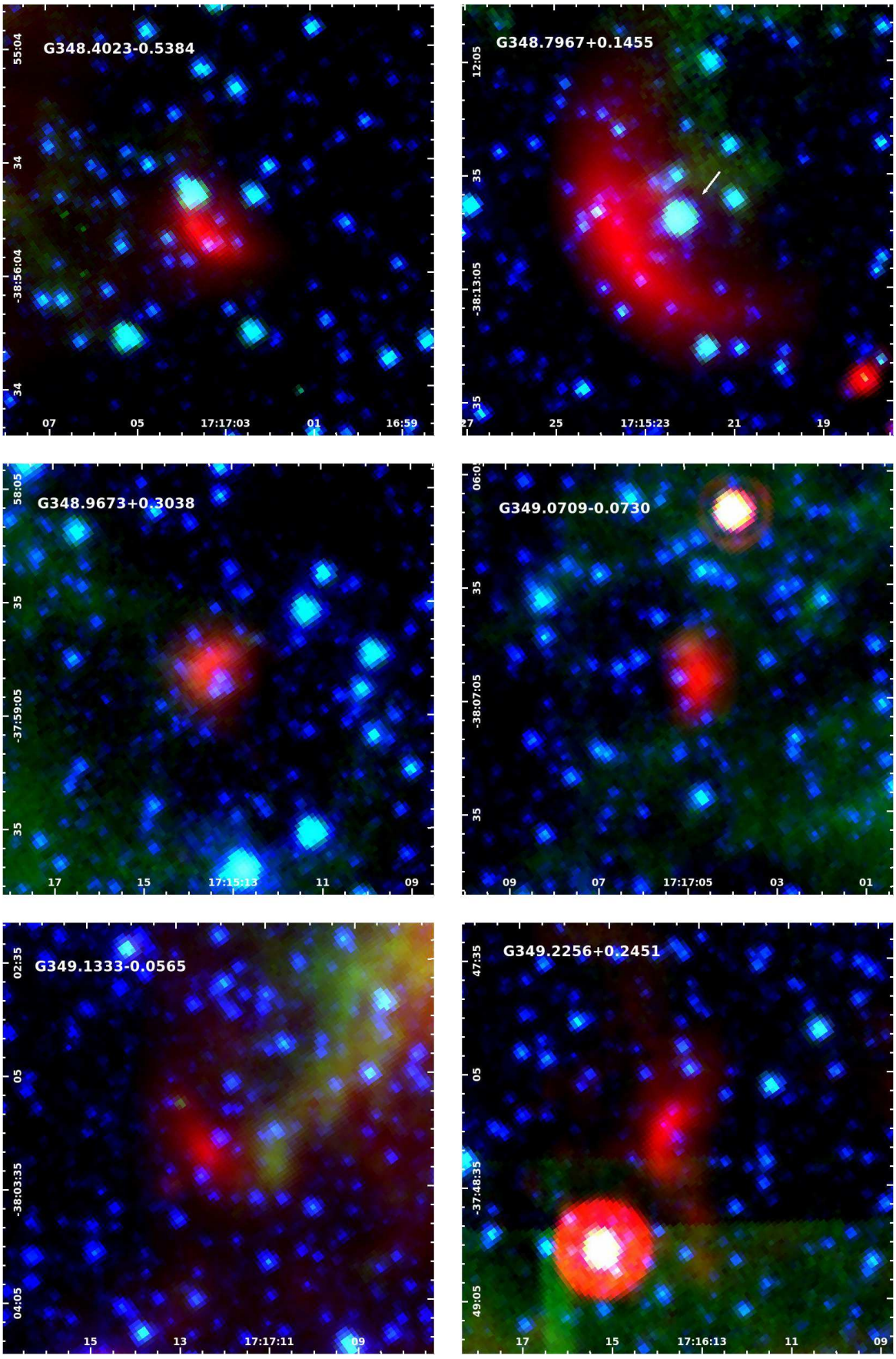
G348.4023-0.5384
55:04
34
-38:56:04
34
07
05
17:17:03
01
16:59
G348.7967+0.1455
12:05
35
-38:13:05
35
27
25
17:15:23
21
19
G348.9673+0.3038
58:05
35
-37:59:05
35
17
15
17:15:13
11
09
G349.0709-0.0730
06:05
35
-38:07:05
35
09
07
17:17:05
03
01
G349.1333-0.0565
02:35
05
-38:03:35
04:05
15
13
17:17:11
09
G349.2256+0.2451
47:35
05
-37:48:35
49:05
17
15
17:16:13
11
09

Figure A111.

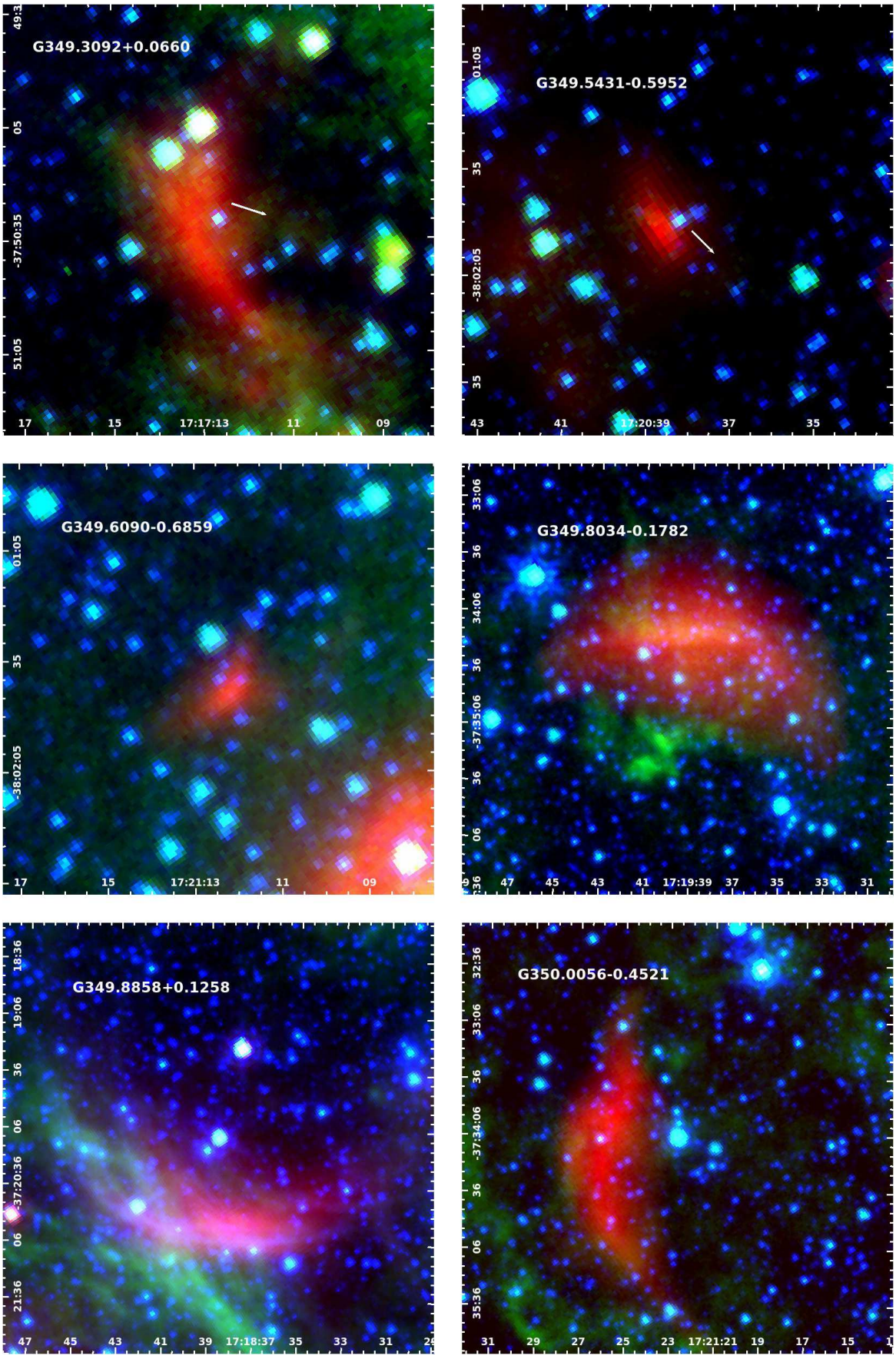
G349.3092+0.0660
G349.5431-0.5952
G349.6090-0.6859
G349.8034-0.1782
G349.8858+0.1258
G350.0056-0.4521

Figure A112.

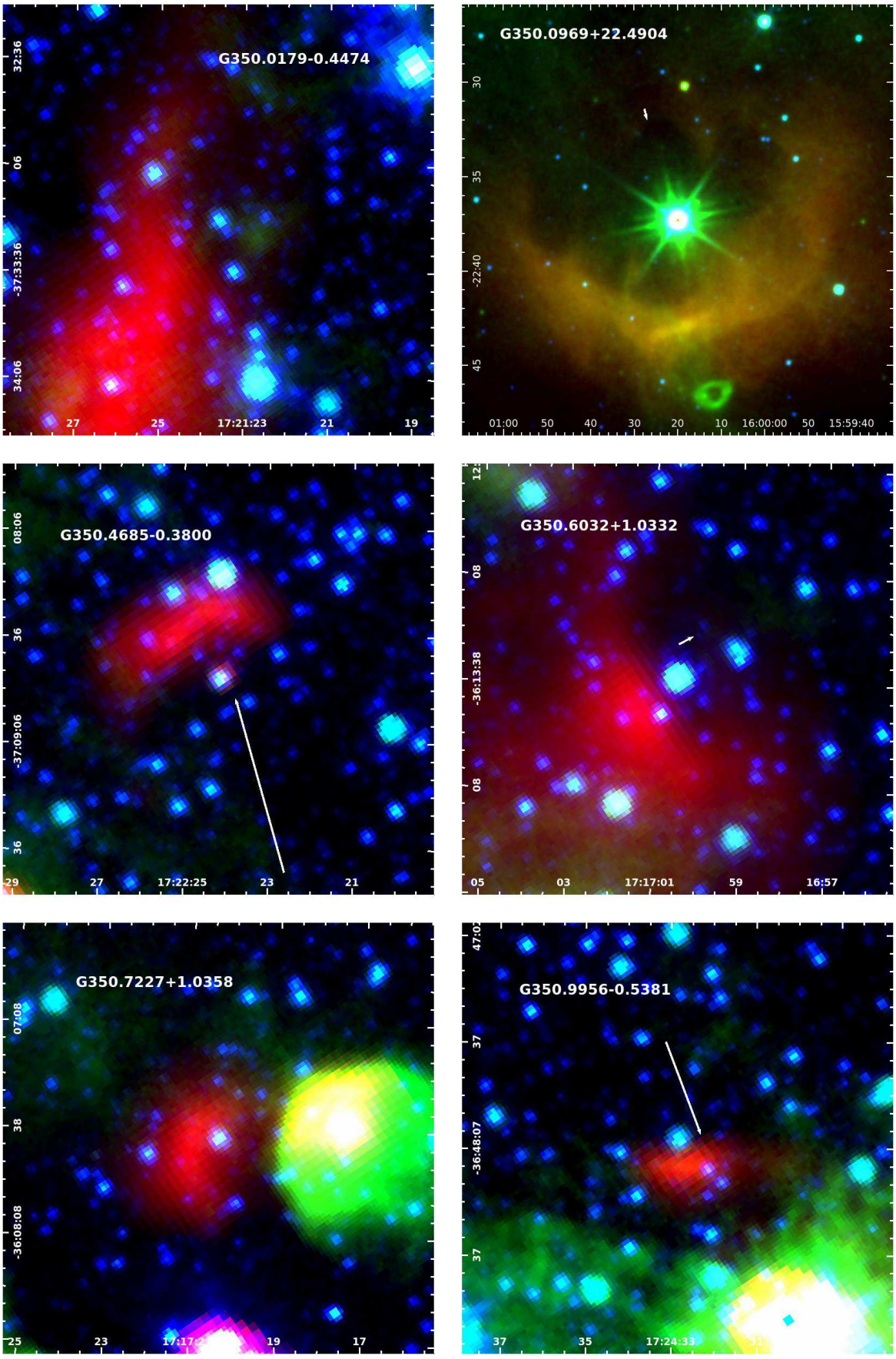
G350.0179-0.4474
G350.0969+22.4904
G350.4685-0.3800
G350.6032+1.0332
G350.7227+1.0358
G350.9956-0.5381

Figure A113.

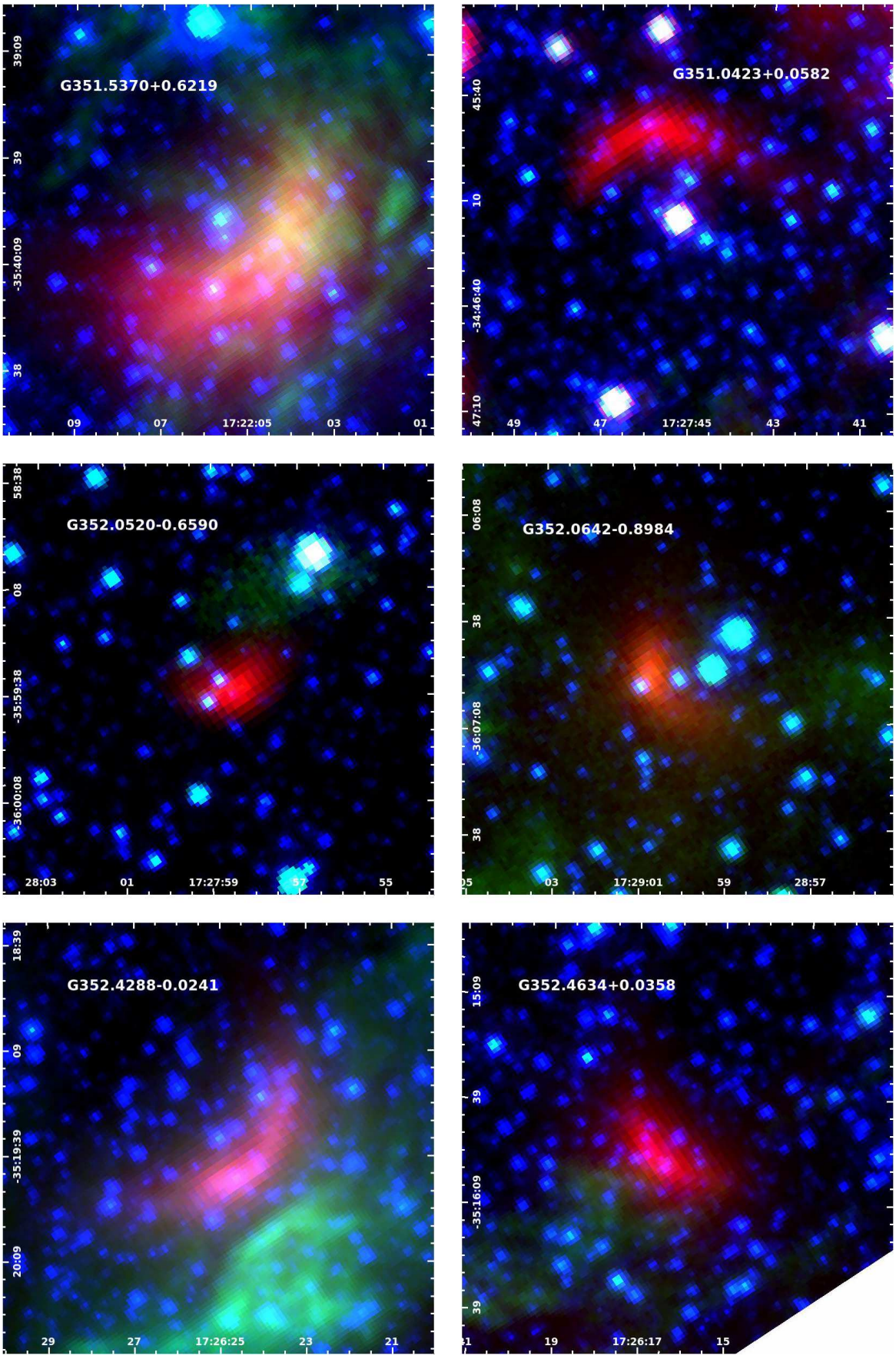
G351.5370+0.6219
39:09
39
-35:40:09
38
09
07
17:22:05
03
01
G351.0423+0.0582
45:40
10
-34:46:40
47:10
49
47
17:27:45
43
41
G352.0520-0.6590
58:38
08
-35:59:38
-36:00:08
28:03
01
17:27:59
57
55
G352.0642-0.8984
06:08
38
-36:07:08
38
03
17:29:01
59
28:57
G352.4288-0.0241
18:39
09
-35:19:39
20:09
29
27
17:26:25
23
21
G352.4634+0.0358
15:09
39
-35:16:09
39
19
17:26:17
15

Figure A114.

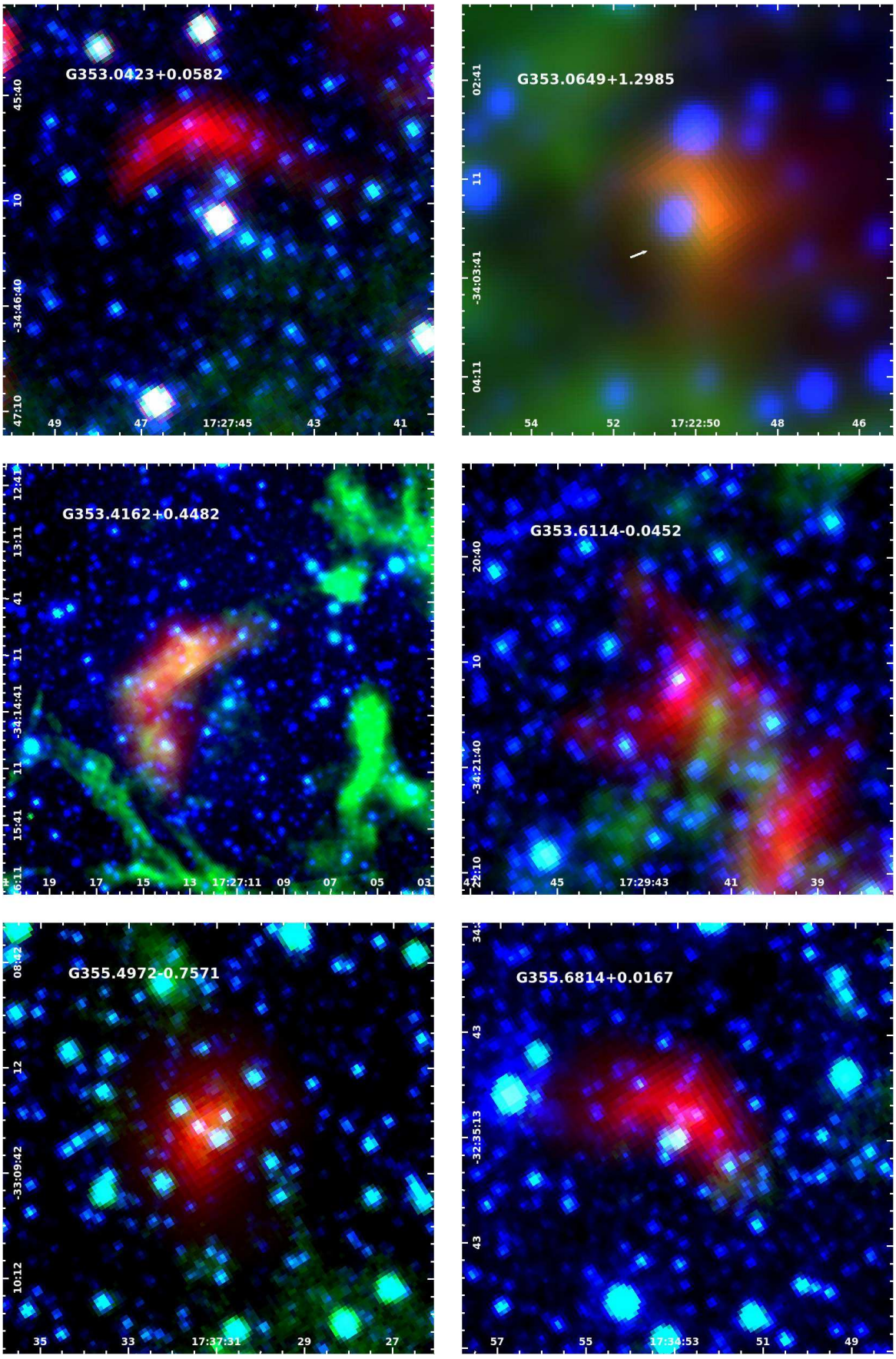
G353.0423+0.0582
G353.0649+1.2985
G353.4162+0.4482
G353.6114-0.0452
G355.4972-0.7571
G355.6814+0.0167

Figure A115.

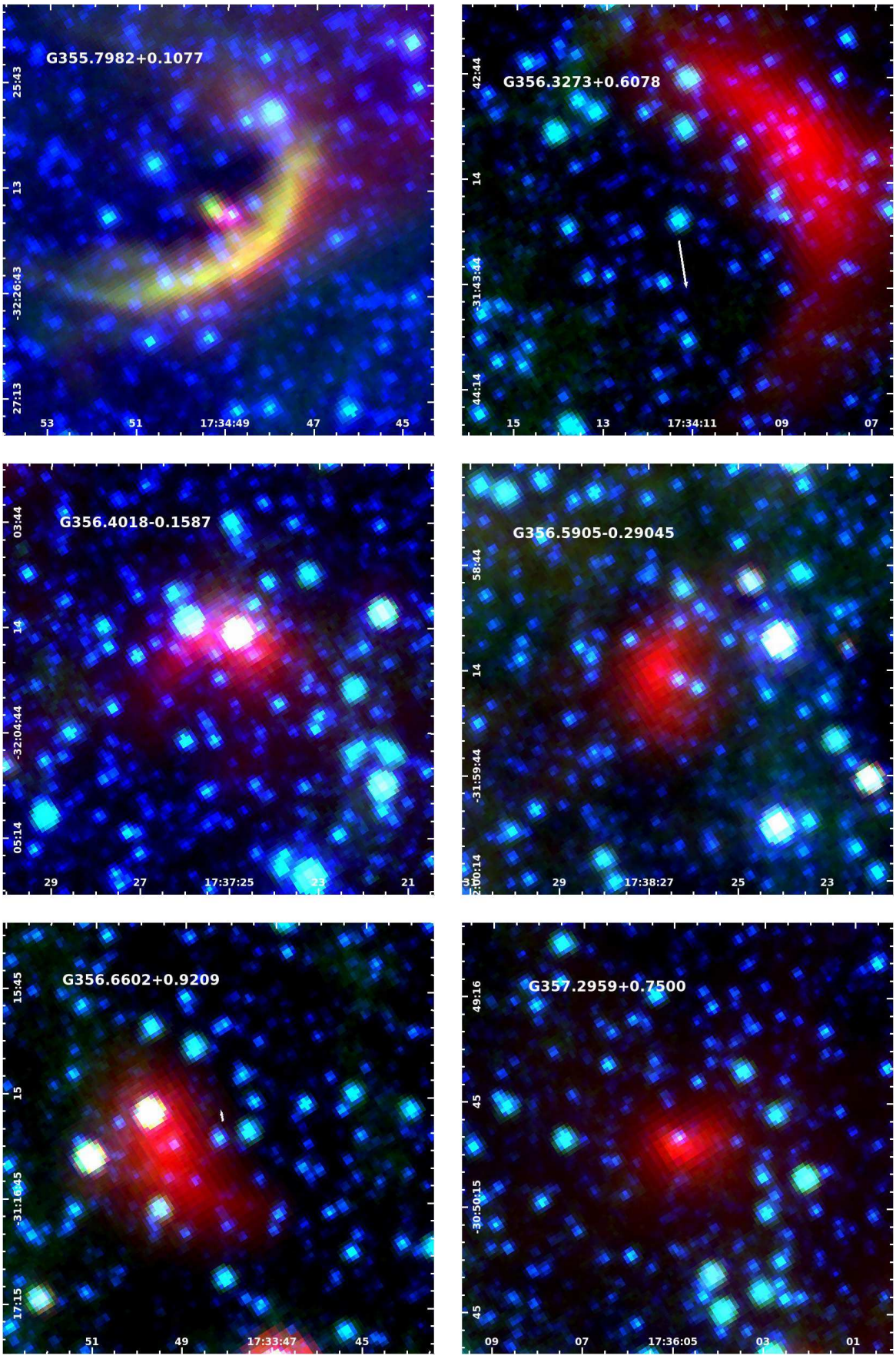
G355.7982+0.1077
25:43
13
-32:26:43
27:13
53
51
17:34:49
47
45
G356.3273+0.6078
42:44
14
-31:43:44
44:14
15
13
17:34:11
09
07
G356.4018-0.1587
03:44
14
-32:04:44
05:14
29
27
17:37:25
23
21
G356.5905-0.29045
58:44
14
-31:59:44
29
17:38:27
25
23
G356.6602+0.9209
15:45
15
-31:16:45
17:15
51
49
17:33:47
45
G357.2959+0.7500
49:16
45
-30:50:15
45
09
07
17:36:05
03
01

Figure A116.

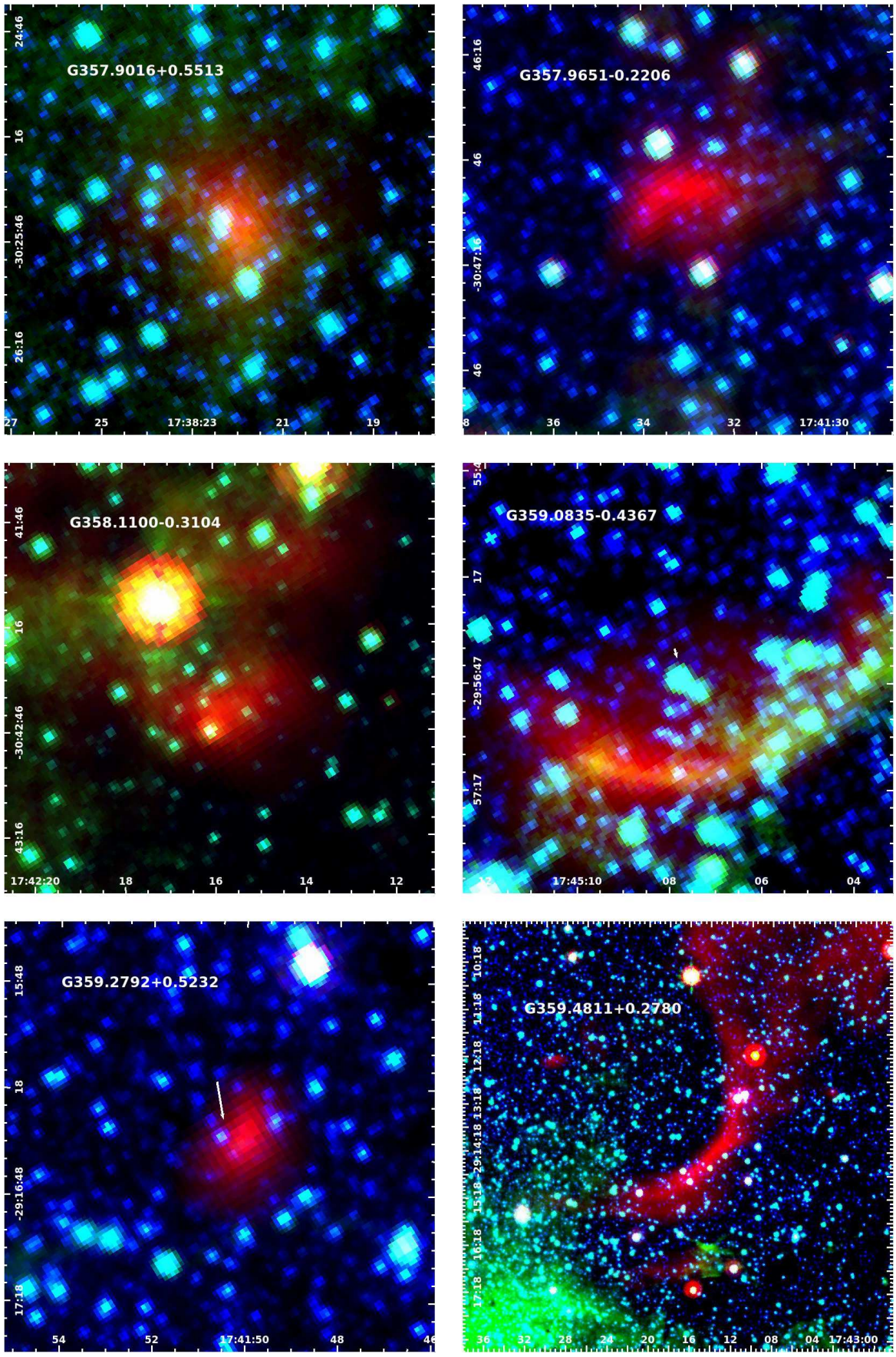
G357.9016+0.5513
G357.9651-0.2206
G358.1100-0.3104
G359.0835-0.4367
G359.2792+0.5232
G359.4811+0.2780

Figure A117.

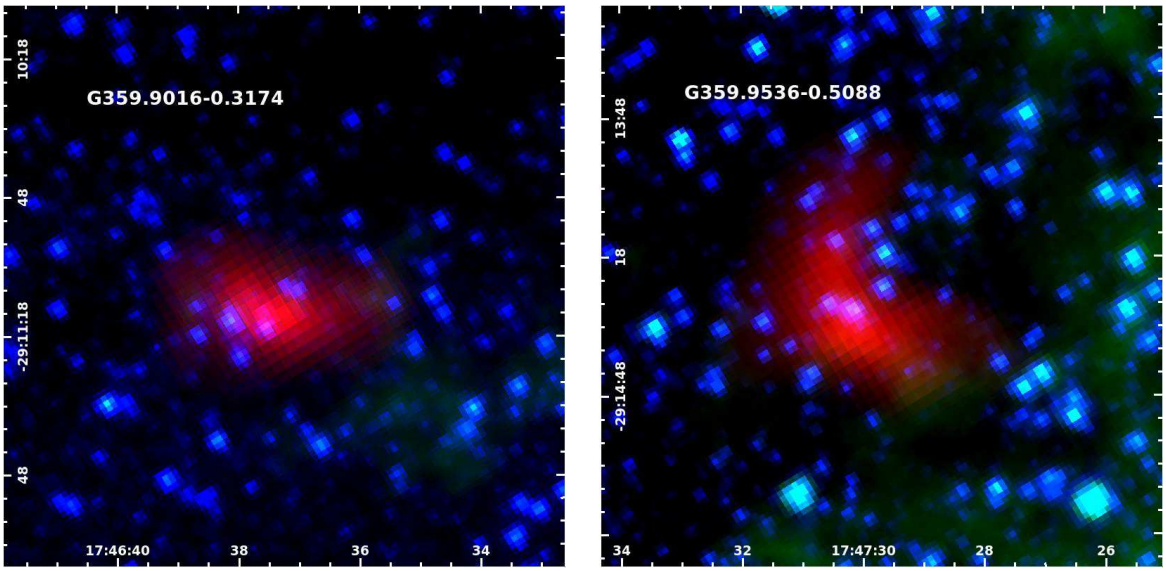
G359.9016-0.3174
10:18
48
-29:11:18
48
17:46:40
38
36
34
G359.9536-0.5088
13:48
18
-29:14:48
34
32
17:47:30
28
26

Figure A118.